

Atomic Hydrogen Dynamics and Neutral Depletion in a High Power Linear Plasma Device

Samuel Joseph Cousens

A thesis presented for the degree of
Doctor of Philosophy
of The Australian National University

Electronic Materials Engineering
Research School of Physics
The Australian National University

March 2020



Declaration

This thesis is an account of research undertaken between March 2015 and March 2020 at the Research School of Physics, ANU College of Science, The Australian National University, Canberra, Australia.

Except where acknowledged in the customary manner, all material presented in this thesis is, to the best of my knowledge, original and has not been submitted in whole or part for a degree in any university.

A handwritten signature in black ink, appearing to read "Samuel Joseph Cousens".

Samuel Joseph Cousens

March 13 2020

For those who inspire my imagination.

Acknowledgements

Firstly, I would like to acknowledge my supervisor, Cormac Corr. Your enthusiasm and knowledge have no limits. I thank you for your guidance, patience and positivity throughout the last five years. This thesis would not have been possible without your help and support.

Thank you to the staff of the plasma department that have always been there to share their knowledge and assist with the trickier questions. I would like to thank John Howard, Boyd Blackwell and Clive Michael. I wish to acknowledge the talented technical staff of the plasma department, especially Michael Blacksell for constant technical assistance and advice, who is never too busy to help students. Mark Gwynneth, Amy Shumack, and Tom Kitchen for their technical advice and assistance during this work.

A thank you to Jesse Santoso, whom I shared an office for many years. For the constant discussions about science, politics, pop culture and everything else. Juan Caneses for helping a new Ph.D. student to get started on this journey with useful advice and assistance. I also wish to thank the other postgraduate students in the department for their friendship throughout the years, Matt Thompson, Stuart Nulty, Alex Thorman, Romana Lester, Thomas Body, Ka Po (Danny) Tee, Campbell Strachan, Felicity Lee and Declan Pratt.

I would like to thank the Australian Government for their financial support of this research through the Australian Government Research Training Program (RTP) Scholarship.

I would like to thank my family for their continued support throughout my life. My parents and siblings especially for always being there for me.

I wish to acknowledge my friends in Tasmanian; Caitlyn, Bec, Brad, Ishka and Alex for their continued friendship.

Finally I wish to thank my fiancèe Samantha, who has put up with the long hours and unavailability over the past few years. Who without, I do not know how I would have made it through. You push me to do my best, keep me laughing and never let me get down.

Publications and Conferences

Publications

S. Cousens, J. Santoso, C. Corr *Depletion of atomic hydrogen in a high power helicon discharge* **Plasma Sources Science and Technology** **29**, 11(2020) 11LT01

T. Body, **S. Cousens**, J. Kirby, C. Corr *A volume-averaged model of nitrogen-hydrogen plasma chemistry to investigate ammonia production in a plasma-surface-interaction device* **Plasma Physics and Controlled Fusion** **60**, 7(2018) 1-16

Z. Chen, Y. Krasik, **S. Cousens**, A. Ambujakshan, C. Corr, X. Dai *Generation of underwater discharges inside gas bubbles using a 30-needles-to-plate electrode* **Journal of Applied Physics** **112**, 15(2017) 153303 7

Conference Presentations

Gaseous Electronics Meeting XXI 2020 - Canberra, Australia

36th ITPA Diagnostics Topical Group Meeting 2019 - Canberra, Australia

2nd Asia-Pacific Conference on Plasma Physics (AAPPS-DPP) 2018 - Kanazawa, Japan

Gaseous Electronics Meeting XX 2018 - Magnetic Island, Australia

Australian Institute of Physics Congress 2017 - Brisbane, Australia

Gaseous Electronics Meeting XIX 2016 - Geelong, Australia

Awards

2nd Asia-Pacific Conference on Plasma Physics (AAPPS-DPP) 2018 - Student Poster Prize - Basic and Fundamental Plasmas

Abstract

Neutral particles are an important constituent of low temperature plasma. Neutral particles are involved in collisions in the plasma, where they can form new species and are an energy and momentum sink. However, there are few methods that make direct measurements of neutral species in the plasma.

A two-photon absorption laser-induced fluorescence (TALIF) diagnostic is established to investigate the properties of neutral atomic hydrogen in a high density pulsed plasma. A Nd:YAG-pumped dye laser at 205.1nm is used to directly probe the ground state of atomic hydrogen, by monitoring the fluorescence at 656nm. The TALIF diagnostic is capable of making both spatially and temporally resolved measurements of the atomic hydrogen.

The TALIF diagnostic is used to examine the atomic hydrogen densities and temperatures in high power (1-20kW) discharges in the MAGnetised Plasma Interaction Experiment (MAGPIE) helicon device. Neutral atomic hydrogen is observed to decrease in density above 5kW applied RF power, where the plasma pressure becomes comparable to the gas pressure. This decrease in density is explained to be due to neutral depletion of the atomic hydrogen in the centre of the chamber, which to the author's knowledge are the first experimental measurements of neutral depletion of hydrogen in a linear plasma device.

Temporal measurements in the afterglow of the higher power ($>5\text{kW}$) plasma discharge show a replenishment of atomic hydrogen in the early afterglow. This replenishment is observed to be consistent with depletion of atomic hydrogen during the discharge and is due to the neutrals flowing back in to the depleted regions after

the plasma has decayed. Radial measurements show a slight increase in atomic hydrogen further from the plasma core.

Atomic hydrogen is shown to display increasing temperature with higher applied powers with a constant radial temperature profile. There is no observed evidence of a secondary hotter population of atomic hydrogen.

A two-state decay of atomic hydrogen after the plasma discharge is observed at lower applied power (1kW). It is determined that different processes account for the two different decay rates with the second slower decay rate being due to atomic losses at the chamber walls. A single decay rate is observed at the higher powers which is also explained to be due to the same process.

Table of Contents

Declaration	ii
Dedication	iii
Acknowledgements	vi
Publications and Conferences	ix
Abstract	xi
1 Introduction	1
1.1 High Density Plasma Devices	1
1.1.1 Fusion Energy	2
1.1.2 Negative Ion Sources for Neutral Beam Injection Systems	7
1.1.3 Wakefield Accelerators	9
1.2 Linear Plasma Devices	10
1.2.1 DC Plasma Discharge Devices	10
1.2.2 Radio Frequency Plasma Generation	14
1.3 Hydrogen Plasmas	16
1.3.1 Collisions	17
1.3.2 Hydrogen Reactions	18
1.4 Neutral Behaviour in Plasma Devices	20
1.4.1 Measuring Neutral Species	20

TABLE OF CONTENTS

1.4.2	Neutral Depletion	25
1.5	Thesis Structure	28
2	The MAGPIE Helicon Plasma Device	31
2.1	Magnetized Plasma Interaction Experiment - MAGPIE	31
2.1.1	Chamber and Design	32
2.1.2	RF Power System	35
2.1.3	Magnetic Field Configuration	37
2.1.4	Gas and Pumping System	39
2.2	Experimental Uses	42
2.2.1	Device for Studying Plasma-Surface Interactions	42
2.2.2	Diagnostic Development and General Plasma Studies	43
2.3	Diagnostics	43
2.3.1	Langmuir Probe	44
2.3.2	Optical Emission Spectroscopy	47
2.4	Summary	48
3	Two-Photon Absorption Laser-Induced Fluorescence Diagnostic	49
3.1	Basic Theory	50
3.1.1	Atomic Hydrogen TALIF	52
3.2	Diagnostic Set-Up	53
3.2.1	Laser Set-up	55
3.2.2	Detection Set-Up	59
3.2.3	Data Acquisition and System Control	61
3.2.4	Signal Analysis	65
3.3	Calculations and Calibrations	66
3.3.1	Density Calculations	67
3.3.2	Temperature Calculations and Spectral Features	70

TABLE OF CONTENTS

3.3.3	Velocity Calculation	84
3.3.4	Lifetimes and Decay Constants	85
3.4	Summary	87
4	Atomic Hydrogen and Neutral Depletion	89
4.1	Plasma Parameters	90
4.2	Atomic Hydrogen Power Scans	99
4.2.1	Power Dependence	100
4.2.2	Pulse Length	101
4.2.3	Atomic Hydrogen Temperature	103
4.2.4	Molecular Gas Temperature	107
4.3	Depletion Dynamics	108
4.3.1	Depletion Due to Ionisation	110
4.3.2	Depletion Due to Gas Heating	112
4.3.3	Depletion Due to Plasma Pressure	114
4.4	Summary	118
5	Temporal and Radial Atomic Hydrogen Dynamics	120
5.1	Time Resolved Afterglow Dynamics	121
5.1.1	Plasma Afterglow Dynamics	121
5.1.2	Atomic Hydrogen Afterglow Density	124
5.1.3	Atomic Hydrogen Temperature	128
5.1.4	Loss Mechanisms of Atomic Hydrogen	131
5.1.5	Atomic Hydrogen Afterglow Pressure	135
5.2	Time Resolved Radial Profiles	137
5.2.1	Radial Plasma Density	137
5.2.2	Radial Atomic Hydrogen Density	144
5.2.3	Radial Atomic Hydrogen Temperature Profiles	153

TABLE OF CONTENTS

5.3 Summary of Neutral Behaviour and Depletion	157
6 Conclusion	160
6.1 Two-Photon Absorbed Laser-Induced Fluorescence Diagnostic	160
6.2 Atomic Hydrogen Dynamics	161
6.3 Future Work	163
A TALIF Dye Recipe	169
Bibliography	170

Chapter 1

Introduction

High density linear plasma devices such as the helicon that can produce plasma density above 10^{19}m^{-3} with input powers of only a few kW are very promising for a range of applications.^[1] An issue with the helicon plasma source is the observed density limit where an apparent maximum density is achieved due to complete ionisation of the neutral species.^[2] This density limit has been attributed to neutral depletion. Neutral depletion is where the neutral density is reduced by the interactions with the plasma.^[3] This chapter will introduce high density plasma devices providing a few examples where high density plasma sources are used including the fusion device ITER. The role that neutral species play in plasmas and the current methods of measuring neutral species in the plasma with their advantages and disadvantages will be presented. Following this will be a detailed discussion of the previous research on neutral depletion. Finally, the introduction concludes with a layout of this thesis.

1.1 High Density Plasma Devices

Plasma devices that can achieve high plasma densities ($n_e = >10^{19}\text{m}^{-3}$) are highly advantageous to plasma research across many applications from plasma processing to nuclear fusion and plasma thrusters. A few of the potential applications of the

1.1. HIGH DENSITY PLASMA DEVICES

high density plasma sources are discussed. Special consideration is given to hydrogen plasmas and the hydrogen species that are present in such plasmas.

1.1.1 Fusion Energy

Since the mid 1900s fusion energy has been a dream of providing limitless clean energy and today has become one of the largest global efforts in physics. As the world becomes more conscious of the effects that traditional methods of energy production, such as the burning of fossil fuels, have on the environment and climate, alternative sources of energy need to be found. Yearly increases in energy demand also greatly compound the issue with the International Energy Agency reporting a 117% increase in energy demand in 2017 since 1990 levels.^[4]

Nuclear fusion provides a possible solution to the world's growing energy demands, offering virtually limitless electricity production that is also environmentally acceptable.^[5] There is a large amount of energy stored inside atoms that can be utilised to generate electricity. There are two main methods to extract the nuclear energy stored within atoms; fission and fusion. The current generation of nuclear power plants use the fission process; where heavy nuclei such as uranium are split into two lighter nuclei. In the fission reaction, the excess energy is carried away in the form of high energy neutrons which are used to generate steam and drive a turbine to produce electricity.

Nuclear fusion is the opposite process whereby two lighter nuclei fuse to create a single heavier nuclei and energetic neutrons. It is this process that occurs within stars to produce and release energy. A worldwide collaboration including China, India, Japan, Korea, Russia, USA and the European Union (EU) are working to build a prototype fusion device, ITER (formally standing for International Thermonuclear Experimental Reactor), at Cadarache in southern France.^[6] ITER will be the first realisation of the global collaboration towards nuclear fusion and aims to demonstrate the feasibility of electricity production from a nuclear fusion reactor.^[7] ITER is designed to provide 500MW output for an input of 50MW, that is an energy gain, $Q \geq 10$. A schematic of ITER is shown in Figure 1.1. The main

1.1. HIGH DENSITY PLASMA DEVICES

vacuum vessel is shown in yellow on the left half of the schematic where the plasma is confined. At the bottom of the main vacuum vessel is the divertor which is shown in the lighter yellow colour.

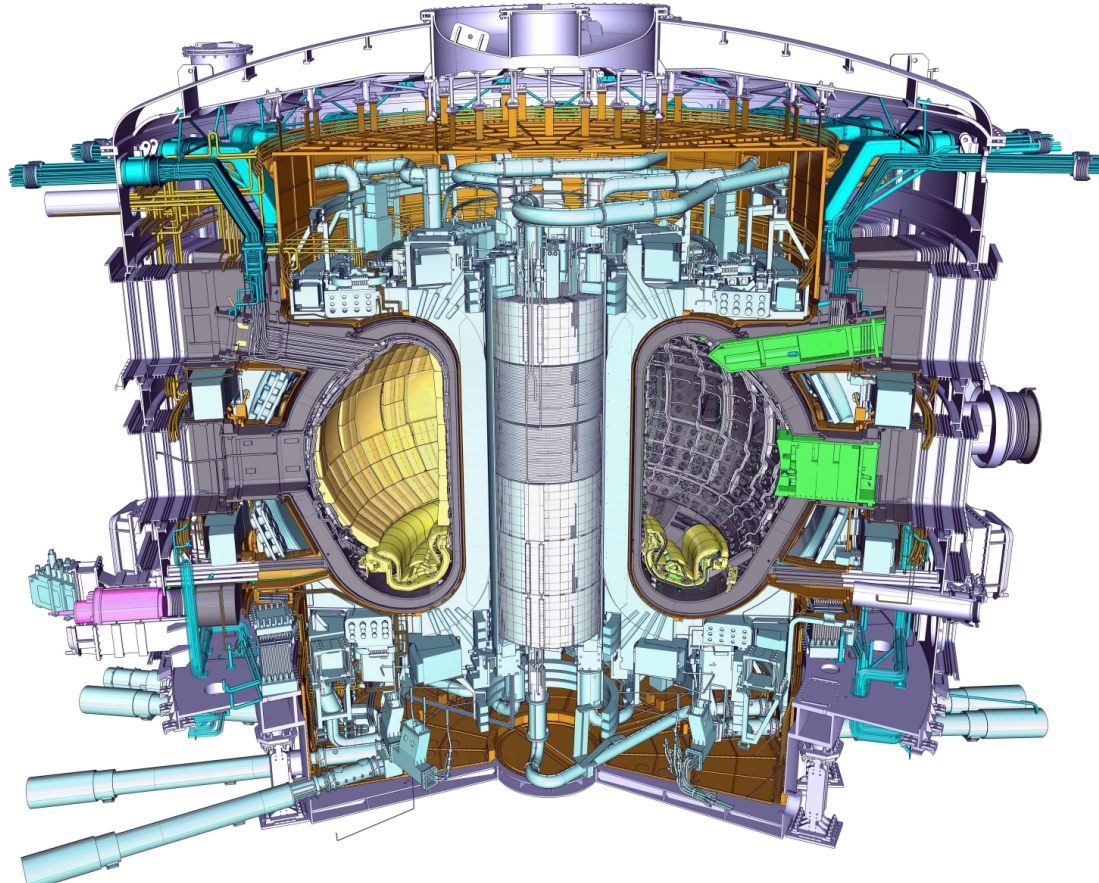


Figure 1.1: Schematic of the ITER tokamak. Reproduced from [8]

Fusion Reactor Designs

The reaction of most interest is the fusion of hydrogen and deuterium:



This reaction requires temperatures in excess of 150 million kelvin.[9] Under such extreme conditions, the fusion plasma cannot be directly contained in a conven-

1.1. HIGH DENSITY PLASMA DEVICES

tional vessel as the wall materials would rapidly degrade. It is therefore necessary that fusion plasmas are confined so that they do not make direct contact with the reactor walls. The main method by which this is achieved is through magnetic confinement, where the magentic field lines guide the plasma along a closed loop within the reactor chamber. Magnetic confinement reactors can be divided into toroidal tokamak designs, of which ITER is such a design, and the toroidal helix stellarator design, such as Wendelstein 7-X[10] at the Max Planck Institute for Plasma Physics in Germany.

The tokamak reactor design consists of a large toroid shaped main vacuum vessel which the plasma is confined within. Two sets of super conducting magnetic coils, the toroidal and poloidal coils, produce closed magnetic flux surfaces within the fusion main chamber to confine the plasma away from the chamber walls.[11]

However, plasma-surface interactions cannot entirely be removed and there are two distinct surface regions within the ITER reactor that will directly face the plasma. The first is the reactor walls which is the first physical boundary to the plasma. The plasma-facing first walls will be impacted by neutrons from the DT fusion reaction (Equation 1.1) that are not confined by the magnetic field. The blanket of the first wall will use energy from the neutrons to provide heat for electricity generation and thermal and nuclear shielding to the vacuum vessel and further external components.[12, 13]

The second region in the ITER tokamak where the wall will be in direct contact with the plasma is the divertor. The plasma is deliberately brought into contact with the divertor and neutralised to extract both the waste helium from the DT fusion reaction and excess heat.[9]

The Divertor and Plasma-Material Interactions

The magnetic field in ITER has been designed to bring particles that drift outside of the confined plasma in the core to the divertor.[14] The plasma that is directed into the divertor will have an electron temperature $\sim 1\text{-}10\text{eV}$ while the wall will be

1.1. HIGH DENSITY PLASMA DEVICES

at a cooled temperature ($\sim 1000\text{K}$) compared to the hot plasma in the core. The lower surface temperature is necessary to protect the integrity of the plasma facing components (PFCs) on the divertor and extend the lifespan of these materials. A schematic of the ITER divertor is shown in Figure 1.2, the divertor can also be seen at the bottom of the vacuum vessel in Figure 1.1.

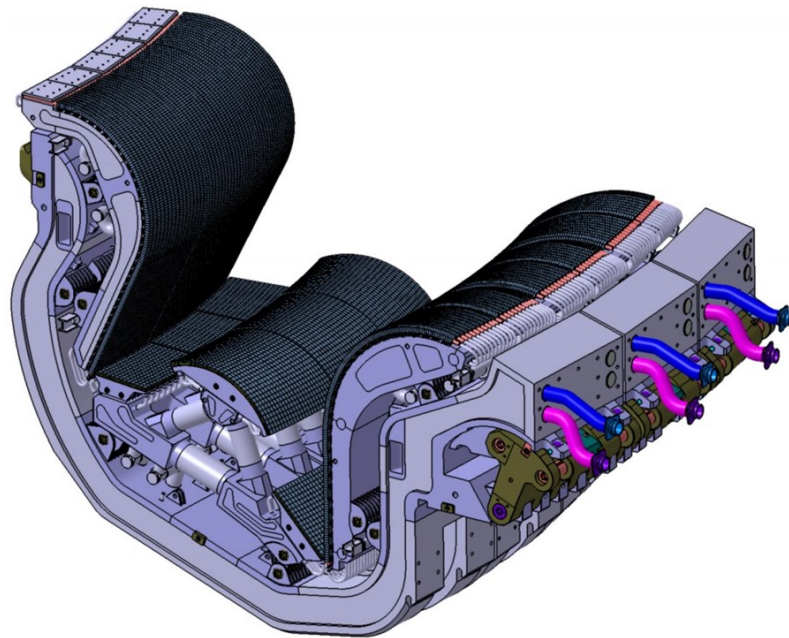


Figure 1.2: Schematic of the ITER divertor. Reproduced from [6]

Even though the plasma is significantly cooler in the divertor compared to the plasma core, the particle and heat flux are still high enough to cause significant erosion of the plasma facing components. Sputtering of materials from the surfaces can contaminate the fusion core, leading to radiative cooling and reducing the fusion reaction.[14] van Eck *et al.* provides a summary of the typical conditions that will be expected in the divertor of ITER.[15] Electron densities of approximately 10^{21}m^{-3} with an electron temperature of 1-5eV. Particles fluxes of $10^{24}\text{-}10^{25}\text{m}^{-2}\text{s}^{-1}$ are expected on the divertor with heat fluxes of 10 MW m^{-2} raising the surface temperatures up to 1000K.[15, 16] It has been decided that the divertor will be constructed from tungsten, due to its reduced sputtering rate and low tritium retention.[17] However under transient heat loads the melting of tungsten and the ejection of material is an ongoing concern.[12]

1.1. HIGH DENSITY PLASMA DEVICES

The magnetic field lines in ITER are shown in Figure 1.3. The plasma is confined within the closed magnetic field loops. The cross section of the magnetic fields can be seen close to the divertor, this is called the 'separatrix', charged particles on the outside of this last closed loop will be directed into the divertor region of the tokamak.

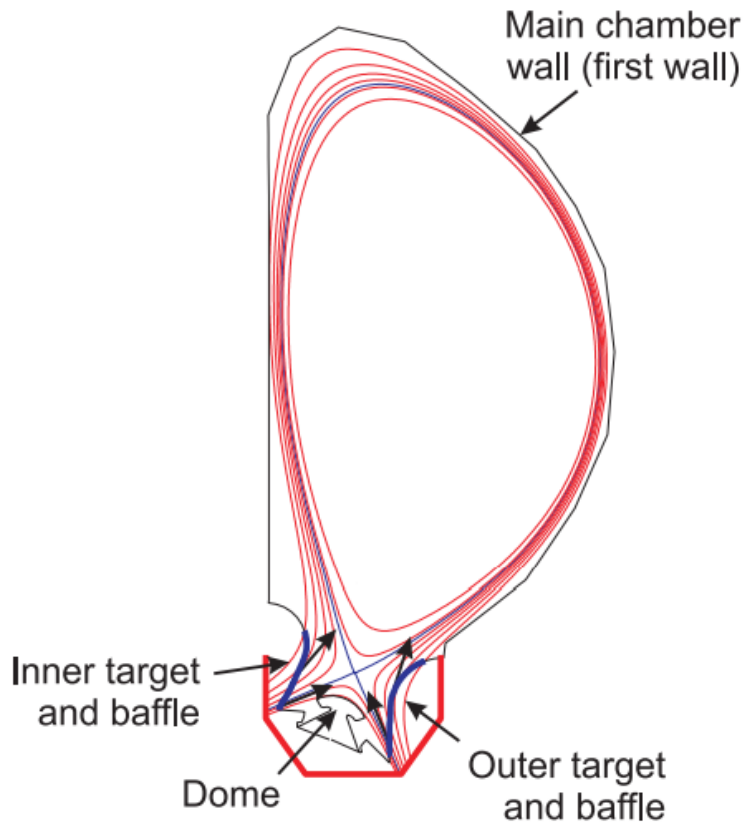


Figure 1.3: Schematic of the mangetic field lines in ITER. Reproduced from [18]

One of the methods of cooling the incoming plasma is via seeding of neutral gas impurities into the divertor region creating a 'detached regime'. These neutral species are excited by collisions with the plasma and are excited to higher energy levels, absorbing energy from and cooling the plasma. The neutral species direct the energy away in the form of radiation, hence this method is called radiative cooling. The neutral candidates for radiative cooling in the divertors are focused on noble gases and nitrogen.[19, 20] Limiting the contamination of the core from these added impurities is an ongoing area of research.[21, 22, 23] Another concern is the formation of new compounds from the added species, such as ammonia, when nitrogen is used as the cooling species. Ammonia has been shown to form in plasma

1.1. HIGH DENSITY PLASMA DEVICES

that comprise of mixed hydrogen and nitrogen gases.[24]

Various linear plasma devices are able to investigate fusion-relevant plasma effects on materials and the applicability of radiative cooling and detachment in high power linear plasma devices around the world. Examples includes MAGNUM PSI[25] and PISCES[26]. Due to the larger costs associated with building and operating tokamaks, it is advantageous to conduct more de-localised and varied research on smaller high power plasma devices. The MAGnetised Plasma Interaction Experiment (MAGPIE) linear helicon plasma device has been constructed at The Australian National University to investigate high power plasma physics in linear devices and plasma-material interactions.[27] The MAGPIE device is discussed in greater detail in Chapter 2.

1.1.2 Negative Ion Sources for Neutral Beam Injection Systems

Neutral beam injection systems work by accelerating ions to high energies before neutralising them to create the energetic neutral beam. The general neutralisation process is achieved by passing accelerated ions through a neutral gas and the ensuring collisions transfer electrons to the high energy ions.[28] This neutralisation process is not very efficient for positive ions at high energies ($>100\text{keV}$), however the process remains efficient for negative ions.[29] Some examples of current neutral beam injection systems are BATMAN[30, 31] and ELISE[32] which is to be the ion source for ITER. These neutral beam injection systems require high throughput negative ion sources that are a high priority for heating magnetically confined fusion devices.

Conventional negative ion sources use an inductively coupled plasma (ICP) source as shown in the simplified schematic in Figure 1.4. The general operation of a negative hydrogen ion source can be found in [33]. In the current generation of negative ion sources a caesium oven is located directly under the source to continuously evaporate caesium into the plasma chamber to lower the surface work function for negative ion production at surfaces. Following is a transverse filter to

1.1. HIGH DENSITY PLASMA DEVICES

cool and redirect electrons, a plasma grid which is positively biased to provide a surface for negative ion production and finally an extraction grid is used to accelerate the negative ions.

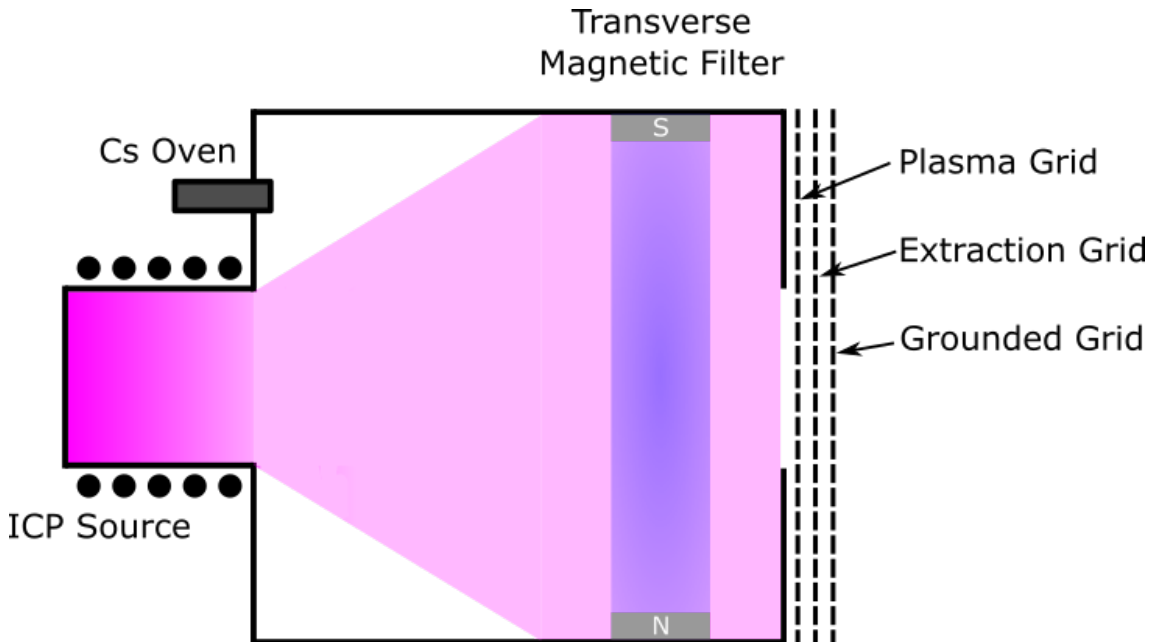


Figure 1.4: Simplified schematic of a typical negative ion source.

These devices produce negative ions by surface localised reactions that requires the continuous surface treatment with caesium.[34]. Caesium has the lowest work function of any of the metals and most readily gives up an electron to form negative ions from neutral species such as molecular hydrogen. These ICP sources are expected to only just meet the requirement for ITER and caesium has its own problems, such as achieving uniform caesium layers over the large grid to provide stable and uniform current densities.[33]

Another possible method for negative-ion production is to use higher density plasma devices, such as helicon devices, which can achieve significantly higher densities than an ICP device. These higher densities coupled with lower temperatures are shown to enhance the rate of negative ion production[35] and may potentially provide high enough densities of atomic and ionic hydrogen that caesiation requires.[36, 37] Helicon plasma sources with 20kW applied power are able to achieve densities that requires 100kW in an ICP source. This is due to better power cou-

pling in helicon devices.[38] The possibility of helicon sources as negative ion sources has encouraged numerous groups to investigate the validity of helicon negative ion sources.[39, 40, 41, 42]

1.1.3 Wakefield Accelerators

Over the last 50 years accelerators have been used to probe the fundamental structure of the physical world. This has recently cumulated in the discovery of the Higgs Boson in the Large Hadron Collider (LHC)[43, 44], a 26.7km circumference accelerator at The European Organization for Nuclear Research (CERN), Geneva.

Today's accelerators are limited by an accelerating gradient of 100MeV m^{-1} by RF breakdown and degradation of the cavity walls.[45] Therefore to achieve tera-electron volt (TeV) energies of particles, tens of kilometres are required. Circular geometry accelerators are capable of achieving these energies but synchrotron radiation also poses limitations that require accelerators on the scale of 100km.[46]

Plasma-based accelerators are seen as the next generation of accelerators due to plasma being able to support electric fields that are orders of magnitude larger than current accelerators.[47] The plasma is able to support waves or wakes that travel at velocities near to the speed of light, which are excellent for acceleration particles to relativistic energies.[45]

The Advanced Proton Driven Plasma Wakefield Acceleration Experiment (AWAKE) at CERN will be the first proton-driven wakefield experiment in the world.[48] A detailed description of the AWAKE experiment can be found in [49]. The AWAKE experiment will test the principle proof-of-concept of the wakefield acceleration created from the proton-driven plasma, however there is still a lot of future research required for these wakefield accelerators. The key issues have been stated as requiring shorter proton pulses and scalable plasma sources.[45] High power helicon plasma sources are a current area of research for the next generation plasma source for wakefield accelerators. [50]

1.2 Linear Plasma Devices

Linear plasma devices are extremely useful for studying plasma physics and behaviour in a divertor type environment, as well as for developing high density plasma. While linear plasma devices will not be able to completely match the complexity of a tokamak divertor, they can come very close to the relevant plasma parameters for plasma-material interactions.[51] The divertor of the ITER tokamak needs to withstand steady-state heat fluxes up to 10MWm^{-2} [52], with electron densities of 10^{21}m^{-3} , electron temperatures up to 10eV and ion fluxes of $\sim 10^{24}\text{-}10^{25}\text{m}^{-2}\text{s}^{-1}$.[53] Various linear devices are able to achieve the majority of these conditions. Linear devices allow ease of study, are designed with easily removable component, have easily controlled plasma parameter, configurable magnetic geometries and excellent diagnostic access. High density plasma devices generally allow steady-state operation and the higher accessibility of linear devices allows measurements to be conducted in a more cost effective and easier way.[54] It is due to these reasons and the relatively low cost, compared to tokamak devices, that make linear plasma devices an excellent choice for plasma studies.

1.2.1 DC Plasma Discharge Devices

There are a collection of DC plasma sources that are capable of producing high density plasma. They operate at high pressures (1Torr) and require a complex differential pumping system. These include cascaded arc discharges such as MAGNUM-PSI at the Eindhoven Institute of Technology, The Netherlands[55, 56], reflex arc discharge source in NAGDIS-II at Nagoya University, Japan[57] and DC arc sources such as PISCES-B at The University of California San Diego[26]. A list of these devices with their operating conditions, discharge type, typical electron densities and temperatures, and ion fluxes are shown in Table 1.1.

Table 1.1: Parameters of high density linear plasma devices. The expected conditions in the ITER divertor is included for comparison.

Device Name	Discharge Type	Electron Density (m^{-3})	Electron Temperature (eV)	Ion Flux ($\text{m}^{-2}\text{s}^{-1}$)	Magnetic Field Strength (T)	Pulse length (s)	Reference
NAGDIS-II (Nagoya University, Japan)	Cusp arc	up to 10^{20}	0.1-10	10^{23}	0.25	Steady state	[57]
PISCES-A (UCSD, USA)	Reflex arc	10^{16} - 10^{19}	3-20	10^{20} - 10^{22}	0.02	Steady state	[58, 59]
PISCES-B (UCSD, USA)	Reflex arc	10^{16} - 10^{19}	3-50	10^{20} - 10^{23}	0.04	Steady state	[60, 26]
PSI-2 (FZJ, Germany)	DC arc	10^{16} - 10^{19}	1-40	10^{20} - 10^{23}	0.1	Steady state	[61, 62]
MAGNUM-PSI (FOM-DIFFER, The Netherlands)	Cascaded arc	10^{19} - 10^{21}	0.1-10	10^{23} - 10^{25}	0.4-1.7	110 depending on B field/ steady state	[63, 64]
MPEX (ORNL, USA)	Helicon	up to 6×10^{19}	1-10	10^{23}	0.6-1.4	1	[65]
CSDX (UCSD, USA)	Helicon	up to 2×10^{19}	3-6	10^{21}	up to 0.24	Steady state	[66]
ITER divertor	Tokamak	10^{20} - 10^{21}	1-10	10^{24} - 10^{25}	5	500	[67]

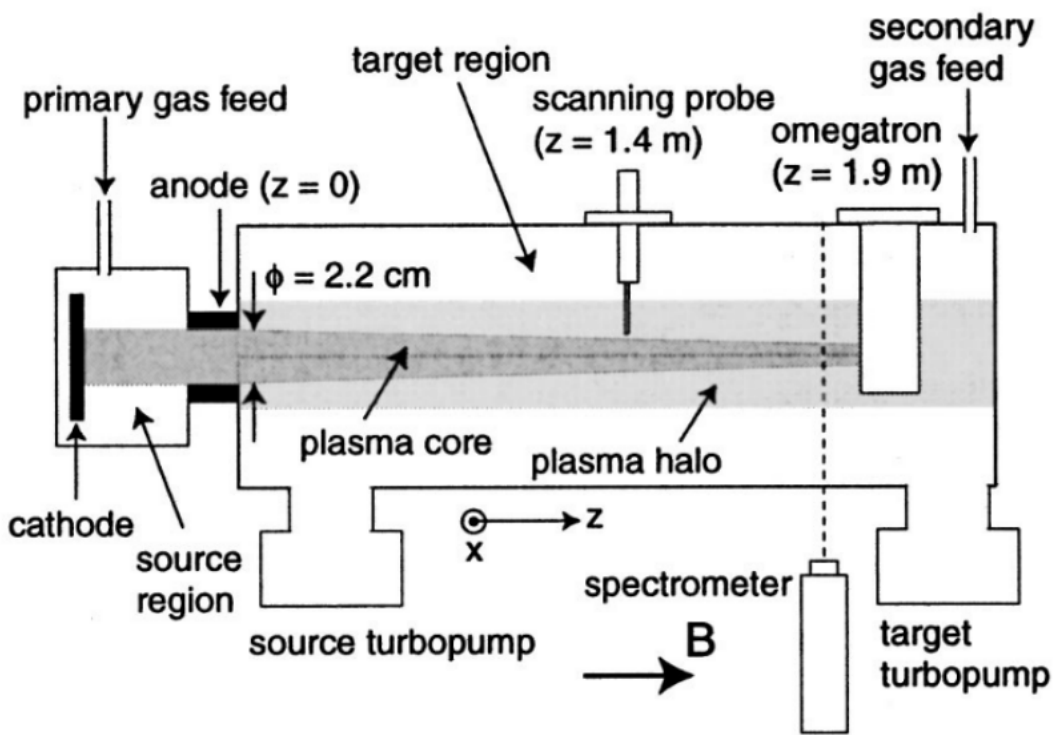


Figure 1.5: Schematic of NAGDIS-II. Reproduced from [68]

In NAGDIS-II, the plasma is generated in the source region by a steady-state power supply that drives a DC current between a heated LaB_6 disk cathode and a grounded anode.[68] A schematic of the NAGDIS-II device is shown in Figure 1.5. The electrons that are emitted from the LaB_6 cathode do not hit the anode directly, they are instead reflected by negative potentials of the target and the cathode and bounce along the plasma column.[69] These types of plasma sources are termed a reflex arc. The NAGDIS-II device can achieve electron densities up to 10^{20} m^{-3} and temperatures of 1-10eV.[57]. These high densities and low electron temperatures allow the physics of plasma detachment, that is important in the operation of the ITER divertor, to be studied.

The PISCES-B source is also a DC reflex arc type source.[69] These plasma sources are able to operate at lower magnetic fields $\sim 0.1 \text{ T}$ since the discharge relies on cross-field transport, where the discharge arc is across the magentic field.[51]

PILOT/MAGNUM PSI uses a cascaded arc plasma source, it is a DC plasma source that generates high density, low temperature plasma. Cascaded arc plasma sources require higher pressures than other discharge types and strong magnetic fields ($\sim 1\text{T}$) for transport and confinement of the plasma with the differential pumping system. Shown in Figure 1.6 is a schematic of a cascaded arc plasma source.

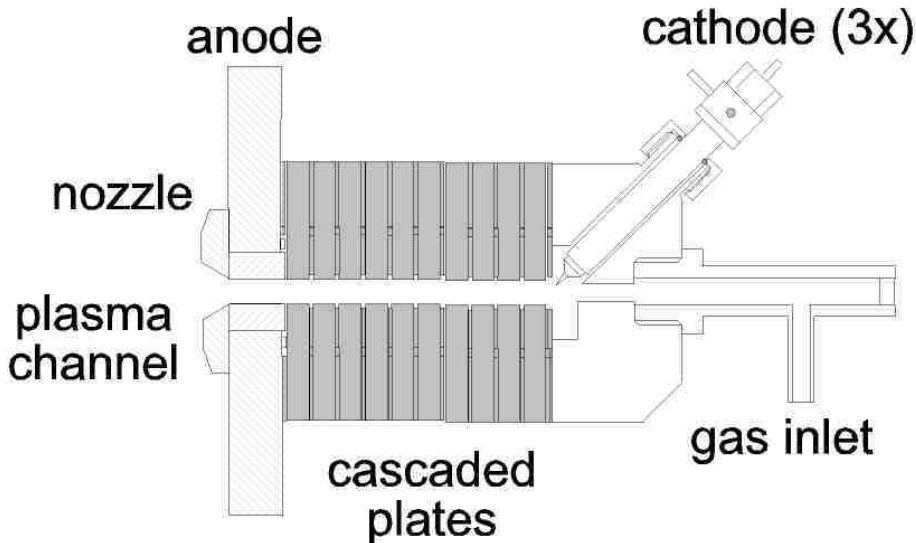


Figure 1.6: Schematic of a cascaded arc plasma source. Reproduced from [70]

As shown in Figure 1.6, the general construction of a cascaded arc plasma source contains a needle-shaped cathode usually made from LaB_6 and an anode. Very high voltages and currents are required to create the breakdown. These are quite often wall stabilised by insulated cascaded plates to maintain the electric field between the cathode and anode. These plasma devices have produced some of the highest electron densities in a linear plasma device, up to 10^{21}m^{-3} . Table 1.1 contains a summary of the plasma parameters achieved (electron density and temperature, ion flux) and the operating conditions (magnetic field strength, pulse length) of a selection of high density linear plasma devices.

While these DC discharge sources are able to produce very high plasma densities, they can suffer from metal impurities in the plasma due to sputtering of the source. This makes RF sources with an external antenna an attractive alternative

because there are no internal electrodes.[51] These RF sources provide continuous operation with reduced impurity generation.

1.2.2 Radio Frequency Plasma Generation

A large majority of radio frequency plasmas in industry and laboratory use capacitively coupled plasmas (CCP). A discussion of CCP devices can be found in [71, 72]. In a capacitively coupled plasma it is the strong electric fields that create breakdown in the gas. The easiest way to produce a plasma with low power is by using a capacitively coupled plasma device. The voltages required to create breakdown depends on parameters of the device such as operating gas pressure and the distance over which the voltage is applied. The way in which the power is coupled into the plasma has a large effect on the densities and temperatures that can be achieved in the plasma device. It can also effect the stability of the plasma.

One such example of a CCP plasma device is the parallel plate discharge as shown in Figure 1.6 (left). In this device one electrode is operated with RF power and the other is grounded. This creates a time varying electric field between the electrodes, where the power can be coupled through both collisions between the accelerated electrons and neutral particles, causing ionisation and excitation, and also through collisionless heating where the time varying electric field transfer energy to the electrons.

Another method to create plasmas which have higher densities is through inductively coupled plasmas (ICP). A discussion of ICP sources can be found in [71, 72] and a review in [73]. An ICP usually has an antenna separated from the plasma by a dielectric barrier as shown in Figure 1.7 (right), the antennas are usually wound around a cylinder in a cylindrical configuration. These antennae have both a capacitive component due to the electric fields from the antenna as well as an inductive component from the electromagnetic field created by current in the antenna.

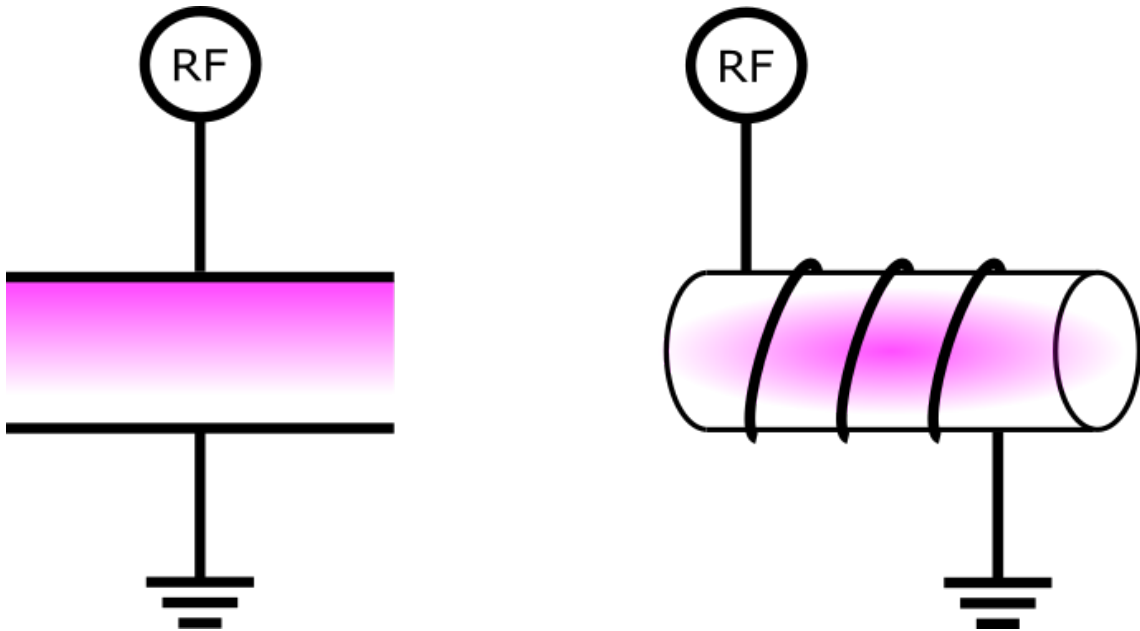


Figure 1.7: Simple schematic of a capacitively coupled plasma (CCP) device (left) and an inductively coupled plasma (ICP) device (right).

ICP plasma systems display a transition from a predominately capacitively coupled plasma (E mode) to one that is dominated by the inductive coupling (H mode). The E mode is seen to dominate at lower powers and pressures and transitions to the H mode at higher power or pressure. The transition depends on the plasma device geometry and the gas used. At low plasma densities, the skin depth of the plasma, $\delta = c/\omega_{pe}$, where c is the speed of light and ω_{pe} is the electron plasma frequency will be quite large and the wave is not coupled to the plasma. As the density is increased (usually through an increase in RF power) the inductive mode is induced.

Another mode is available in discharges that have an applied external DC magnetic field where electromagnetic waves, such as helicon waves, create an additional method of heating in the plasma. This helicon mode (W mode) has resonant absorption of the RF wave and couples to power to the plasma. A helicon wave is a circularly polarised EM wave that propagates along the magnetic field. Helicon waves penetrate deeper into the plasma than inductive systems, providing greater

power transfer into the plasma through interactions with the propagating wave along the plasma device. The mechanism through which the helicon waves couple to the plasma is not fully understood, it has been suggested that it occurs through both collisional and collisionsless mechanisms, such as inductive heating or Landau damping respectively.[74, 75] Helicon plasmas are known for achieving high densities with modest powers and in some cases complete ionisation in the plasma core. A thorough review of helicon sources, theory and their applications by Shinohara can be found in [1]

Early work on helicon sources was carried out by Boswell[76] and Chen.[77] The first use of helicon modes in the laboratory was first achieved by Boswell in 1970, using a double sided antenna.[78] Helicon plasma versatility makes them useful in a range of areas: fusion material interactions, plasma processing, space plasmas and propulsion. The MAGPIE device at The Australian National University utilises a helicon antenna for producing high density plasmas.[27] Other helicon plasma sources are the Controlled Shear Decorrelation Experiment (CSDX)[66] at University of California San Diego and the Materials Plasma Exposure Experiment (MPEX)[65] at Oak Ridge are both examples of high power helicon plasma sources. Plasma conditions of these devices can be found in Table 1.1 above.

1.3 Hydrogen Plasmas

There are six different ground-state forms that hydrogen can exist in within a plasma; there are the neutral species, atomic hydrogen (H) and molecular hydrogen (H_2), the positive ions (H^+ , H_2^+ and H_3^+) and also the negative hydrogen ion (H^-). Each of these species can undergo collisions and reactions with the other species and can depend strongly on the species energies.

1.3.1 Collisions

Atoms and molecules within the plasma interact with each other through collisions where they are scattered in a different directions to their initial trajectory. The frequency of collisions between two species is defined by:

$$\nu_{A,B} = v_{th} n_A n_B \sigma_{A,B} \quad (1.2)$$

where $\nu_{A,B}$ is the collisional frequency between species A and B, v_{th} is the thermal velocity between the two species, n_X is the density of each of the species and $\sigma_{A,B}$ is the cross section of the collision between A and B.

A hard-sphere model can be considered for collisions between two neutral species. These collisions occur when the Van der Waals radii of the two neutral species overlap. The cross section of the neutral-neutral collision is given as:

$$\sigma_{A,B} = \sigma_{B,A} \approx \pi(r_A + r_B)^2 \quad (1.3)$$

where r_X is the Van der Waals radius of the individual species. For atomic hydrogen, the Van der Waals radius has been approximated as 0.12nm [79] and for molecular hydrogen as 0.152nm[80].

For charged-neutral collisions Samuell[81] and Hjartson[82] have previously estimated the cross-sections by approximating the charged species as hard spheres. They assume that the electrons and protons have a negligible radii. They assume that the charged species have the same cross sections as their charged counterparts. For H_3^+ , it is assumed that the cross section is proportional with the number of atoms in the collision. The cross-sections for the atomic and molecular hydrogen scattering reactions are found in Table 1.2.

Table 1.2: Cross sections $\sigma(\text{m}^{-2})$ for neutral-neutral and neutral-charged collisions. [81]

	H	H_2	H^-	H^+	H_2^+	H_3^+
H	1.8×10^{-19}	2.3×10^{-19}	1.8×10^{-19}	1.8×10^{-19}	2.3×10^{-19}	2.8×10^{-19}
H	2.3×10^{-19}	2.8×10^{-19}	2.3×10^{-19}	2.3×10^{-19}	2.8×10^{-19}	3.3×10^{-19}

1.3.2 Hydrogen Reactions

Each of the hydrogen species may undergo reactions with any of the other species in a hydrogen plasma. This can lead to a very complex set of reactions, each of which can have reaction rates that strongly depend on the electron and ion temperatures. As this thesis focuses on atomic atomic, the important reactions for atomic hydrogen will be considered. In high-density plasmas, the dominant production mechanism of atomic hydrogen is the dissociation of molecular hydrogen ($e^- + \text{H}_2 \rightarrow 2\text{H} + e^-$). Other important production mechanisms for atomic hydrogen include dissociation of H_2^+ ($e^- + \text{H}_2^+ \rightarrow \text{H} + \text{H}^+ + e^-$), dissociative recombination ($e^- + \text{H}_2^+ \rightarrow 2\text{H}$), dissociative attachment ($e^- + \text{H}_2 \rightarrow \text{H}^- + \text{H}$), and charge exchange ($\text{H}^+ + \text{H}_2 \rightarrow \text{H}_2^+ + \text{H}$). There are also important loss mechanisms that are important for atomic hydrogen, they are direct ionization ($e^- + \text{H} \rightarrow \text{H}^+ + 2e^-$), charge exchange ($\text{H} + \text{H}_2^+ \rightarrow \text{H}_2 + \text{H}^+$), and associative detachment ($\text{H} + \text{H}^- \rightarrow \text{H}_2 + e^-$). Hydrogen plasma is a lot of more complex than simply atomic hydrogen, a list of the dominate reactions that occur within a hydrogen plasma and the corresponding reactions rates are shown in Table 1.3.

Table 1.3: Set of dominate reactions and reaction rates for species in hydrogen plasmas.

Reaction	Rate Coefficient ($m^3 s^{-1}$)	Reference
$e^- + H_2 \rightarrow H_2^+ + 2e^-$	$7.27 \times 10^{-15} T_e^{0.549/T_e - 0.001} + 1.37 \times 10^{-14} T_e^{-0.557} e^{-20.3/T_e}$	[83]
$e^- + H_2 \rightarrow 2H + e^-$	$1.54 \times 10^{-14} T_e^{-0.0636} e^{-8.63/T_e} + 1.11 \times 10^{-13} T_e^{-0.813} e^{-13.4/T_e}$	[83]
$e^- + H_2 \rightarrow H + H^-$	$4.43 \times 10^{-17} T_e^{-1.29} e^{-11.7/(T_e + 0.158)} + 1.33 \times 10^{-19} T_e^{-1.39} e^{-3.77/T_e}$	[83]
$e^- + H \rightarrow H^+ + 2e^-$	$9.74 \times 10^{-15} T_e^{0.174} e^{-14.3/(T_e + 0.001)} + 6.35 \times 10^{-15} T_e^{0.433} e^{-16.4/T_e}$	[84]
$e^- + H_2^+ \rightarrow H + H^+ + e^-$	$3.50 \times 10^{-13} T_e^{-1.25} e^{-3.19/(T_e + 0.008)} + 1.77 \times 10^{-13} T_e^{-0.0924} e^{-3.04/T_e}$	[85]
$e^- + H_3^+ \rightarrow H_2^+ + H^-$	$1.93 \times 10^{-15} T_e^{-1.07} e^{-6.26/(T_e + 0.131)} + 5.35 \times 10^{-17} T_e^{-0.371} e^{-2.07/T_e}$	[85]
$e^- + H_3^+ \rightarrow H_2 + H^+ + e^-$	$2.69 \times 10^{-13} T_e^{-2.45} e^{-15.6/(T_e + 0.003)} + 1.01 \times 10^{-12} T_e^{-0.464} e^{-26.8/T_e}$	[85]
$e^- + H^- \rightarrow H + 2e^-$	$4.58 \times 10^{-13} T_e^{0.287} e^{-4.41/(T_e + 0.117)} + 2.71 \times 10^{-14} T_e^{0.62} e^{-1.82/T_e}$	[86]
$e^- H_2^+ \rightarrow 2H$	$2.29 \times 10^{-14} T_e^{-0.571} + 3.31 \times 10^{-15} e^{-152/T_e}$	[86]
$e^- H_3^+ \rightarrow 3H$	$3.36 \times 10^{-15} T_e^{-0.716} + 3.73 \times 10^{-14} T_e^{-0.67} e^{-6.40/T_e}$	[86]
$e^- H_3^+ \rightarrow H + H_2$	$2.03 \times 10^{-15} (T_e^{-0.189} + 0.040 T_e^{-1.49}) + 5.57 \times 10^{-14} T_e^{-1.23} e^{-6.21/T_e}$	[86]
$e^- + H \rightarrow H^- + h\nu$	$5.75 \times 10^{-20} (T_e^{-0.0285} + 0.94 T_e^{-0.05}) + 6.54 \times 10^{-19} T_e^{-5.18} e^{-72.4/T_e}$	[86]
$H + H_2^+ \rightarrow H_2 + H^+$	$1.59 \times 10^{-14} T_i^{-0.859} e^{-4.61/(T_i + 0.786)} + 1.64 \times 10^{-15} T_i^{-0.353} e^{0.258/T_i}$	[86]
$H + H^- \rightarrow H_2 + e^-$	$2.16 \times 10^{-13} T_i^{-1.89} e^{-12.7/(T_i + 1.17)} + 1.30 \times 10^{-15} T_i^{-0.418} e^{-0.192/T_i}$	[86]
$H + H^- \rightarrow 2H + e^-$	$3.81 \times 10^{-15} T_i^{0.280} e^{-3.76/(T_i + 0.626)} + 4.55 \times 10^{-16} T_i^{0.603} e^{-0.375/T_i}$	[86]
$H_2 + H_2^+ \rightarrow H + H_3^+$	$6.29 \times 10^{-15} T_i^{-1.46} e^{-2.22/(T_i + 0.356)} + 2.71 \times 10^{-16} T_i^{-1.30} e^{-0.317/T_i}$	[86]
$H_2 + H^+ \rightarrow H + H_2^+$	$5.54 \times 10^{-16} T_i^{0.453} e^{-3.26/(T_i - 0.001)} + 5.98 \times 10^{-18} T_i^{-2.88} e^{-0.310/T_i}$	[86]
$H_2 + H^+ \rightarrow H_3^+ + h\nu$	1.63×10^{-21}	[87]
$H^+ + H^- \rightarrow 2H$	$4.46 \times 10^{-14} T_i^{-0.281} + 1.26 \times 10^{-14} e^{-1.96/T_i}$	[86]
$H_2^+ + H^- \rightarrow H_2 + H$	$2.23 \times 10^{-14} T_i^{0.425} + 8.93 \times 10^{-14} e^{-0.261}$	[88]

1.4 Neutral Behaviour in Plasma Devices

A limiting factor in achieving high plasma densities is due to the behaviour and interactions of the neutral species in the plasma. The neutral species are a source of ion production and collisions with neutrals can affect the plasma transport properties and plasma confinement.[89] The neutral species can be deeply involved in the plasma chemistry, being particularly important in plasma recombination and negative ion production.[90] It has been observed that low pressure plasma discharges reach a maximum plasma density, an upper limit, whereby further increasing the applied power no longer increases the plasma density.[2, 3, 91]

The neutral species in plasma need to be correctly understood to have a complete understanding of the plasma itself. The neutral species in hydrogen plasmas are of particular interest due to their relevance in high power linear devices for applications to fusion, negative ions sources and wakefield accelerators (as discussed earlier).

Hydrogen plasmas display an extremely complex and diverse array of plasma dynamics. This provides extremely rich and complex plasma chemistry where the excited electronic states and excited rotational and vibrational states all contribute to various reaction pathways.[92] Hydrogen is also a highly chemically active species and readily reacts with other plasma species or with surface materials.[93, 94] Additionally, plasma dynamics in hydrogen plasma are observed to strongly depend on isotopic composition adding additional complexities.[36] Hydrogen being the lightest element has heavier isotopes that are double and triple its mass. This leads to unique reaction and transport dynamics between the isotopes and noticeable shift in the energy levels.[95]

1.4.1 Measuring Neutral Species

A number of different techniques exist to measure neutral species in a plasma. As with all plasma diagnostics, these techniques can be divided into two categories: non-perturbing measurements and perturbing measurements. A non-perturbing di-

agnostic does not disturb the plasma in any manner, while a perturbative measurement disturbs or interacts the plasma as part of making the measurement and can create disturbances that alter the property being measured. Ideally all measurements would be non-perturbing, however it is not always possible and perturbing diagnostics must be employed.

The pressure gauge is possibly the simplest method to measure neutral density. However pressure gauges are not ideal for most plasma applications. Typically a pressure gauge is mounted on the chamber walls, which will only provide a localised edge measurement.[96, 97] Pressure is also an indirect measure of the density, as pressure is the product of both the density and the temperature. To ascertain the density from a pressure measurement, accurate knowledge of the neutral temperature is required. Additionally, the majority of pressure gauges measure the combined pressure of all the species and do not differentiate between species, making it impossible to determine individual densities in multi-species plasma.

There are many different types of pressure gauges with different methods of measuring pressure. Different gauges have practical ranges over which they can operate this usually dictates when a gauge can be used for a certain application. Table 1.4 contains some of the most common gauges available for measuring the pressure.

Mass spectrometry can be used to determine the species composition in the plasma. The mass spectrometer technique operates by bending the path of a charged species in a magnetic field. The higher the charge on a species the greater the force it feels from the magnetic field and the heavier a species the less it will respond to the force. Thus a mass spectrometer measures the mass-to-charge ratio of ions. To measure the neutral species the ions from the plasma are blocked, usually with an ionic repulsion filter at the front of the mass spectrometer. Inside the mass spectrometer the neutral species are ionised and detected according to their charge-to-mass ratio. Mass spectrometry is able to determine absolute densities when carefully designed and calibrated.[98] Like pressure gauges, mass spectrometry measures the species at the wall or the interface between the plasma chamber and the mass spectrometer chamber.

Table 1.4: Types of pressure gauges with their method of detection and practical pressure range.

Instrument Name	Physical Phenomena	Detection Method	Practical Pressure Range (Torr)	Reference
Pirani Gauge	Heat transfer from wire to environment	Wire current	10^{-3} to 1000	[99]
Thermocouple Gauge	Heat transfer from wire to environment	Wire temperature	10^{-3} to 5	[99]
Ionisation Gauge	Current ionises gas at grid	Ion current on collector	10^{-10} to 10^{-3}	[99]
Diaphragm	Deflection of flexible membrane	Various	above 10^{-2}	[99]
Bourdon tube	Mechanical stress under pressure	Mechanical movement	1 to 1000	[99]

Due to the collisional nature of plasma, there is a distribution of excited states for each species throughout the plasma. The excited species will spontaneously decay from the excited states to lower energy levels with radiative emissions. Optical emission spectroscopy (OES) is the technique that looks directly at the naturally emitted radiation from the plasma. Figure 1.8 shows an example spectra from a hydrogen plasma, highlighted are the H_α and H_β emission from atomic hydrogen at 656.28nm and 486.13nm, respectively. The Fulcher band which is a rotational molecular H_2 emission is also labelled on the Figure. As the radiative emission is from the excited state of the species as it decays to a lower energy state, the information that is gained from optical emission spectroscopy is about the excited state. To then determine information about the ground state species, models are required, such as collisional-radiative models for hydrogen.[100, 101] These models can be difficult to construct even for simple species as the rates of various processes, such as excitation, ionisation and recombination are greatly affected by small changes in plasma conditions such as electron density and temperatures.[102] Thus, accurate knowledge of the electron parameters is also required using optical emission spectroscopy to determine neutral densities.

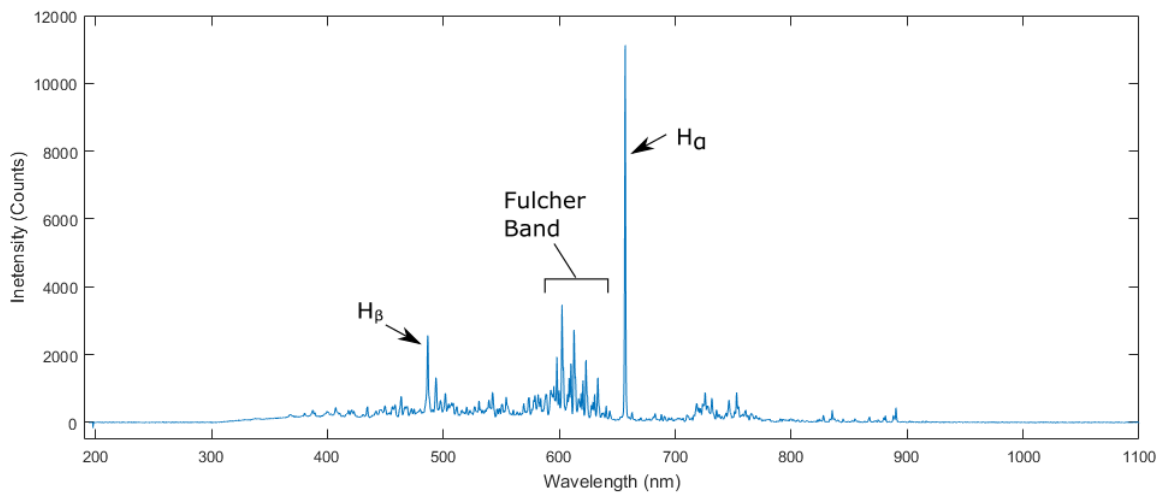


Figure 1.8: Spectra of a hydrogen plasma with the H_α and H_β atomic emission lines labelled. The Fulcher band from molecular hydrogen is also shown.

Optical emission spectroscopy provides advantages over pressure gauges, col-

lection optics are able to measure into the interior of the plasma and are not restricted to the edge. Optical emission spectroscopy is a line-integrated measurement and to make localised measurements requires multiple viewing angles and complicated techniques to reconstruct the profiles, such as Abel inversion.[103]

Laser absorption spectroscopy techniques provide a way to achieve better spatial and spectral resolution than optical emission spectroscopy. Absorption of the incoming photons result in an electronic excitation transition in the absorbing species. A simple excitation and emission scheme is shown in Figure 1.9, the state is excited by the absorbed photon and decays back down to the lower state by emitting a photon. Due to the absorbed transition being induced by the incident photon, the technique probes the initial state as opposed to the excited (emitting) state. Laser absorption spectroscopy measures the decrease in the laser energy due to the absorption of the laser with the absorbing species and has been used extensively for neutral hydrogen.[104, 105]

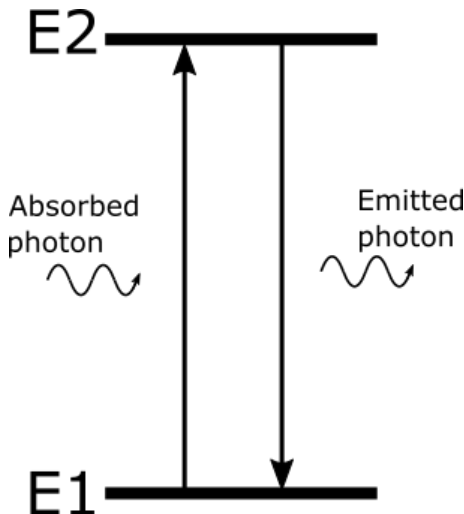


Figure 1.9: Absorption and emission scheme by photons in a two energy level system.

Another laser absorption diagnostic is laser-induced fluorescence (LIF).[106] With laser-induced fluorescence the species is excited to a higher energy state via the absorption of a photon. The corresponding decay of the excited higher energy state releases a photon (fluorescence) which is recorded. Laser induced fluorescence can be

induced with multiple photons, provided the sum of the photon energies add to the difference between the energy levels.[107] Setting up of a two-photon absorbed laser induced fluorescence (TALIF) diagnostic to investigate neutral species, specifically atomic hydrogen, in high power discharges in a linear plasma device is the main focus of this research. A complete discussion of the TALIF diagnostic system and the underlying physics is presented in Chapter 3.

1.4.2 Neutral Depletion

With the increasing availability and use of high power linear plasma devices, the effect of neutral depletion has become more apparent. It has been observed that there may be a maximum plasma density that can be attained by high power linear devices. Miljak and Chen [2] attributed this observed density limit to neutral depletion. Neutral depletion has been widely measured in a range of different plasma sources and the cause of the depletion attributed to different mechanisms. Here a short overview is provided of the cause of neutral depletion and some of the reported occurrences of neutral depletion in the literature. There are three main mechanisms believed to lead to neutral depletion in linear devices; ionisation, gas heating, and high plasma pressure.[3]

In what were probably the first measurements of neutral depletion Boswell *et al.* [108] measured the Doppler broadening of argon lines in a helicon plasma device. They found that argon atoms were ten times hotter in the centre of the discharge compared to the edge and surmised that atomic argon density in the core is 10 times less than at the edge. This form of neutral depletion is termed gas heating depletion, where a non-uniform neutral heating by the plasma results in a hotter gas temperature in the plasma core. With a uniform neutral pressure, the neutral density in the centre will be reduced due to the higher gas temperature.[109]

Neutral depletion due to gas heating has been observed even at moderately low powers. Rossnagel *et al.* [110] found in an argon electron cyclotron resonance (ECR) source that the gas density was reduced by 86% during the discharge. Nakano *et al.* [111] found in an argon ECR plasma that the neutrals were 450K hotter under

the source compared to downstream resulting in neutral depletion.

Gas heating has been measured in inductively coupled plasma (ICP) sources. At 200W in an argon ICP plasma, Hebner [112] measured an increase in gas temperature from room temperature to 900K. Following this, Hori *et al.* [113] found neutral depletion of 40% in an ICP device by investigating the radial profile which they explained to be due to gas heating of neutrals by ion-neutral collisions.

Another method of neutral depletion is due to high ionisation (known as ion pumping), where all of the neutrals that diffuse into the centre of the plasma discharge are ionised. The newly created ions are then accelerated out the plasma core by electric fields and recombine to form neutrals at the walls.[114] Gilland *et al.* [115] concluded that ionisation was the cause of neutral depletion in their argon helicon plasma. They determined the mean free path for ionisation (λ_i) in their argon discharge was approximately 0.1cm. As the mean free path for ionisation is less than 10% of their chamber diameter, they concluded that ion pumping (they refer to as neutral pumping) is the cause of neutral depletion. Neutral depletion due to ionisation has been modelled by Fruchtman.[114, 116]

Tynan *et al.* [117, 118] observed neutral depletion, which was attributed to ion pumping, occurring with an argon discharge in an helicon device with a surface wafer. It was found that the gas density was non-uniform and this could lead to over-etching in plasma processing.

When the plasma density becomes high, for instance when ionisation is high or the plasma is magnetically confined, the neutral species can often be depleted from the core. This is observed to occur when the plasma pressure becomes comparable to the neutral pressure.[119, 120] Under these conditions neutral depletion is known to be due to both plasma pressure and gas heating of the neutrals by the plasma.[3]

Aanesland *et al.*[121] measured the ground state xenon atom density in a helicon discharge using two-photon absorption laser-induced fluorescence (TALIF). They determined neutral depletion by comparing the xenon density during the plasma discharge to the xenon density without the plasma. Under conditions that produced maximum depletion they measured an 85% decrease in density at the

centre. The profile at the centre has a 6cm flat profile and then slowly increased in density towards the edge recovering to 40% depletion. They suggest that it is likely the neutrals are pushed into regions with lower magnetic field, that is into the source. Liard *et al.* [122, 123] further investigated the results by Aanesland through modelling and neutral density measurements with TALIF. They included an axial magnetic field to existing transport theory to explain neutral depletion. The model showed that increasing the magnetic field reduces neutral depletion, however, they considered a constant plasma density, whereas plasma density will increase with magnetic field at constant power. They also showed that plasma confinement is reduced with increasing neutral depletion. Liard *et al.* [124] later showed that neutral depletion occurs very quickly in the centre of the xenon discharge, on the order of milliseconds, taking about 50ms for the centre to reach steady state depletion. At the edges the time-scales are longer. After the plasma discharge it took almost two seconds for complete repletion of the neutral xenon in the core.

Cho [125] also modelled neutral behaviour in a pulsed plasma discharge. They showed the depletion occurring during the plasma pulse and replenishing after the pulse. They showed that a lower pressure leads to much greater neutral depletion and achieves a steady state more quickly.

McNeely *et al.* [126] used optical emission spectroscopy and pressure measurements with a baratron to determine neutral depletion of up to 70% compared to the initial gas density in an RF driven H⁻ ion source. They observed that the depletion fraction increased with gas flow rate. This dependence on gas flow was much stronger than the decrease in depletion due to increasing gas pressure.

O'Connell *et al.* [127] showed that depletion due to gas heating and high plasma pressure are competing mechanisms linked to the fill pressure. At low pressures, the high plasma pressure caused by high ionisation rates led to significant neutral depletion. With higher fill pressures, the depletion due to the plasma pressure is lessened and depletion due to gas heating increases.[128]

Galente [129] investigated neutral depletion in hydrogen and deuterium up to 2.5kW applied RF power but did not observe depletion of the neutral species in

the discharge. To the author's knowledge, neutral depletion has not been directly experimentally observed in a helicon hydrogen plasma to this date.

Fruchtman [114, 116, 119, 130, 131] has done extensive research on neutral depletion and modeled the mechanisms that lead to neutral depletion occurring in linear plasma devices. A thorough review by Fruchtman of the experimental observations and the mechanisms that cause neutral depletion can be found in [3].

Recent modelling suggest that neutral depletion is occurring in the MAGPIE plasma device at high RF powers.[132] Shown in Figure 1.10 are results of the neutral atomic and molecular hydrogen from 2D-axisymmetric model of a 20kW applied RF power hydrogen discharge in MAGPIE. The model calculates significant depletion of both the atomic and molecular hydrogen. Atomic hydrogen is shown to be depleted along the axial core and increasing in density radially. Molecular hydrogen also displays radial depletion, however is generally depleted to a greater extent overall and is focused down towards the end of the target chamber.

1.5 Thesis Structure

This thesis is a detailed investigation into the dynamics of neutral atomic hydrogen in the MAGPIE device at high powers (up to 20kW). This thesis includes a description of the newly established two-photon absorption laser-induced fluorescence diagnostic to measure the atomic hydrogen. The TALIF diagnostic is directly utilised to measure the depletion of atomic hydrogen in the MAGnetised Plasma Interaction Experiment (MAGPIE) device. An overview of the physics and operation of the diagnostic is also covered. The structure of the thesis is follows:

The MAGnetised Plasma Interaction Experiment (MAGPIE), the helicon plasma device which is investigated in this research, is discussed in Chapter 2. This chapter also contains a description of some of the diagnostics and techniques that are used in this thesis.

The focus of Chapter 3 is the two-photon absorption laser-induced fluores-

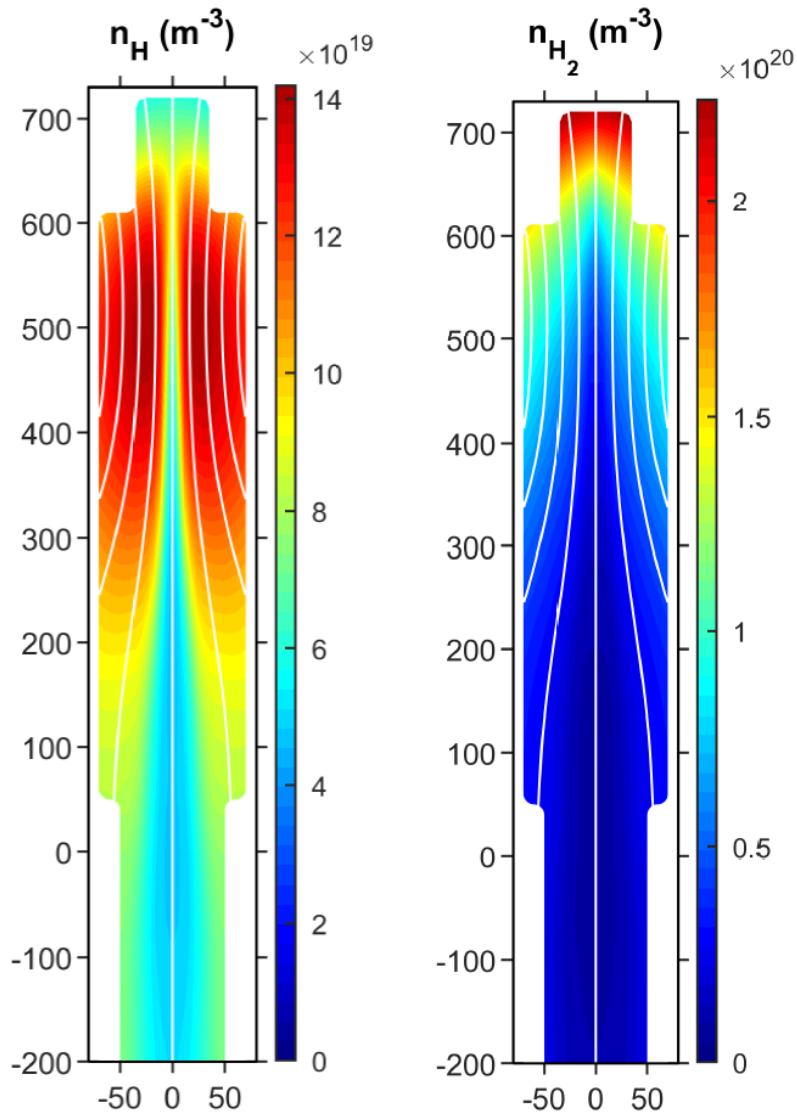


Figure 1.10: Model of the atomic hydrogen and molecular hydrogen density in the MAGPIE helicon device with 20kW applied RF power. Reproduced from [132]

cence diagnostic that has been newly established as part of this research. It begins with a discussion of the laser-induced fluorescence technique. Following is a description of the operation and control of the diagnostic system. The chapter will conclude with a detailed explanation of the physics for determining neutral temperatures and densities, including calibrations and spectral broadening considerations.

1.5. THESIS STRUCTURE

Chapter 4 presents measurements of atomic hydrogen density and temperature in the MAGPIE helicon device. The measurements are restricted to the plasma afterglow due to very low signals during the plasma discharge, possibly due to depletion of atomic hydrogen. A single spatial position in the radial centre of MAGPIE is the focus of this chapter. The plasma conditions will also be discussed and explanation will be given as to how the plasma affects the neutral behaviour, such as neutral depletion in the plasma chamber. This chapter includes the first experimentally measured depletion of atomic hydrogen in a helicon plasma device.

In Chapter 5, the parameter space is expanded to include the temporal evolution of atomic hydrogen into the plasma afterglow. The loss mechanisms of atomic hydrogen in the plasma afterglow is modelled and compared to experimental measurements to determine the dominate loss processes. Following, the radial profile of atomic hydrogen and the electron density is investigated and presented. These measurements will be related back to and build on the discussions in Chapter 4.

The conclusion and summary of this research is in Chapter 6. It also provides an overview of possible future directions for this research.

Chapter 2

The MAGPIE Helicon Plasma Device

The experiments conducted in this thesis were conducted in the MAGPIE device at the Australian National University. MAGPIE is a 2m long helicon plasma device which consists of two chambers, the source region and the target region. MAGPIE uses a RF power source and a helicon antenna to produce plasma. MAGPIE has previously been described in detail[27]. This chapter will provide a thorough discussion of the device, its control systems and some of the diagnostics that are relevant to this work.

2.1 Magnetized Plasma Interaction Experiment - MAGPIE

The MAGPIE helicon plasma device is designed primarily for studying fusion relevant plasma material interactions as well as basic plasma studies (negative ion production, plasma detachment). Linear plasma devices are also excellent for developing and testing diagnostics as they have better diagnostic access along the device as opposed to the difficult diagnostic access on fusion devices. In this way, linear devices make excellent test-beds for equipment and specialised studies relevant to

2.1. MAGNETIZED PLASMA INTERACTION EXPERIMENT - MAGPIE

fusion devices. Materials can be placed into the target region of MAGPIE where they are exposed to plasmas and can afterwards be investigated using material diagnostic methods. Additionally, diagnostic techniques allow changes in the plasma to be measured, due to the presence of materials in the plasma.

2.1.1 Chamber and Design

The MAGPIE device consists of two chambers, the source chamber and the target chamber. The source chamber is a 1m long borosilicate glass tube with 10cm diameter and it is in this chamber that the plasma is produced. At one end of the source chamber, a second target chamber is connected. The second chamber is a four sided, 68cm long stainless steel target chamber with a 16cm inner diameter. A schematic of MAGPIE is shown in Figure 2.1 highlighting the sections of the MAGPIE device.

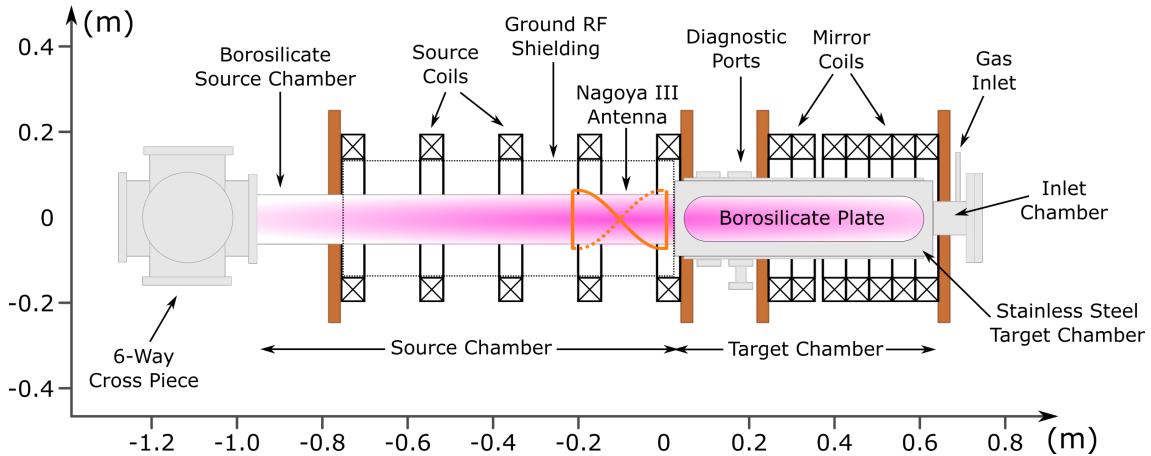


Figure 2.1: Schematic of MAGPIE device.

In addition to the two main chambers, at the other end of the source chamber, a stainless steel vacuum 6-way cross piece is connected. The 6-piece allows additional components, such as diagnostics, to be added to the downstream region of the MAGPIE device. Connected to the underside of the 6-way cross is a butterfly valve that allows additional control of gas pressure in MAGPIE. Below the butterfly valve is the vacuum system which consists of an Edwards nEXT400 Turbomolecular Pump

2.1. MAGNETIZED PLASMA INTERACTION EXPERIMENT - MAGPIE

with a pumping speed of 400 L/min, a backing Edwards E2M40 High Vacuum Pump with a pumping speed of 700 L/min and an ammonia cold-trap.

At the opposite end of the MAGPIE device, attached to the end of the target chamber, is a small 11cm long, 6cm diameter inlet chamber. The gas inflow and pressure gauges are all connected to this small inlet chamber. This design whereby the gas is introduced into the target chamber is to assist in creating higher plasma densities in the target chamber.

MAGPIE has two independent sets of water-cooled electromagnetic coils. The source coils are a broadly spaced set of five of coils around the source chamber and the mirror coils are a closely packed set of seven coils around the target chamber. Each individual coil has an outer diameter of 42cm, inner diameter of 28cm and a 5cm thickness and contains 14 turns of copper tubing. The coils are water-cooled by pumping water through the hollow tubing. Each set of coils are controlled independently and can operate with currents up to 1000A, however only for a short duration (minutes) for currents above \sim 500A due to thermal heating of the coils.

A 180 degree left handed 22cm long 12cm diameter Nagoya III helicon antenna used for plasma generation is located on the outside of the source chamber close to the interface with the target chamber. The edge of the helicon antenna is located at position $z=0$ in Figure 2.1. RF shielding surrounds all of the source chamber underneath the source coils. Each of the operational systems on MAGPIE are further discussed in more detail below.

Diagnostic Access

The target chamber of MAGPIE has four interchangeable side plates. Side plates available include: full borosilicate glass, stainless steel and stainless steel plates with two 70mm diameter ports or five 40mm diameter ports. The set-up of the target chamber sides, for the two-photon absorption laser induced fluorescence diagnostic, is shown in Figure 2.2. A full stainless steel plate is on the bottom of the chamber.

2.1. MAGNETIZED PLASMA INTERACTION EXPERIMENT - MAGPIE

The two sides are stainless steel plates with two diagnostic ports on each. As can be seen in the schematic of the side plate set-up, the port on the right has a small sapphire window connected. It is through this port that the excitation laser for TALIF diagnostic (discussed in the Chapter 3) will enter the chamber. A borosilicate glass plate is on top of the target chamber. The borosilicate glass has a high transparency for all relevant fluorescent wavelengths for this research.

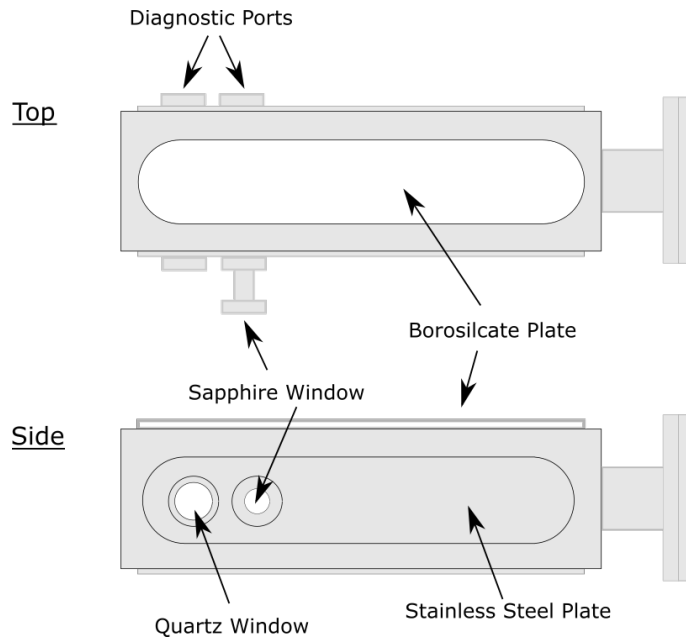


Figure 2.2: Schematic of target chamber with the side plate configuration used for the TALIF diagnostic in this work.

The stainless steel end plate of the target chamber can be replaced with plates that have either a single 75mm diameter diagnostic port in the centre or three 40mm diameter off-centre ports. These end plates can also be used on each side of the six-piece at the pump end of the source chamber. Different windows can be attached to the ports to allow optical access from either end of the MAGPIE device or additionally the ports can be used to insert various probes into the chamber. The exchangeable ports and side plates on both the target chamber and the ends of the device make MAGPIE easily adaptable for various diagnostics.

2.1.2 RF Power System

There is a choice of RF power supplies used for MAGPIE, depending on the input power desired. The low power system consists of a Rhode-Schwarts SM300 radio frequency signal generator which outputs through an Electron Navigation Industries (ENI) A150 low-noise radio frequency pre-amplifier before a second Alpha RF Systems 77Dx amplifier.

Alternatively MAGPIE is supplied power from an AMPEGON high power RF transmitter for higher power operation up to 20kW. Two AMPEGON transmitters were part of the H-1 heliac stellarator system that operated at the ANU from 1992 until its decommissioning in 2017. One of these transmitters is connected to MAGPIE to provide much higher power operation. Each transmitter uses a high-power tube RF amplifier and can supply 200kW pulsed power or 40kW of continuous power. It has a frequency range of 4-20MHz. For this research all investigations were carried out at a frequency of 13.56MHz.

MAGPIE is designed to operate at continuous RF power at 1kW or pulsed at powers up to 20kW. Above 1kW the excessive heat loads on the chamber wall prevent continuous operating and MAGPIE is restricted to operating in a pulsed mode. At 20kW RF power, a 1% duty cycle is used to reduce overheating.

When using antennas to couple power into the plasma, the antenna-plasma system behaves as a load with a complex impedance. The impedance depends on the antenna and plasma properties, which change with feedstock, input power and magnetic field. To maximise the power into the plasma and protect power supplies by reducing reflected power, the impedance needs to be matched. To achieve this a tunable matching network is used. For MAGPIE a standard π -type is used as shown in Figure 2.3. The network consists of a fixed $1.5\mu\text{F}$ inductor (L_1), which is connected between two grounded 3kV variable vacuum capacitors with 50-500pF and 85-200pF for C_1 and C_2 respectively. Each of the capacitors are manually tunable to match the impedances between the plasma and the RF generators. This matching network provides impedance matching for a broad radio-frequency range

2.1. MAGNETIZED PLASMA INTERACTION EXPERIMENT - MAGPIE

from 7-28MHz possible from the RF power supplies. A Pearson 6600 50mV/A current probe around the output of the matching box is used to measure the antenna current.

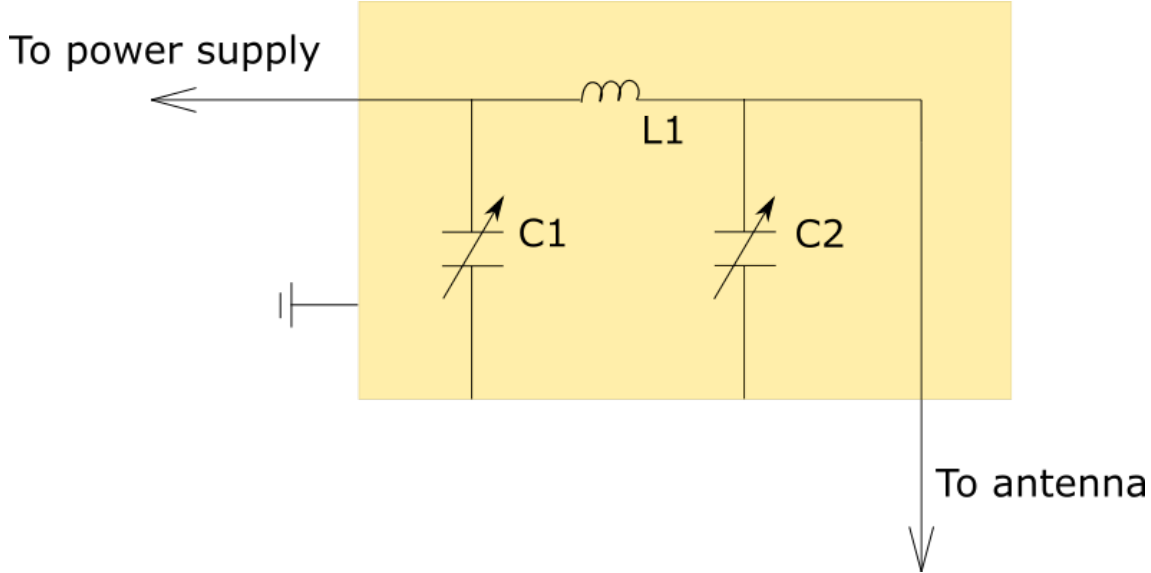


Figure 2.3: Schematic of the π -type impedance matching network for MAGPIE.

$L_1 = 1.5\mu\text{H}$ inductor. C_1 and C_2 are variable vacuum capacitors with capacitance 50-500pF and 85-200pF.

Ideally when the RF transmitter is switched off it will be an instantaneous removal of applied power. In practice, there is an intrinsic ramp-down of the transmitted power. This becomes more noticeable when operating in higher power regimes. It is important to take this ramp-down into consideration because there is still power being applied to the plasma during this time and it will impact on the plasma parameters. The antenna current during the ramp-down phase at the end of the RF pulse is shown in Figure 2.4, the absorbed power by the plasma will follow closely the antenna current. It takes $40\mu\text{s}$ (0.04ms) for the transmitters to completely stop supplying current through the antenna. During this time the plasma may continue to be excited and created. It is not until after the current in the antenna has entirely gone to zero that the plasma will decay. It is important to be aware of the switch-off regime of the power supplies as it may create different decay rates in the afterglow during the ramp-down and no applied power stages.

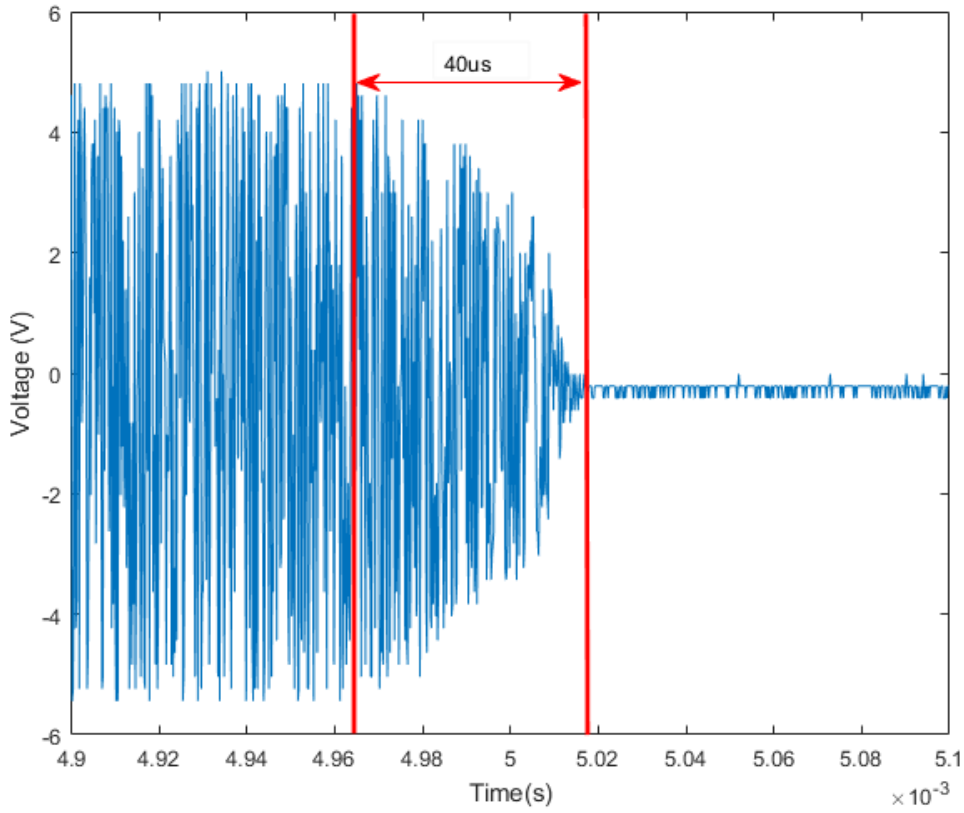


Figure 2.4: Antenna current 1kW.

2.1.3 Magnetic Field Configuration

MAGPIE has two independent sets of electromagnets, the source and mirror fields as shown in the schematic of MAGPIE in Figure 2.1. Each consists of a set of water-cooled electromagnets connected in series. The source coils consist of five electromagnets broadly spaced by 180mm. Whilst the mirror coils consist of seven closely packed coils in the target region, only five coils are connected in series. The two coils closest to the source regions are not used in this work. The mirror coils derive their name from the magnetic mirror (also called a magnetic trap) where charged particles are trapped by the pinch of the magnetic fields at the ends and force the particles in the opposite direction. Each set of coils is powered by a separate Magna-Power Electronics TS +LXI Programmable DC power supply capable of supply up to 1000A. In this work, a constant magnetic field configuration of 50A source current and 300A mirror field current has been used for all measurements.

2.1. MAGNETIZED PLASMA INTERACTION EXPERIMENT - MAGPIE

The magnetic field strength in MAGPIE is shown in Figure 2.5. The top plot shows a 3D plot of the magnetic field strength with the maximum 1000A in both the source and the mirror coils. The black lines show the outline of the MAGPIE chamber walls. The magnetic field strength remains fairly constant across most of the source chamber while decreasing at the pump end. The strong peak in the target chamber creates a magnetic pinch where plasma is focused towards the centre of the chamber creating higher plasma densities.

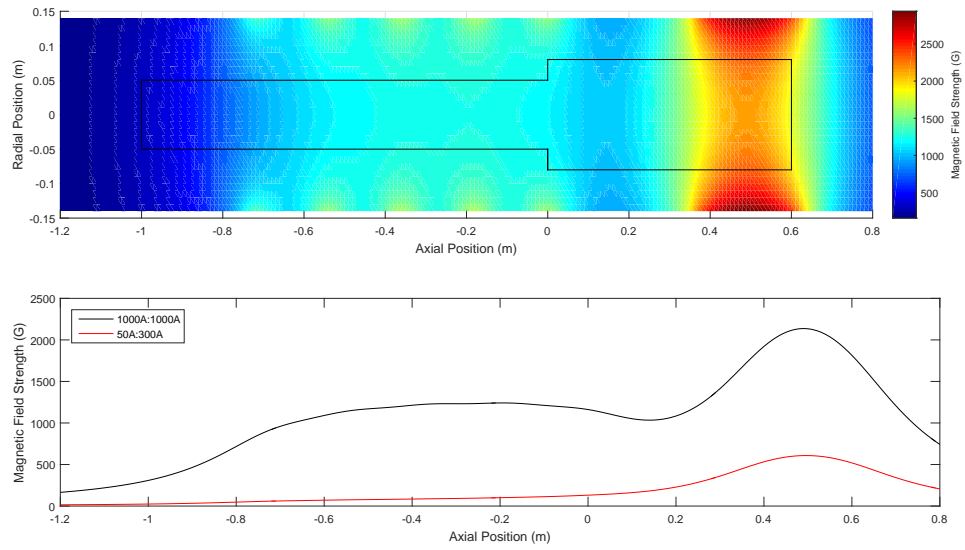


Figure 2.5: (Top) Surface plot of the magnetic field strength from the maximum 1000A:1000A coil configuration on MAGPIE. Back lines show the outline of the MAGPIE chamber. The antenna edge is at $z=-0.02\text{m}$ and the TALIF measurement position is at $z=0.13\text{m}$ (Bottom) Magnetic field strength along the centre of MAGPIE for the maximum 1000A:1000A coil configuration (black) and the standard 50A:300A coil configuration used in this work (red).

The bottom plot in Figure 2.5 shows the magnetic field strength along the axial component along the centre of MAGPIE. In black is the magnetic field strength with the maximum 1000A:1000A current configuration. The field strength is slightly more than 1000G in the source region and peaking upstream in the target chamber at approximately 2000G. Shown in red is the magnetic field strength for the standard 50A:300A current configuration that is used in this research. This magnetic field configuration can be operated continuously without becoming too hot which

is a necessity for the long scan times ($\sim 1\text{hr}$) for a single TALIF scan. The maximum magnetic field strength under these conditions is approximately 600G. The measurements made in this work are focused on the axial position $z=150\text{mm}$, at this position the magnetic field strength is 200G.

The dual coil systems in MAGPIE create a magnetic pinch in the target chamber, that is the field lines direct towards the radial centre of the chamber. This focuses the charged species in the plasma towards the centre due to smaller Larmor radii and provides higher plasma densities. A plot of the magnetic field lines is shown in Figure 2.6 for the standard 50A:300A operating conditions. The two sets of coils are both shown in red, the source coils are the wider spaced coils on the left while the closer packed mirror coils are on the right, only the five operating mirror coils are shown in the figure. The outline of the MAGPIE chamber is highlight by the black lines. The edge of the helicon antenna is located at $z=-0.02\text{m}$ position.

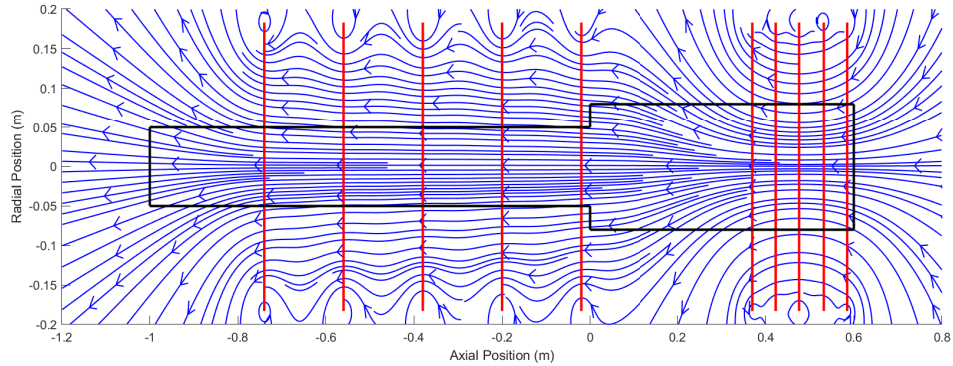


Figure 2.6: Plot of the magnetic field lies under the standard 50A:300A operating conditions. The centre of the electromagnets are shown in red and the outline of the MAGPIE chamber is in black. The five source coils are on the left and the mirror coils are on the right.

2.1.4 Gas and Pumping System

The gas pressure is monitored through the use of three different gauges, a MKS Baratron Type 120A Pressure Transducer, a Granville-Phillips convecron gauge and ionisation gauges. In general, the ionisation gauge is used to monitor the vacuum

2.1. MAGNETIZED PLASMA INTERACTION EXPERIMENT - MAGPIE

pressure, that is without gas flow, as the vacuum pressure is of the order of 10^{-6} Torr. The baratron is used for measuring the pressure under typical operating conditions 5-15 mTorr and the convectron gauge measures from this range up to atmospheric pressures.

Vacuum pressure is maintained through the use of two pumps. An Edwards E2M40 dual stage rotary vane vacuum pump provides a first stage of the vacuum which pulls the pressure down to 10^{-2} Torr. The Edwards nEXT 400 mechanical turbomolecular pump brings the base pressure down to 10^{-6} Torr. Between the 6-way piece and the turbomolecular pump is a butterfly valve. The butterfly valve is used to restrict the pumping rate of the system by gradually isolating the pumping system from the MAGPIE chamber. For all measurements presented in this work the butterfly valve is kept fully open.

Gas is let into the end of the target chamber through a stop valve via a 4.8mm diameter pipe. A mass flow controller allows the rate of gas flow to be controlled. Up to three different gas species can be connected to MAGPIE at one time, to allow gas mixtures to be used for plasmas in MAGPIE. Gas pressure will not be constant across the entire chamber as the pressure is measured at the gas inlet positions. The relationship between the pressure at the gas inlet and the gas pressure at $z=150\text{mm}$ into the target chamber is shown in Figure 2.7, which is fit by a linear relationship over the measured range. The change in pressure was determined by measuring the pressure with the baratron at both positions with identical gas flow conditions, that is with both pumps are full speed and the butterfly valve completely open. For all plasma discharges in this work the gas is flowing with a pressure of 10mTorr measured at the inlet. In the following chapters, measurements have been made focusing on the axial position $z=150\text{mm}$, therefore maintaining the gas pressure at 10mTorr (as measured at the gas inlet) the pressure at this position is 9.1mTorr.

MAGPIE has 4 gas inlets combining into a single inlet pipe that introduces gas into the target end of the chamber. One has a stop valve directly to atmosphere and is used for venting and bringing up to atmospheric pressure to change components. Two of the inlets are controlled via an MKS 100 sccm mass flow controller. Finally the fourth inlet is controlled by a needle valve. These valves allow differing

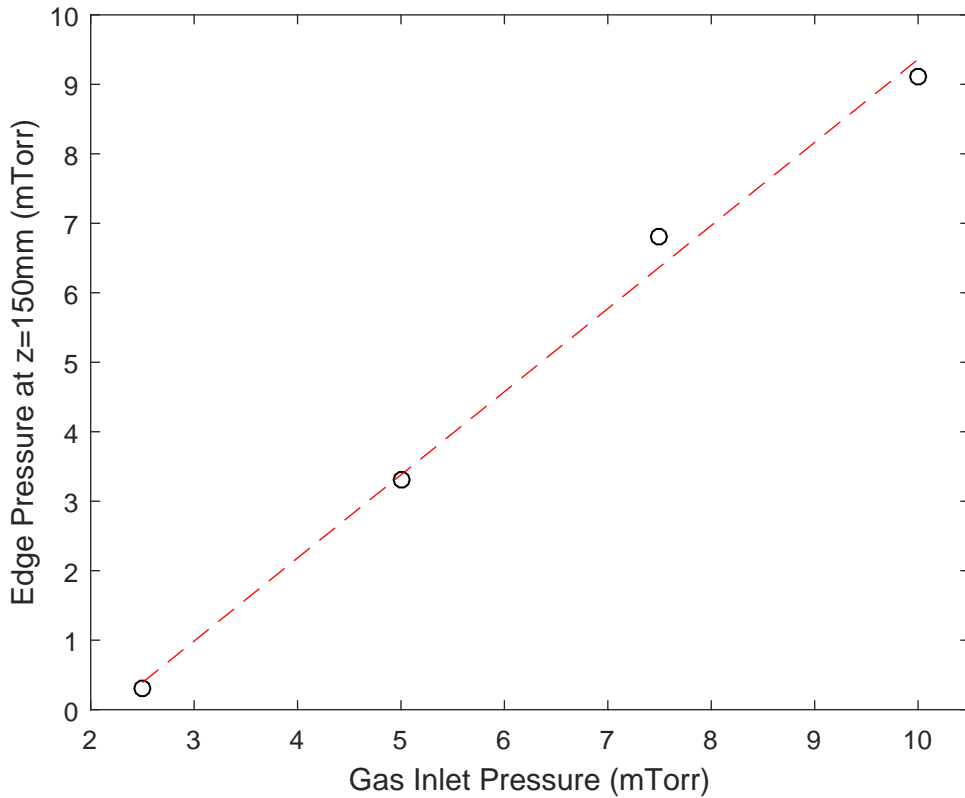


Figure 2.7: The measured edge pressure in the target chamber at $z=150\text{mm}$ as a function of the measured pressure at the gas inlet.

levels of control over gas flow. MAGPIE can currently be operated with variety of gases; hydrogen, deuterium, helium, nitrogen, argon and krypton.

When using plasma comprised of mixed gases, there are associated changes in the plasma chemistry. One important example is the formation of ammonia and other NH-compounds in mixed hydrogen-nitrogen plasmas. As ammonia is toxic it needs to be efficiently collected and disposed of. It also can damage the pumps in the vacuum system. As such ammonia traps are added to the exhaust line when operating with such plasmas.

The ammonia traps consists of a large container placed in the exhaust line after the turbomolecular pump but before the oil backing pump. The container has a bell jar inside of it that is open to the atmosphere but isolated from the exhaust. The bell is filled with liquid nitrogen at -270 degrees, this will cause the ammonia to

condense to a liquid (freeze) and remain in the trap. Stop valves before and after the container allow it to be isolated from the exhaust and easily removed to be emptied.

2.2 Experimental Uses

This section will discuss the main functions and important research capabilities of the MAGPIE device. Linear plasma systems, such as MAGPIE, offer convenient insight into plasma physics without added complexity of geometry and quite often simpler control systems.

2.2.1 Device for Studying Plasma-Surface Interactions

One of the main objectives of the MAGPIE device is to investigate fusion relevant plasma-material interactions. Materials in the divertor are expected to be exposed to extreme plasma conditions such as 10^{20} m^{-3} plasma densities, electron temperatures up to 100eV and ion fluxes of $10^{24} \text{ m}^{-2} \text{ s}^{-1}$.[\[54, 133, 134\]](#) While the conditions in MAGPIE do not quite reach these levels, reaching plasma densities (n_e) of 10^{19} m^{-3} , there are ways to reproduce these conditions, such as longer exposure times to produce the same fluence.

MAGPIE has multiple removable target holders that are used to place materials into the target chamber to investigate surface effects for plasma exposed materials as well as the interactions in the plasma through the interactions occurring at the surface. The target holders can be electrically biased to increase the effective electron temperature and use a voltage to heat and maintain a constant temperature to simulate the heat loads expected in the divertor region.

MAGPIE is also able to conduct general purpose plasma-surface interactions and previous investigations have included using graphite, diamond, copper, stainless steel and various polymers.[\[81\]](#)

2.2.2 Diagnostic Development and General Plasma Studies

The easy diagnostic access in MAGPIE's design makes it excellent as a test-bed for setting up or developing new diagnostics. As discussed in Section 2.2.1, the interchangeable side plates on the target chamber make it easy to switch out the diagnostic ports, windows and probe holder for the diagnostic requirements. Additionally the end plate of the target chamber and the three of the six plates on the six-way piece at the end of the source chamber, are interchangeable and provide extra availability for diagnostic applications. The sixth position currently has a quadrupole mass spectrometer for chemical analysis of the plasma species and has been used in mixed H₂/N₂ studies examining ammonia production.[24] The MAGPIE device was previously used in the development of the coherence imaging system, which is to be used on ITER as part of its set of diagnostics.[135, 136, 137]

This easy adaptability of MAGPIE makes it excellent for general studies of the plasma. MAGPIE is one of the few high power helicon devices in operation (>20kW).[1, 138, 139] This allows MAGPIE to study the maximum density limit in helicon plasmas and as well as the corresponding neutral depletion. Part of this research has involved the initial set-up, implementation and development of a two-photon absorption laser-induced fluorescence diagnostic. Following, the TALIF diagnostic is subsequently used to investigate neutral atomic hydrogen in the MAGPIE device and the role it plays in neutral depletion and the helicon density limit.

2.3 Diagnostics

A range of routine diagnostics are available on MAGPIE. This section briefly describes the experimental set-up and operation of only diagnostics that are relevant to this thesis.

2.3.1 Langmuir Probe

One of the most fundamental diagnostics in plasma physics is the Langmuir probe. The uncompensated single Langmuir probe was originally designed by Langmuir in 1924.[\[140\]](#) When the probe is biased with respect to the plasma it will draw a current. By varying the bias on the probe, electrons and ions of different energies will be collected by the probe. Sweeping the voltage on the probe and measuring the current, the electron energy distribution function (EEDF) can be determined and can yield plasma properties directly from the current-voltage (IV) characteristic. Plasma properties that can be determined from the Langmuir probe include electron density and temperature, ion density and the floating and plasma potentials.

Langmuir Probe Theory

Figure 2.7 shows a typical IV characteristic from a single Langmuir probe. The IV curve can typically be considered to have three regions. Region I is the ion saturation current, where the probe is biased negative with respect to the plasma and all of the positive ions are collected by the probe. Above the floating potential (Φ_f), the voltage at which the probe draws no current, is Region II. This region extends up to the plasma potential (Φ_p), the potential of the plasma relative to the ground. This region is known as the electron retardation region, voltages within this region will draw both electrons and ions. As the probe is still biased negative with respect to the plasma, only electrons with sufficient energy to overcome the electrostatic repulsion of the probe are collected by the probe. As the electrons that are collected by the probe depend on the electron energy, the electron energy distribution function (EEDF) can be determined from Region II.[\[141\]](#) Region III is the electron saturation region, this occurs when the probe voltage is greater than the plasma voltage $V_p > \Phi_p$. In this region, only electrons are being collected by the probe. At a certain voltage all of the electrons are being collected by the probe, this is known as the electron saturation voltage. The ion saturation (I_{sat}), electron

2.3. DIAGNOSTICS

saturation (E_{sat}), floating potential (V_f) and plasma potential (V_p) are highlighted on the IV curve in Figure 2.8, which define the edge of each of the three regions discussed.

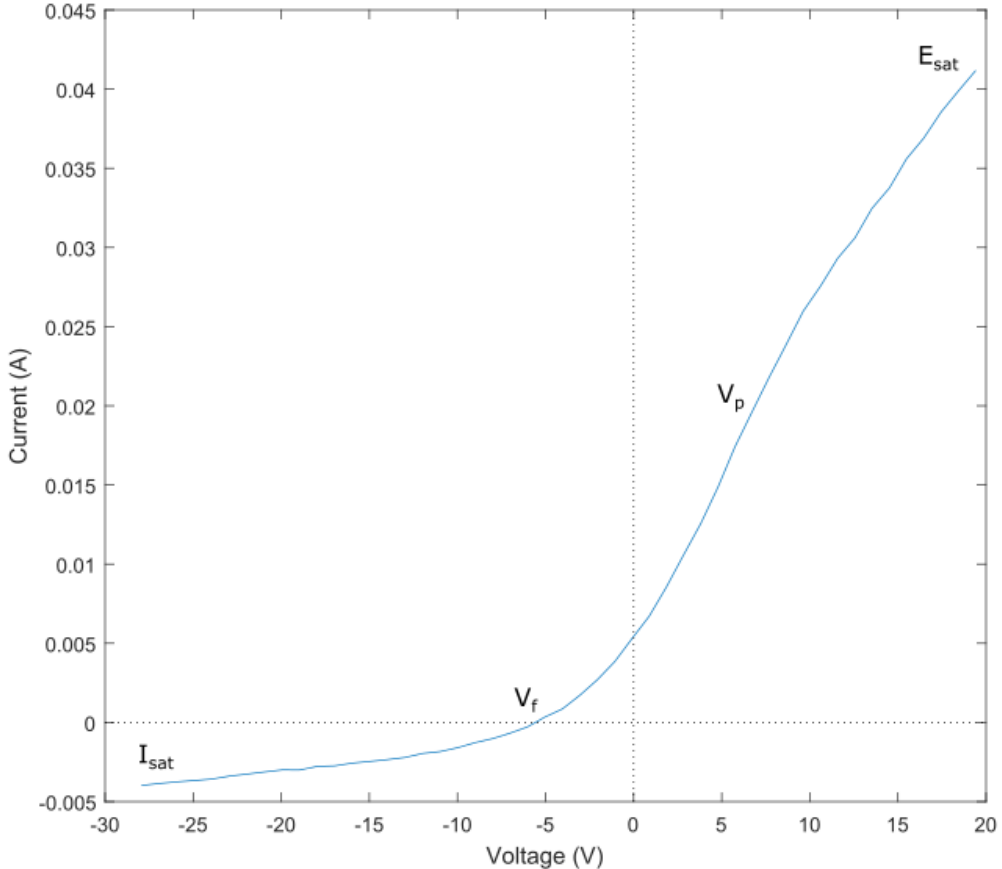


Figure 2.8: IV curve showing the ion saturation (I_{sat}), electron saturation (E_{sat}), floating (V_f) and plasma (V_p) potentials.

For the assumption that the electrons have a Maxwellian velocity distribution, the current drawn by the probe is given by:[142]

$$I = n_e q_e A_p \left(\frac{k T_e}{m_i} \right)^{\frac{1}{2}} \left[\frac{1}{2} \left(\frac{2 m_i}{\pi m_e} \right)^{\frac{1}{2}} \exp \left(\frac{q_e (V_p - V_f)}{T_e} \right) - \frac{A_s}{A_p} \exp \left(-\frac{1}{2} \right) \right] \quad (2.1)$$

where n_e is the electron density, T_e is the electron temperature, A_p and A_s are the surface area of the probe tip and sheath respectively. The second term is the ion

2.3. DIAGNOSTICS

saturation current. In an unmagnetised plasma the ion saturation current is given by:[142]

$$I_{sat} = -q_e J_i = -0.61 e n_e A_p \sqrt{\frac{T_e}{m_i}} \quad (2.2)$$

With a known electron temperature, the plasma density can be determined from the ion saturation current. The electron temperature can be determined from the slope of the I-V characteristic and is given by:[142]

$$T_e = e(I - I_{sat}) / \frac{dI}{dV} \quad (2.3)$$

Langmuir Probe System

Two Langmuir probe systems have been used in this research. The first, a commercial Impedans Langmuir Probe system which consists of an Impedans electronics box and an uncompensated single Langmuir probe.[143] The Impedans Langmuir software controls the voltage scanning and measures the current from the probe. This system provides time resolved and averaged measurements of the IV curve from the probe in the plasma.

The second system used is an in-house built Langmuir probe with a dogleg-shape at the end for spatial measurements. A detailed description of this probe can be found in [132]. The voltage is swept with a high-current linear amplifier and the current measured with a current probe. The signal is recorded on a Tektronix DPO-3014. The probe tips in both Langmuir probes are exchangeable, the length and diameter of the probe tips are measured using a digital caliper. The densities are then calibrated using the effective surface area of the probe tip.

Measurements of the electron density and temperature conducted in the afterglow of the plasma discharge have been made using the Impedans Langmuir system. Due to the large current draw associated with Langmuir probes in high density

2.3. DIAGNOSTICS

plasmas, the in-house built probe was used for all measurements made during the plasma discharge.

2.3.2 Optical Emission Spectroscopy

Optical emission spectroscopy (OES) is a widely used plasma diagnostic due to it being non-intrusive and generally inexpensive. Collisions of the electrons result in populations of excited states of the ions and neutrals. The radiative decay of these excited states can be used as an identifier of species present in the plasma such as newly formed species or impurities, as well as being able to determine densities and temperatures.

The optical emission spectroscopy diagnostic consists of a Princeton Instruments IsoPlane SCT320 with a Princeton Instruments PI-MAX 4 1024i intensified charge coupled device (ICCD) camera. A camera lens is used to focus the plasma emission onto the PI-MAX detector. A schematic of the set-up for optical emission spectroscopy is shown in Figure 2.9 showing the camera attached to the spectrometer. The IsoPlane SCT320 is a Schmidt-Czerny-Turner type spectrometer with a 320mm focal length. An adjustable slit with a range of $10\mu\text{m}$ to 12mm is attached on front of the spectrometer. A rotatable turret within the spectrometer holds three different gratings that can be selected between. Each of the three gratings has 1200 grooves/mm but with a different blaze, 300nm and 500nm, the third has a UV holographic coating.

The PI-MAX 1024i camera contains a 1024x1024 pixel array on a 13.08mm square substrate that is cooled to -20°C during operation. A selection of camera lenses and mirrors are available for the region of interest to be imaged. The spectrometer and camera are controlled through the Princeton Instruments LightField software.

Wavelength calibration of the spectrometer is carried out using a Princeton Instruments IntelliCali Dual Neon/Argon and Mercury lamps. A broad source visible-infrared Princeton Instrument IntelliCali Intensity lamp is used to create a

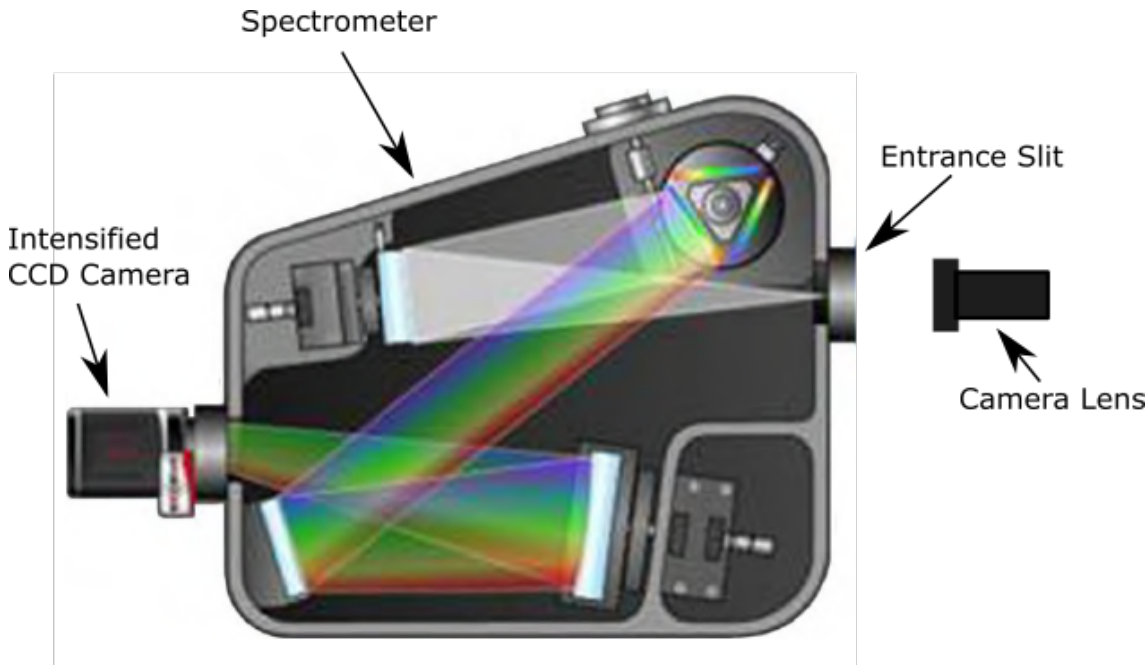


Figure 2.9: Schematic of the optical emission spectroscopy diagnostic. Adapted from [144]

relative intensity calibration across the wavelengths of interest. For experiments where absolute intensity calibration is needed, a calibration source such as a tungsten ribbon lamp or blackbody oven are used.

2.4 Summary

This chapter has presented the Magnetised Plasma Interaction Experiment (MAGPIE) device, a high power ($>20\text{kW}$) helicon source. The device design has been described in detail, including the two chamber, source and target, the radio-frequency power system, the magnetic coil configuration and the gas and pumping system. The main experimental uses and previous research conducted using MAGPIE has been presented, as well as a selection of diagnostics that are of relevance to the research presented in this research.

Chapter 3

Two-Photon Absorption Laser-Induced Fluorescence Diagnostic

In this chapter, the single photon laser induced fluorescence (LIF) and two-photon absorption laser induced fluorescence (TALIF) techniques will be discussed. First an overview of the basic theory for the techniques will be covered, followed by a discussion of the choice of transition selection for investigating atomic hydrogen.

Secondly, a detailed description of the new TALIF diagnostic system that has been established as part of this research will be provided. This will include a discussion of the laser and detection systems for the fluorescence. Challenges that arose with the diagnostic and were overcome included: maximising fluorescence signals, large plasma emissions at the fluorescence wavelengths, achieving high resolution timing, and laser drifts and fluctuations. There will also be an overview of the hardware and equipment used to provide precision timing and control for the diagnostic. A LabviewTM program was written to control various aspects of the diagnostic which will also be briefly discussed.

3.1. BASIC THEORY

The chapter will conclude with a discussion of the physics and calculations involved in determining the parameters of atomic hydrogen in the plasma, including the use of krypton as a calibration for atomic hydrogen. A discussion of the spectral features of the absorption is covered focusing on conditions relevant to the MAGPIE plasma device.

3.1 Basic Theory

Laser induced fluorescence (LIF) is part of a large family of laser-based diagnostics. In the case of laser-induced fluorescence it is the photon emission from: atomic, molecular and even ionic species that has been excited to a higher energy level through the absorption of laser radiation. In contrast, this can be compared to laser absorption where it is the reduction of laser intensity due to absorption in the plasma that is measured.

LIF is a well-established method for determining properties of neutrals and ions in plasmas. A photon is absorbed by a species exciting a bound electron from a lower energy state to a higher one. Generally it is the ground state that is excited as it is the most populated state in low temperature plasmas. The excited electron will spontaneously decay to a lower energy state emitting a photon in the process that is equal to the energy difference between the excited and final states. This excitation process can also be achieved using two photons, known as two-photon absorption laser-induced fluorescence (TALIF). Figure 3.1 shows a basic excitation and emission scheme for LIF (left) and TALIF (right). The final state does not necessarily need to be the same as the initial state for LIF, as there are multiple decay paths and generally the emission with the highest branching ratio is the easiest to measure.

As LIF is an absorption technique, it is the excitation photons as well as the emitted photons that provide information on the populations and species of interest. It is the intensity of the incident photons that determine the fluorescence that corresponds to the density of the species. The increasingly narrow line widths of modern lasers ($\sim 10^{-3}$ nm) allow this technique to resolve the Doppler broadening

3.1. BASIC THEORY

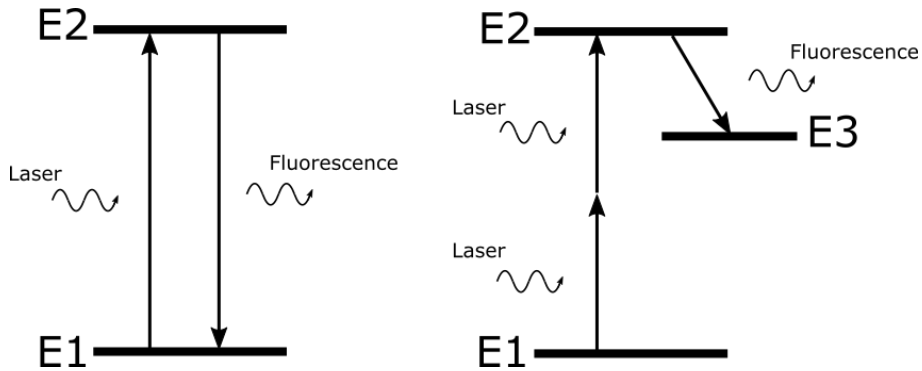


Figure 3.1: Basic excitation schemes for LIF (left) and TALIF (right). A single photon excites to a higher energy level in single photon LIF, the final state does not need to be the same as the initial state. The TALIF scheme uses two photons that sum to the energy difference between the states to excite the electron, the emission will generally be to a different energy level.

of the absorption and determine the temperatures for the species of interest. The Doppler-shifted line absorption provide information of the velocity and flows along the injection angle of the laser.

Due to excitation only occurring along the laser beam, LIF is a highly localised technique that can provide excellent spatial resolution (<mm) in the plasma. Equally good temporal resolution (ns) can be achieved by using short pulse lasers. However, this technique requires large absorbing populations to provide high levels of fluorescence to achieve measurable signals.

The TALIF technique uses two photons to excite the species to a higher energy state and provides many advantages over using single photons, as in LIF. While the ground state usually has the highest population density, nearly all transitions out of the ground state will be in the UV. For hydrogen, all of the ground state absorptions with a single photon are in the vacuum ultraviolet (VUV). The lowest energy transition, the (Ly_α), from 1s to 2p requires 121.6nm photons. These VUV lasers require extensive vacuum systems and expensive mirrors for the transmission of the photons. Using two photons to achieve excitation circumvents this issue as photons of lower energy can be used. This is because the absorption transition can be achieved with photons that add to the energy. While photons of any energy

3.1. BASIC THEORY

can be used, in practice it is generally two photons of exactly half the transition energy that are used to achieve absorption. This provides the added benefit of only requiring a single laser. For the Ly_α transition, photons of 243.2nm can be used for the absorption, which are above the vacuum threshold for light and are cheaper to produce.

As TALIF uses two photons, it has its own set of selection rules, $\Delta J = 0, 2$. This condition makes TALIF inherently non-resonant as single photon decay back to the initial state is a forbidden transition and will have long lifetimes. Therefore in many TALIF schemes the excitation state will decay to a different third energy state as shown in Figure 3.1. As the density of the third state is generally much less than the ground state, the plasma will not be optically thick at the fluorescence wavelength and there will be less re-absorption.

Due to the absorption requiring two photons, TALIF has very small cross-sections. This means that little absorption will occur with an unfocused beam. To get meaningful absorption, the laser beam needs to be focused to create an area of higher photon intensity. This allows TALIF to be highly spatially selective in the area probed. This provides another advantage over LIF which in a typical experimental set-up will be absorbed along the entire path length in the plasma and advanced optical set-ups are required to achieve greater spatial resolution.

3.1.1 Atomic Hydrogen TALIF

There are multiple excitation schemes that have previously been investigated for hydrogen with laser induced fluorescence. Figure 3.2 shows the low level excitation schemes for atomic hydrogen. The 1s to 2p (Ly_α) or 3p (Ly_β) using a single photon have excitation photons of 121.6nm and 102.5nm respectively and require extensive vacuum systems and expensive mirrors for transmission of the photons. The TALIF excitation from 1s to 2s requires 243nm photons but the excited state is metastable and has a long lifetime, 10^5 s. The decay is then detected from the 2p radiative state with which the 2s is collisionally coupled. This produces longer detection times and much higher backgrounds.

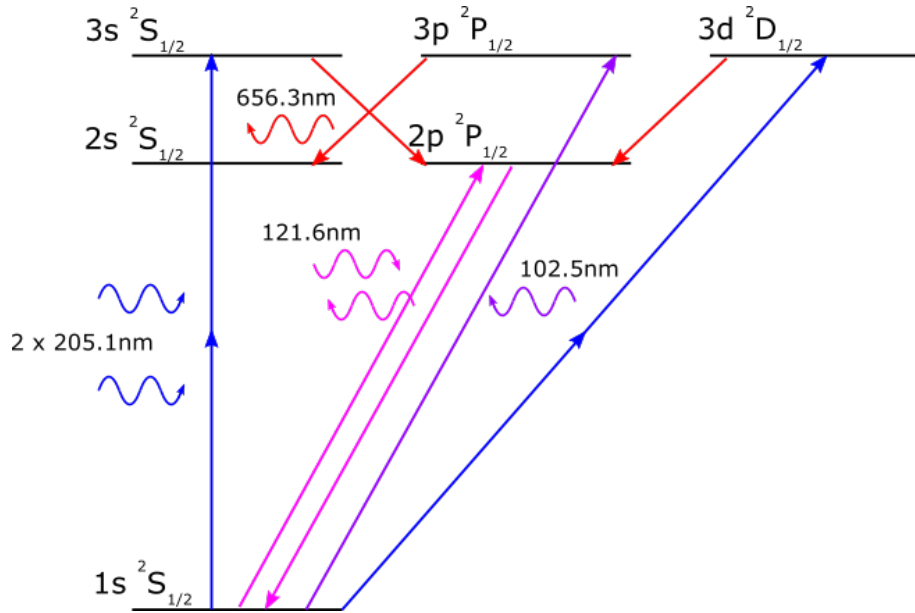


Figure 3.2: Ground state excitation schemes for hydrogen and subsequent fluorescence.

The Ly_β transition between $n=1$ and $n=3$ state in hydrogen is a single photon transition from the $1s$ to the $3d$ state. This excitation can also be induced using two photons to conserve the angular momentum of the interaction and excite to the $3s$ or $3d$ state. The excitation from $1s$ to $3s,d$ requires photons at 205.15nm and both emit at 656.3nm in the visible, for which there are detectors and optics readily available. The particular transition of interest to this diagnostic is the $1s^2S_{\frac{1}{2}} \rightarrow 3d^2S_{\frac{1}{2}}$ of atomic hydrogen.

3.2 Diagnostic Set-Up

The TALIF system requires a high intensity short-pulsed UV laser system for sufficient absorption to produce measurable fluorescence. The set-up requires UV optics for directing and focusing the laser into the plasma. The diagnostic also requires a detection system for collecting and maximising the fluorescence. This section covers the physical set-up, control and operation of the TALIF diagnostic.

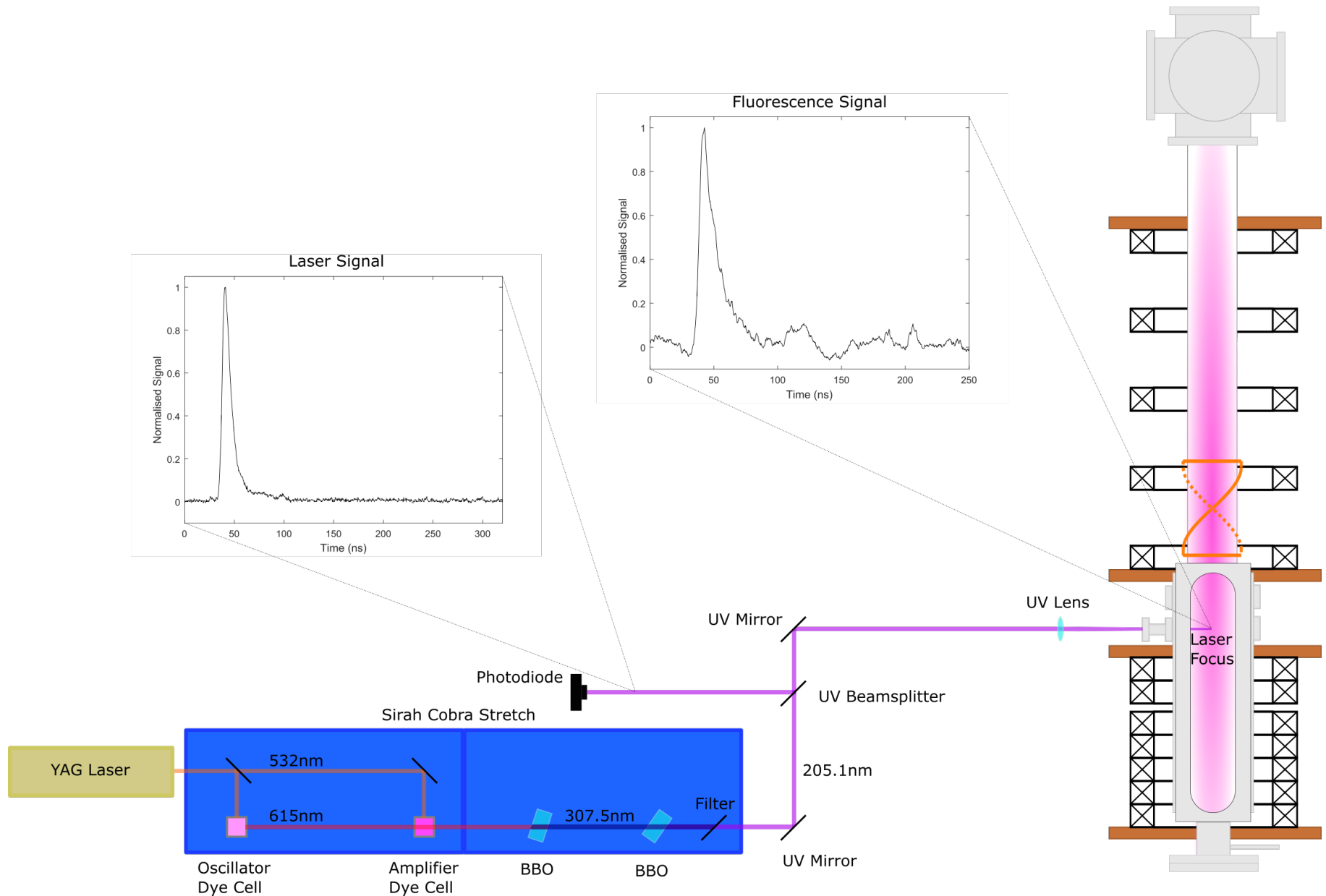


Figure 3.3: Simplified schematic of the two-photon absorption laser induced fluorescence diagnostic.

3.2.1 Laser Set-up

A three stage laser is used to produce the necessary 205.15nm photons for the two-photon absorption of atomic hydrogen. UV photons are not easy to produce with a single laser, however, one way to produce UV lasers is to create it in stages, such as with dye lasers and frequency mixing. Shown in Figure 3.3 is a schematic of the TALIF laser set-up used in this research. The three stages are the Nd:YAG pump laser, a dye laser, followed by a set of frequency mixing crystals. UV mirrors and lenses are used to direct and focus the beam into the plasma.

The first stage is a Spectra-Physics Quanta-Ray INDI neodymium-doped yttrium aluminium garnet (Nd:YAG) pulsed laser. The laser has a repetition rate of 10Hz and outputs 450mJ/pulse at 1064nm. A potassium dideuterium phosphate (KD*P) crystal frequency doubles the output to 532nm with a maximum energy output of 200mJ/pulse. This produces short pulse length, high-intensity laser pulses and it is for this reason that Nd:YAG lasers are quite often used as pump sources for dye lasers. The Nd:YAG laser is controlled via the front panel of the instrument.

The second stage uses the Nd:YAG to pump a Sirah Cobra Stretch scanning dye laser capable of harmonic frequency generation. Dye lasers operate by using a laser to pump the population in a dye mixture and fluoresce an output of a certain wavelength. The dye used in this research is a rhodamine 101/rhodamine B mixture (recipe for dye mixture found in Appendix A) that has a centre fluorescence at 615nm. The dye laser has two separate stages; first the oscillator to produce a seed of the fluorescence dye output with good beam quality and spectral purity and secondly the amplifier to increase pulse energy. This two-stage dye system helps to reduce amplified spontaneous emission (ASE) commonly associated with high energy pulsed lasers. Problems associated with ASE include different temporal profiles of the laser, larger optical bandwidths and a lower degree of polarisation.

As is often the case with dye lasers the emission curve is very broad, on the order of tens of nm. The rhodamine 101/rhodamine B mixture outputs over a wavelength range 600-630nm. A diffraction grating is used to provide wavelength

3.2. DIAGNOSTIC SET-UP

control of the dye output, greatly reducing the bandwidth of the output beam. The wide bandwidth of the dye and tunable nature of the grating allows scanning of the wavelengths. By scanning the wavelength, the laser is able to absorb across the entire broadened absorption peak of species of interest.

The 615nm output from the dye laser is frequency tripled in the third stage. A second harmonic generation (SHG) crystal, SHG-250 BBO, frequency doubles the dye output to 307nm. A second frequency mixing crystal THG-197 BBO mixes the fundamental 615nm with the frequency doubled 307nm to produce 205nm photons. A set of four Pellin-Broca prisms are used to filter out the unwanted wavelengths and select only the frequency tripled output.

The dye laser is controlled via Sirah Control, a LabVIEWTM based program. This controls the position of the grating to select the desired emitted wavelength. Sirah Control allows wavelength scans to be set-up, specifying the wavelength scan range and the size of the steps. In this work, the laser step size is 0.1pm (picometer) or 10^{-4} nm. The scan is set up in such a way so that the laser will wait for a trigger signal from an external source before moving to the next wavelength in the scan.

Motor position tables are produced using the inbuilt powermeters to maximise the frequency conversion of the BBO crystals. This is because the angle of the crystals affect the conversion percentage. The powermeters and autotrackers can do this automatically, however in this research it was determined that a look-up table for the motor position provided a greater intensity of the 205nm laser.

It is necessary to record the laser energy of the pulses as the amplitude of the fluorescence is dependent on the energy of the laser pulse (covered in more detail later in the chapter). A UV beam split is used to direct a small percentage of the UV laser to a Thorlabs DET10A/M fast photodiode which detects 200-1100nm light. The photodiode outputs a voltage dependent on the energy of the light upon it. The temporal shape of the 205.15nm laser pulse can be seen in Figure 3.4. The pulse has a FWHM \sim 7ns.

The laser energy is calibrated using the Thorlabs photodiode and a Newport 1918-R Power Meter with a Newport 919P-003-10 Thermopile Sensor. The ther-

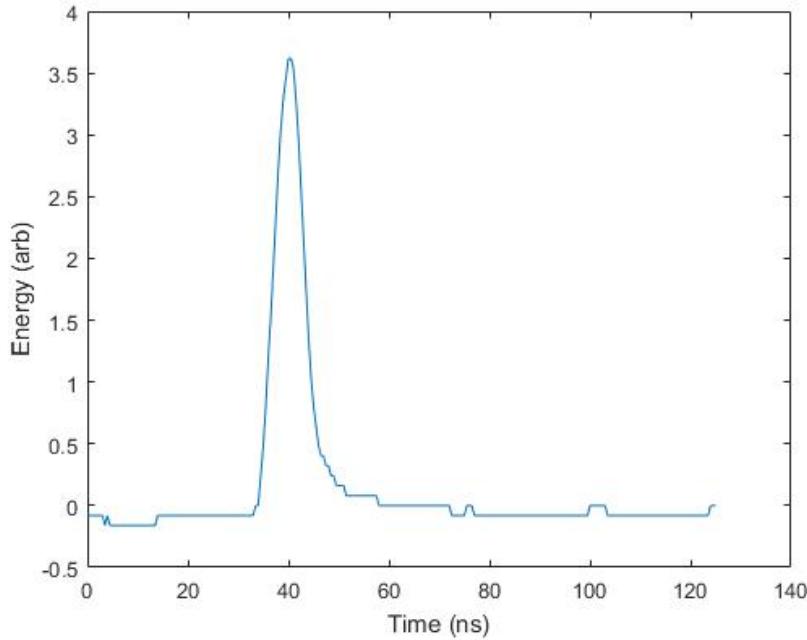
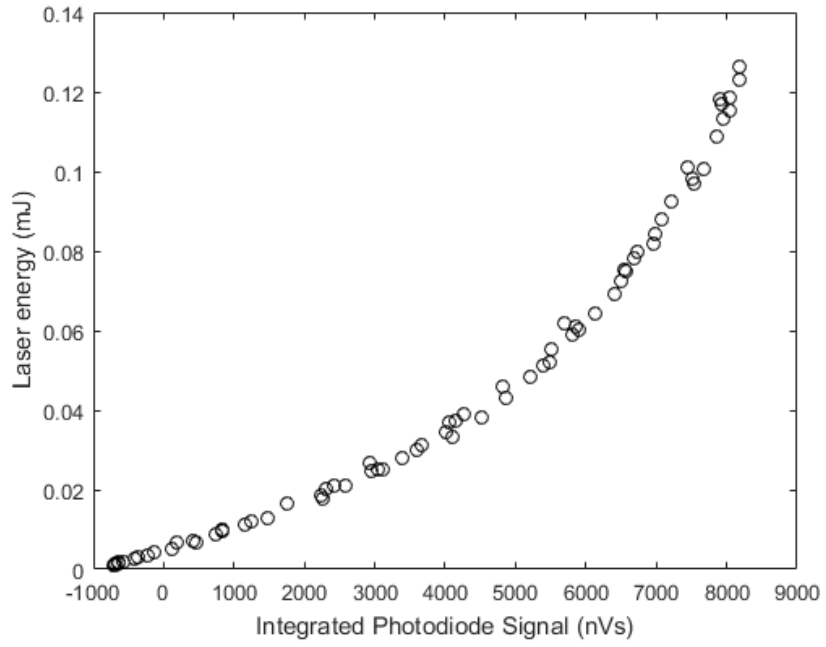


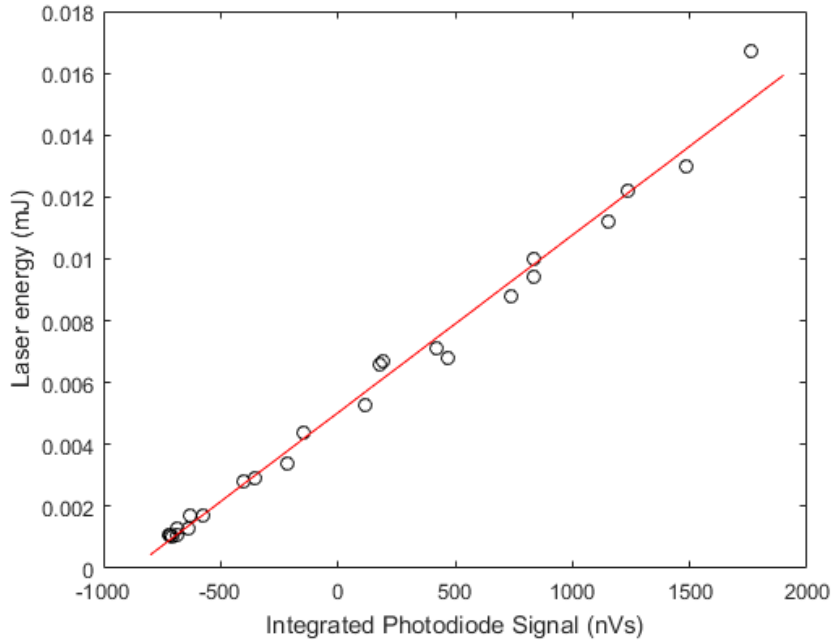
Figure 3.4: Temporal profile of the 205.15nm laser pulse.

mopile sensor can accurately measure laser shot energies from $20\mu\text{J}$ - 2J or optical power from $40\mu\text{W}$ - 3W . The thermopile sensor is placed inside the target chamber of MAGPIE, directly where the TALIF measurements in this work are taken. This measures the total power of the unfocused laser beam. As the repetition rate of the laser is 10Hz, the average laser energy is 1/10th of the power. This energy is then plotted against the integrated signal from the photodiode. This method accounts for energy losses at the mirrors and the optical windows of MAGPIE. The calibration for the laser energy against the photodiode signal is shown in Figure 3.5.

The photodiode calibration for the full range of the laser energy is shown to have a non-linear type relationship as seen in Figure 3.5a. It is typical of photodiodes to display non-linear detection under high intensity light such as lasers. The photodiode signals outputs a negative voltage under low-energy or no light conditions, this is most likely due to dark current and the op-amp offset voltage and is accounted for with the calibration. At the lower end of the laser energy, the photodiode signal is linearly proportional to the laser energy as shown in Figure 3.5b. Due to saturation effects that occur at higher laser energy in TALIF diagnostics, the



(a) Photodiode dependence on laser energy



(b) Linear fit of photodiode calibration

Figure 3.5: (a) Full fit of the photodiode calibration against the laser and in (b) is the linear section of the photodiode detection where the laser energy was maintained.

3.2. DIAGNOSTIC SET-UP

laser energies used in this research are restricted to the linear region of this fit. Laser saturation effects are discussed later in the spectral effects section of this chapter.

The laser is directed towards the MAGPIE chamber by a series of UV mirrors. One of the mirrors is mounted on a linear platform to allow movement behind the two optical ports on the side of MAGPIE. Additionally it is mounted on a micrometer actuator controlled platform to allow fine control over the position. This can be used for alignment with the detection system and for small movement in axial position across the window ports. A 25.4mm f=400mm UV fused silica plano-convex lens is used to focus the laser into the plasma, this lens is also mounted on a linear platform that allows the focal point to be moved radially in the chamber.

3.2.2 Detection Set-Up

Detection of the fluoresced light is a major component of the diagnostic. Consideration must be given to the equipment used for detection, due to the very small fluorescence signal and the large background emissions from the plasma. Due to this it is important that the detection equipment used has a high sensitivity. Consideration also needs to be given to the optical detection range of the detector. It needs to be able to detect (high quantum efficiency) the fluorescence emission of both the species of interest and the calibration species.

A Hamamatsu R3896 multialkali photomultiplier tube was chosen as the detection method for the fluorescence. This photomultiplier tube has a detection range of 185-900nm, which is suitable for many fluorescence experiments and provides an amplification of 9.5×10^6 . A Hamamatsu C1392-56 fast gated socket unit is used as part of the assembly with the photomultiplier tube. Two power supplies provide the DC bias for the PMT assembly. A Hewlett-Packard 6516A DC power supply provides negative 0-1000V and a TET Electronics ARGOS DC power supply provides positive 0-200V. The gain of the PMT is controlled by adjusting the bias voltage from these two power supplies. The PMT requires that the voltage from the powers supplies remain in the ratio 5:1.

3.2. DIAGNOSTIC SET-UP

The gated socket unit is usually gated 'off', that is it has a reverse bias on the first dynode which prevents photoelectrons from reaching the dynode during the 'off' time. It is gated 'on' with +5V ttl signal to the gate input terminal on the socket unit. This gating provides a 10^4 difference between the gated 'on' and 'off' times and will reduce saturation of the PMT from the bright plasma emission.

A lens set-up shown in Figure 3.6 is used to focus on the fluorescence from the probed spot and remove as much background light as possible. The fluorescence light is emitted isotropically from the focus point of the laser, as such larger lenses allow greater collection of the fluorescence. Therefore, larger 50.8mm diameter $f=15\text{cm}$ lenses are used to provide the largest solid angle of emission. The 656nm H_α from the hydrogen plasma is an intense emission from the plasma that cannot be filtered out due to the fluorescence at the same wavelength. To further remove the background emission from the plasma, an adjustable size aperture is placed after the 50.8mm lenses, with the fluorescence focused through the centre of the aperture. After the aperture, two 25.4mm lenses are used to focus the fluorescence directly onto the photocathode detector of the PMT.

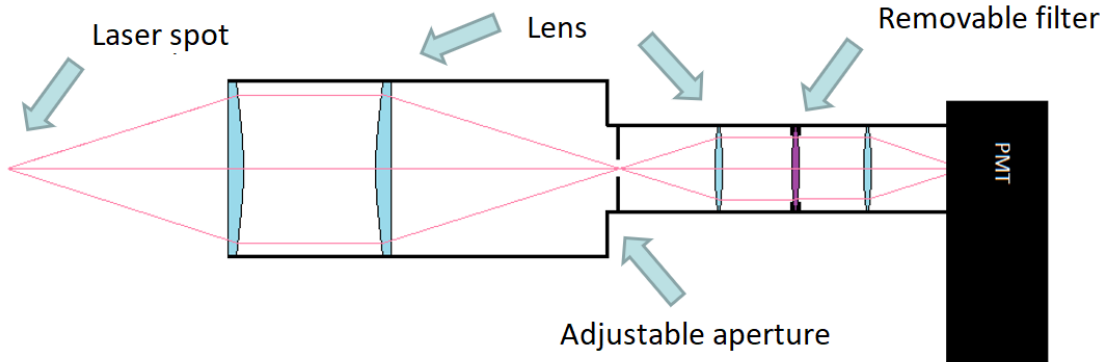


Figure 3.6: Schematic of detection optics set-up.

As part of the detection set-up a removable filter is used to select the fluorescence wavelength. The filter additionally blocks a large percentage of the background emission from the plasma as well as stray laser light being collected on the PMT. The filter is exchangeable using a Thorlabs filter holder to select for the fluorescence of

3.2. DIAGNOSTIC SET-UP

interest. A 656nm bandpass filter ($\Delta\lambda_{FWHM} = 10\text{nm}$) is used for atomic hydrogen, and a high pass $>800\text{nm}$ is used for krypton.

The entire PMT and optics assembly is mounted on a linear platform, this moves the focus of the optics assembly radially from the centre of the chamber. Additionally there are two micrometer actuator controlled platforms, one provides finer position control in the radial direction. This allows full 0-40mm radial range in MAGPIE. At 40mm the chamber walls block optical access. The other platform provides up to 50mm range in the axial direction. This also provides full range of the available optical access through the optical ports.

3.2.3 Data Acquisition and System Control

The Nd:YAG laser operates at 10Hz, therefore in the interest of protecting the internal components of the laser, all timing is established from the 10Hz sync output of the laser. A schematic of the hardware set up is shown in Figure 3.7. The output is connected to the trigger input of an Agilent 33250A Function/Arbitrary Waveform Generator. The function generator controls the pulsing of the RF to MAGPIE by providing an on/off +5V ttl signal to the Ampegon RF transmitter. The pulse duration and frequency of the plasma discharge are controlled by the function generator. A delay is added to the signal to pulse the RF at the required time in regards to the next laser shot. This is shown in the timing schematic in Figure 3.8. This set-up isolates the high power RF supply from the rest of the control system and can simply be controlled separately through the function generator.

The function generator outputs a sync signal with the same frequency and time as the laser sync pulse. This outputs a trigger signal to a National Instruments BNC-2110 Data Acquisition Board which is connected to a National Instruments PXI PC. This provides a trigger pulse for a LabviewTM program to sync the timing with other equipment. The function generator also provides a trigger pulse for an Agilent Technologies InfiniiVision DSO-X 3014A oscilloscope via the same sync output.

3.2. DIAGNOSTIC SET-UP

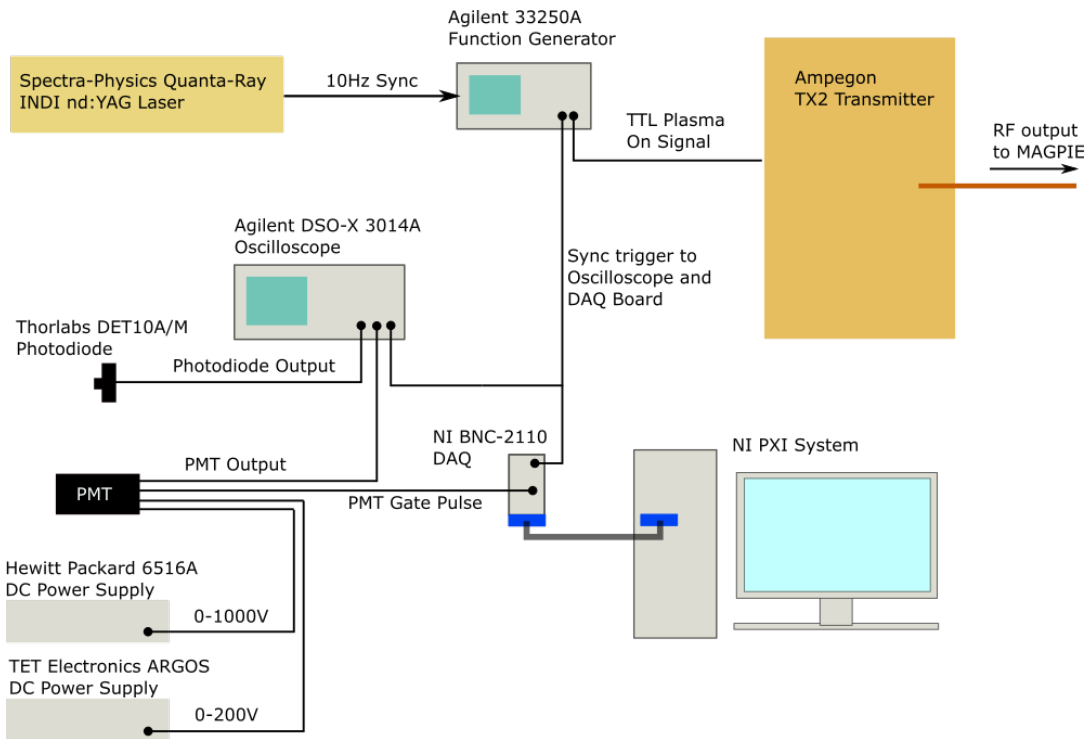


Figure 3.7: Schematic of the physical hardware controlling timing and data collection for the TALIF diagnostic.

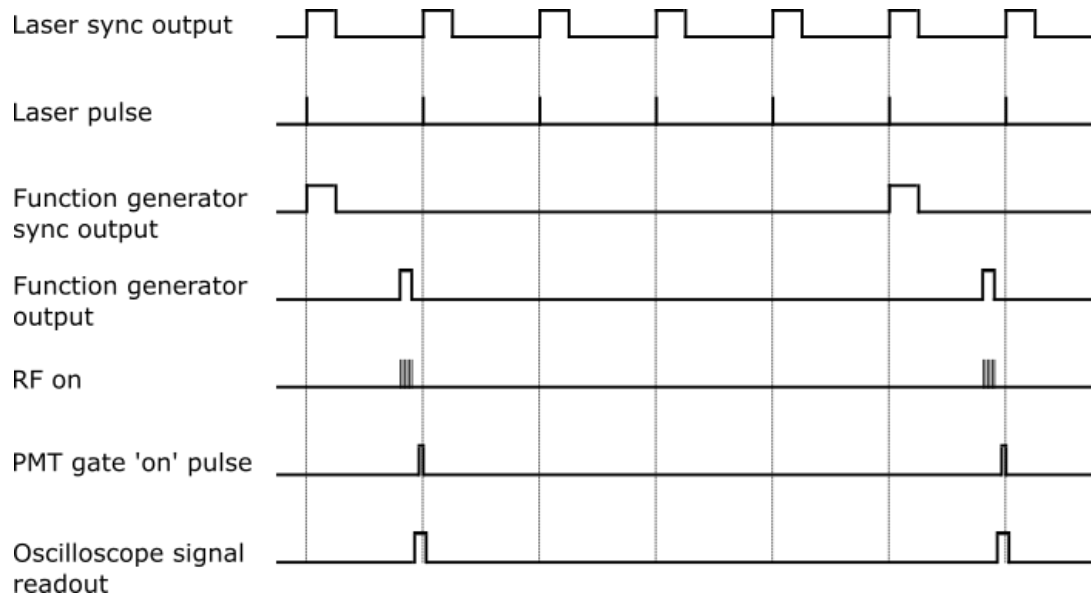


Figure 3.8: Schematic of the syncing of the diagnostic components.

3.2. DIAGNOSTIC SET-UP

A LabviewTM program has been written to control and provide timing for the TALIF diagnostic. It controls the gating of the photomultiplier tube by providing a +5V ttl pulse from the DAX board to the PMT gate input which switches it 'on' and maintains it gated open for the duration of the laser pulse and the fluorescence. The PMT gated 'on' width is controlled by the length of gate pulse. The required gate width is input into the front panel of the LabviewTM program.

The output of the PMT is connected to the Agilent Technologies InfiniiVision DSO-X 3014A oscilloscope. The parameters of the oscilloscope are entirely controlled through the LabviewTM program. Parameters that are controlled via the program are: sampling rate, time window and time delay. It also allows the number of averages and the type of averaging to be selected.

The basic flow of the developed LabviewTM program is shown in Figure 3.9. After setting up the experimental run parameters and initialising the connected Agilent oscilloscope, the program will wait for a trigger pulse from the function generator, which is synchronous with the laser pulse. If the program does not receive a trigger in the specified time frame then it will exit and return an error informing the user. Upon receiving a trigger, a delayed pulse is sent to the PMT to gate 'on' for the next laser pulse. The program will then average measurements from the PMT on the oscilloscope until the desired number of averages is obtained. If multiple measurements are required at the same wavelength, then the program will take the same number of measurements again and record this measurement separately. Once the number of measurements are completed the program outputs a TTL signal to the laser, signalling the laser to move to the next wavelength and repeat the process until all wavelengths have been scanned. A full 15pm wavelength scan with 64 averages per wavelength measurement and 0.1pm resolution takes approximately 1.5 hours.

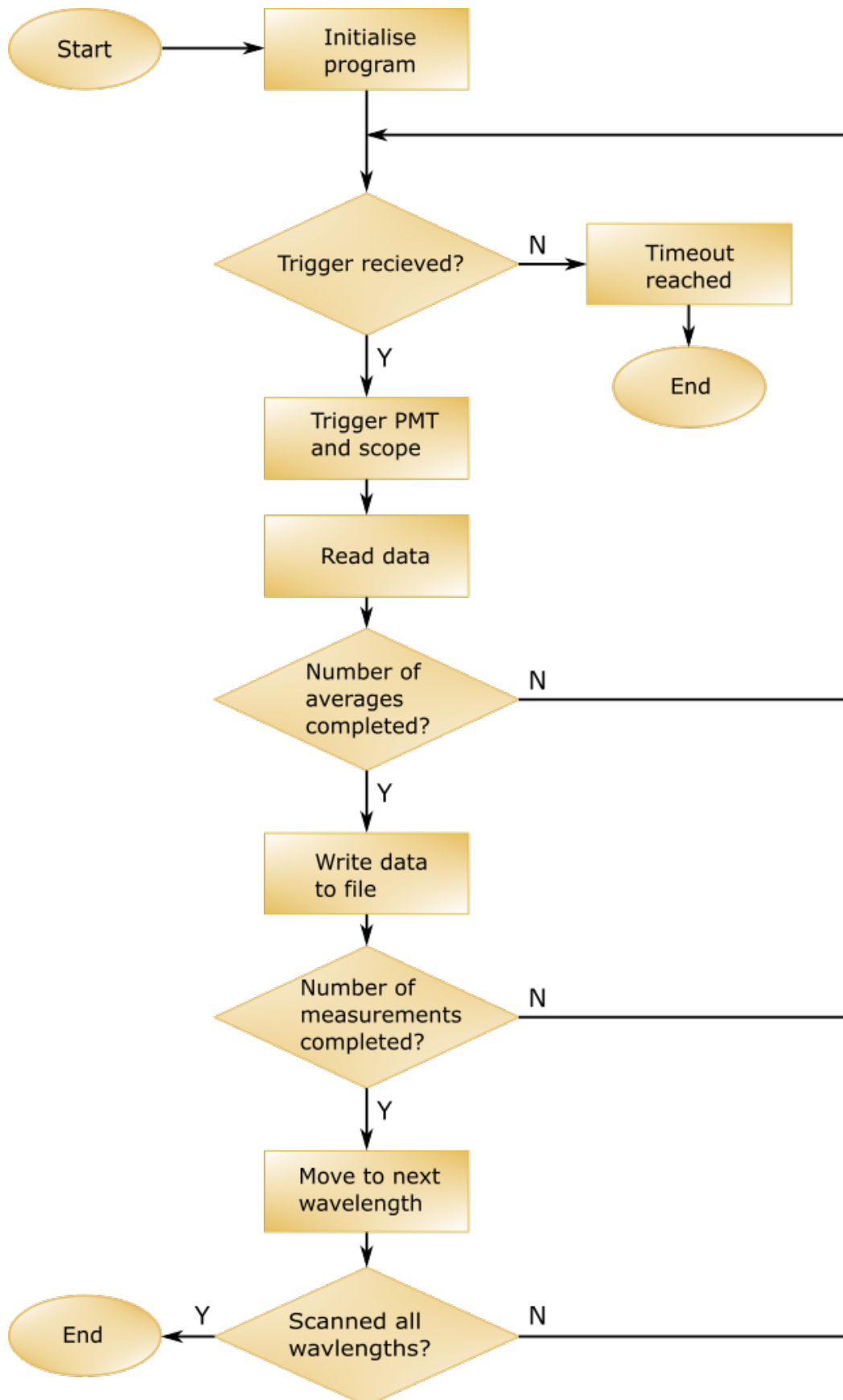


Figure 3.9: LabviewTM flowchart to control TALIF diagnostic system developed during this research.

3.2.4 Signal Analysis

The most important outputs from the TALIF diagnostic are the laser energy and the fluorescence signal itself. Shown in Figure 3.10 is a plot of the measured laser pulse (black) and the corresponding recorded fluorescence (red) from the atomic hydrogen population in a hydrogen plasma discharge. The data has been independently normalised to display on the same plot.

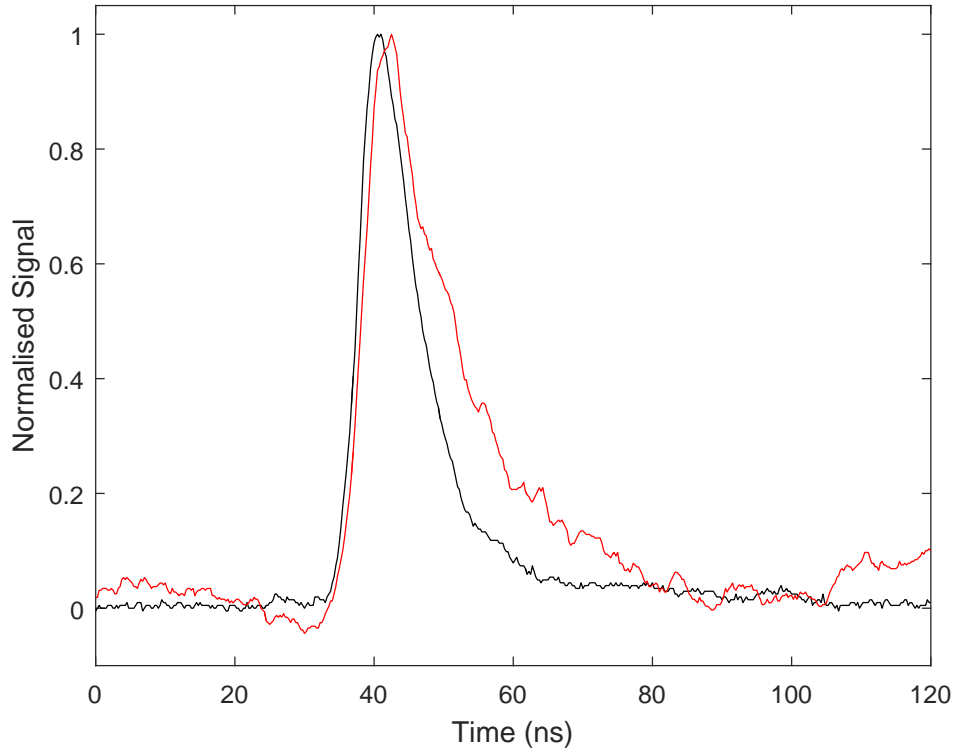


Figure 3.10: Normalised plot of a measured laser signal (black) and the corresponding measured fluorescence signal (red).

The probed species can have a wide energy distribution within the plasma due to broadening effects, such as Doppler broadening and the laser linewidth. This wide distribution requires that the laser wavelength is scanned over a small wavelength range (typically $<0.1\text{nm}$) to measure the entire population of the probed species. Figure 3.11 shows the integrated fluorescence intensity for each wavelength in the wavelength scan. The intensity of each fluorescence is corrected for the laser

3.3. CALCULATIONS AND CALIBRATIONS

pulse energy. It is extremely important to record the laser energy as drifts in the laser energy were observed over the long data accumulation times. The broadening effects and laser energy corrections are covered in the next section of this chapter. One wavelength scan with 32 averages (32 laser shots) per laser wavelength takes approximately 1 hour to complete. Over this time the laser pulse energy and linewidth remains fairly steady. The energy and linewidth also remains within measured errors over months of operation and only needs to be recalibrated with a change of the laser dyes.

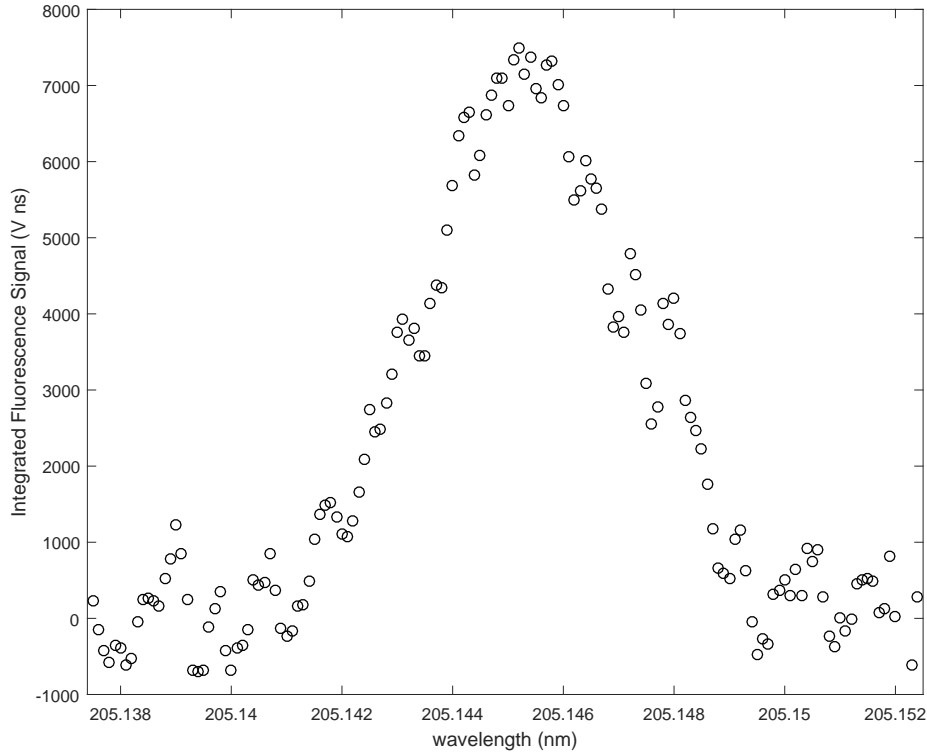


Figure 3.11: Wavelength scan against the integrated fluorescence signal of atomic hydrogen (656nm) corrected for laser energy.

3.3 Calculations and Calibrations

The TALIF diagnostic can be used to determine densities, temperatures and velocities of the species of interest simply by scanning across the absorption. However,

3.3. CALCULATIONS AND CALIBRATIONS

careful attention must be given to the calibration and the broadening mechanisms of the absorption. This section will give a thorough explanation of determining these parameters and the considerations that must be taken into account.

3.3.1 Density Calculations

As species in a plasma have a spread of velocities, the laser wavelength needs to be scanned across a range to probe the entire population. The density of the species n_i will be proportional to the area under the fluorescence scan. This integrated fluorescence signal depends on the density and can be considered to consist of three other factors; the absorption, the emission and the detection. In general the fluorescence can be written as:[145]

$$S_f = n_i f_{exc} q_f f_{det} \quad (3.1)$$

where f_{exc} consists of the components related to the excitation of the species, such as the cross section of the two-photon absorption and the laser properties.

Important laser properties for the excitation are the laser intensity, excitation frequency and the temporal and spatial beam profiles. The temporal and spatial beam profiles can be neglected from the relating signal to density if calibrated using a species with a similar excitation scheme. q_f is the quantum efficiency of the excited transition. q_f includes the branching ratio A_{kl} from state k to l for the fluorescence of interest and the lifetime of the excited state. Finally the f_{det} relates to the properties and efficiency of the detection system for the fluorescence of the species of interest. Important properties that must be considered are the transmission coefficients of the detection optics, this includes all of the lenses and filters as each will have an independent transmission coefficient, the quantum efficiency of the detector and the solid angle of detection. Combining all of these terms gives a more complete equation relating the density and the fluorescence signal, the subscripts are dropped for ease of reading:

$$S_{PMT} \propto n\sigma^{(2)} \left(\frac{I}{\nu}\right)^2 A\tau T\xi \frac{\Delta\Omega}{4\pi} G \quad (3.2)$$

Here, n is the density of the species, $\sigma^{(2)}$ is the cross section for the two photon absorption, I is the laser intensity, as the excitation involves two photons the signal increases by the square of the laser intensity and ν is the frequency of the excitation photons. Terms relating to the laser profiles have been dropped from the equation as they can be calibrated for. A is the Einstein coefficient for the spontaneous emission of the fluorescence transition and τ is the lifetime of the excited state. T is the total optical transmission of the detection system, ξ is the quantum efficiency of the detector for the fluorescence wavelength, while $\frac{\Delta\Omega}{4\pi}$ and G are the solid angle of collection and the gain multiplication, respectively.

Hydrogen Calibration

To determine the density, temperature and other plasma parameters, a calibration procedure is needed. Calibration of the signal for density is carried out using the noble gas calibration method described in detail in [107, 146]. This calibration method relies on using a noble gas that has a two photon absorption transition close to the absorption in the species of interest. A close transition is required so that the laser properties remain constant for both excitations and can be calibrated out. Noble gases naturally exist in the atomic state which allows the density to be easily measured and calibrated against the fluorescence signal.

Neutral krypton is an excellent choice for calibrating the two photon laser induced fluorescence of the Ly_β of atomic hydrogen. Krypton has a ground state transition $4p_1^6 S^0 \rightarrow 5p'[3/2]_2$ at 102.1nm (204.2nm for 2 photons) and decays to the $5s'[1/2]_1$, fluorescing with 826.3nm photons.[107] This excitation is very close in energy to the $1s^2 S_{\frac{1}{2}} \rightarrow 3d^2 S_{\frac{5}{2}}$ of hydrogen and makes a suitable calibration species. Both of these TALIF excitation and fluorescence schemes are shown in Figure 3.12.

Using Equation 3.2 for the fluorescence signal and taking the ratio of the krypton to hydrogen gives:

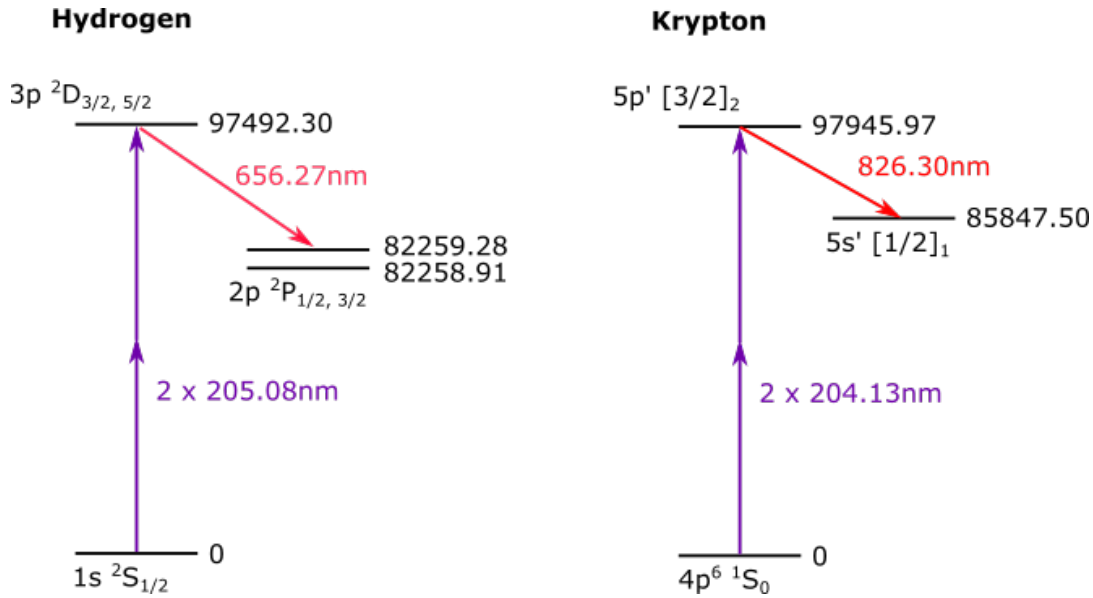


Figure 3.12: TALIF excitation scheme for hydrogen and krypton.

$$\frac{S_{Kr}}{S_H} = \frac{n_{Kr}\sigma_{Kr}^{(2)} \left(\frac{I_{Kr}}{\nu_{Kr}}\right)^2 A_{Kr}\tau_{Kr}T_{Kr}\xi_{Kr} \frac{\Delta\Omega}{4\pi} G_{Kr}}{n_H\sigma_H^{(2)} \left(\frac{I_H}{\nu_H}\right)^2 A_H\tau_H T_H \xi_H \frac{\Delta\Omega}{4\pi} G_H} \quad (3.3)$$

If the solid angle remains constant between calibration and experiment then it will cancel out. Rearranging for atomic hydrogen density (n_H) gives:

$$n_H = n_{Kr} \frac{S_H}{S_{Kr}} \left(\frac{I_{Kr}\nu_H}{I_H\nu_{Kr}}\right)^2 \frac{\sigma_{Kr}^{(2)}}{\sigma_H^{(2)}} \frac{A_{Kr}}{A_H} \frac{\tau_{Kr}}{\tau_H} \frac{T_{Kr}}{T_H} \frac{\xi_{Kr}}{\xi_H} \frac{G_{Kr}}{G_H} \quad (3.4)$$

The majority of the terms in the expression remain constant and are previously measured in the literature; the excitation frequency (ν), the Einstein coefficients (A), the excited state lifetime (τ) and the quantum efficiency of the detector (ξ) for both hydrogen and krypton can be defined as a calibration factor (CF) in Equation 3.5. Values for each of these terms can be found in Table 3.1. If the same gain is used for calibration and experiment then the gain factor can be neglected. Otherwise the detector signal-to-gain calibration should also be determined.

$$CF = \left(\frac{I_{Kr}\nu_H}{\nu_{Kr}}\right)^2 \frac{\sigma_{Kr}^{(2)} A_{Kr} \tau_{Kr} T_{Kr} \xi_{Kr} G_{Kr}}{\sigma_H^{(2)} A_H \tau_H T_H \xi_H} \frac{n_{Kr}}{S_{Kr}} \quad (3.5)$$

3.3. CALCULATIONS AND CALIBRATIONS

Table 3.1: Table of values for H and Kr used for TALIF calibration

	H	Kr
λ (nm)	656.27	826.30
$A(s^{-1})$	4.4×10^{-7} [147]	2.7×10^{-7} [148]
τ (ns)	16.0[146]	35.4[146]
T	0.9394	0.9018
ξ	0.15	0.04

The intensity of the laser (I_{Kr}) used for exciting krypton is measured using the fast photodiode described in the experimental set-up. The ratio $\frac{n_{Kr}}{S_{Kr}}$ in Equation 3.5 is determined by isolating the pumps in MAGPIE and filling the chamber with krypton gas to a measured constant pressure. This allows the density of krypton to be calculated. The signal is determined from a TALIF scan of the krypton gas. A plot of the TALIF signal for increasing krypton density is shown in Figure 3.13 where $\frac{n_{Kr}}{S_{Kr}}$ is determined from the slope. The offset in the plot is due to integrating the voltage output from the PMT which has a slight background negative voltage output.

Substituting Equation 3.5 into Equation 3.6 gives a calibrated equation for the absolute density of atomic hydrogen in terms of the integrated fluorescence signal, the laser intensity, the calibrated gain and the determined calibration factor:

$$n_H = \frac{S_H}{I_H^2 G_H} CF \quad (3.6)$$

3.3.2 Temperature Calculations and Spectral Features

There are many mechanisms that broaden the absorption line and need to be understood and accounted for to correctly calculate the densities and temperatures. This is especially important for calculating the temperature of a species as it is related to the Doppler broadening of the absorption profile. Incorrectly assuming or neglecting

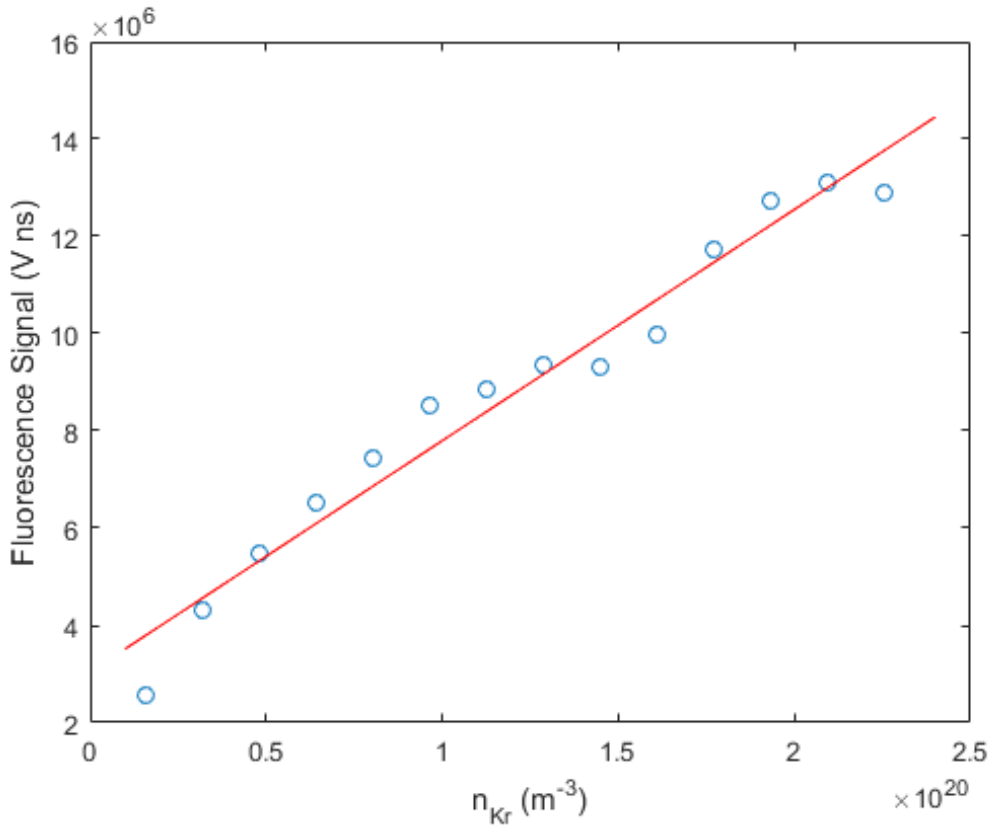


Figure 3.13: Plot of krypton density against the integrated PMT signal.

broadening effects can lead to significant overestimation of the Doppler broadening and hence the temperature.

Doppler Broadening

One of the major sources of broadening for absorption is Doppler broadening caused by the thermal motion of absorbing species. The greater the spread of thermal motion the larger the observed broadening will be. This is caused by the motion of an atom relative to the incident photon from the laser. The frequency of the photon relative to the atom is given by:

$$\Delta\nu = \nu_0 \frac{v}{c} \quad (3.7)$$

3.3. CALCULATIONS AND CALIBRATIONS

where $\Delta\nu$ is the shift in frequency observed by the absorbing atom, ν_0 is the unshifted frequency of the exciting photon, v and c are the velocity of the atom and speed of light respectively.

A Maxwellian distribution describes the velocity profile of a system of particles in thermodynamic equilibrium. It is assumed that the particles will have a Maxwellian distribution. The velocity distribution of the absorbing population can therefore be fit with a Gaussian function:

$$f(\nu) = \sqrt{\frac{m}{2\pi kT}} \exp \left[-\left(\frac{m(\nu - \nu_0)^2}{2k_B T} \right) \right] \quad (3.8)$$

where m and T are the mass and temperature of the absorbing species, respectively, ν_0 is the average velocity and k_B is the Boltzmann constant. The broadening of this Gaussian is then given by:

$$\sigma_D = \nu_0 \sqrt{\frac{k_B T}{mc^2}} \quad (3.9)$$

or in terms of the full width half maximum of the measured absorption:

$$\Delta\nu_{FWHM} = \frac{\nu_0}{c} \sqrt{8\ln 2 \frac{k_B T}{m}} \quad (3.10)$$

If all other broadening mechanisms can be neglected or accounted for, then the temperature population can be determined by:

$$T = \frac{\sigma_D^2 \nu_0^2 m}{c^2 k} \quad (3.11)$$

Isotopic Broadening

Each isotope of a species will have the centre absorption wavelength shifted due to the nuclear structure effecting the energy levels in the atom. The extent of the wavelength shifting depends on the species and is inversely related to the mass. Lighter species such as hydrogen, will have greater wavelength shifts for its isotopes than heavier elements such as krypton.

Table 3.2 contains the shift in wavelength ($\Delta\lambda_0$) for the $4p_1^6S^0 \rightarrow 5p'[3/2]_2$ transition for the isotopes of krypton along with the atomic mass and natural abundance of each.

Table 3.2: Table of wavelength shift from Kr84 for the $4p_1^6S^0 \rightarrow 5p'[3/2]_2$ transition, atomic mass and natural abundance of the naturally occurring isotopes of krypton.

Kr isotope	$\Delta\lambda_0$	atomic mass (u)	abundance
Kr78	-6.05×10^{-14} [149]	77.9204	0.35%
Kr80	-4.10×10^{-14} [149]	79.9164	2.25%
Kr82	-2.06×10^{-14} [149]	81.9135	11.6%
Kr83	-1.15×10^{-14} [150]	82.9141	11.5%
Kr84	0	83.9115	57.0%
Kr86	$+1.81 \times 10^{-14}$ [149]	85.9106	17.3%

The broadening of the krypton fluorescence was modelled using the data in Table 3.2. Each isotope is considered to have a Maxwellian distribution centred around its centre absorption wavelength and is broadened due to Doppler broadening. As ^{78}Kr has a very low abundance, 0.35%, it is ignored in the model. Figure 3.14 shows the individual contributions from each of the most abundant naturally occurring isotopes of krypton in dashed lines for T=50K. The total broadening is shown in the solid blue line. Even at the low temperature of 50K, the individual isotopes in krypton have very little effect on the broadening. At room temperature

3.3. CALCULATIONS AND CALIBRATIONS

(T=300K) the Doppler broadening further dominates any broadening that is due to the isotopes and the isotopic broadening is negligible.

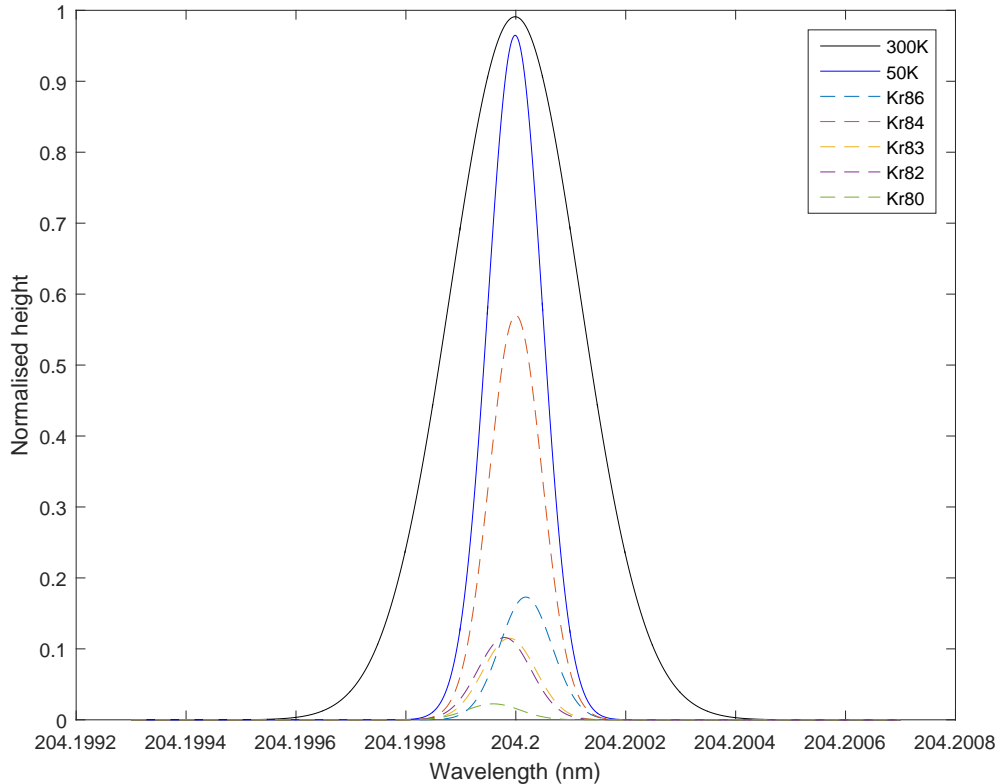


Figure 3.14: Model of the broadening due to the isotopes of krypton. The dashed lines are the individual contributions from the most abundant isotopes and the solid blue line is the total observed broadening with T=50K. The solid black line is the combined peak at T=300K.

Krypton is a heavy element and does not display a large shift in energy levels between isotopes, conversely hydrogen is much lighter and the change in energy levels between its isotopes makes them individually resolvable with LIF diagnostics. Table 3.3 contains the transition wavelength for the Ly_β for each of the naturally occurring isotopes of hydrogen. The transitions for hydrogen and deuterium are found in the literature. The wavelength for tritium is estimated by recognising that the shift arises due to, and is proportional to, the reduced mass of the atomic system (μ).[151]

3.3. CALCULATIONS AND CALIBRATIONS

$$\mu = \frac{m_1 m_2}{m_1 + m_2} \quad (3.12)$$

As the relative abundance of hydrogen is mostly comprised of 1H , there is little to be gained from modelling the abundances. Therefore for modelling the isotopic energy shifts it is assumed that each isotope has the same relative abundance.

Table 3.3: Table of data for isotopes of hydrogen

H isotope	Ly_β wavelength (nm)	atomic mass (u)	abundance
H	102.571	1.0078	99.98%
D	102.544	2.0141	0.02%
T	102.535	3.0160	trace

The isotopic splitting of hydrogen is shown in Figure 3.15 for a neutral temperature (T_H) of 1000K. In MAGPIE the approximate maximum neutral temperatures observed at higher powers is 1000K. It is seen that at this temperature all three isotopes are individually resolvable. It is not until much higher temperatures, such as those found in fusion devices, that the absorptions of hydrogen isotopes begin to overlap. Fitting for three populations still allows the isotopes to be measured. It can be seen in the figure the differences between the Doppler broadening for different temperatures, hydrogen has the largest FWHM while tritium has the smallest because of its larger mass.

Laser Line Width Broadening

The largest contributor to broadening of the absorption other than the above discussed Doppler broadening (λ_D) is caused by laser apparatus function (λ_l). The laser apparatus function includes all mechanisms that can broaden the laser width, these include fluctuations of power and frequency between pulses and the laser linewidth. Short pulsed lasers, such as those used in LIF type studies, typically have larger linewidths than continuous wave (CW) lasers which directly contribute to the laser apparatus function. Shown in Figure 3.16 is a schematic illustrating how the laser

3.3. CALCULATIONS AND CALIBRATIONS

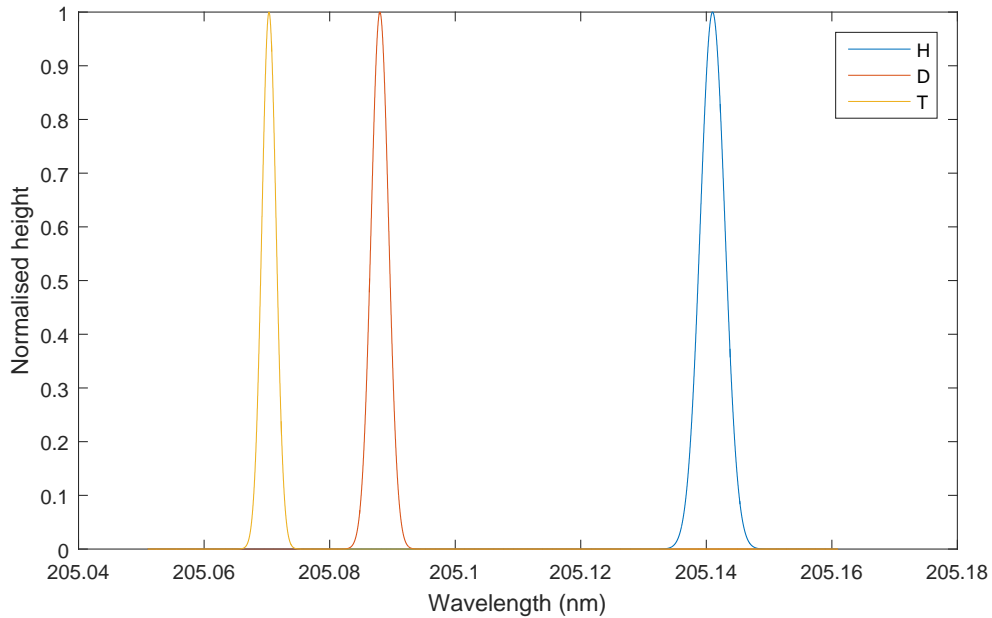


Figure 3.15: Resolvable isotopes of hydrogen using TALIF at T=1000K.

linewidth affects the absorption. As the wavelength is scanned further from the absorption wavelength, a broader laser will still be able to excite the fluorescence due to the combination of $\lambda - \Delta$ and $\lambda + \Delta$ in laser pulse. To correctly determine the temperature through the Doppler broadening any broadening from the laser must be accounted for.

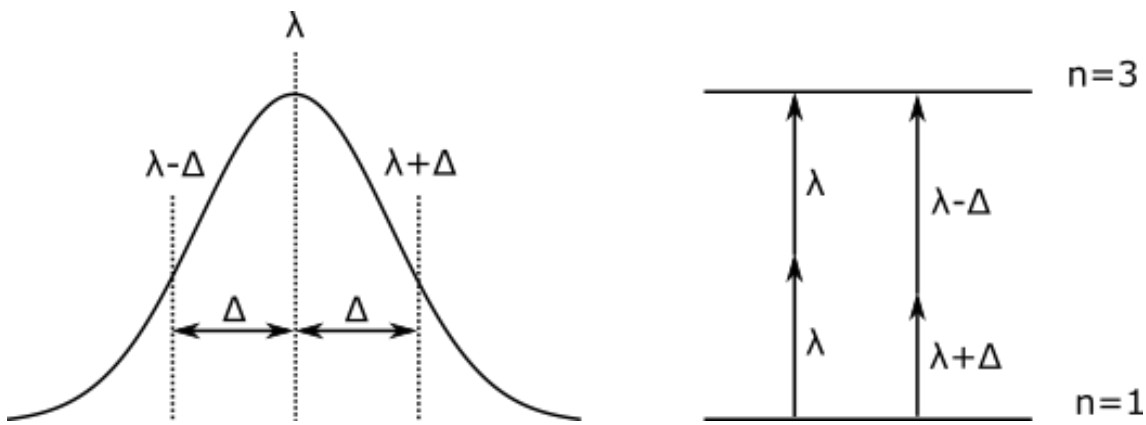


Figure 3.16: Photons of wavelengths from the edges of the laser linewidth (left) are able to excite a two photon excitation (right) by the contribution energy to cause the transition.

3.3. CALCULATIONS AND CALIBRATIONS

In the TALIF experiment the photon is counted twice because it is a two photon excitation. The total broadening will therefore be a double convolution of the laser apparatus function(λ_l) and the Doppler broadening(λ_D) as shown in Equation 3.13 where $\Delta\lambda_{abs}$ is the full width half maximum of the absorption.

$$\Delta\lambda_{abs} = \sqrt{\Delta\lambda_D^2 + 2\Delta\lambda_l^2} \quad (3.13)$$

For this experiment, the laser apparatus function has been determined using a mixed H₂/D₂ plasma by the method outlined by Lamara.[\[152\]](#) As discussed in the previous subsection, the Ly_β excitation scheme can resolve atomic hydrogen and deuterium populations at low temperatures. The excitation for atomic hydrogen (2x205.144nm) and deuterium (2x205.088nm) are very close which allows two TALIF scans to be completed in a narrow wavelength scan. The properties of the laser should remain the same across such a small range. Using Equation 3.13, separate equations can be made for both hydrogen and deuterium.

$$\Delta\lambda_{abs,Hy} = \sqrt{\Delta\lambda_{D,Hy}^2 + 2\Delta\lambda_l^2} \quad (3.14)$$

$$\Delta\lambda_{abs,Du} = \sqrt{\Delta\lambda_{D,Du}^2 + 2\Delta\lambda_l^2} \quad (3.15)$$

where subscripts *Hy* and *Du* represent hydrogen and deuterium respectively. Hydrogen and deuterium atoms are expected to be in thermal equilibrium and have the same temperature ($T_H = T_D$). From Equation 3.10, the broadening is proportional to the square root of temperature and inverse mass. A deuterium atom has twice the mass of a hydrogen atom. Therefore:

$$\Delta\lambda_{D,Du}^2 = \frac{\Delta\lambda_{D,Hy}^2}{2} \quad (3.16)$$

3.3. CALCULATIONS AND CALIBRATIONS

Combining Equations 3.14-3.16 gives:

$$\Delta\lambda_l = \sqrt{\frac{2\Delta\lambda_{abs,Du}^2 - \Delta\lambda_{abs,Hy}^2}{2}} \quad (3.17)$$

Shown in Figure 3.17 is the fluorescence scan across both the atomic hydrogen and deuterium absorptions. A FWHM of 5.64pm and 4.05pm are measured for hydrogen and deuterium peaks respectively. Using Equation 3.17 this gives a laser apparatus function of 1.11pm. This method determines the average broadening caused by the laser linewidth and fluctuations in the outputted laser wavelength. The area under each peak is a 1:1 ratio, agreeing with observations previously.[152, 153, 154]

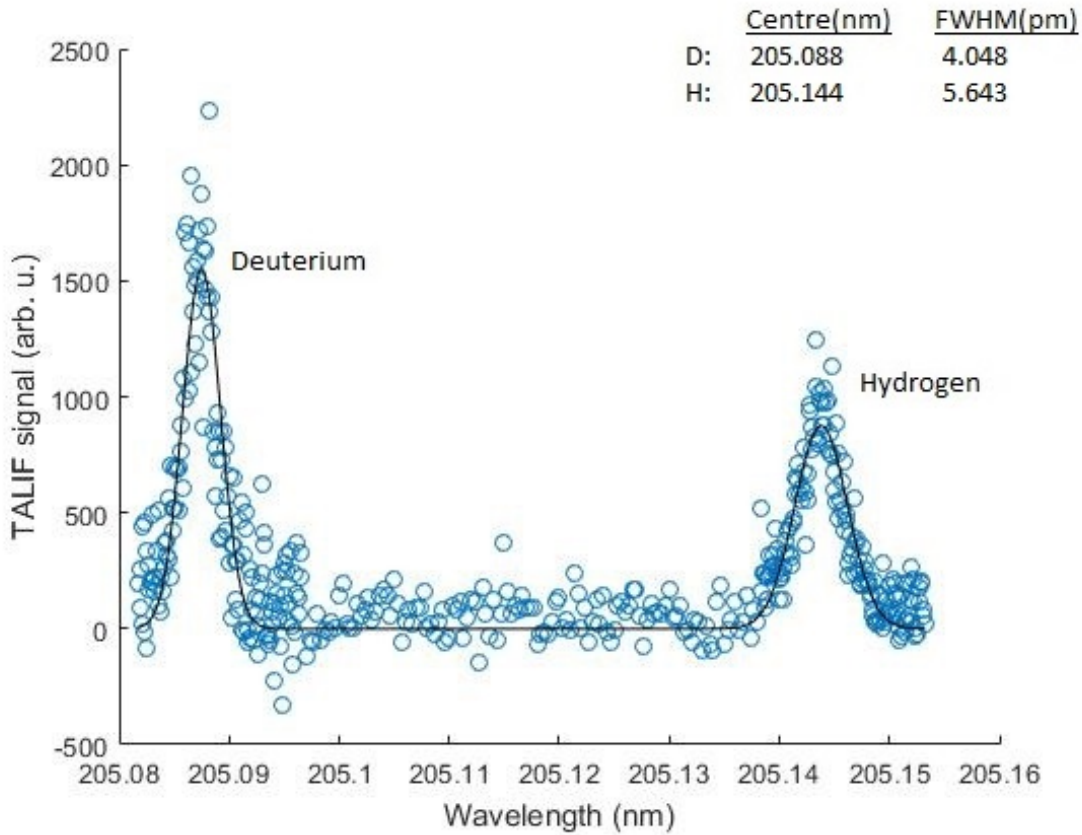


Figure 3.17: Fluorescence scan of mixed 50:50 H₂/D₂ plasma used to determine the laser apparatus function.

Saturation Broadening

If the absorbing population is locally depleted during the excitation then saturation has occurred. When the laser pulse saturates the population, the fluorescence signal will no longer be proportional to the square of the laser intensity as shown in Equation 3.6. The saturated signal will be proportionally lower compared to the laser energy, leading to an underestimation of the density and temperature. The point of saturation depends on a range of experimental conditions including; the density of the absorbing state and the size of the laser spot at the focus, which is affected by the focal length of the lens.

The saturation point is investigated for both krypton and hydrogen by plotting the detected signal against the laser energy, while keeping the experimental conditions the same. The laser wavelength was maintained at the centre absorption wavelength. The chamber was filled with krypton gas to 10mTorr and the TALIF signal plotted against the laser energy as shown in Figure 3.18. Under the experimental conditions and set-up used in this research, 10mTorr krypton displayed a saturation at the centre wavelength at approximately 0.8mJ. Even at lower energies the wings in the absorption will also display saturation due to the lower densities at the edges of the velocity distributions. Therefore the laser energy must be kept lower than the measured saturation point. In this work the laser energy is kept less than 0.1mJ to avoid saturation.

The saturation for atomic hydrogen was determined at $100\mu s$ into the after-glow of a 5ms pulsed 1kW plasma. The plot of the TALIF signal for laser energy is shown in red in Figure 3.18. It is seen that atomic hydrogen displays a change in the relation indicating the saturation point at 1.06mJ.

Zeeman Splitting

In the presence of magnetic fields, the energy levels in atoms lose their degeneracy as the energies of states change. This splitting of energy levels is known as Zeeman

3.3. CALCULATIONS AND CALIBRATIONS

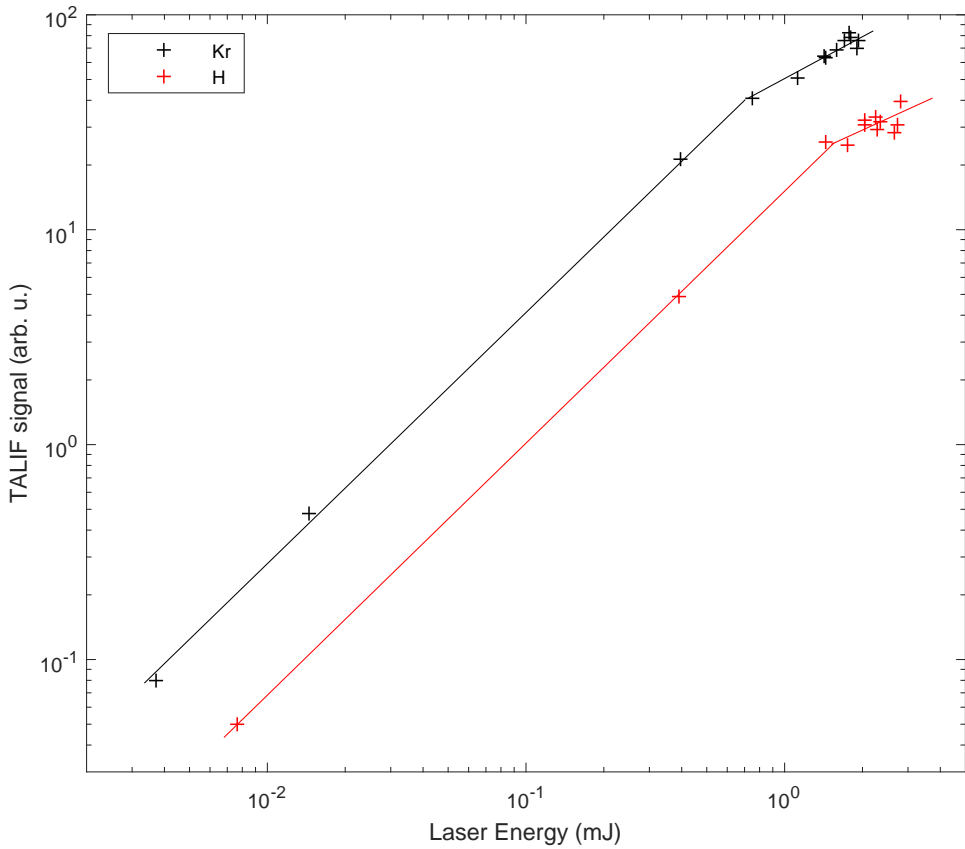


Figure 3.18: TALIF signal against laser energy for atomic hydrogen (red) and krypton (black). The change in the relationship marks the saturation energy for each species in the experimental set-up.

splitting. The energy change in energy levels by Zeeman splitting is given by:[155]

$$\Delta E_Z = \mu_B B g m_j \quad (3.18)$$

where μ_B is the bohr magneton, B is the magnetic field strength, g is the lande g-factor, which is given by:

$$g = 1 + \frac{j(j+1) + s(s+1) - l(l-1)}{2j(j+1)} \quad (3.19)$$

3.3. CALCULATIONS AND CALIBRATIONS

m_j is the change in the total angular momentum for the transition, in the case of TALIF where there are 2 photons, $m_j = 0, \pm 2$. For the $1s^2S_{\frac{1}{2}} \rightarrow 3d^2D_{\frac{5}{2}}$ transition in hydrogen, the $1s$ ground state will split into 2 states in an external magnetic field. The upper $3d$ state splits into 6 separate states and the $3s$ splits into 2 for each of the available j states. The Zeeman split energy levels for the $1s$ to $3s, d$ two photon transition are shown in Figure 3.19 for the allowed m_j .

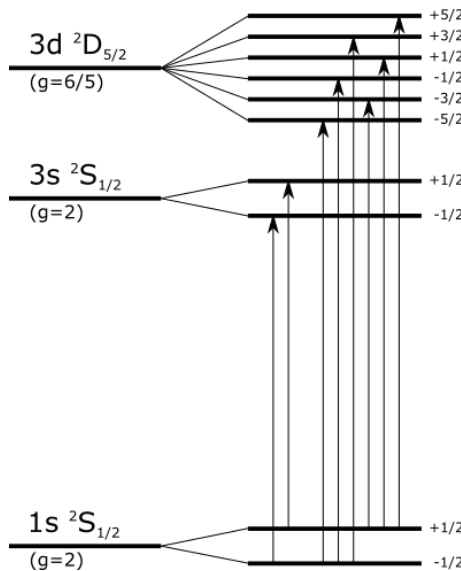


Figure 3.19: Zeeman splitting of the $1s$, $3s$ and $3d$ energy levels for atomic hydrogen. The allowed transition are shown.

When the Zeeman splitting is below resolvable levels it will be displayed as a broadening of the peak and should be considered. As shown and discussed in Chapter 2 the externally supplied magnetic field has a maximum of 0.19T with the 1000A-1000A coil configuration. The shift in absorption wavelength for each of the split energy states for the $1s^2S_{\frac{1}{2}} \rightarrow 3d^2D_{\frac{5}{2}}$ under this maximum field configuration is shown in Figure 3.20 (top). While there is noticeable splitting under this magnetic field, the Doppler broadening is still the major component of the broadening. The final shape of the peak is slightly broadened but the individual states are unresolvable. Shown on the bottom of Figure 3.20 is the Zeeman splitting from the magnetic field under standard operating conditions at the TALIF measurement position ($z=15\text{cm}$). Under standard operating conditions the peak is not noticeably changed by the Zeeman splitting.

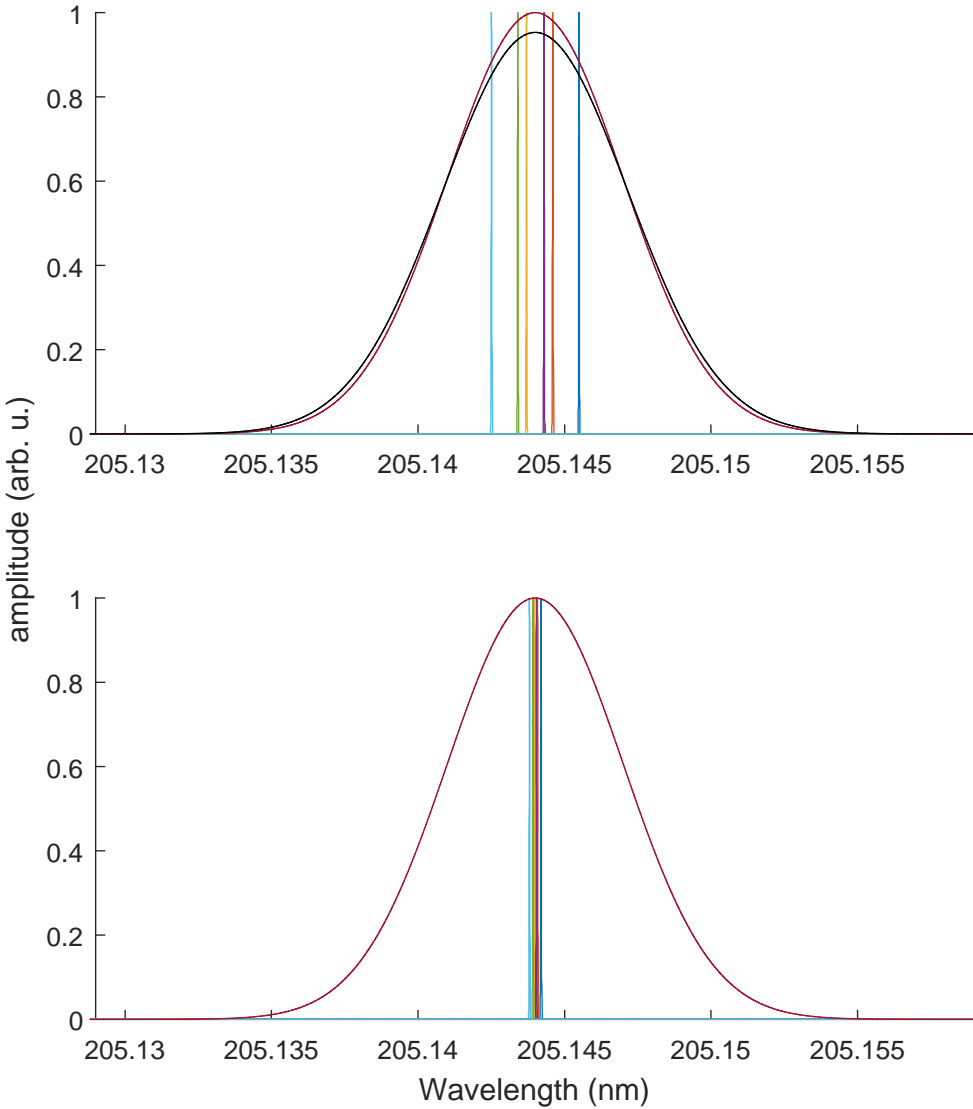


Figure 3.20: Zeeman splitting of the $1s^2 S_{\frac{1}{2}} \rightarrow 3d^2 S_{\frac{5}{2}}$ transition under the maximum magnetic field in MAGPIE (top) and standard operating conditions (bottom). The unbroadened peak is shown in red and the Zeeman broadened peak is shown in black.

It is worth noting however that under strong magnetic fields the Paschen-Bach effect will occur, where the spin and angular momentums are decoupled. The Paschen-Bach effect leads to additional splitting of the states and would be expected under the much larger magnetic fields expected in tokamak devices.

Stark Broadening

In the presence of a strong electric field, the energy levels in the atoms can be split depending on the electric field strength, this is known as stark splitting. As there is no uniform electric fields in MAGPIE, stark splitting is due to the collisions and micro-fields within the plasma. Electric fields in low density and temperature plasmas are generally very small and short lived and don't have a significant effect on the stark splitting of the energy states. It has been shown that collisions with the ions are the dominant stark broadening mechanism for the 656nm H_α state [156]

The stark broadening of the Ly_α transition for a range of plasma densities and temperatures have been computed in [157]. For stark broadening to become meaningful ($\text{FWHM} > 1\text{pm}$), electron densities on the order of 10^2 times higher than those observed in MAGPIE. Therefore stark broadening is considered negligible in MAGPIE.

Pressure Broadening

Broadening of the line width can occur due to perturbations of energy levels in the particles due to collisions with neighbouring particles.[158] Line broadening due to collisions is generally called pressure broadening (Stark broadening is occasionally also grouped under pressure broadening) and can generally be categorised into resonance broadening and Van der Waals broadening. Resonance broadening occurs between particles with allowed dipole transitions.[158] However as the two-photon transition is a forbidden transition between the excited state and the ground state, resonance broadening is negligible in this work.

Van der Waals broadening can occur between different atoms and/or molecules, but over a much smaller distance than the other broadening mechanisms discussed in this work.[158] The Van der Waals broadening is given by:[159]

$$\Delta\lambda_{VW} = \frac{2\gamma}{N} \left(\frac{T_g}{T_0} \right)^\alpha n_0 \quad (3.20)$$

$$\frac{2\gamma}{n_0} = 8.16(\Delta C_6/\hbar)^{2/5}\bar{\nu}^{3/5} \quad (3.21)$$

where, $\Delta\lambda_{VW}$ is the full width half maximum due to Van der Waals broadening, $2\gamma/n_0$ is the reduced width coefficient where n_0 is the total number density, T_g and T_0 are the gas and reference temperatures respectively, ΔC_6 is the Van der Waals constant, α is an empirically determined constant and $\bar{\nu}$ is the relative mean velocity of the interacting particle. Due to the low densities in this work, pressure broadening is expected to have negligible effect on the the broadening of the absorption line-width.

3.3.3 Velocity Calculation

Photons from the laser will be Doppler shifted in the frame of the particles. If the bulk flow of particles is aligned in the same direction as the laser propagation then the photon energy will be shifted according to the velocity of the particles. Bulk particles moving towards the laser will be blue shifted and the absorption will occur for a lower energy and therefore the wavelength will be larger. Figure 3.21 shows an idealised example of the absorption occurring at a higher wavelength when the bulk velocity is towards the laser. The opposite will occur for particles with a velocity distribution away from the laser, it will be red shifted and require a higher laser energy, resulted in the absorption occurring for a lower laser wavelength.

The Doppler relation in Equation 3.22 relates the shift in the centre absorption wavelength or frequency with the average velocity of the species along the direction of the laser propagation:

$$\frac{\Delta\lambda}{\lambda} = \frac{\Delta\nu}{\nu} = \frac{v}{c} \quad (3.22)$$

where $\Delta\lambda$ is the shift in wavelength from the centre wavelength, λ , and $\Delta\nu$ is the frequency shift from the centre frequency, ν . v and c are the average speed of the absorbing species and the speed of light. Accurate measurements of the peak shift

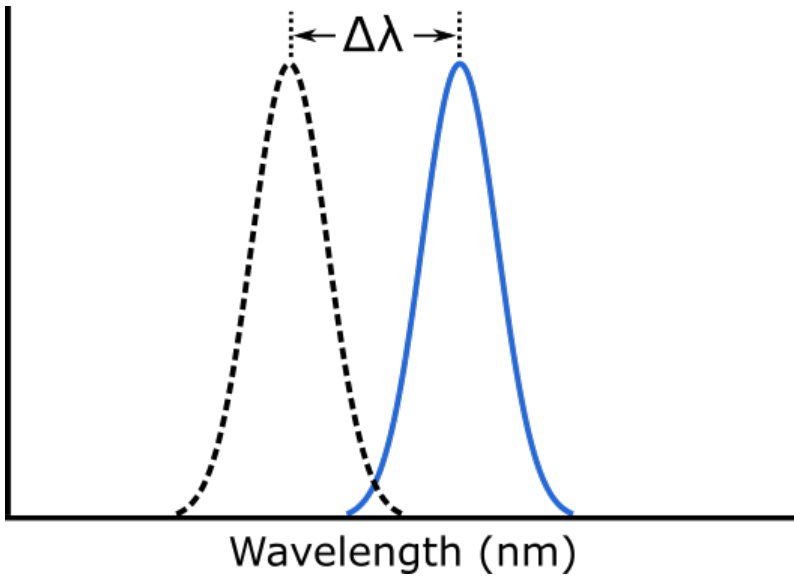


Figure 3.21: Wavelength shift of the centre peak of the absorption due to Doppler shift.

allows the average velocity of the species to be determined. This provides information about the bulk flow of the particles in the plasma. It is important to note that this measurement is in the direction of the laser propagation only.

Velocities of the neutral species have not been determined in this work. The majority of particle flows in MAGPIE are expected to be axial along the device, while measurements presented in this dissertation have been performed side on to the MAGPIE target chamber in the radial direction. Therefore very little shift in the velocity is expected. Accurate measurement and calibration of the wavelength is required to measure wavelength shift and the current TALIF diagnostic does not have this capability. Possible upgrades for measuring the wavelength shift could be to use a spectral analyser or an iodine gas cell.

3.3.4 Lifetimes and Decay Constants

Due to the selection rules, atomic hydrogen can be excited from the 1s ground state to either the 3s or 3d upper state via the two photon absorption. The excitation

3.3. CALCULATIONS AND CALIBRATIONS

to the 3d state has a larger cross section than to the 3s state. The lifetime will depend on the de-excitation channels available to each level. If they are collisionally isolated, they cannot change state through collisions and decay through radiation only. The lifetime of the state will then simply be the natural lifetime of the state. The 3d state has a natural life of 16ns, while the 3s has a longer lifetime of 150ns.

If there is coupling between the states caused by collisions, the states will be populated depending on their statistical weights. In this case the lifetime will be a weighted average of the lifetimes of each decay path available to the excited atoms.

By fitting exponential decay functions of the form:

$$\exp\left(-\frac{t}{\tau}\right) \quad (3.23)$$

to the individual fluorescence signals the lifetimes of the fluorescence can be determined. Shown in Figure 3.22 is a fit of the lifetime using the exponential decay function.

To determine the lifetime of a state under a certain condition and position, the exponential decay function was fitted to the fluorescence signal from the peak of the wavelength scan with the five closest wavelength measurements both above and below the peak. The more intense fluorescence signals close to the centre peak were used because they provide a better signal-to-noise ratio compared with signals near the edge of the absorbed wavelength range. Therefore the presented lifetimes are an average of eleven measurements. Shown in Figure 3.23 are measured fluorescence lifetimes of the excited states in the afterglow for 5kW (top) and 20kW (bottom) plasma. Shown are the 5kW measurements at a radial position of 10mm from the centre and the 20kW at 30mm. There is little variation in the lifetime of the excited states across all measurements in the research for all powers 1-20kW and all radial positions 0-30mm.

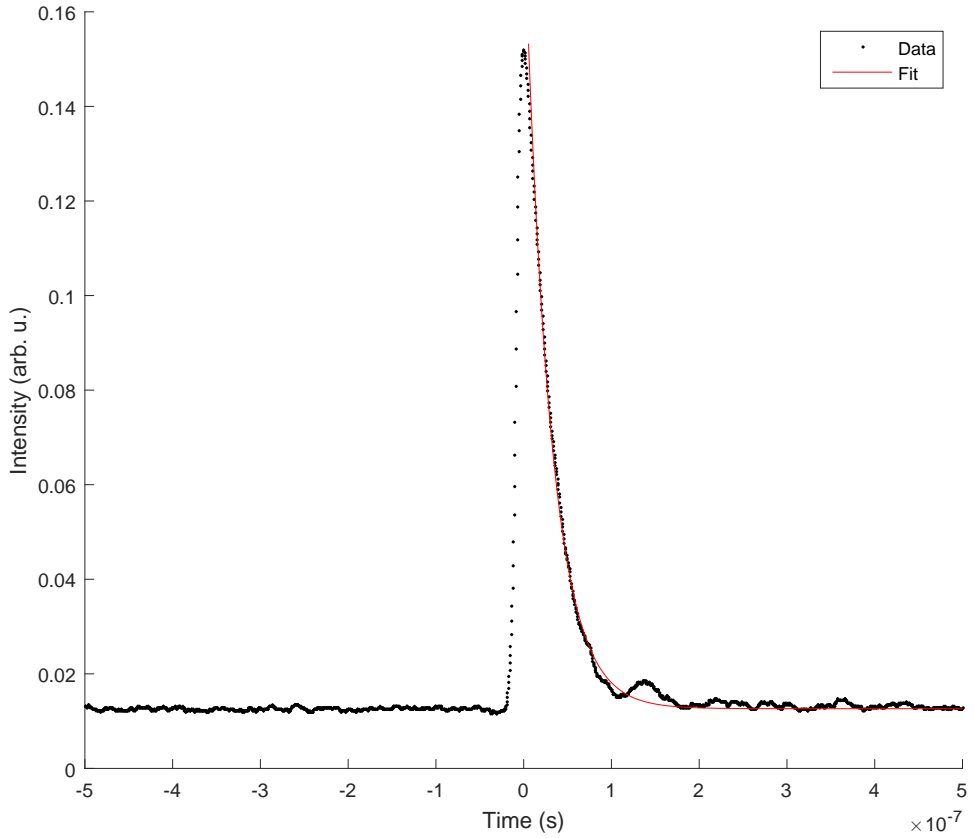


Figure 3.22: Fit of the excited state lifetime to a fluorescence signal.

As shown in Figure 3.23 the lifetimes remain fairly constant, approximately 17ns for 5kW and 25ns for 20kW. Both values are within the errors of each other. The lifetimes for the 5kW example suggest that only the 3d state is being measured by the TALIF and it is appropriate to use the $1s^2 S_{\frac{1}{2}} \rightarrow 3d^2 S_{\frac{5}{2}}$ for calculations. Work by Boogaarts *et al.* measured lifetimes of 10ns in their arcjet plasma, suggesting that collisional coupling was occurring between the 3s,p and d states which agrees with a statistical distribution over the three states.[\[145\]](#)

3.4 Summary

This chapter has presented the newly established two-photon absorption laser-induced fluorescence diagnostic that has been set up as part of this research. The operation

3.4. SUMMARY

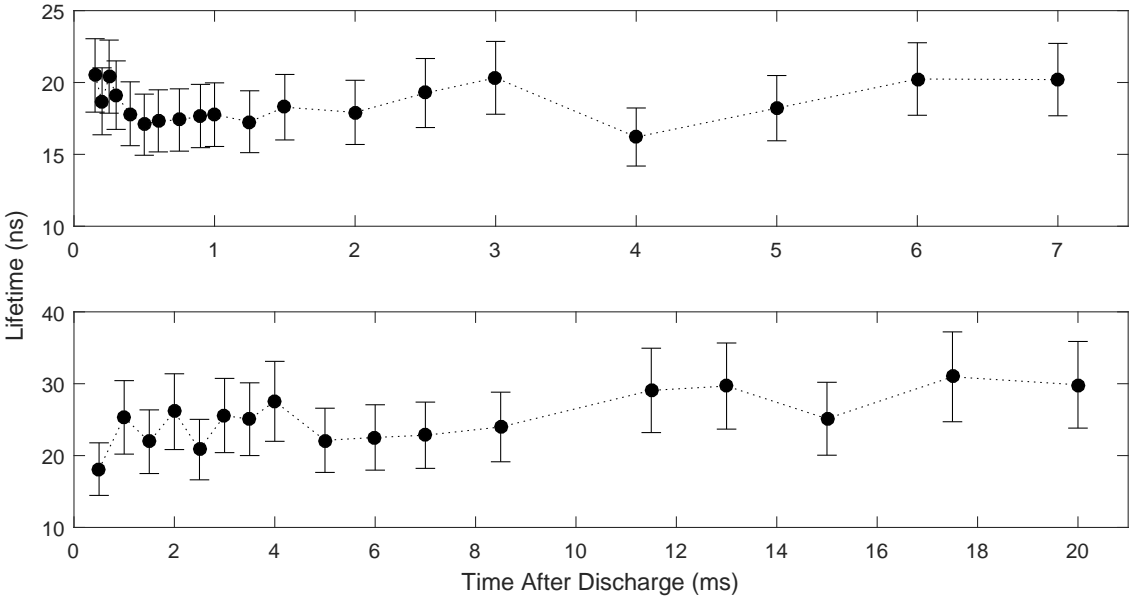


Figure 3.23: Lifetimes of the upper TALIF state from atomic hydrogen. Afterglow measurements for 5kW (top) and 20kW (bottom) plasmas. Measurements are made at radial position 10mm (top) and 30mm (bottom).

and control of the diagnostic has been covered in detail with discussions of the laser set-up, the optics and detection set-up, and the data acquisition and control system, including a discussion of the created LabviewTM program.

A detailed discussion of the physics and calculations of the two-photon absorption laser-induced fluorescence technique is presented. The various broadening mechanisms and their contributions to the total absorption shape have been discussed in detail.

Chapter 4

Atomic Hydrogen and Neutral Depletion

Neutral species play important roles in low temperature plasmas, their temperature affecting both the reaction rates and processes occurring. Neutral species also affect plasma transport and confinement due to collisions and reactions.[\[160\]](#) Neutral depletion has been shown to increase plasma transport due to the lower neutral density lowering the drag on the ions.[\[161\]](#) Knowledge of the neutral species present in the plasma as well as their parameters will be useful for understanding the processes that occur in the high power plasma devices, such as the MAGPIE helicon device, including neutral depletion, and can be empirically compared to models and simulations.

This chapter presents dependencies of neutral atomic hydrogen density and temperature with applied RF power. Measurements of the atomic hydrogen are made 1ms into the afterglow of a 5ms plasma discharge, unless otherwise specified. It is shown that when the plasma pressure exceeds the gas fill pressure, atomic neutral depletion occurs. The plasma pressure, $p_e = n_e k_b T_e$, is the partial pressure due to the plasma species, the electrons and ions. Often the ions are neglected when calculating the plasma pressure as the much lower temperature of ions means that they provide a negligible contribution to the plasma pressure. The pressure from the ions is similarly neglected in this work and is determined from the electron pressure.

This is the first time that such an observation has been made for a hydrogen plasma in a high power helicon device. The effect of gas heating and ionisation on depletion is also discussed.

4.1 Plasma Parameters

Hydrogen plasmas in MAGPIE have been well-researched in previous work.[132, 81, 162] In this section, the discharge properties of the plasma is presented. Samuell investigated the atomic and molecular hydrogen temperatures in a hydrogen plasma at high power (up to 20kW) using optical emission spectroscopy.[81] However the atomic temperature was only measured up to 1kW applied RF power. Atomic hydrogen temperatures up to 20kW will be presented in this thesis. The plasma densities (n_i) and electron temperatures (T_e) are reproduced from work by Santoso.[132] Santoso determined these parameters using an uncompensated single Langmuir probe (SLP), as described in [132]. In this thesis, this work is expanded upon by discussing the plasma pressure and dissociation fraction, measured by TALIF, of the plasma.

This chapter examines the plasma dynamics, specifically atomic hydrogen, in the plasma afterglow of a high power (1-20kW) discharge in the MAGPIE helicon device. All measurements presented in this chapter will focus on one spatial position in the plasma. Measurements are made at the radial centre ($r=0$) and at an axial position upstream ($z=150\text{mm}$) from the antenna in the target chamber. The radial and temporal evolution of the plasma parameters are discussed in Chapter 5. Due to the large background emissions associated with high power plasmas (due to the strong plasma emission at 656nm), measurements are restricted to the afterglow of a plasma discharge pulse. This enables good signal-to-noise of the fluorescence signal.

Plasma Density

Firstly, the plasma density will be considered as a function of applied RF power. In this work it is assumed that due to quasineutrality the electron and ion densities are approximate ($n_e \approx n_i$), the plasma density is therefore referred to as either the

4.1. PLASMA PARAMETERS

density of the electrons or the charged ions. As illustrated in Figure 4.1 the plasma density is seen to increase with power starting at $5 \times 10^{17} \text{ m}^{-3}$ at 1kW applied RF power. As the power is increased there is a slow increase in density up to 3kW, where a density of $1.2 \times 10^{18} \text{ m}^{-3}$ is obtained. At approximately 3-5kW, MAGPIE is observed to switch into the more efficient helicon mode in the pure hydrogen plasma. The transition from the inductively coupled plasma mode to the helicon mode has previously been investigated in MAGPIE.[\[162\]](#) Helicon modes are associated with large increases in plasma density and this is also observed in MAGPIE. The plasma density is observed to seemingly peak at approximately 13kW at $1.7 \times 10^{18} \text{ m}^{-3}$ and further increases are not observed with increasing the applied RF power up to 20kW. This upper density limit was first described by Miljak and Chen in an argon plasma using two half-wavelength helicon antennas at each end of a 1.65m long, 4.5cm quartz tube.[\[2\]](#) They observed an upper plasma density of approximately 10^{20} m^{-3} . This apparent upper density limit has been confirmed in other plasmas, such as krypton.[\[91\]](#)

The plasma density has also been measured in MAGPIE by Caneses using a double Langmuir probe who measured similar ion densities of 10^{19} m^{-3} in a 20kW hydrogen plasma but with the mirror field coils at 200A.[\[162\]](#) Those measurements are in close agreement to those presented here.

Electron Temperature

The exact mechanism of energy dissipation from the helicon wave to the plasma is still unknown. However, helicon sources provide very efficient plasma production due to the non-resonant nature of the power dissipation via collisional damping, delivering higher density production with little change in electron temperature.[\[76\]](#) Shown in Figure 4.2 is the electron temperature as a function of applied RF power at the same $(r,z) = (0, 150\text{mm})$ position.

It is observed that the electron temperature in a low power (1kW) plasma is 3.5eV. This increases abruptly up to 6eV at 5kW and then remains fairly constant

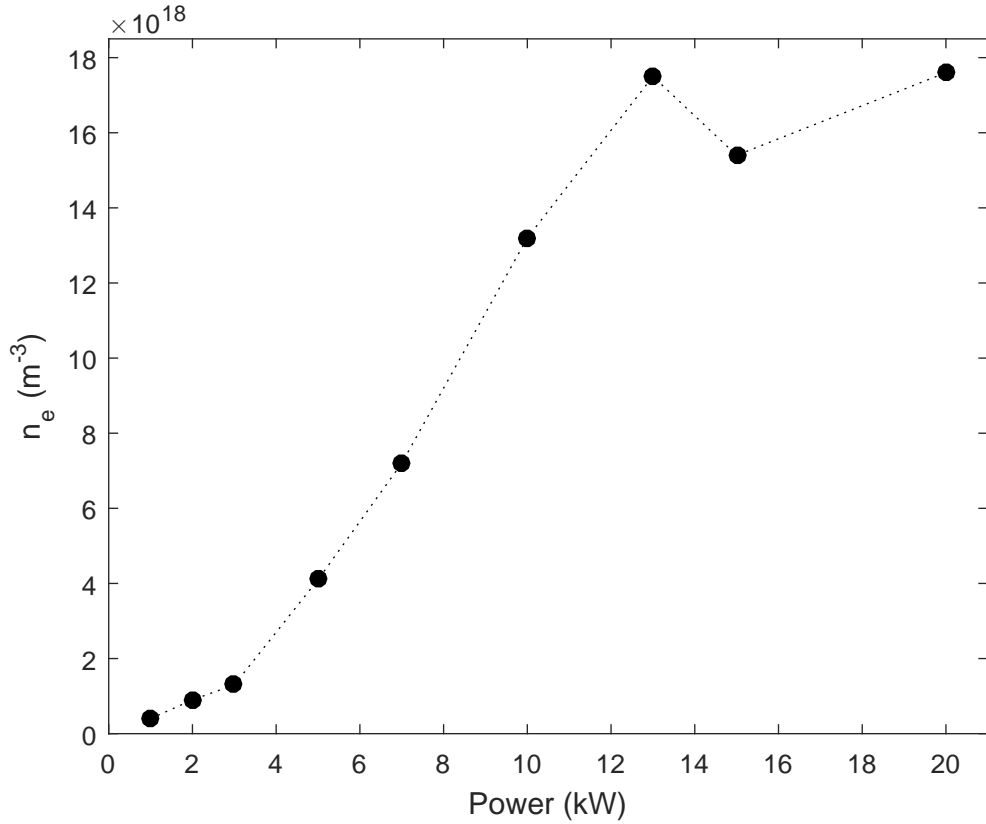


Figure 4.1: Ion density as a function of power under standard operating conditions at $z=150\text{mm}$ and $r=0\text{mm}$. Reproduced from Santoso.[132]

until 20kW. Higher electron temperatures correspond with higher rates of ionisation, which in turn creates a higher plasma density.

Ionisation Fraction

The ionisation fraction has been estimated by using the measured electron density and the H₂ gas fill density by:

$$\text{Ionisation Fraction} = \frac{n_e}{n_e + n_{H_2}} \quad (4.1)$$

Whilst this may not be a precise measurement of the ionisation fraction if neutral depletion is occurring in the centre of the plasma, it does give an estimation of the global average of the ionisation fraction, both ionisation of atomic and

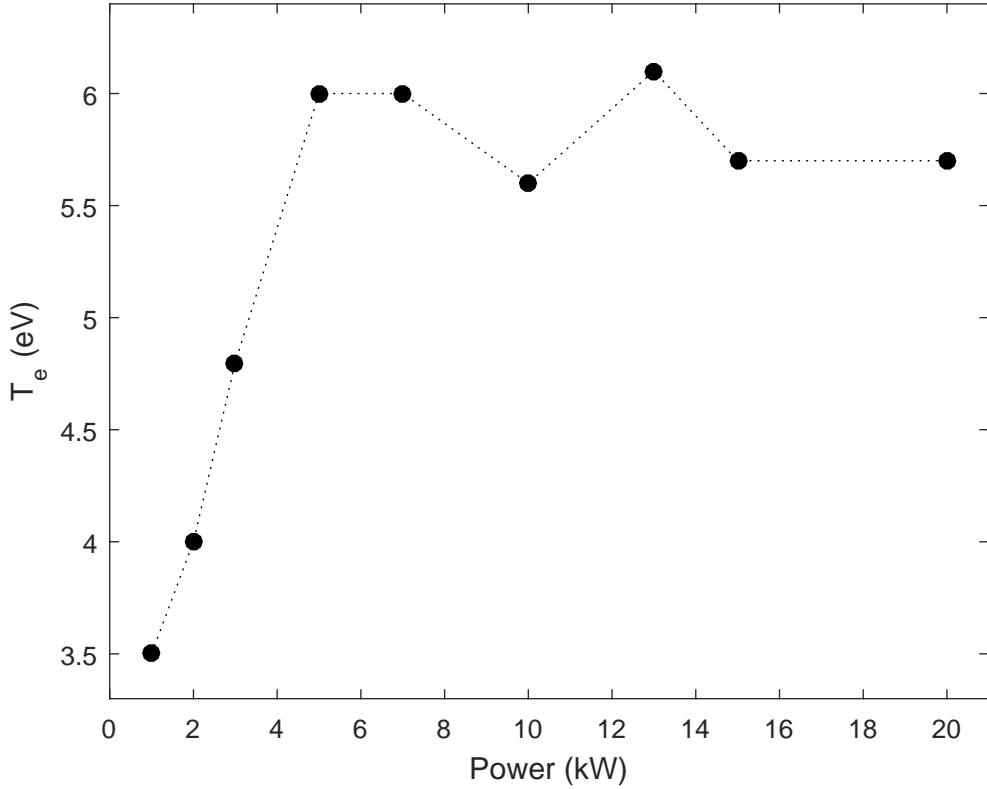


Figure 4.2: Electron temperature as a function of power under standard operating conditions at $z=150\text{mm}$ and $r=0\text{mm}$. Reproduced from Santoso.[132]

molecular hydrogen. If neutral depletion is occurring in the centre of the plasma, as has been observed for other gases in helicon plasma devices, then the molecular hydrogen density may also be depleted. This will lead to the molecular hydrogen density being significantly lower than the fill pressure during the plasma discharge. In turn, the ionisation fraction would then also be significantly higher.

The ionisation fraction as a function of power is shown in Figure 4.3. At 3kW and lower the ionisation fraction is below 1% compared to the initial H_2 density. With MAGPIE switching into helicon mode at approximately 3-5kW, the ionisation fraction increases quickly as it is n_e dependent (not T_e dependent). Once the density plateaus at $\approx 15\text{kW}$, the ionisation fraction is observed to be roughly 10%. Magee observed an almost completely ionised core in krypton where he was able to measure both the neutral and plasma densities.[163] It is expected that the actual ionisation

4.1. PLASMA PARAMETERS

fraction will be larger at higher applied RF power as neutral depletion will cause a lowering of the neutral particles in the plasma core.

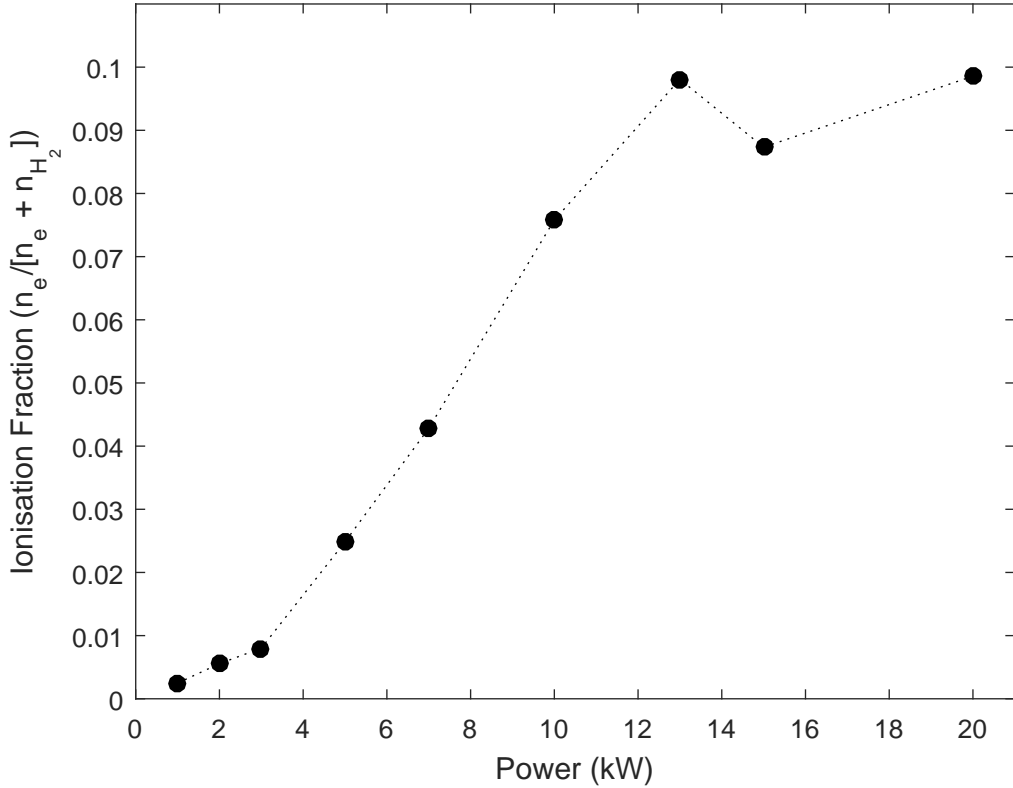


Figure 4.3: Ionisation fraction as a function of power at $(r,z) = (0, 150\text{mm})$ in MAGPIE. Ionisation fraction is calculated assuming that the neutral density during the discharge is the same as the fill pressure density.

Plasma Pressure

One proposed method for neutral depletion occurring in the plasma is due to a higher plasma pressure in the centre pushing neutral species out of the centre towards the chamber wall. The plasma pressure can be calculated using the measured values for electron density (where $n_e \approx n_i$) and temperature through the equation:

$$P_x = n_x k_B T_x \quad (4.2)$$

4.1. PLASMA PARAMETERS

where P_x is the pressure due to species x , n is the density in m^{-3} , k_B is the Boltzmann constant and T is the electron temperature in Kelvin.

As the ion temperature is much lower than the electron temperature,[164] due to the much larger mass of the ions (compared to electrons), the pressure from the ions is expected to be negligible compared to electrons and is therefore ignored. The calculated pressure from the plasma is shown in Figure 4.4. The plasma pressure follows a similar trend to the electron density. For the H₂ 10mTorr input pressure used in this experiment, the pressure at the (r,z) = (0mm, 150mm) position will be 9.1mTorr.(See Chapter 2.4) The plasma pressure is comparable but slightly lower for power <3kW. Above this power (H-W mode transition) the plasma pressure begins to become larger than the base neutral pressure before the plasma is switched on. Above 15kW the plasma pressure is higher than 120mTorr, which is over ten times higher than the neutral pressure.

With the electron pressure reaching comparable pressures to the neutral gas pressure, there is the possibility for neutral depletion to occur. This is known as ion pumping where friction forces push the neutrals into a region of lower plasma density. This is due to the mutual drag on ions and neutrals due to collisions.[3] Ion pumping has been observed as the mechanism for neutral depletion in xenon where a hollow neutral density profile was observed in the centre of the chamber and increasing towards the chamber edge.[121] Ion pumping may be further enhanced in MAGPIE due to the mirror fields which 'pinch' the plasma in the target region to create a high plasma density along the axis. This will be discussed further in Chapter 5.

While electrons are usually isothermal, neutrals often display significant gas heating which has to be taken into account. Gas heating of the neutrals will be discussed in more detail further in this chapter and again revisited in the next chapter.

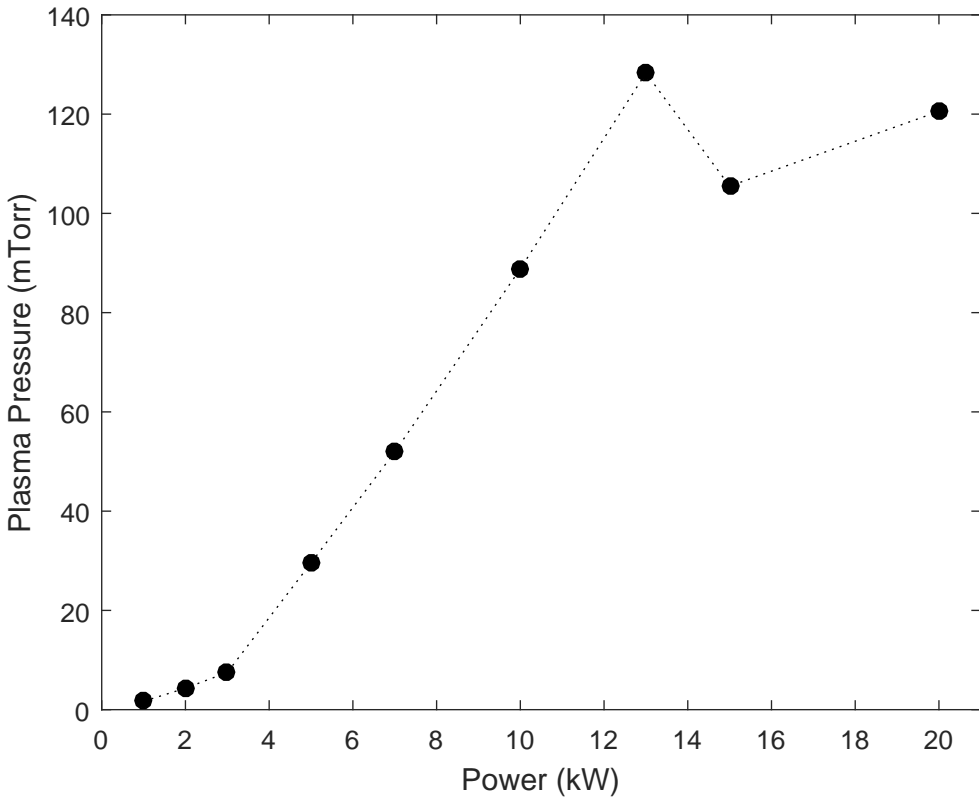


Figure 4.4: Electron pressure as a function of power at $(r,z) = (0, 150\text{mm})$ in MAGPIE.

Wall Pressure Measurements

To further investigate the neutral pressure, the MKS Baratron was moved to the diagnostic port used for the TALIF investigations, $z=150\text{mm}$ from the source. The pressure at the wall of the chamber was measured as a function of increasing power in a continuous plasma. The wall of the target chamber is at $r=80\text{mm}$ from the centre of the chamber. At the higher power measurements, where the high heat loads limit the duty-cycle to 1%, a single long pulse ($\sim 1\text{s}$) was used until the pressure stabilised. At the higher powers increased wall temperature was observed. The increase in wall temperature will increase the depletion due to gas heating. The wall pressure as a function of power is shown in Figure 4.5.

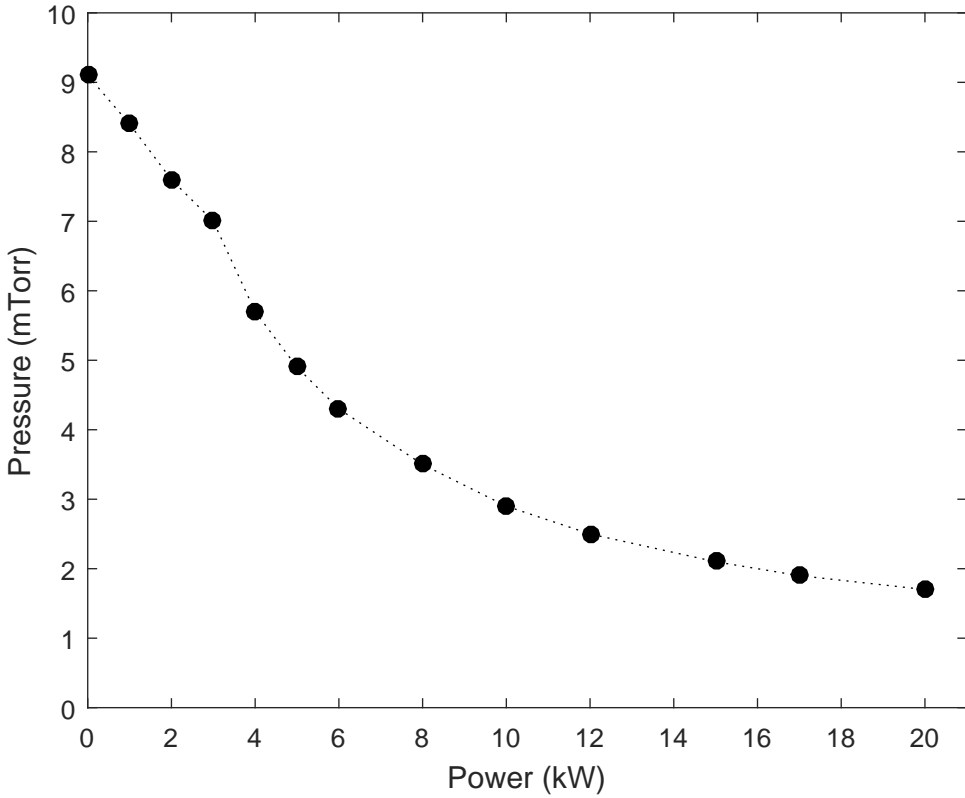


Figure 4.5: Edge pressure at $z=150\text{mm}$ in MAGPIE as a function of applied RF power.

As the applied RF power is increased, a decrease of the pressure is observed at the wall in MAGPIE. A steady linear decrease in pressure is observed to occur up to 3kW applied RF power, with the pressure dropping to 7mTorr. Above 3kW, consistent with the mode switching from inductive to helicon (H to W), a change in the relationship between power and wall pressure is observed, where it changes to an exponential shape. At 20kW, the wall pressure is observed to decrease to 1.7mTorr, greater than a factor of 5 decrease in pressure. Therefore the assumption of a constant molecular hydrogen pressure density in the discussion of ionisation fraction will not be accurate. This change in pressure density should be taken into account for high power plasma devices that may be displacing neutrals.

Liard *et al.* [124] observed similar behaviour with a xenon plasma in a helicon device. At 3kW with a 8.9mT axial magnetic field they observed a 50% decrease in the pressure at the wall of the chamber. They explain this as an enhancement of the

4.1. PLASMA PARAMETERS

pumping speed. They also observed that for low (or zero) magnetic field strengths the neutral density would increase at the edge, which corresponds to the neutral gas accumulating at the wall.

To investigate the effect of magnetic field strength on the edge pressure, the mirror field was scanned from 0A (24G) to the standard 300A (190G) used in this work in steps of 50A, shown in Figure 4.6. The applied RF power was kept at 20kW and the source field was maintained at a constant 50A as the mirror coils are the dominate source of magnetic field at $z=150\text{mm}$ in MAGPIE. The source fields contribute a constant 24G at $(r,z) = (0, 150\text{mm})$.

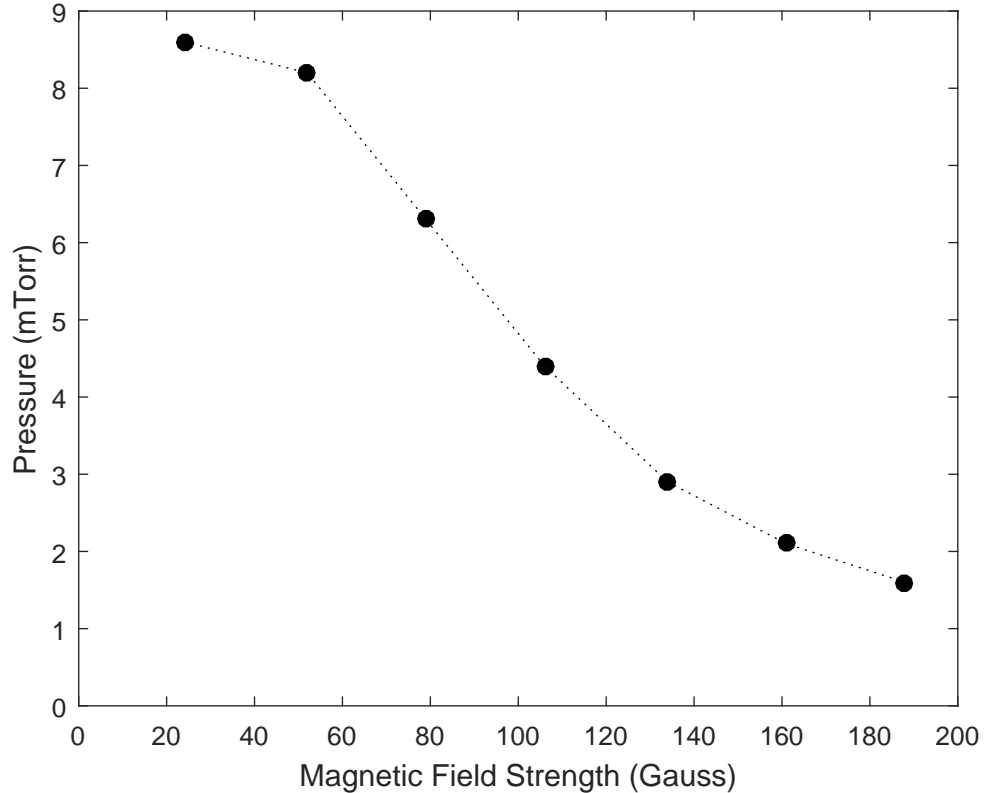


Figure 4.6: Edge pressure at $z=150\text{mm}$ in MAGPIE from a 20kW discharge as a function of the total magnetic field strength.

It is observed that without the magnetic field from the mirror coils there is still a slight drop in the measured pressure at the chamber walls from 9.1mTorr (H_2 fill pressure at $z=150\text{mm}$) to 8.6mTorr. With increasing magnetic field strength the pressure is observed to continue to fall, dropping to 1.7mTorr at 188G, which is the

standard 50A:300A coil current configuration.

It has been suggested by Aanesland *et al.* that the decrease in the wall pressure is due to the neutral gas being dragged along the chamber by the charged particles. The charged particles in the plasma are being directed axially along the chamber due to the force from the magnetic field:

$$F_{||} = -\mu \nabla_{||} B \quad (4.3)$$

where μ is the magnetic moment. However, more work needs to be undertaken to confirm if this is occurring.

4.2 Atomic Hydrogen Power Scans

In diatomic species such as hydrogen there is competition between dissociation and ionisation processes for absorbing the RF power. This creates a plasma that consists of neutral molecular and atomic hydrogen, as well as a range of charged species, e, H^- , H^+ , H_2^+ , H_3^+ . In MAGPIE, the low temperature hydrogen plasma will be a weakly ionised plasma as there is a larger neutral population than charged species. It is important to understand the neutral species in a plasma as they have collisions and reactions with the charged species as well as interactions with the walls of the plasma device and materials that are used in plasma processing. This section will focus on measurements of the atomic hydrogen (H) carried out using the newly established TALIF diagnostic.

Neutrals are an important component in the plasma, they are a source of fuel to further increase the plasma density and are involved in collisions and reactions. Neutral pressure is observed to affect flows[165] and the temperature of the neutral affects reaction rates and wall loadings.[166] While extensive research has been conducted on hydrogen plasmas in the MAGPIE device, there has been little research performed on atomic hydrogen.

4.2.1 Power Dependence

The RF power was scanned from 1-20kW and TALIF wavelength scans were recorded at 1ms into the afterglow of a 5ms plasma pulse. The choice of this short pulse length is due to high heat loads and fluxes on the chamber walls associated with higher power operation, which requires MAGPIE to operate at a 1% duty cycle. A shorter pulse length can also be beneficial as the TALIF diagnostic can be quite time intensive and this reduces the time required to complete a measurement. The molecular H₂ pressure for this power scan is 10mTorr and the magnetic fields on MAGPIE were the 50A:300A standard operating set-up discussed in Chapter 2. The TALIF measurements were made at the usual position of (r,z) = (0mm, 150mm).

It is expected that with increasing applied RF power the atomic hydrogen density will increase as there is a greater amount of dissociation. A much larger set of equations are shown in Table 1.3 that include more production mechanisms for the creation and loss of atomic hydrogen.



However as can be seen in Figure 4.7, which shows atomic hydrogen density as a function of power, the atomic hydrogen does not continue to increase with higher applied RF power. As the applied RF power is increased to 3kW, this is an increase in the measured atomic hydrogen density. Above 4kW though, there is a significant decrease in atomic hydrogen density from 4.4x10¹⁸m⁻³ to 7x10¹⁷m⁻³ at 15kW. The density appears fairly constant from 15kW to 20kW. While this research focuses on atomic hydrogen in the plasma, it is likely that there will also be a corresponding decrease in the molecular hydrogen.

This decrease in density of the neutral atomic species in the plasma, known as neutral depletion, will lead to an upper limit on plasma densities, as seen above 15kW in Figure 4.1, as the neutral species are the source of new plasma through ionisation.

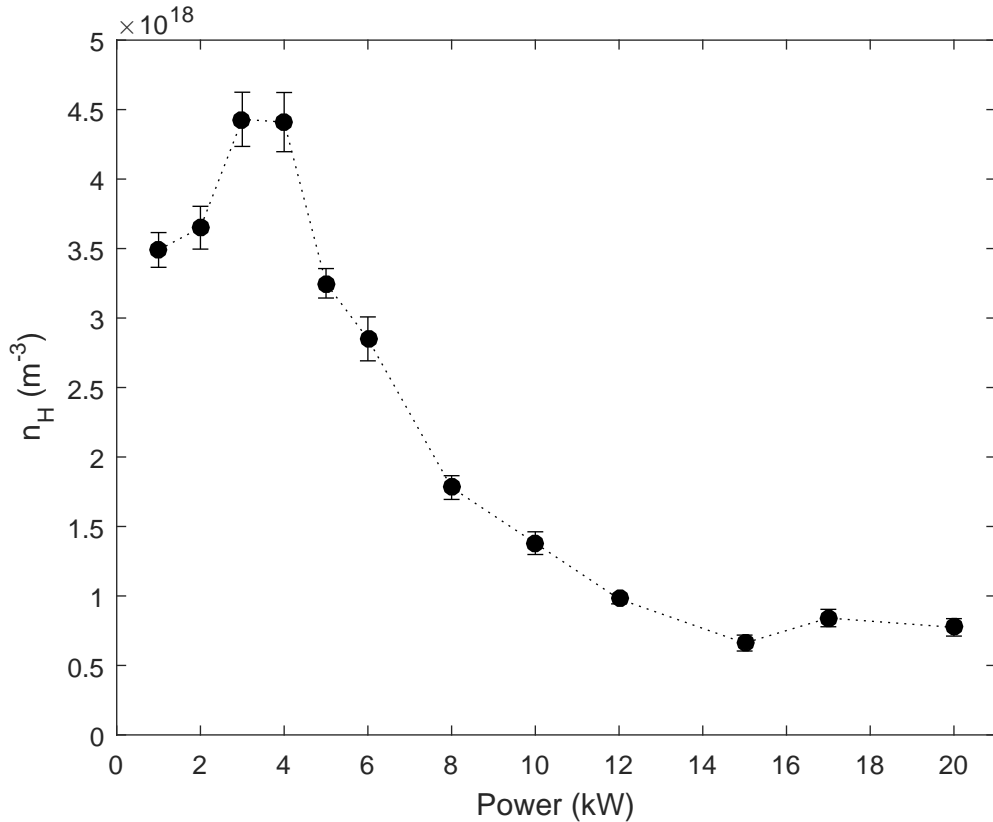


Figure 4.7: Atomic hydrogen density as a function of power.

4.2.2 Pulse Length

Another parameter that can be adjusted that may affect the degree of neutral depletion that is occurring in the plasma is the pulse length (plasma on time). A shorter pulse will produce less plasma as the total energy input will be less, resulting in less ionisation. The affect of the length of the plasma discharge on the H density was measured in a 20kW plasma at the $(r,z) = (0\text{mm}, 150\text{mm})$ position with the standard 50A:300A magnetic field configuration. The measured densities are shown in Figure 4.8.

For the shortest investigated pulse length of $500\mu\text{s}$, a H density of $3.3 \times 10^{18} \text{ m}^{-3}$ is observed. As the pulse length is increased a fast decline in the density is observed with the density in the core becoming less than half with a 1.5ms pulse. The decrease in density with increasing pulse length is less dramatic with pulse lengths

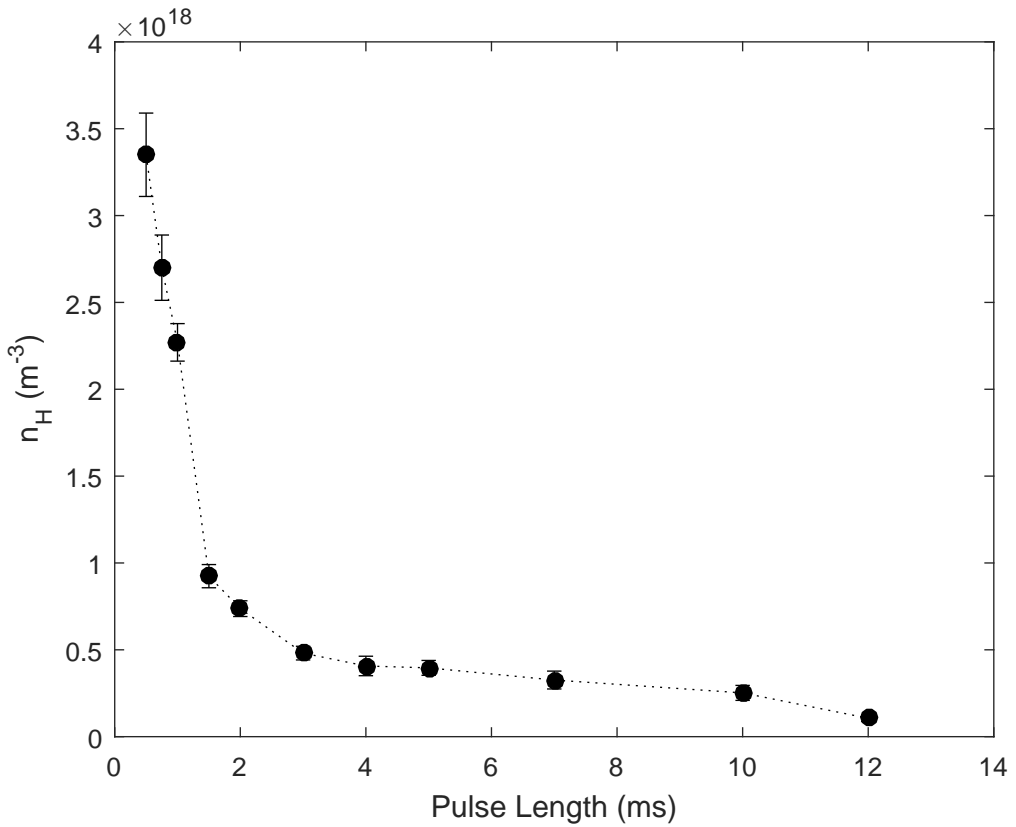


Figure 4.8: Atomic hydrogen density at 1ms after the plasma pulse for varying pulse lengths.

longer than 1.5ms, however, a gradual decrease is still observed. The small change in density observed between a 5ms pulse and the longer pulses suggests that using 5ms is an appropriate pulse length to determine the behaviour of the neutrals at this position, that is the plasma has reached a steady state. By adjusting the pulse length, information about the plasma ignition and production of atomic hydrogen is gained. As there is the largest atomic hydrogen density with the shortest pulse length, the atomic hydrogen is created very early ($<500\mu\text{s}$) in the plasma ignition and is depleted from the core at longer times into the plasma discharge.

The electron density and temperature time evolution through a plasma discharge in MAGPIE at high powers has been previously investigated by Santoso.[132] This work showed the electron density is seen to be fairly constant for the investigated pulse lengths. The electron temperature with 20kW power is seen to steadily in-

crease with longer pulse lengths, increasing from $\sim 2\text{eV}$ in the very early afterglow ($500\mu\text{s}$, 0.5ms), up $\sim 4\text{eV}$ by 12ms .

The decrease in n_H with increasing pulse length is likely due to the increasing n_e and T_e leading to increased neutral depletion of atomic hydrogen (and molecular hydrogen) in the plasma core. Neutral depletion will be discussed in more detail later in this chapter.

4.2.3 Atomic Hydrogen Temperature

The Doppler broadening of the TALIF wavelength scans is used to determine the atomic hydrogen temperature (T_H) by the method described in Chapter 3. The wavelength scans at 1ms and 6ms into the afterglow of the 20kW discharge are shown in Figure 4.9 to highlight the difference in the FWHM for the change in temperature of atomic hydrogen. The measured intensity of the TALIF signal for each wavelength is shown by the circles. The data for 1ms after the plasma discharge is shown with blue points and for 6ms with green points. Gaussian fits for each time in the afterglow are shown in black and red for 1ms and 6ms respectively. The measured TALIF signal and the fits have been normalised to the maximum of each fit to highlight the difference in broadening of each fit. As can be seen there is a difference in the full width at half maximum (FWHM) between the two fits. The difference in the width of TALIF scans is 0.5pm ($5 \times 10^{-4}\text{nm}$), which corresponds to a difference in temperature between 1ms and 6ms into the afterglow of $\sim 0.06\text{eV}$ (700K).

Individual TALIF wavelength scans at 1ms and 4ms into the afterglow of the 5ms plasma pulse are shown in Figure 4.10 at applied RF powers of 1kW and 20kW . The total width of the peak at the half maximum for each scan is shown in Figure 4.10. Larger widths correspond to hotter atomic hydrogen.

Unlike species that are naturally in the atomic state such as krypton, atomic hydrogen is produced by dissociation processes through the collisions in the plasma.

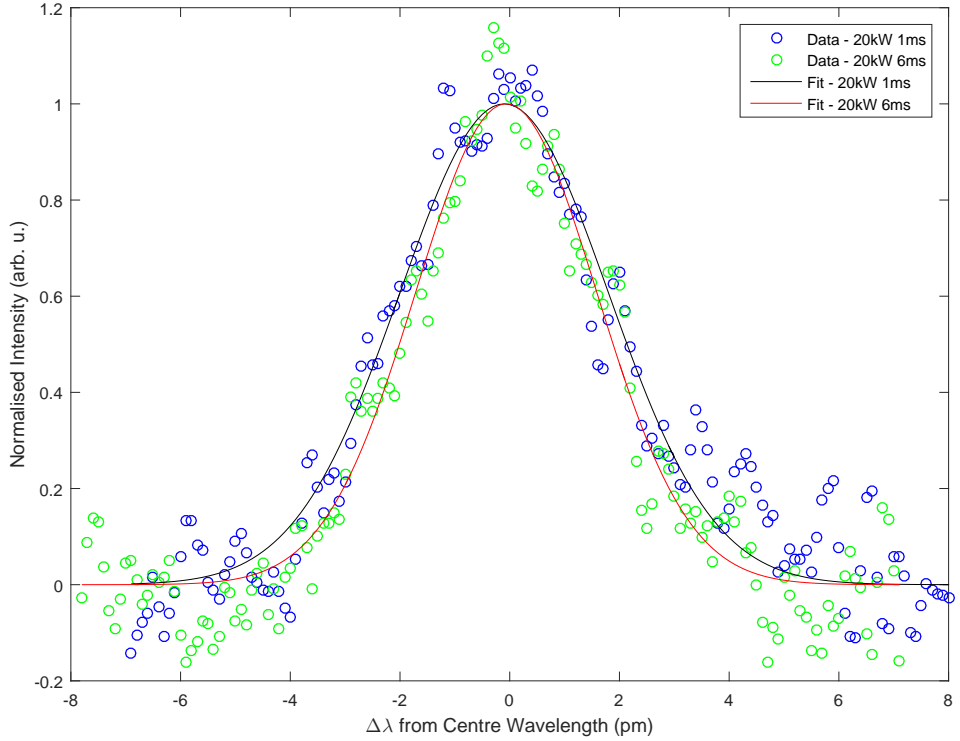
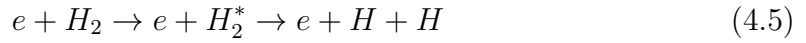


Figure 4.9: TALIF wavelength scan of the data (points) and the fit (solid lines) at 20kW, $r=0\text{cm}$ at 1ms and 5ms in the afterglow of a 5ms plasma discharge.

It has typically been expected that atomic hydrogen are born as Frank-Condon neutrals with 2eV through the reaction:[86]



It has been observed that in certain cases hydrogen plasma can display evidence of two distinct populations of atomic hydrogen, each with their own temperature. Mills *et al.*[167] demonstrated the existence of hot H atoms in a microwave discharge with energies 2-4eV. They also measured hot populations of atomic hydrogen in a GEC type cell in mixed Ar/H₂ and He/H₂ plasmas.[168] A pure H plasma showed a 1eV population of atomic hydrogen, while the mixed cases displayed very hot hydrogen 40-50eV. In the He/H₂ mix approximately 50 percent of the population was of the hot state, while in the Ar/H₂ mix all of the atomic hydrogen was in the

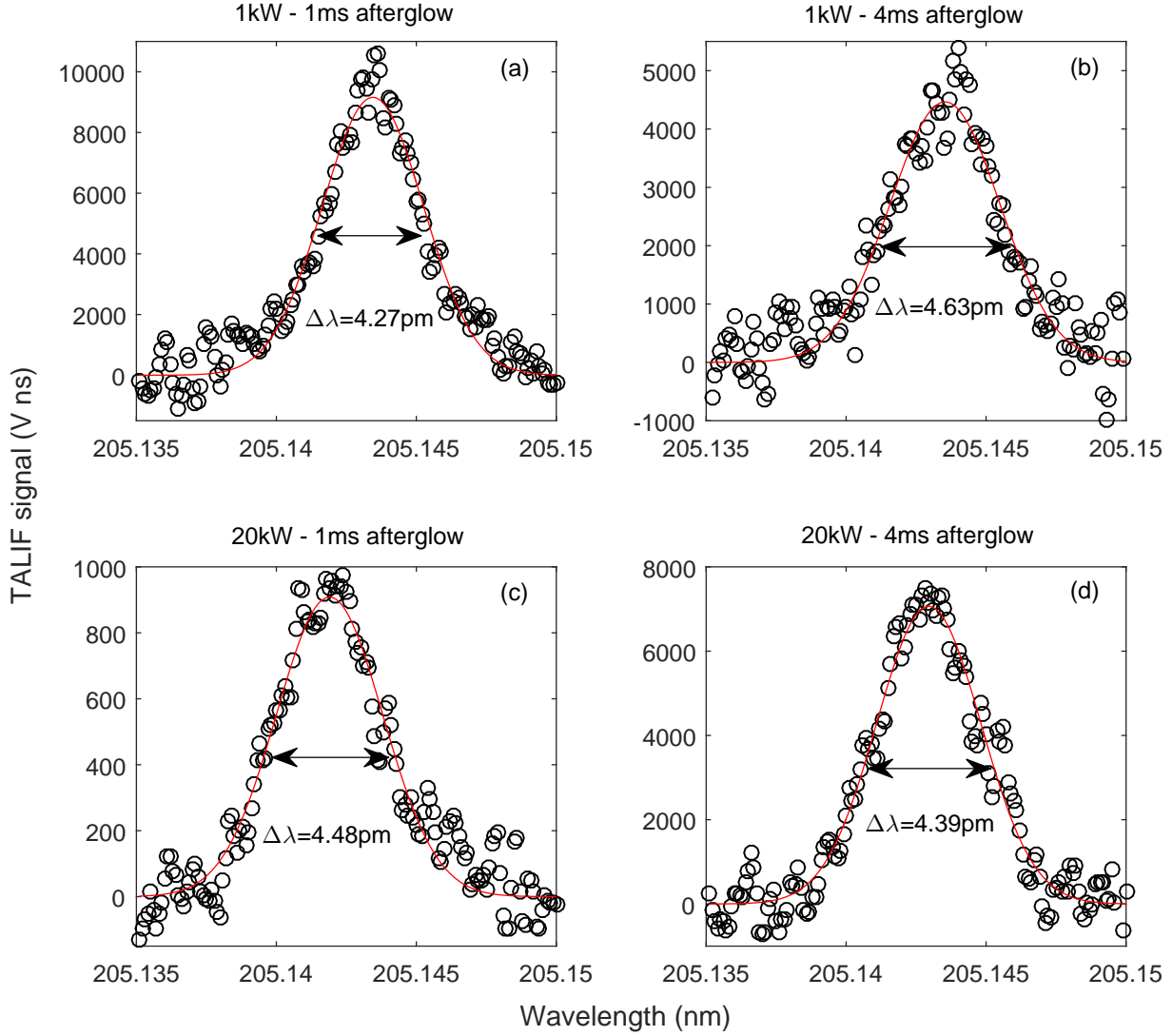


Figure 4.10: TALIF wavelength scans at 1ms and 4ms into the afterglow of a 5ms hydrogen discharge at powers of 1kW and 20kW.

hot state. They proposed that the hot hydrogen was catalytically created through a resonant energy transfer with He^+ and Ar^+ ions. Phillips [169] in H_2O plasmas in a GEC cell determined that the hot hydrogen population (40eV) is dependent on pressure and weakly dependent on absorbed energy. Only atomic hydrogen displayed the broadening of the emission line with no observed broadening of the oxygen lines. Tatarova[170] and Felizardo[171] both showed hot populations of atomic hydrogen in a microwave discharge with T_H of 4-9eV.

Wings on the Gaussian peak of a TALIF scan can suggest that a second hotter population of H exists in the discharge. While the majority of TALIF scans show no evidence of broadening in the wings, some scans do possibly display wings, such as the 1ms afterglow 1kW discharge in Figure 4.10. This TALIF scan is looked at more closely in Figure 4.11 to analyse the possibility of a second hot H population.

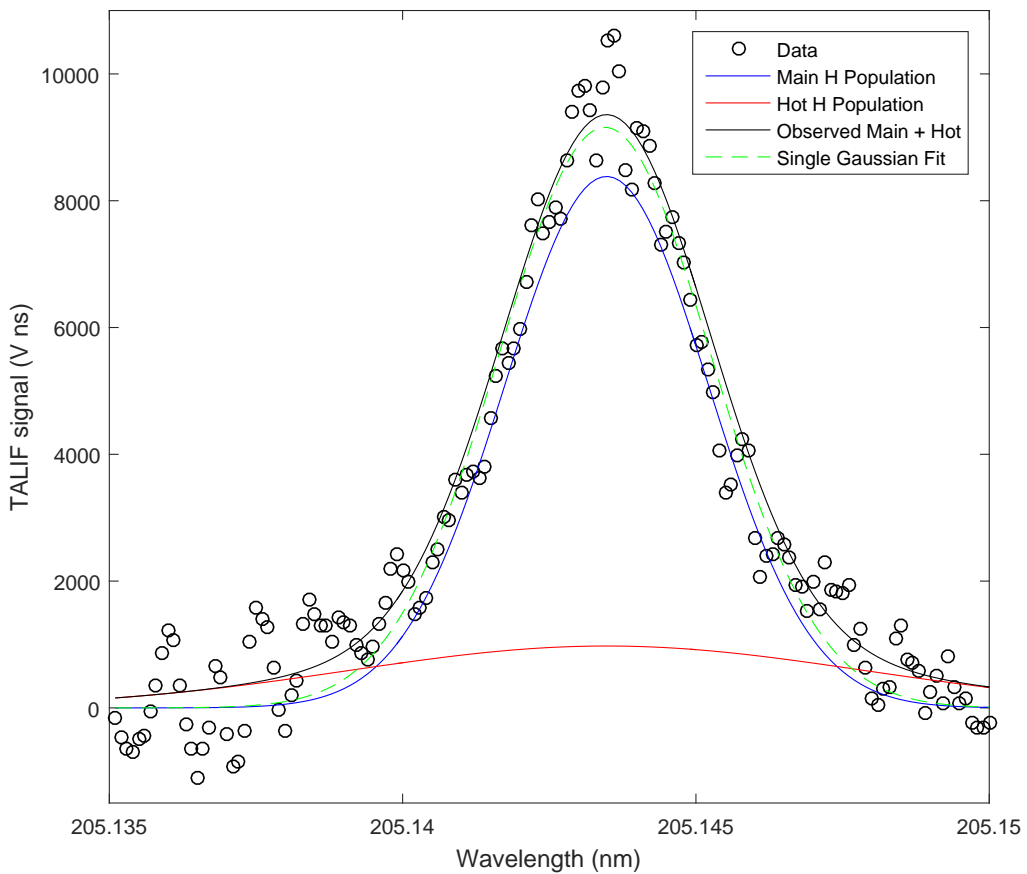


Figure 4.11: TALIF wavelength scan at 1ms into the afterglow of a 5ms hydrogen discharge at 1kW. A double Gaussian fit is shown to display the possibility of an additional hotter population in red with the main cooler population in blue. The sum of the two Gaussian distributions is shown in black. The original single Gaussian fit is shown in the green dashed line.

To investigate the possibility of a second hotter atomic hydrogen population the TALIF scan is fitted with a double Gaussian. Shown in Figure 4.11 are two fits to represent the bulk H population (blue) and the second for the hotter H population

(red). The combined fit for two Gaussians (black) fits quite well with the data. The single Gaussian fit used in this thesis for determining the atomic hydrogen density and temperature is shown in the dashed green line. The broadening of the hot population gives $T_H = 0.4\text{eV}$ (4600K) and the colder population has an atomic temperature of 0.03eV (350K). As these wings on the TALIF scans are not present in the majority of scans it is difficult to conclude if there is a hotter population present and further research is required. It should also be noted that these scans are measured in the plasma afterglow and it is possible that the neutrals have thermalised by this time.

As the secondary population would have a $T_H = 0.4\text{eV}$, it is concluded that they are not Frank-Condon atomic hydrogen. This agrees with the work of Galante *et al.* [172] where they did not observe a second hotter population since their neutral hydrogen spectrum is well described by a single Maxwellian. All neutrals were observed to have temperatures of $\sim 0.08\text{eV}$ energies, the same temperature as measured in the steady-state.

Figure 4.12 shows the measured T_H as a function of increasing RF power at 1ms into the afterglow of a 5ms pulse. There is a general increase in the atomic H temperature with increasing power. A trend (red) has been fitted to the data for guidance. The larger discrepancies at higher powers are expected as at 1ms in the discharge afterglow, the atomic density at higher applied powers is still quite low, leading to a lower signal-to-noise ratio.

4.2.4 Molecular Gas Temperature

The molecular gas temperature in MAGPIE has been previously investigated by Samuell.[173] The H_2 gas temperature was determined using the relative intensities of the Q-branch of the Fulcher- α ro-vibrational transitions. The set-up used is the same as discussed in Chapter 2.4.2. The use of ro-vibrational states to determine the gas temperature of molecular species is a well established technique.[174]

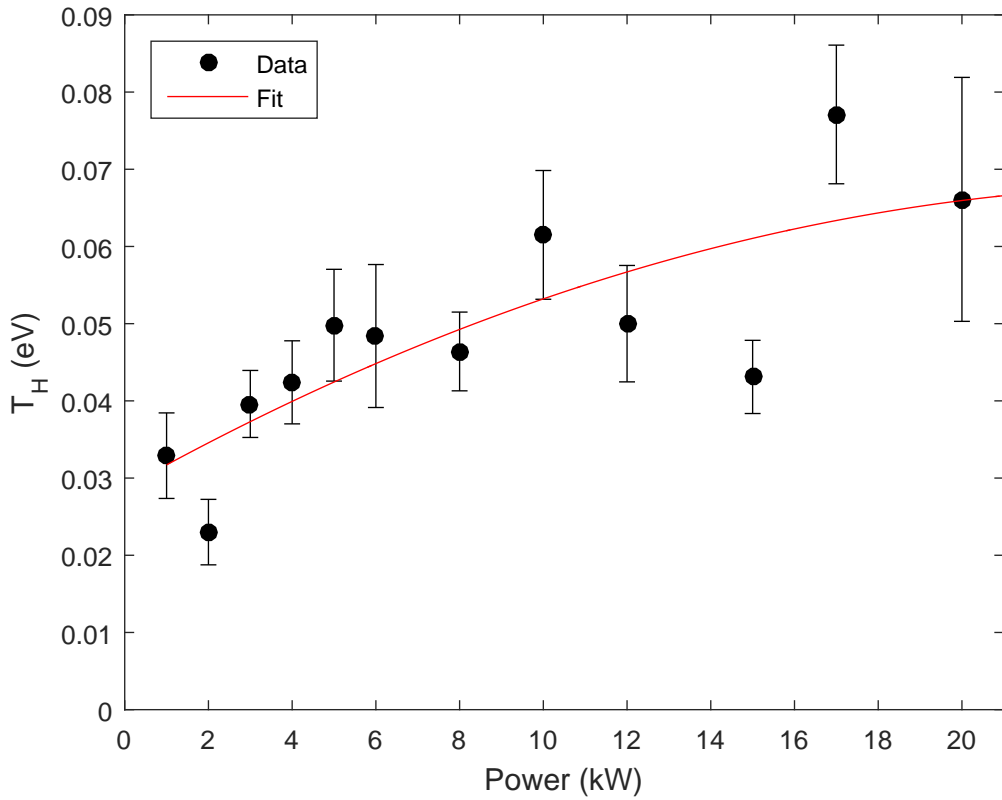


Figure 4.12: Atomic hydrogen temperature as a function of power at 1ms after a 5ms discharge.

The H₂ gas temperature as a function of power (1-20kW) is shown in Figure 4.13. The molecular hydrogen temperature increases with increasing applied RF power. At 1kW the H₂ molecular temperature is $\sim 0.04\text{eV}$ (460K) and rapidly increases with power in the low kW power range. At higher applied RF power the increase in T_{H₂} is slower. At 20kW, T_{H₂} $\sim 0.105\text{eV}$ (1200K).

4.3 Depletion Dynamics

As discussed in Chapter 1, neutral depletion has been observed in many different plasmas and there are different conditions that lead to each depletion in each example. In particular, the key processes for neutral depletion are: (1) gas heating; (2) high plasma pressure; and (3) ionisation. Heating of neutral species in the core due

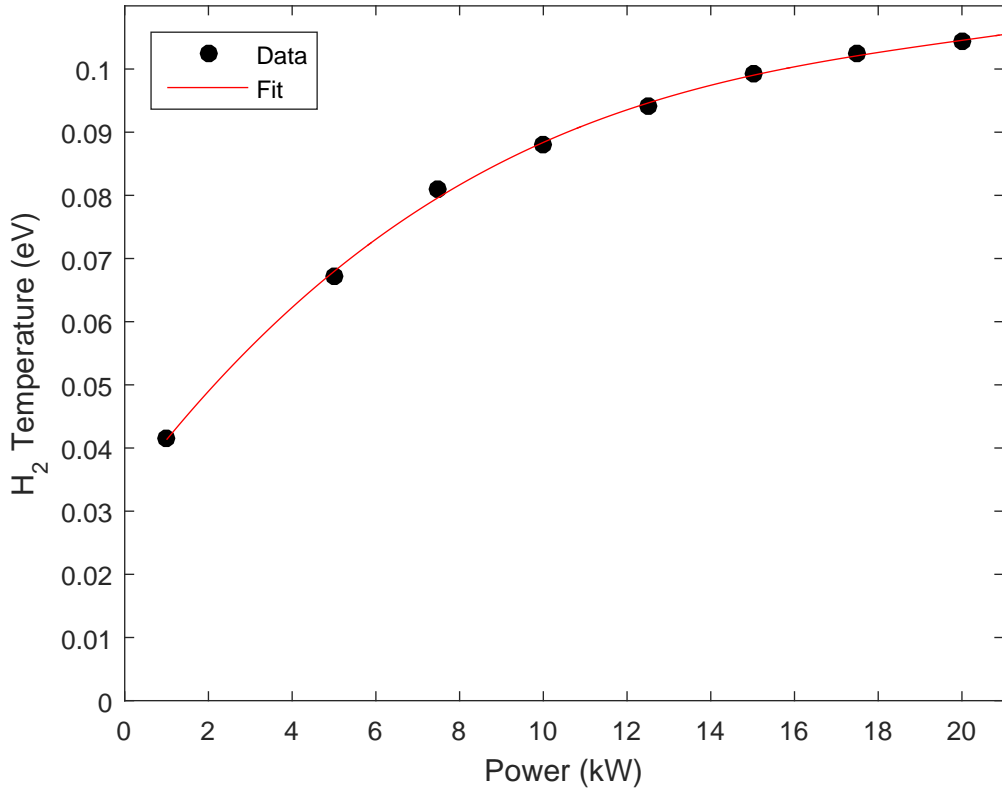


Figure 4.13: Molecular hydrogen temperature as a function of power. Reproduced from Samuell *et al.*[173]

to collisions with the plasma creates a higher pressure region in the core. This higher pressure region pushes neutrals out towards regions of lower pressure, generally near the walls where the gas will be closer to room temperature.[175]

In a plasma where the plasma pressure is comparable to the fill pressure, significant neutral depletion occurs not only by gas heating but also by pressure balance. The high plasma pressure pushes the neutrals out of the core through collisions. It has been shown that the resulting neutral depletion can enhance plasma transport to the surroundings, increasing particle loss and decreasing plasma density.[176]

In magnetised plasmas with high ionisation in the plasma core, the neutral species can become depleted in this region. The newly formed ions are accelerated out of the core quicker than the neutral species are able to replenish the depletion.[3]

This section will investigate the possible methods contributing to neutral depletion and discuss whether they are responsible for the observations observed in the atomic hydrogen density profiles.

4.3.1 Depletion Due to Ionisation

Neutral depletion through ionisation usually requires an external magnetic field that restricts the motion of the ions. When a neutral particle drifts into the highly ionised region in the plasma, it is highly likely it will be ionised by electron collisions. The magnetic field will confine the newly created ion and it will diffuse along the magnetic field lines. For an axial magnetic field used in linear plasma devices, the ions will diffuse to the end plate where they will recombine. It is the very short lifetimes of the neutral species in the plasma core that leads to the decreased neutral density in the core.[163]

The mean free path of ionisation is given by:[71]

$$\lambda_i = \frac{\nu_n}{n_e \langle \sigma \nu \rangle_{ion}} \quad (4.6)$$

where ν_n is the neutral thermal velocity, n_e is the electron density and $\langle \sigma \nu \rangle_{ion}$ is the electron energy ionisation rate.

The neutral thermal velocity is given by:

$$\nu_n = \sqrt{\frac{k_B T_n}{m_n}} \quad (4.7)$$

where k_B is the Boltzmann constant, T_n is the neutral temperature and m_n is the mass of the neutral species.

4.3. DEPLETION DYNAMICS

The rate coefficient for electron energy ionisation is given by:[84]

$$9.74 \times 10^{-15} T_e^{-0.174} e^{-14.3/T_e - 0.001} + 6.35 \times 10^{-15} T_e^{0.433} e^{-16.4/T_e} \quad (4.8)$$

The mean free path of ionisation for atomic hydrogen in MAGPIE as a function of power was calculated using the measured values of electron density, electron temperature and atomic hydrogen temperature, this is shown in Figure 4.14. Under the plasma conditions at 1kW, the mean free path of ionisation is approximately 40m. This length is far larger than the diameter of the target chamber (16cm), therefore it is unlikely for a hydrogen atom to ionise while diffusing through the plasma core. With increasing power it is observed that the mean free path of ionisation decreases, above 10kW it becomes approximately 20cm (still larger than chamber diameter).

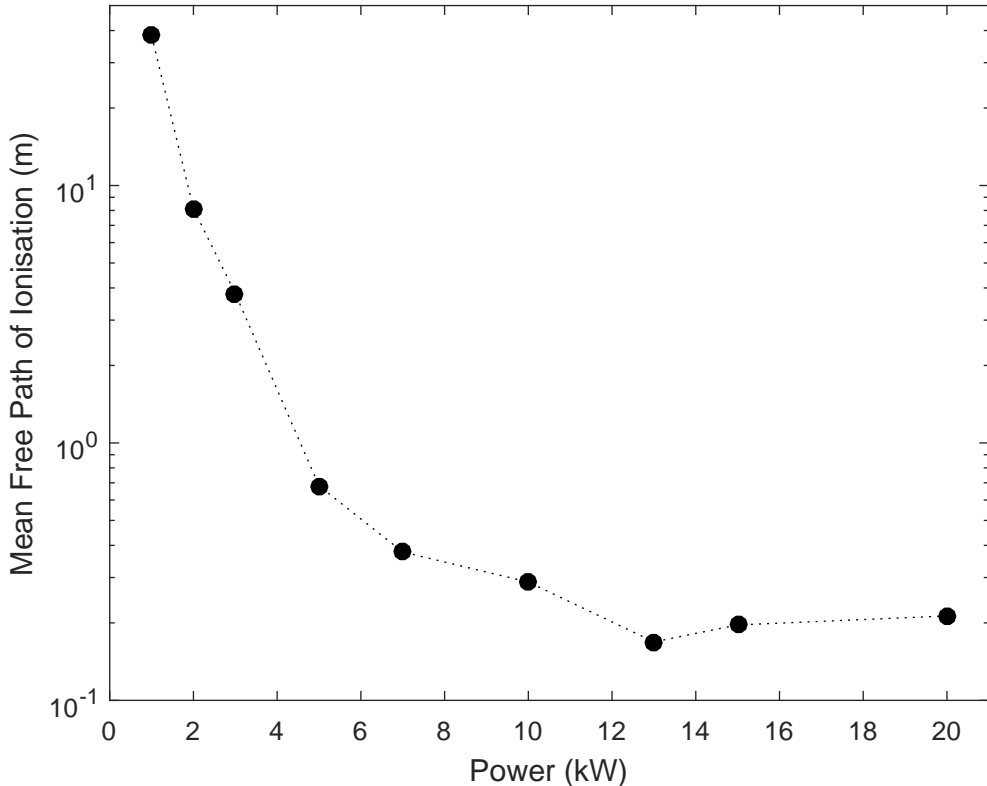


Figure 4.14: Mean free path of ionisation of the atomic hydrogen as a function of power.

The light mass of the hydrogen atom contributes to the long means free path of ionisation even in high power discharges. Neutral depletion due to ionisation has been observed in heavy ion helicon plasmas, such as argon[115] and krypton[163]. This occurs when the mean free path of ionisation is much shorter than the diameter of the plasma chamber. Hence it is not a dominant mechanism here. Unlike in the work by Yun *et al.* [118] where they observed hollow neutral pressure profiles in the centre of the chamber, which they concluded is due to ion pumping effect, where ions are accelerated out of the centre of the chamber by the pre-sheath faster than neutral species drift in from the walls. In this work the axial magnetic field accelerates the ions along the chamber rather than towards the chamber sides.

4.3.2 Depletion Due to Gas Heating

Depletion due to gas heating, also known as neutral pumping, occurs when there is larger heating to the gas in the centre of the discharge compared with closer to the walls. This extra heating increases the gas pressure and hence pressure gradients, which leads to a lower density. In this way the neutral species will have a lower density in the hotter region compared to the original fill density.

The neutral depletion fraction due to gas heating is given by:[127]

$$\frac{n_n}{n_0} = \frac{T_{Room}}{T_n} = 1 - D_{Dep} \quad (4.9)$$

where the depletion fraction ($\frac{n_n}{n_0}$) is related to the initial room temperature of the filling gas (T_{Room}) and the temperature of the neutral species in the plasma T_n . n_n is the density of neutrals in the plasma and n_0 is the initial density at room temperature. Whilst it is difficult to define depletion due to gas heating of atomic hydrogen due to the fill pressure being molecular hydrogen and hence the initial fill pressure of H is zero, it is useful to consider depletion compared to room temperature, as increasing temperature will lead to lower densities of atomic hydrogen. Using the measured values of the atomic (circles) and molecular

4.3. DEPLETION DYNAMICS

(squares) hydrogen temperature and the fit to the data, shown in Figures 4.12 and 4.13 above, the expected depletion due to the gas heating is calculated and shown in Figure 4.15.

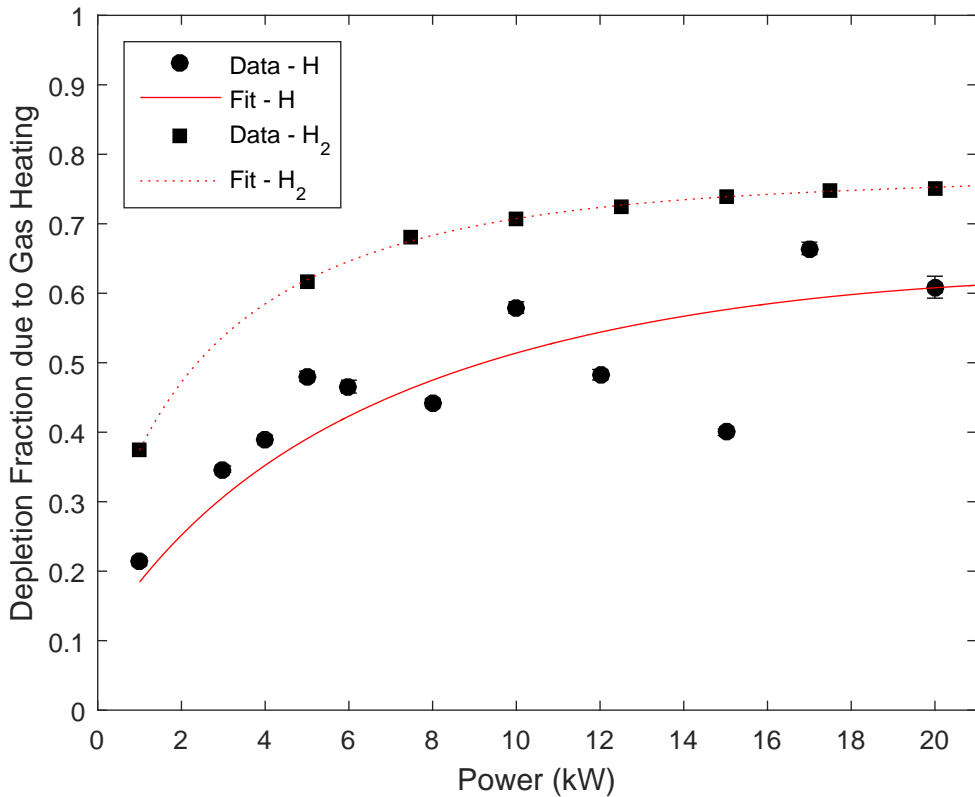


Figure 4.15: Expected neutral depletion fraction due to gas heating as a function of power for atomic (circles) and molecular hydrogen (squares). The atomic hydrogen temperatures have been measured in the plasma afterglow, while the molecular temperatures are measured during the plasma discharge.

At 1kW applied RF power the atomic hydrogen depletion due to gas heating, from the measurements of T_H , is expected to be $\sim 20\%$. Determination of the atomic hydrogen is difficult as there is no density before the plasma discharge to compare with, as it is formed during plasma production. Increasing the applied RF power leads to greater levels of gas heating due to the associated higher atomic temperatures from increased collisions. At lower powers there is a quicker rate of increase in the gas heating compared to the higher powers ($< 20\text{kW}$) where it becomes a slow

4.3. DEPLETION DYNAMICS

increase with increasing power. At 10kW, the gas heating depletion from the fit is shown to be 50%, while increasing the power to 20kW gives a gas heating depletion of 60%.

The molecular hydrogen temperature is measured during the plasma pulse and is hotter than the atomic hydrogen afterglow temperature. At 1kW applied RF power the molecular hydrogen is expected to be depleted by 38% due to gas heating alone. The effect of depletion due to gas heating on molecular hydrogen increases significantly up to 5kW to approximately 60%. Above 5kW the depletion due to gas heating increases more slowly for increasing power, becoming approximately 75% at 20kW. As the atomic hydrogen temperature has been measured during the plasma afterglow, the depletion due to gas heating during the plasma discharge may be closer to the depletion of the molecular hydrogen temperature curve.

4.3.3 Depletion Due to Plasma Pressure

Another factor that can cause neutral depletion is high plasma density. When high plasma densities and/or temperatures are achieved in the plasma core, the plasma pressure can become high enough to expel neutrals from the core.[\[127\]](#) This neutral depletion occurs when the plasma pressure becomes comparable to the pressure of the neutral species.[\[119\]](#) It is the collisional forces between the ions and neutrals that push the neutral species into regions of low plasma density. [\[121\]](#) A summary of the collisions in a hydrogen plasma is discussed back in Section 1.3, the is the collisions between the neutral and the charged species that are causing the neutrals to be pushed out.

For the purpose of investigating neutral depletion due to the plasma pressure, a uniform pressure density will be considered across the plasma and the pressure remains at the fill pressure without the plasma discharge. The total pressure will consist of the sum of the pressure of the individual species present:

$$P_{Tot} = P_e + P_{ions} + P_H + P_{H_2} \quad (4.10)$$

4.3. DEPLETION DYNAMICS

The pressure of each species can be written in terms of density and temperature from Equation 4.2, where $p_e = n_e k T_e$. The contribution from the ions is assumed to be negligible compared to the electron pressure as $T_i \ll T_e$. The neutral species H and H₂ will also be considered as a single neutral species as they will both be depleted due to the electron pressure. Although different species have been observed to display different degrees of depletion.[177] The depletion due to electron pressure (D_e) can then be defined as[178]:

$$\frac{n}{n_g} = 1 - D_e = 1 - \alpha \frac{P_e}{P_{Tot}} \quad (4.11)$$

where, n is the depleted neutral density, n_g is the original neutral density and $\alpha = \mu_i / \mu_n$ is the balance of diffusion of the neutrals into the depleted region with the ambipolar diffusion of the ions. μ_i and μ_n are the mobility of the ions and neutrals respectively. If the mobility of the ions and the neutrals are similar under the plasma conditions then, $\alpha = 1$.[120]

Considering $\frac{P_e}{P_{Tot}} = 1$ when the electron pressure is equal to the total pressure, in this case to maintain uniform pressure density, the density of the neutral species must go to zero. While this will not be strictly true, it does give an indication of when there may be significant neutral depletion due to plasma pressure. Shown in Figure 4.16 is $\frac{P_e}{P_{Tot}}$ plotted against the applied power. At just above 3kW the electron pressure becomes equal to the H₂ fill pressure and it is expected that significant neutral may be seen. This is in agreement with the atomic hydrogen density measurements above which suggest that neutral depletion is occurring at powers greater than 4kW. At these higher powers the pressure is no longer expected to be radially uniform across the chamber, as the plasma pressure becomes much higher, the neutral pressure may be expected to remain similar to the fill pressure or decrease as seen in [124].

The mean free path of collision between a hydrogen atom and a charged proton can be considered to determine if it is likely that depletion is caused by collisions with the plasma. Under the high power conditions in MAGPIE at z=150mm, it is

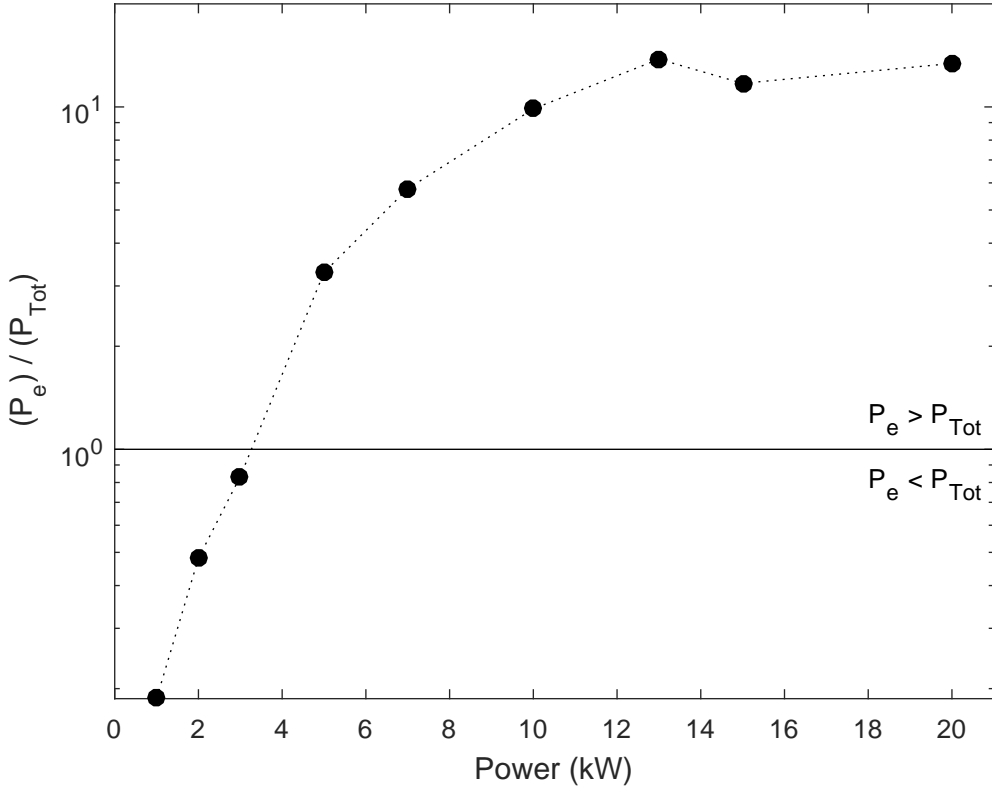


Figure 4.16: $\frac{P_e}{P_{Tot}}$ against applied RF power. The solid line at 1 indicates where the electron pressure is equal to the H₂ fill pressure.

expected that the main ion will be H⁺.[132] We therefore consider just collisions with H⁺ ignoring e⁻, H₂⁺ and H₃⁺ to be the main collision with plasma. Considering Eqn 1.2 for the collisional frequency for a hydrogen atom with a proton gives:

$$\nu_{H^+,H} = v_{th,H^+} n_{H^+} \sigma_{H^+,H} \quad (4.12)$$

The mean free path of the collisions is given by the thermal velocity of the hydrogen atom divided by the collisional frequency:

$$\lambda_{H^+} = \frac{v_{th,H}}{\nu_{H^+,H}} \quad (4.13)$$

4.3. DEPLETION DYNAMICS

substituting Eqn 4.12 into Eqn 4.13 gives:

$$\lambda_{H^+} = \frac{v_{th,H}}{v_{th,H^+}} n_{H^+} \sigma_{H^+,H} \quad (4.14)$$

From Eqn 4.7, the thermal velocity, it is seen that the ratio of the thermal velocity of atomic hydrogen to a proton is the square root of their temperatures. The expected ion temperature T_i in MAGPIE is approximately 1eV.[27, 132] and using an approximate atomic hydrogen temperature of 0.05eV, this ratio can be estimated. The H^+ density is assumed to be approximate to the ion density, $n_i = 1.8 \times 10^{19} m^{-3}$. The cross-section, $\sigma_{H^+,H} = 1.8 \times 10^{-19} m^{-2}$ is taken from Table 1.2. Evaluating gives a mean free path of a collisions between a hydrogen atom and plasma is approximately 0.07m (70mm), slightly shorter than the radius of the target chamber. H_2^+ and H_3^+ have larger cross sections of collisions with atomic hydrogen than H^+ , as such the mean free path may be shorter if accounting for the heavier ions. Therefore a hydrogen atom is likely to be scattered before crossing the chamber. The pressure of the plasma can push the neutral out of the centre region.

Atomic Hydrogen Density as a function of Electron Pressure

By plotting the electron pressure against the atomic hydrogen density as shown in Figure 4.17, it is seen that there is a linear relation between the two for a set of the data points. These data points that have the linear relation correspond to the points that have a $\frac{P_e}{P_{Tot}} > 1$, that is when the electron pressure is significantly high, then significant neutral depletion is expected. The upper limit of this relation corresponds with the maximum atomic hydrogen density achieved. This suggests that the decrease in n_H that is observed is linearly related to the electron pressure. As the plasma pressure linearly depends on the electron pressure this supports the argument that the neutral depletion observed is due to the high electron pressure. To completely understand and determine the mechanisms that are causing the depletion of neutrals in MAGPIE, temporal and spatial measurements are needed.

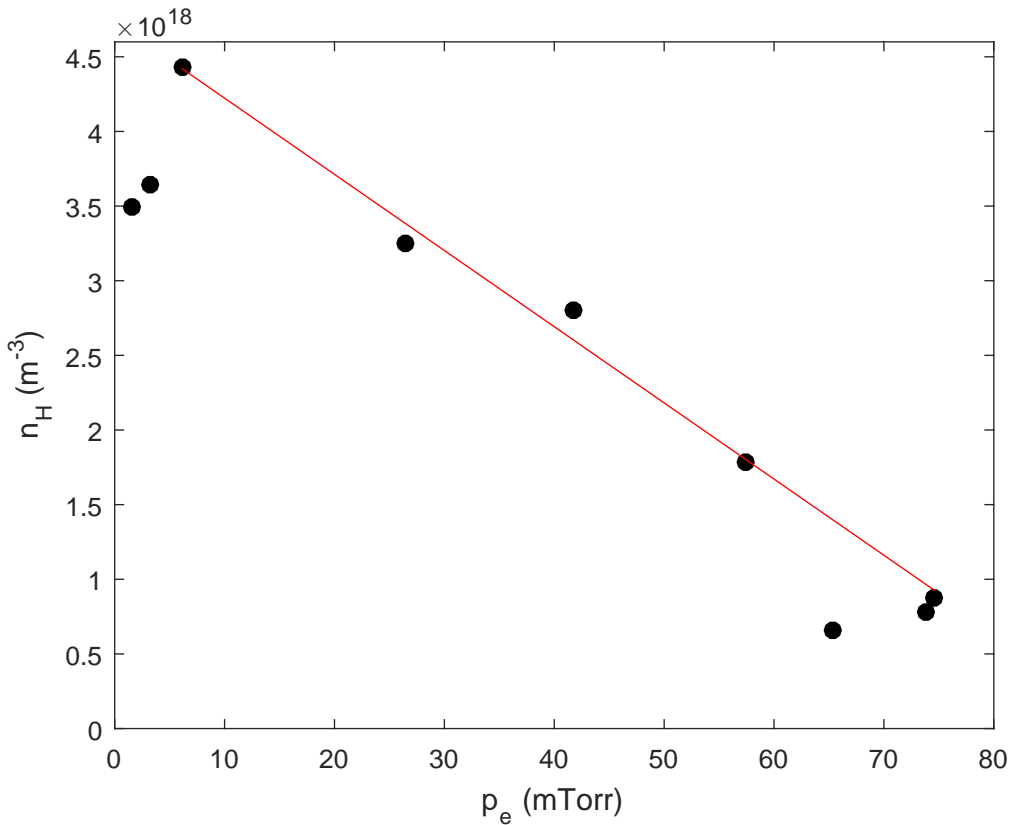


Figure 4.17: Atomic hydrogen density as a function of electron pressure.

4.4 Summary

In this chapter the plasma density and electron temperature in the MAGPIE helicon device have been presented as a function of power (up to 20kW) for a hydrogen plasma. From these measurements a discussion of the plasma conditions that may give rise to neutral depletion, notably the high plasma pressure, have been made.

The neutral atomic hydrogen density and temperature have been measured in the plasma afterglow using the newly set-up two-photon absorbed laser-induced fluorescence diagnostic. The atomic hydrogen density was observed to decrease with increasing applied RF power. At 20kW, longer plasma discharge lengths also displayed a decrease in the atomic hydrogen density.

An examination of the fluorescent scans show that it is unlikely for two distinct atomic hydrogen temperature populations to exist. The Doppler broadening

4.4. SUMMARY

of the scans has been used to determine the temperature of the hydrogen atoms. It is observed that the temperature of atomic hydrogen increases with higher applied RF power.

A study of the mechanisms that lead to neutral depletion in the core of the linear plasma device conclude that it is a mix of mechanisms that are causing a depletion of the atomic hydrogen in the plasma. The heating of neutral atomic hydrogen can cause up to 60% in a 20kW discharge compared to room temperature. However the high plasma pressure, which is more than 10x higher than the fill pressure is the largest contributor to neutral depletion.

Chapter 5

Temporal and Radial Atomic Hydrogen Dynamics

This chapter examines the temporal evolution and radial profile of the plasma and the neutral atomic hydrogen in the afterglow of high power (<20kW) hydrogen plasmas in the MAGPIE helicon plasma device. All of the measurements in this chapter will focus on a single axial position upstream ($z=150\text{mm}$) of the antenna in the target chamber of MAGPIE. Langmuir probe measurements have been carried out in 10mm steps for radial positions 0-60mm. The TALIF measurements are also in 10mm steps with a limited range of 0-30mm due to the frame of MAGPIE blocking the detection.

The temporal and spatial profiles will provide additional information on the neutral atomic hydrogen behaviour observed in the previous chapter. The temporal evolution of atomic hydrogen density into the plasma afterglow gives support for neutral depletion occurring during the plasma discharge. At the lowest power, 1kW, before neutral depletion has become a dominant mechanism in the plasma, it displays a two stage decay in afterglow. At higher powers (5-20kW), a different behaviour is observed in the afterglow, an initial replenishment of atomic hydrogen before being followed by a decay.

Radial measurements display a slightly lower density of atomic hydrogen in the centre compared to closer to the chamber walls. A flat radial temperature means that gas heating is unable to explain this behaviour. To the best of the author's knowledge, neutral depletion of atomic hydrogen has not been observed in high power linear plasma devices until now.

5.1 Time Resolved Afterglow Dynamics

This section presents time resolved measurements of the electron density, atomic hydrogen density and temperature into the afterglow of a hydrogen discharge in the MAGPIE helicon device. This is followed up with a discussion of the loss mechanisms of atomic hydrogen in the afterglow of the plasma discharge.

5.1.1 Plasma Afterglow Dynamics

The Impedans Langmuir probe system discussed in Chapter 2 was used to measure the plasma parameters (n_e , T_e) in the afterglow of the plasma discharge. The plasma afterglow has not been well characterised in MAGPIE previously. Although the RF power is switched off, there will still be plasma species present for a duration in the afterglow of the plasma discharge. This duration depends on the lifetimes of the states of the species and the reaction pathways available for them to neutralise.

The electron density (n_e) evolution into the afterglow of a 5ms plasma pulse with 10mTorr H₂ fill pressure is shown in Figure 5.1. The steady state electron density as a function of power is discussed previously in Section 4.1. A set of powers (1kW, 5kW, 10kW, 20kW) are investigated up to 1.2ms into the plasma afterglow, further into the afterglow the electron density drops below the detection limits of the Langmuir probe measurement system. The neutral gas pressure before the discharge was maintained at 10mTorr and the magnetic field was kept at the standard 50A:300A configuration. For all powers 1-20kW, n_e is observed to start highest initially in the afterglow and rapidly decays into the afterglow. At 1kW

5.1. TIME RESOLVED AFTERGLOW DYNAMICS

applied RF power and at 0.05ms into the afterglow $n_e = 6.0 \times 10^{16} \text{ m}^{-3}$ and decreases with increasing time into the afterglow. The electron density is observed to increase with increasing applied RF power. At 5kW, initial n_e ($t=0.05\text{ms}$) has increased to $4.4 \times 10^{17} \text{ m}^{-3}$, and continues to increase to $7.0 \times 10^{17} \text{ m}^{-3}$ and $9.9 \times 10^{17} \text{ m}^{-3}$ for 10kW and 20kW respectively. By 1.2ms into the afterglow, the density has decreased by 3 orders of magnitude compared to 0.05ms. The electron density decay into the afterglow has an almost exponential decay, becoming more exponential in the later afterglow, with a similar decay rate for all applied RF powers. The dominant electron loss mechanisms are electron ion recombination and diffusion to the walls.[179]

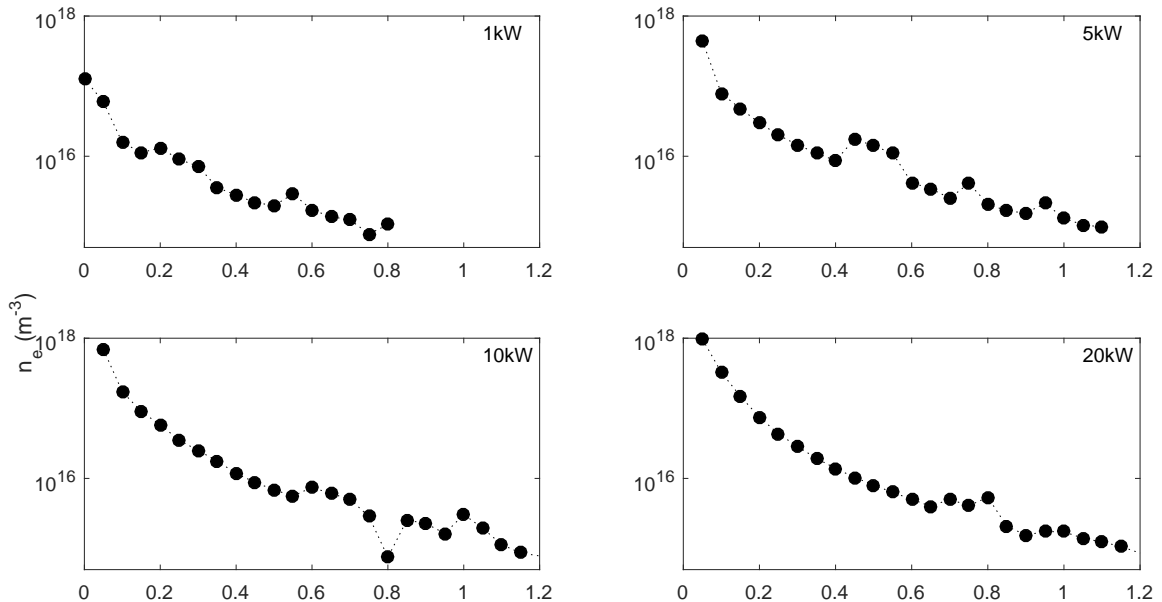


Figure 5.1: Electron density into the afterglow of a 5ms hydrogen plasma discharge with a fill pressure of 10mTorr for a set of power 1-20kW.

The electron temperature in the afterglow is calculated from fitting the linear part of the slope in the $\log(I)$ vs V . The very low densities in the afterglow make this measurement particularly error prone as the probe quickly switches from ion saturation to electron saturation in only a few volts. However, very little change is observed in T_e in the afterglow after cooling within 10s of μs , remaining fairly constant at $\sim 1\text{eV}$ from 0.1ms to 1.2ms.

5.1. TIME RESOLVED AFTERGLOW DYNAMICS

Using Equation 4.2, the pressure due to electrons in the afterglow is calculated. The electron pressure as a function of time after the plasma discharge is shown in Figure 5.2 for the set of powers being investigated. Here the plasma pressure is given in mTorr to allow it to be easily compared to the measured neutral gas fill pressure. It is seen that in the 1kW case the electron pressure drops dramatically in the first 0.05ms and is less than 0.1mTorr after 0.2ms.

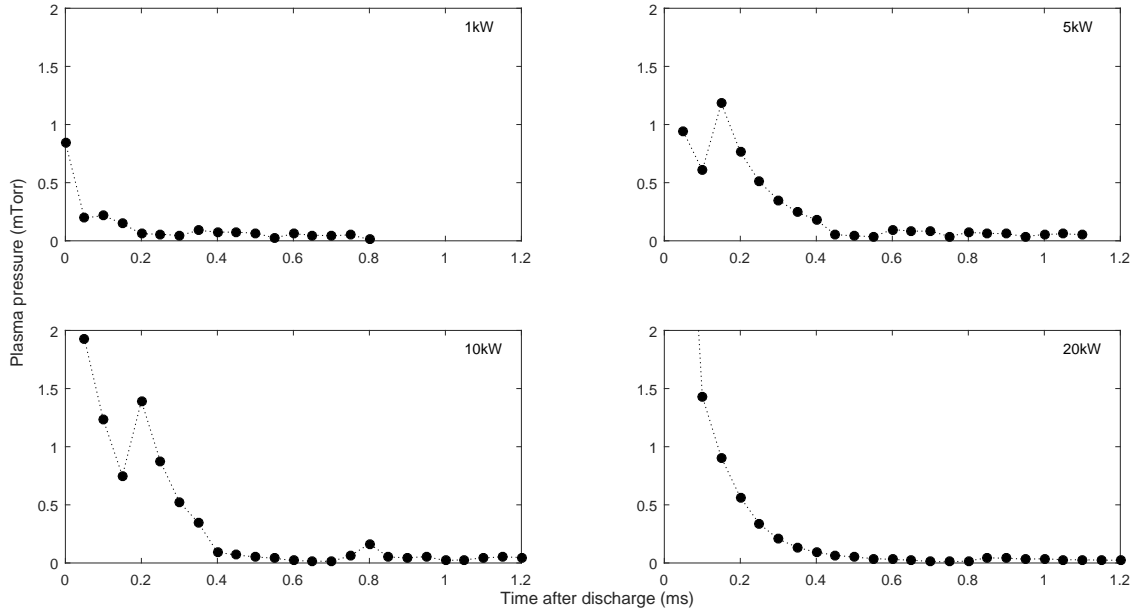


Figure 5.2: Plasma pressure into afterglow for a set of power 1-20kW.

At higher powers, $>5\text{kW}$ the electron pressure is more substantial in the early afterglow. For 5kW the electron pressure is observed to last longer into the afterglow taking 0.4ms to drop below 0.1mTorr from a pressure of 1.2mTorr. At 10kW the electron pressure at the earliest measurement in the afterglow (0.1ms) has a pressure of 2mTorr before also taking 0.4ms to lower to less than 0.1mTorr. For 20kW input power the pressure starts high in the early afterglow due to the much higher electron density. At 0.05ms into the afterglow of a 20kW pulse the electron pressure is 4.3mTorr. This data point is not shown on the figure to allow the electron decay into the afterglow to be shown clearly.

For all applied RF powers the plasma pressure is observed to quickly drop well below the gas fill pressure, on the order of 10s of μs . The plasma pressure was demonstrated to be higher than the neutral fill pressure and largely contributing to the neutral depletion in the plasma core, in Chapter 4. It is observed that in the afterglow the plasma pressure drops below the fill pressure quickly. This is due to the fast decrease in both plasma density and electron temperature as soon as the plasma is switched off. Without the high plasma pressure causing the neutral depletion, the neutral species may be expected to replenish the centre of the chamber.

5.1.2 Atomic Hydrogen Afterglow Density

It is important to study the temporal dynamics of the neutral species to provide a full picture of the neutral population. As neutral depletion has been shown to be occurring during the plasma discharge (Chapter 4) then the neutral density may increase later in the afterglow as plasma pressure drops. This section presents time resolved measurements of atomic hydrogen in the afterglow of the plasma pulse. The timing of the laser and photomultiplier tube were adjusted with respect to the plasma pulse to probe atomic hydrogen during the afterglow. The earliest time measured is $250\mu\text{s}$ (0.25ms) after the plasma pulse for the lowest power of 1kW. For the higher powers investigated, 5kW, 10kW and 20kW, the low density in the early afterglow did not provide an adequate signal-to-noise ratio so soon after the plasma pulse. Hence the earliest measurements were made later into the afterglow ($\approx 1\text{ms}$). TALIF measurements were made up to 20ms after the plasma pulse for 10kW and 20kW input power.

Apart from the power and time after the plasma discharge, all other conditions were kept constant. A 5ms plasma pulse length was used with the standard 50A:300A magnetic field coil configuration. The input H_2 pressure measured at the gas inlet was kept at 10mTorr. All measurements are made at the centre of the target chamber in MAGPIE and $z=150\text{mm}$ upstream of the antenna.

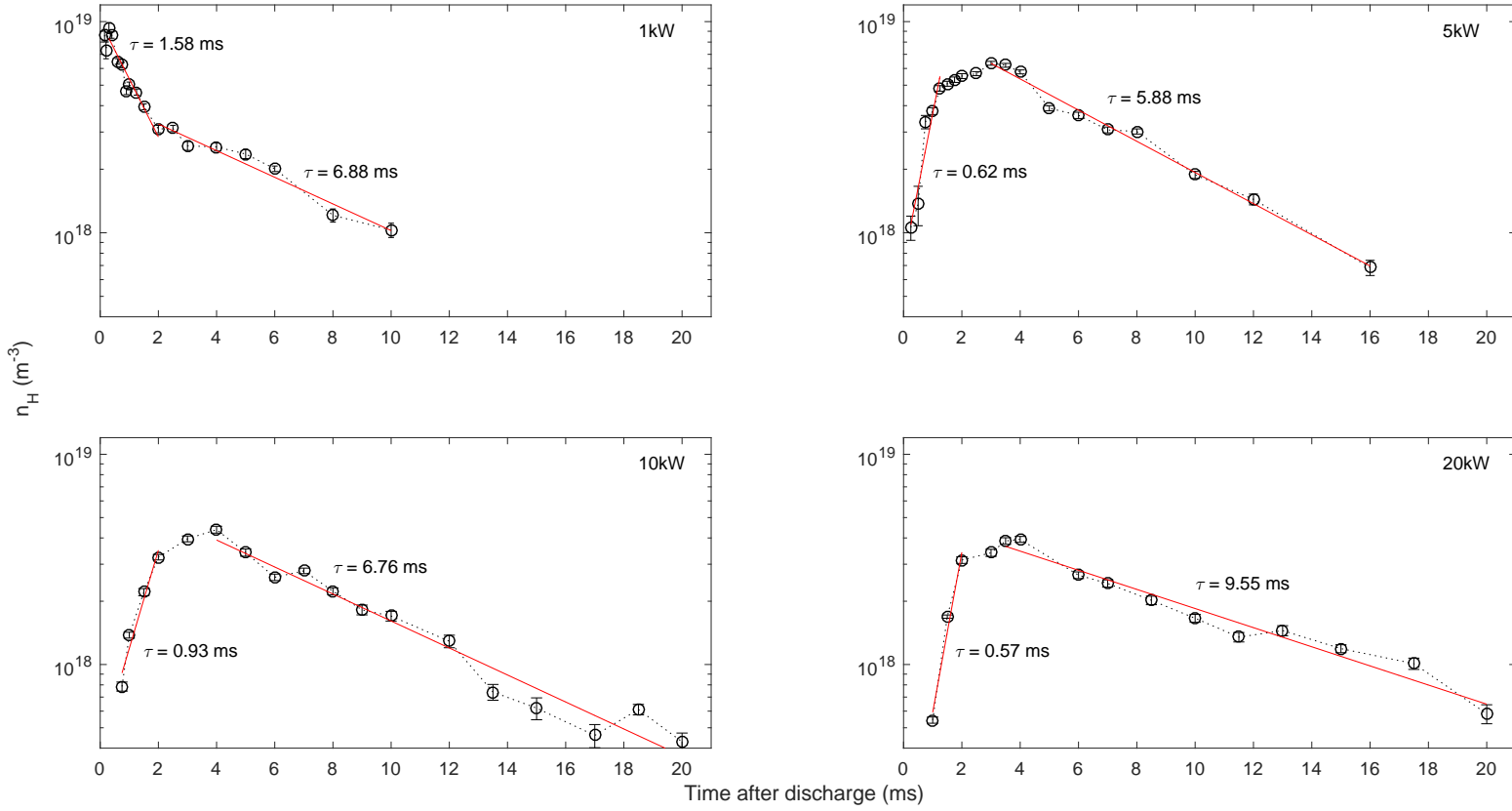


Figure 5.3: Density of neutral atomic hydrogen into the afterglow of a 5ms plasma discharge for a set of antenna power (1, 5, 10, 20kW). Shown in red are the fitted trends of the exponential increase and decay as a function of time into the afterglow.

The evolution of the atomic hydrogen density in the afterglow of the plasma discharge is shown in Figure 5.3. With 1kW applied RF power the density rapidly decreases into the afterglow of the plasma discharge. The atomic hydrogen density displays a two stage decay in the afterglow. There is an initial fast decay with a rate $\tau_1 = 1.58\text{ms}$. This is followed by a slower decay rate $\tau_2 = 6.88\text{ms}$ that continues for the rest of the measured afterglow.

Rousseau *et al.* [180] observed a two rate decay of H atoms in the afterglow of a microwave discharge. They used the Pulsed Induced Fluorescence (PIF) technique to measure the H_α emission. The PIF technique was first developed by Bouchoule and Ranson.[181] They measured decay lifetimes of $\tau_1 = 2.8\text{ms}$ and $\tau_2 = 30\text{ms}$ for the fast and slow decay rates respectively. Tserepi [182] explained this two rate decay as the earlier fast rate decay occurring by the fast adsorption of atomic H on empty surface sites created by the energetic species during the plasma discharge. The longer decay time is due to their Pyrex chamber having a low recombination coefficient. The second slower decay is due to the slower recombination process occurring at the walls.

Samuell *et al.* also observed a two stage decay of atomic hydrogen in the afterglow of the plasma pulse while investigating the loss probabilities in MAGPIE.[183] They also used the PIF technique and observed decay rates of $\tau_1 = 1.3\text{ms}$ for the initial fast decay and $\tau_2 = 7.6\text{ms}$ for the second decay. These measurements are in close agreement with the decay rates measured for the 1kW applied RF power presented in this work.

Gaboriau and Beouf produced a global (0D) model for low pressure high power hydrogen discharges.[184] They included the heat equation for neutral hydrogen in their model to determine the temperature and account for gas heating and increased gas pumping. They predict that above 10kW, the gas density profile will no longer be constant, which in turn leads to increasing T_e and slower increase in plasma density with power. They also observed that the hydrogen atom wall recombination coefficient (γ) strongly couples with gas depletion. For higher values of the wall recombination coefficient the gas depletion is reduced.

As the power is increased, the atomic hydrogen density is observed to be much lower in the early afterglow compared to 1kW. This change in behaviour corresponds to the change in operating mode from inductive to helicon, which occurs at approximately 4kW.[\[162\]](#) When the system operates in the helicon mode the atomic hydrogen displays interesting behaviour, it is observed to increase in the early afterglow. The density peaks at approximately 3ms at 5kW and peaking at approximately 4kW for 10kW and 20kW. As shown in Figure 5.3, at this position in MAGPIE ($r,z = 0, 150\text{mm}$), 10kW and 20kW do not achieve densities as high as those seen in 1kW and 5kW. The initial increase in density is due to the replenishment of atomic hydrogen back into the centre of the chamber, as the atomic hydrogen has been depleted during the plasma discharge at the higher powers. This is followed by the same slower recombination process as in the lower power cases.

The observed increase in density into the afterglow is consistent with neutral depletion occurring in the plasma core discussed in Chapter 4. It is proposed that the atoms from the edge region replenish the depleted core after the plasma has been switched off. The replenishment of the atomic hydrogen in the afterglow cannot come from dissociative processes as there is no mechanism with the plasma switched off. Additionally the electron density is shown to have dropped off by three orders of magnitude by 1ms into the afterglow and cannot be recombined with ions in the bulk to form neutral atomic hydrogen.

Figure 5.4 shows the change in density at various times in the afterglow for different powers. It is observed in the early afterglow (1ms) that 1kW power has the highest atomic hydrogen density in the core of the plasma. There is a decreasing relationship with increasing power with H density being lower at 5kW and further decreasing at 10kW and 20kW. 1kW continues to decrease into the afterglow for all times measured (3ms, 6ms, 10ms). At 3ms into the afterglow there is an observed increase in density from 1ms at higher powers (5kW, 10kW, 20kW). After 3ms the higher power plasmas display a continual drop in density for all times measured.

There are comparable density profiles for the higher powers, however increasing power results in a lower atomic hydrogen density in the afterglow. The decrease

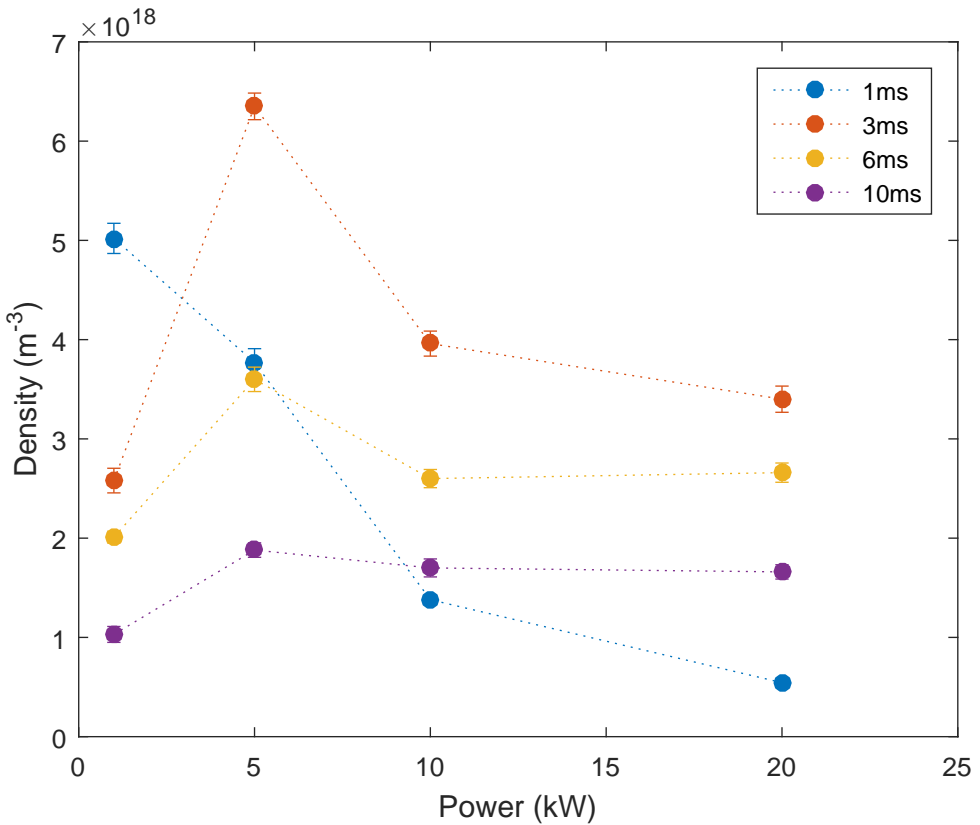


Figure 5.4: Atomic hydrogen density with increasing power at different times in the afterglow of a 5ms plasma discharge.

in density with increasing power is mostly likely due to increased depletion of the atomic hydrogen in the core of the plasma when it is switched on.

5.1.3 Atomic Hydrogen Temperature

For each of the TALIF measurements the temperature of atomic hydrogen (T_H) has been determined from the Doppler broadening of the absorption. The temperatures for powers 1kW, 5kW, 10kW and 20kW into the afterglow are shown in Figure 5.5. At 1kW, T_H is hottest (0.1eV) initially in the afterglow at $250\mu\text{s}$ (0.25ms) after the RF power is switched off. The H atoms quickly cool to 0.04eV ($\sim 400\text{K}$) by $400\mu\text{s}$ (0.4ms) into the afterglow and remain at a steady temperature of 0.02-0.04eV further into the afterglow. That is after $\sim 400\mu\text{s}$ (0.4ms) atomic hydrogen has cooled to room temperature (0.026eV $\sim 300\text{K}$). During this time the hydrogen atoms thermalise with

their environment. For 5kW, T_H decreases from approximately 0.1eV at 1ms to the same 0.02-0.04eV value by $500\mu\text{s}$ (0.5ms) for the rest of the measured afterglow. In the 10kW and 20kW afterglow, the earliest measured temperatures, of 0.06eV and 0.085eV respectively, are not as high as that for the lower powers. This is most likely due to the inability to measure the atomic hydrogen temperature earlier in the afterglow due to the low densities. It is expected that the atomic hydrogen temperature will be higher during the plasma discharge. The high power cases also converge to the same steady temperature but with a longer thermalisation time period of approximately 1.5ms.

Samuell and Corr measured atomic hydrogen temperatures of 850K during a 1kW H₂ discharge.[173]. This is fairly consistent with the earliest T_H measurement at $150\mu\text{s}$ (0.15ms) in the afterglow 1kW which has a measured T_H of $\sim 0.1\text{eV}$ (1160K) which is slightly higher.

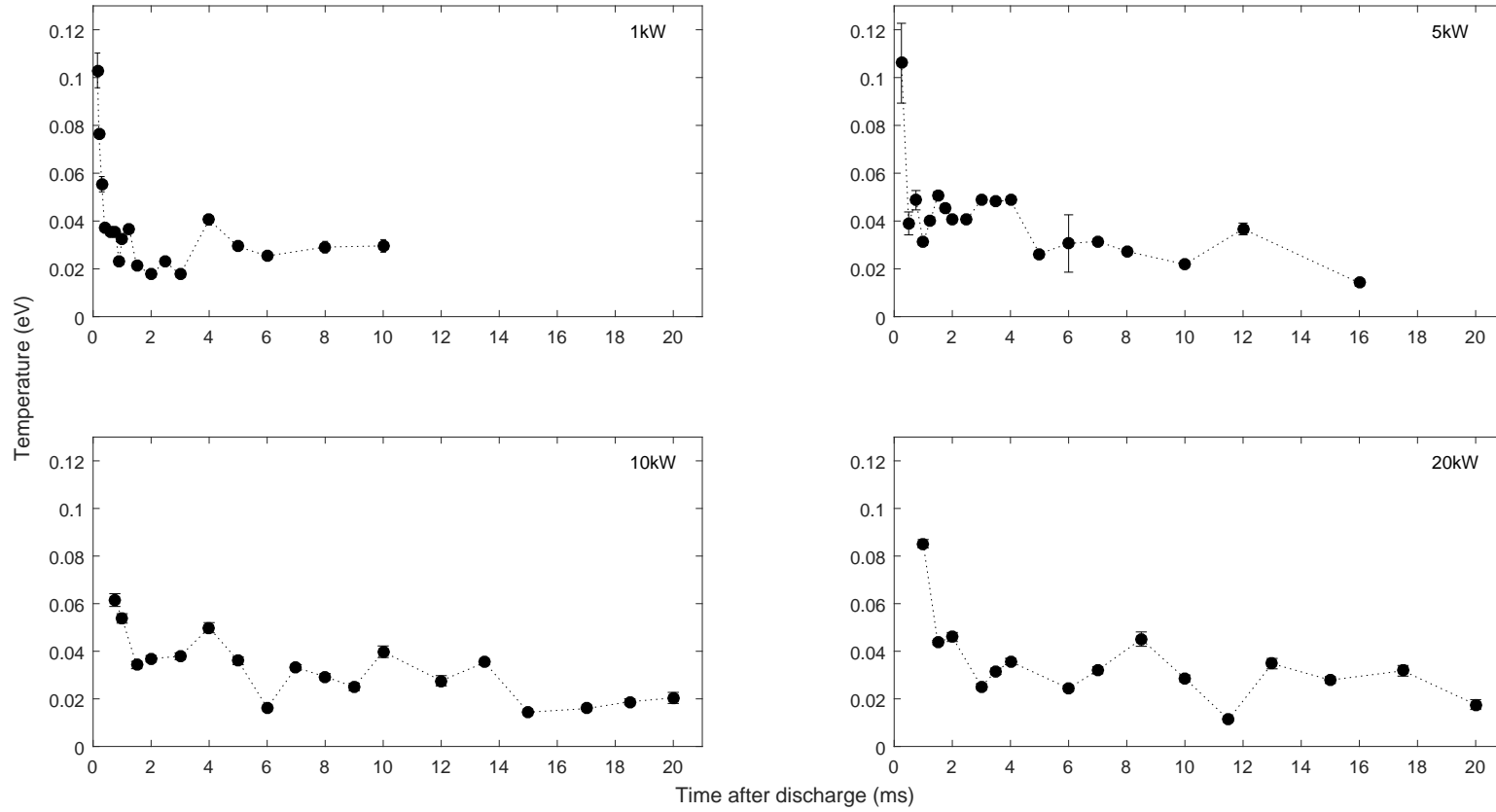


Figure 5.5: Temperature of neutral atomic hydrogen into the afterglow of a 5ms plasma discharge for a set of antenna power (1, 5, 10, 20kW).

5.1.4 Loss Mechanisms of Atomic Hydrogen

There have been conflicting arguments for the loss process of atomic hydrogen after the plasma discharge, as to whether there is indeed two separate decay mechanisms for atomic hydrogen loss or whether the cooling of atomic hydrogen affects the loss rate to account for the two stage process.[152, 180] The change in atomic hydrogen can be modelled by considering the creation and loss mechanisms available for hydrogen atoms in the afterglow of the plasma discharge. A similar approach to the previous work in the literature for atomic hydrogen loss is considered to investigate this discrepancy.[152, 180] The evolution of the local atomic hydrogen density can be written as:

$$\frac{\partial n_H}{\partial t} + \vec{\nabla}(n_H \cdot \vec{v}) = Sources - Losses \quad (5.1)$$

where, $\partial n_H / \partial t$ is the change in the H density as a function of time and $\vec{\nabla}(n_H \cdot \vec{v})$ is the diffusion due to the density gradient in the plasma, with \vec{v} is the thermal velocity. The sources and losses are the processes of creation and destruction of the atomic hydrogen. In the afterglow of the plasma, there are no sources of atomic hydrogen creation as the electrons have decayed as shown in Figure 5.1 and there is no energy input for dissociation of H_2 . The major loss mechanism in the plasma bulk is due to recombination with molecular H_2 :



The rate of this reaction is given by:

$$2k_r n_H^2 n_{H_2} \quad (5.3)$$

as the reaction involves two hydrogen atoms it depends on the square of the atomic hydrogen density n_H^2 and also depends on the local density of the molecular hydrogen n_{H_2} as this reaction requires a third body, (in this case H_2). The reaction

5.1. TIME RESOLVED AFTERGLOW DYNAMICS

constant is given by $k_r = 19.3 \times 10^{-31} T^{-1}$ ($\text{m}^6 \text{mol}^{-2} \text{s}^{-1}$).[185] At pressures below 1 Torr, the volume recombination process is usually neglected as a loss mechanism as the contribution is very small.[180, 186]

Another major loss factor of atomic hydrogen is through surface recombination at the chamber walls. When atomic hydrogen impacts upon the chamber walls it has a chance to adsorb to the surface as defined by a sticking coefficient. The adsorbed hydrogen may then recombine with another adsorbed hydrogen to produce molecular H₂ and be returned to the bulk. Additionally this adsorbed hydrogen may be released back into the gas phase before recombination. The surface loss probability (γ_H) is the probability of the atomic hydrogen both adsorbing to the wall and recombining to remove atomic hydrogen from the system.

Loss at the walls is determined by the diffusion coefficient. The diffusion term can be written as:[152]

$$\vec{\nabla}(n_H \cdot \vec{v}) = \frac{D}{\Lambda^2} n_H \quad (5.4)$$

where D is the diffusion coefficient and Λ is the characteristic length of diffusion. The diffusion coefficient is shown to depend on gas temperature and pressure:[187]

$$D = 12.5 \frac{T_g^{1.72}}{P} (\text{cm}^2 \text{s}^{-1}) \quad (5.5)$$

where T_g is the temperature of the neutral species in kelvin and P is the pressure in pascals. The characteristic length of diffusion can be broken into two terms as shown by Chantry:[188]

$$\Lambda^2 = \Lambda_0^2 + \frac{\Omega}{\Sigma} \frac{2(2 - \gamma)}{\gamma} \frac{D}{v_H^2} \quad (5.6)$$

where the first term depends on the reactor geometry and the second term considers the probability of recommendation at the walls. Ω is the plasma volume, Σ is the surface area inside the chamber, γ is the surface recombination probability as described above and $v_H^{\vec{v}}$ is the thermal velocity of the hydrogen atoms:

$$v_H^{\vec{v}} = \sqrt{\frac{k_B T_H}{m_H}} \quad (5.7)$$

Here, the plasma volume and chamber surface area is calculated only for the target chamber with the dimension discussed in Chapter 2. The source chamber is neglected as the source walls are made of PyrexTM which has a much lower surface recombination probability for hydrogen compared to the stainless steel source chamber walls. The surface recombination probability for stainless steel has been measured in the literature, $\gamma \sim 0.03\text{-}0.15$.[\[182, 189, 190\]](#) The surface recombination probability has been left as a free parameter in these calculations. The best fits to the measured atomic hydrogen decay rates use a γ value at the higher end of the literature values in the range 0.13-0.15 in close agreement with that measured by Samuell *et al.* [\[183\]](#)

The geometric shape, Λ_0 is given by Chantry for a cylinder:[\[188\]](#)

$$\frac{1}{\Lambda_0^2} = \left(\frac{\pi}{L}\right)^2 + \left(\frac{2.405}{R}\right)^2 \quad (5.8)$$

here the geometric shape is consider to be cylinder due to the internal structure of the target chamber.

Combining Equations 5.3-5.8 into Equation 5.1 to get a final description of the change in the local atomic hydrogen density:

$$\frac{\partial n_H}{\partial t} = -\frac{D}{\Lambda^2} n_H - 2k_r n_{H_2} n_H^2 \quad (5.9)$$

with Λ^2 given by Equation 5.6.

Lamara *et al.* [152] argue that the cooling of atomic hydrogen in the early afterglow leads to the two rate decay of atomic hydrogen in the plasma afterglow. The fit to the measured atomic temperature shown in Figure 5.5 is used to determine the changing recombination rate (k_r) and diffusion coefficient (D). Equation 5.9 is solved numerically with different initial densities to fit to the observed atomic hydrogen density profiles in the afterglow. The theoretical density and the measured density are shown in Figure 5.6.

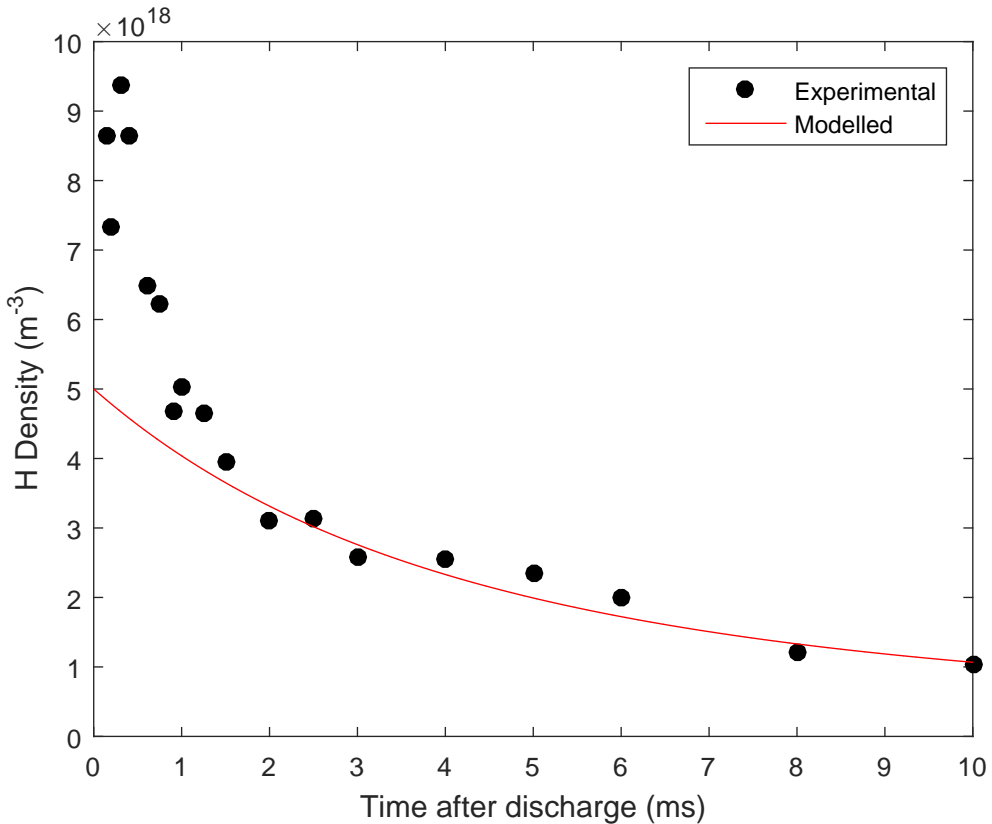


Figure 5.6: Atomic hydrogen density measurements (black dots) in the afterglow of a 5ms 1kW plasma compared with theoretical model (red line).

It is seen that the theoretical model can be used to predict the second decay rate (τ_2) in the afterglow of the 1kW plasma. This work did not find that the initial fast cooling of atomic hydrogen could explain the two rate decay observed, however the loss of atomic hydrogen due to recombination at the chamber walls appears to be

well modelled by the second slower decay rate. The atomic hydrogen temperature is fairly constant in the well-fit region. The decrease due to recombination with molecular hydrogen in the plasma volume is observed to be negligible in the model compared to the loss in atomic hydrogen due to the recombination at the chamber walls.

The theoretical model is also able to model the decrease in the atomic hydrogen observed at higher powers. Figure 5.7 shows the atomic hydrogen density in the afterglow of a 5ms 20kW discharge. The experimental measurements are shown in black dots and the theoretical model with the red line. This supports the argument that the loss in atomic hydrogen in the afterglow is dominated by surface losses, mainly recombination at the surface. The increase in the early afterglow is due to repletion of atomic hydrogen into the centre of the chamber (i.e. the depleted region during the plasma discharge). As discussed earlier in this thesis, the repletion is due to diffusion of atomic hydrogen as there are not any creation process on these time scales. As the atomic hydrogen is depleted in the centre of the chamber and diffusing back in during the plasma afterglow, this suggests that there is a hollow profile for atomic hydrogen.

5.1.5 Atomic Hydrogen Afterglow Pressure

Equation 4.2 can be used to calculate the pressure from the H atoms from their measured density and temperature. The atomic hydrogen pressure is shown as a function of time into the afterglow for different powers in Figure 5.8. It is observed that the highest measured H pressure is in the earliest afterglow of the 1kW plasma (due to higher H densities). These measurements are consistent with neutral depletion occurring at the higher power ($>4\text{kW}$) discharges. At 1kW, the pressure of atomic hydrogen is observed to drop significantly in the first 1ms of the afterglow. The pressure continues to drop as the atomic hydrogen density and temperature decrease.

When operating in the helicon mode at higher power, the trend for the neutral atomic pressure follows that of the neutral density into the afterglow. The

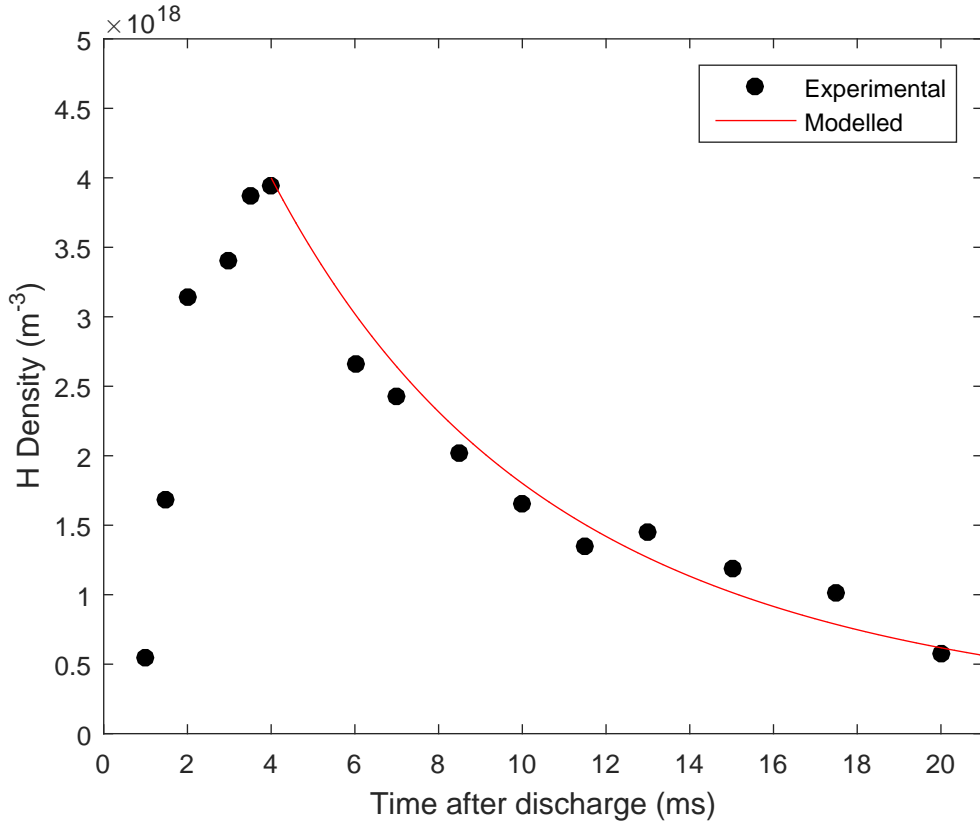


Figure 5.7: Atomic hydrogen density measurements (black dots) in the afterglow of a 5ms 20kW plasma compared with theoretical model (red line).

neutral pressure starts at a negligible level and slowly increases over the first 4ms into the afterglow. The atomic hydrogen pressure peaks at approximately 0.4mTorr in the afterglow of the 5kW plasma and decreases after this peak. 10kW and 20kW are observed to have H pressure peaks of approximately 0.03mTorr and 0.04mTorr respectively, at 4ms into the afterglow. The pressure from atomic hydrogen is lower than both the maximum electron pressure during the pulse and the initial H_2 pressure of 9.1mTorr at the position of the measurements. This supports that the atomic hydrogen is responding to external forces from other species, whereby it is being pushed out by the high electron pressure in the core during the plasma discharge. In the afterglow, atomic hydrogen diffuses back in towards the centre as electrons decay and there is a pressure gradient inwards.

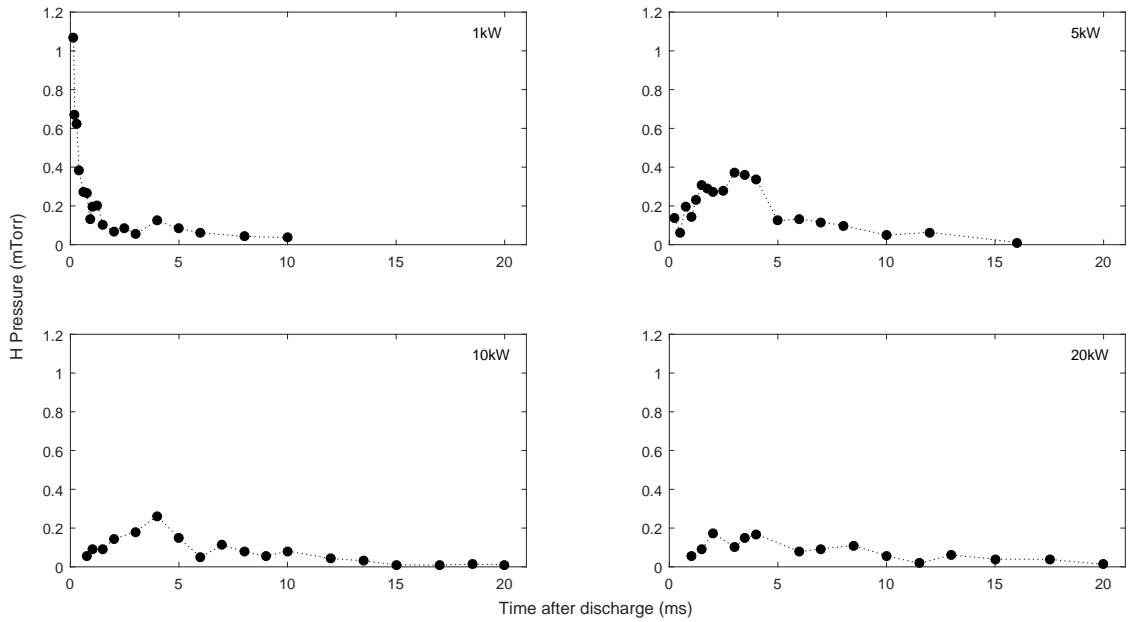


Figure 5.8: Neutral pressure from the atomic hydrogen into afterglow for a set of power 1-20kW.

5.2 Time Resolved Radial Profiles

In this section, the time evolution of atomic hydrogen density and temperature into the afterglow at multiple radial positions have been measured in the target chamber ($z=150\text{mm}$). Measurements were restricted to the range 0-30mm due to the frame of the target chamber blocking the optical access of the detection system.

5.2.1 Radial Plasma Density

Radial measurements can directly show the depletion of the neutral species. At higher powers ($> 4\text{kW}$) the electron pressure is shown in Chapter 4 to be higher than the background H_2 pressure. High electron density in the core, shown in Figure 5.9, leads to neutral depletion as the neutrals are pushed out from the centre. These measurements are by Santoso who used a higher current of 400A in the mirror coils and therefore in this work the plasma may be slightly less confined. The magnetic field strength at the $z=150\text{mm}$ position with mirror coil currents of 300A and 400A

5.2. TIME RESOLVED RADIAL PROFILES

is 190G and 240G respectively.[132] As can be seen in the radial electron density measurements, the electron density is highest in the centre ($1.5 \times 10^{19} \text{ m}^{-3}$) of the chamber and decreases towards the chamber walls, dropping to $5 \times 10^{17} \text{ m}^{-3}$ at 50mm. The electron temperature is fairly constant at approximately 6eV radially from the centre to 20mm before displaying a slight increase to approximately 7.8eV at 35mm. After 35mm the electron temperature steeply decreases to 2.5eV at 50mm. The constant radial temperature profile and radially decreasing electron density support that there is a high plasma pressure in the centre that is causing the neutral species to be depleted in the core. This section will investigate the radial profiles of the atomic hydrogen density and examine whether the neutral species have been depleted on the axis of the plasma.

It is seen that the plasma density drops an order of magnitude over 40mm from the centre of the discharge, this is of the same order of magnitude for the mean free path of collisions for a hydrogen atom with the plasma discussed in Section 4.3. Providing further evidence that the plasma is able to push the neutral species out of the centre region of the chamber where there is high plasma pressure.

As discussed in Chapter 2, the electron density is determined using the Langmuir probe. Temporally and spatially resolved measurements were made upstream from the antenna in the target chamber at $z=150\text{mm}$. This is to compare with the atomic hydrogen measurements made with the TALIF diagnostic. A set of RF powers were investigated (1, 5, 10, 20kW) with the standard 50A:300A magnetic field configuration. The molecular hydrogen pressure was maintained at 10mTorr for all measurements. The Langmuir probe tip was moved radially in steps of 10mm from the centre of the chamber ($r = 0\text{mm}$) to 60mm.

Shown in Figures 5.10-5.13 is the electron density (n_e) into the early afterglow of the plasma pulse for different powers (1, 5, 10, 20kW). The earliest measured time in the afterglow is $50\mu\text{s}$ (0.05ms) as the ramp down of the RF transmitters is of this order. This ensures that all supplied RF power is off by the time the measurements are made. Each subfigure shows the evolution for a single radial position 0-60mm. A 3D plot of the combined n_e which shows the evolution of the density into the afterglow and along the radial position is included for each power.

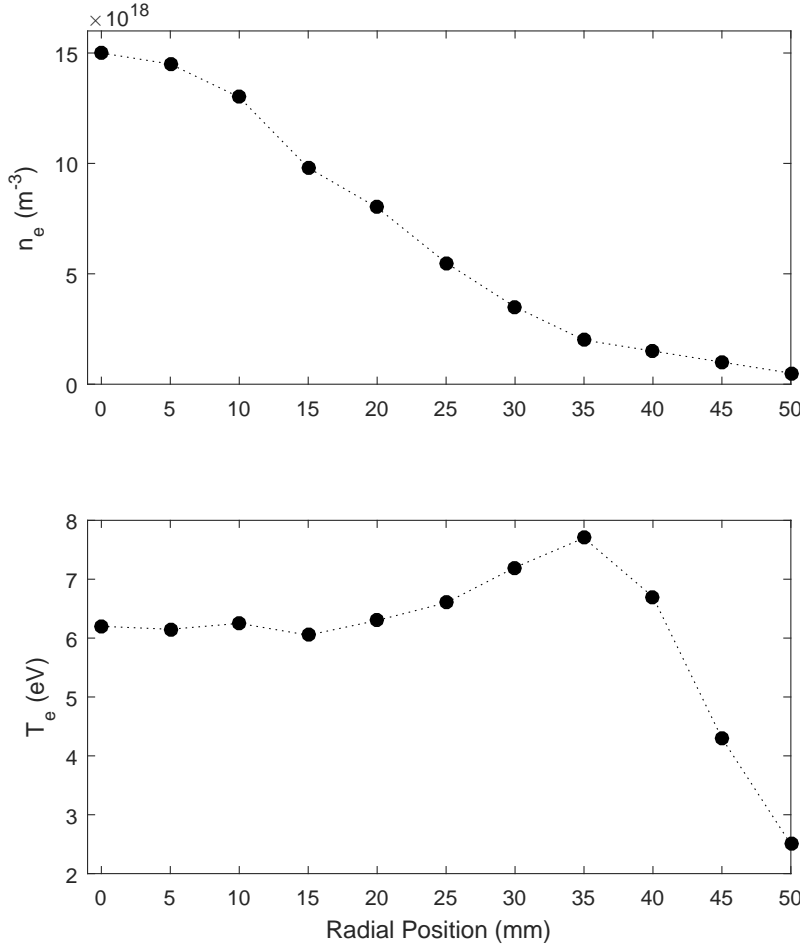


Figure 5.9: Radial profiles of the electron density (top) and temperature (bottom) at $z=150\text{mm}$ during a 20kW hydrogen plasma discharge. Reproduced from [132].

Looking at the densities for 1kW applied RF power in Figure 5.10 it is seen that n_e is highest in the centre of the chamber at $r = 0\text{mm}$ at $6 \times 10^{16} m^{-3}$. From the centre to a radial position of 60mm the electron density is fairly constant. At $50\mu\text{s}$ (0.05ms) after the plasma pulse all measured densities are within $3-6 \times 10^{16} m^3$. At each radial position n_e decays with an identical shape relation, in all cases dropping by an order of magnitude by $200\mu\text{s}$ (0.2ms) after the RF pulse. n_e continues to further decay into the afterglow dropping below $10^{15} m^3$ by $500\mu\text{s}$ (0.5ms) where it can effectively be considered negligible.

5.2. TIME RESOLVED RADIAL PROFILES

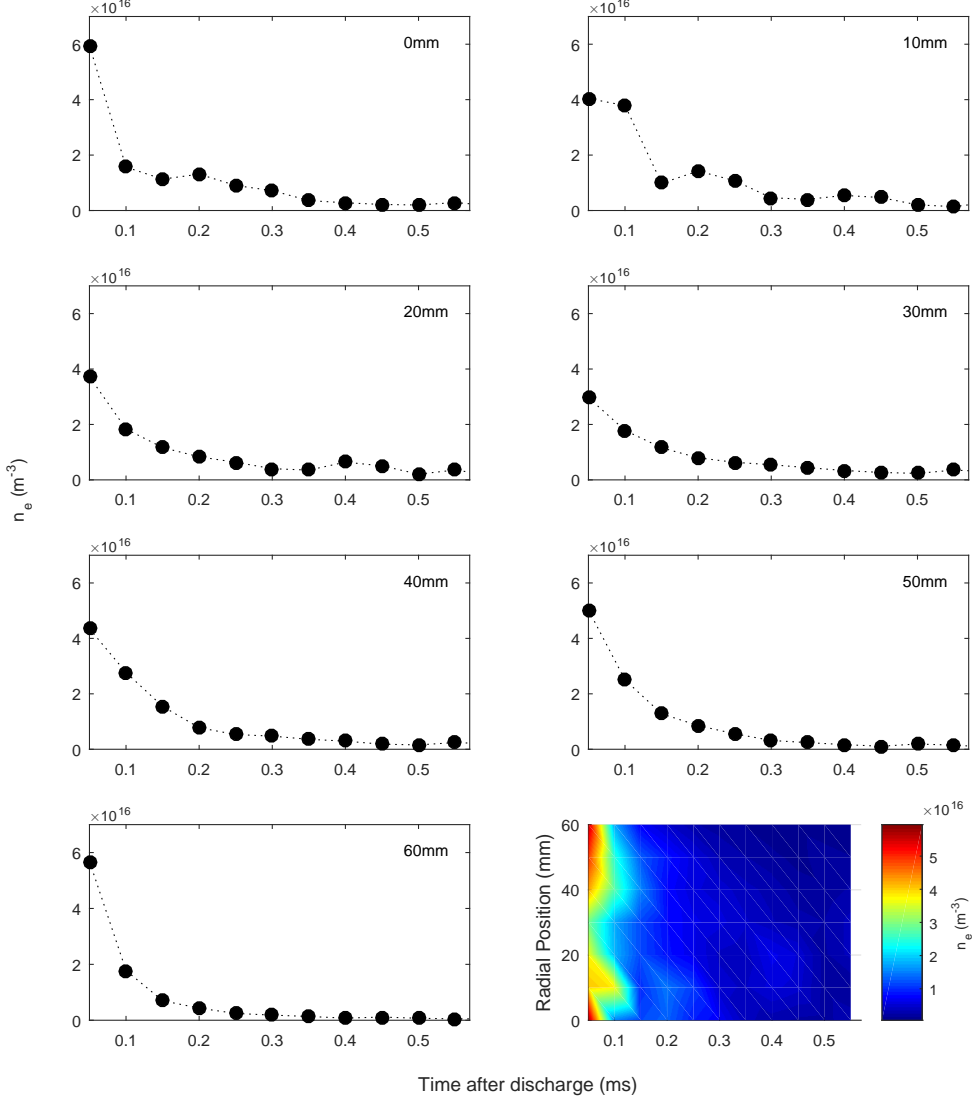


Figure 5.10: Electron density in the early afterglow of a 5ms 1kW plasma pulse with the standard operating conditions. Subplots show different radial positions, $r = 0\text{-}60\text{mm}$. A 3D plot shows the electron density as a function of time and radial position in the afterglow.

As the applied RF power is increased to 5kW, a large jump in n_e occurs consistent with MAGPIE entering the helicon mode. Figure 5.11 shows $n_e \approx 4.5 \times 10^{17} \text{ m}^{-3}$ at $50\mu\text{s}$ (0.05ms) in the afterglow in the centre of the chamber. At 10mm radially outward from the centre, the electron density is comparable to the centre, however the electron density decreases radially beyond 10mm. At 60mm, n_e is less than

5.2. TIME RESOLVED RADIAL PROFILES

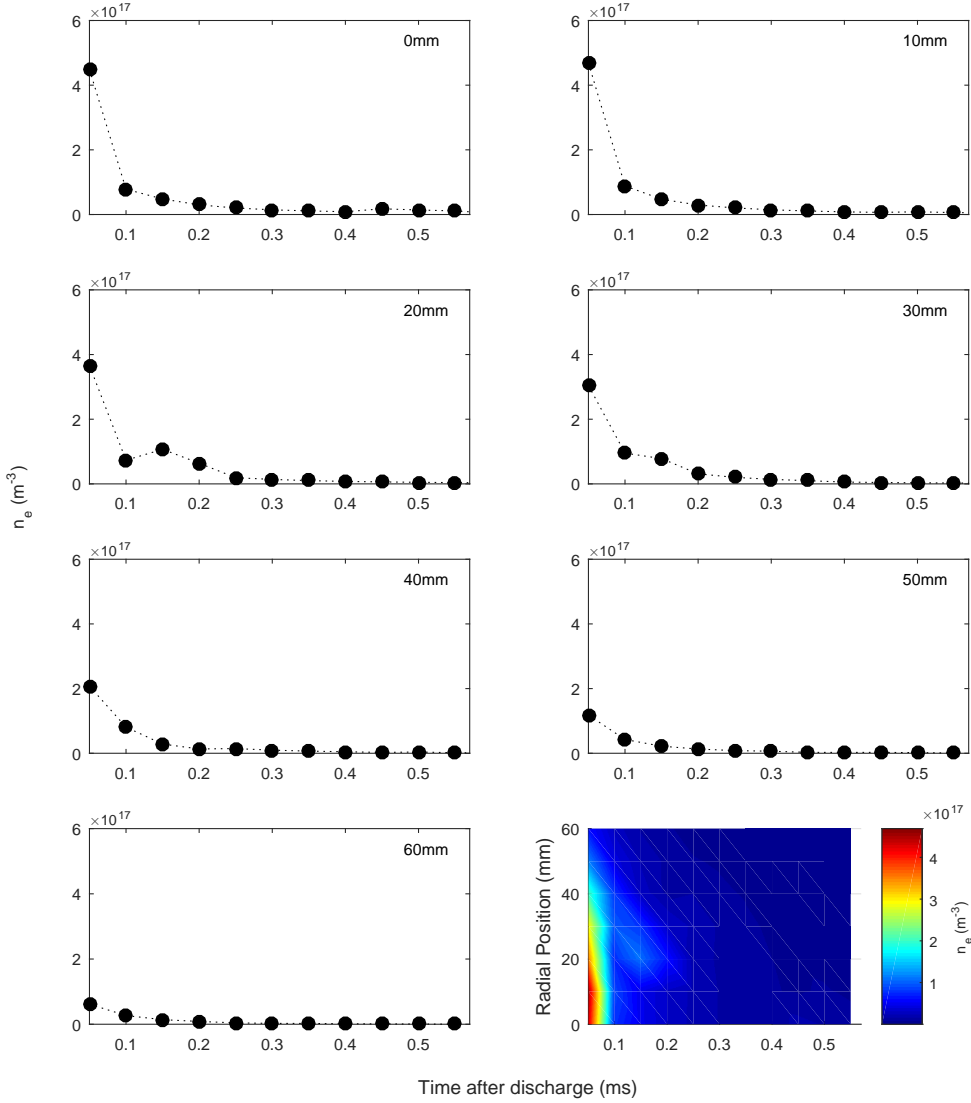


Figure 5.11: Electron density in the early afterglow of a 5ms 5kW plasma pulse with the standard operating conditions. Subplots show different radial positions, $r = 0\text{-}60\text{mm}$. A 3D plot shows the electron density as a function of time and radial position in the afterglow.

10^{17}m^3 . All radial positions display an identical n_e decay after the plasma discharge is switched off.

5.2. TIME RESOLVED RADIAL PROFILES

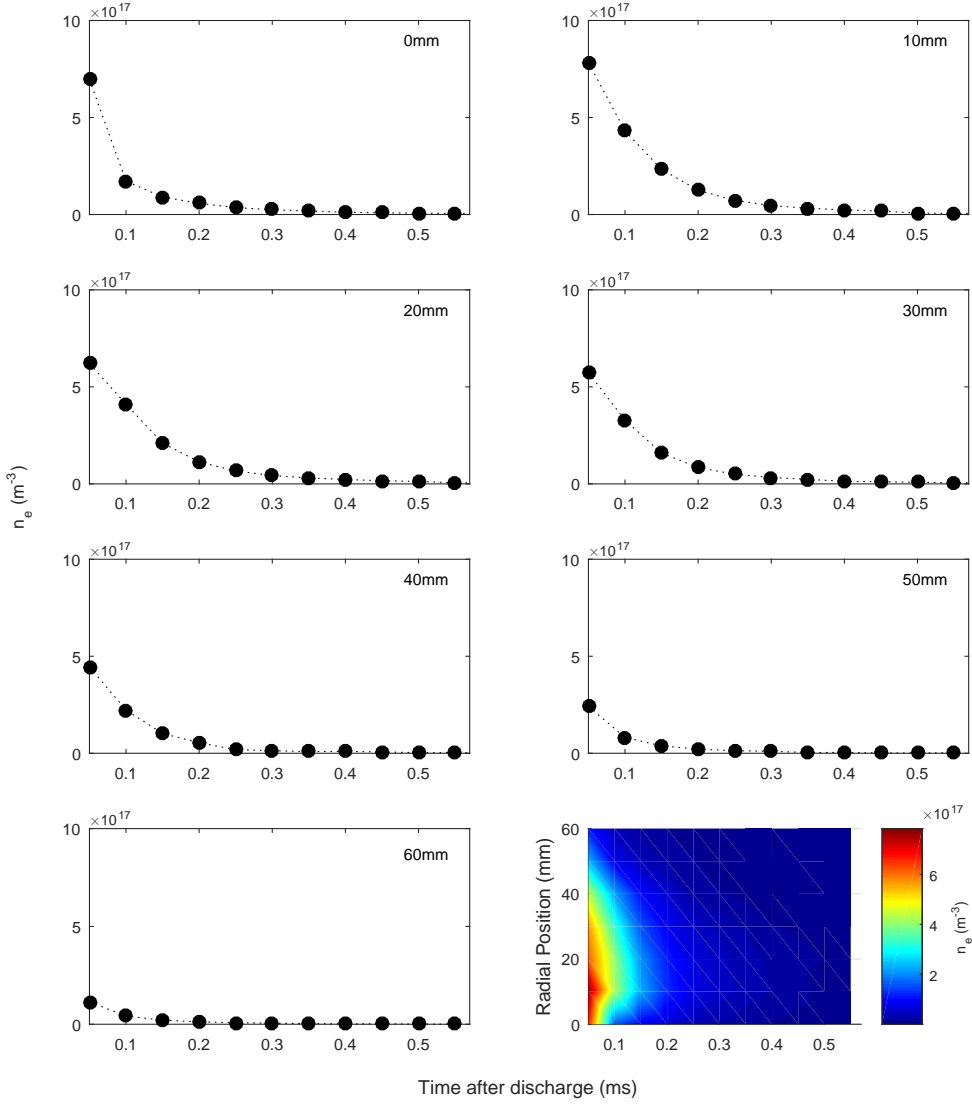


Figure 5.12: Electron density in the early afterglow of a 5ms 10kW plasma pulse with the standard operating conditions. Subplots show different radial positions, $r = 0\text{-}60\text{mm}$. A 3D plot shows the electron density as a function of time and radial position in the afterglow.

Following a 10kW plasma pulse, $n_e = 8 \times 10^{17} \text{ m}^{-3}$ in the earliest afterglow at $r = 10\text{mm}$, shown in Figure 5.12. This electron density at $r = 10\text{mm}$ is slightly higher than in the centre, but possibly too small to be significant and could be investigated further to see if there is a slight dip in n_e directly in the centre. The same radial decrease is observed for 10kW as for 5kW where n_e is lower the further from the

5.2. TIME RESOLVED RADIAL PROFILES

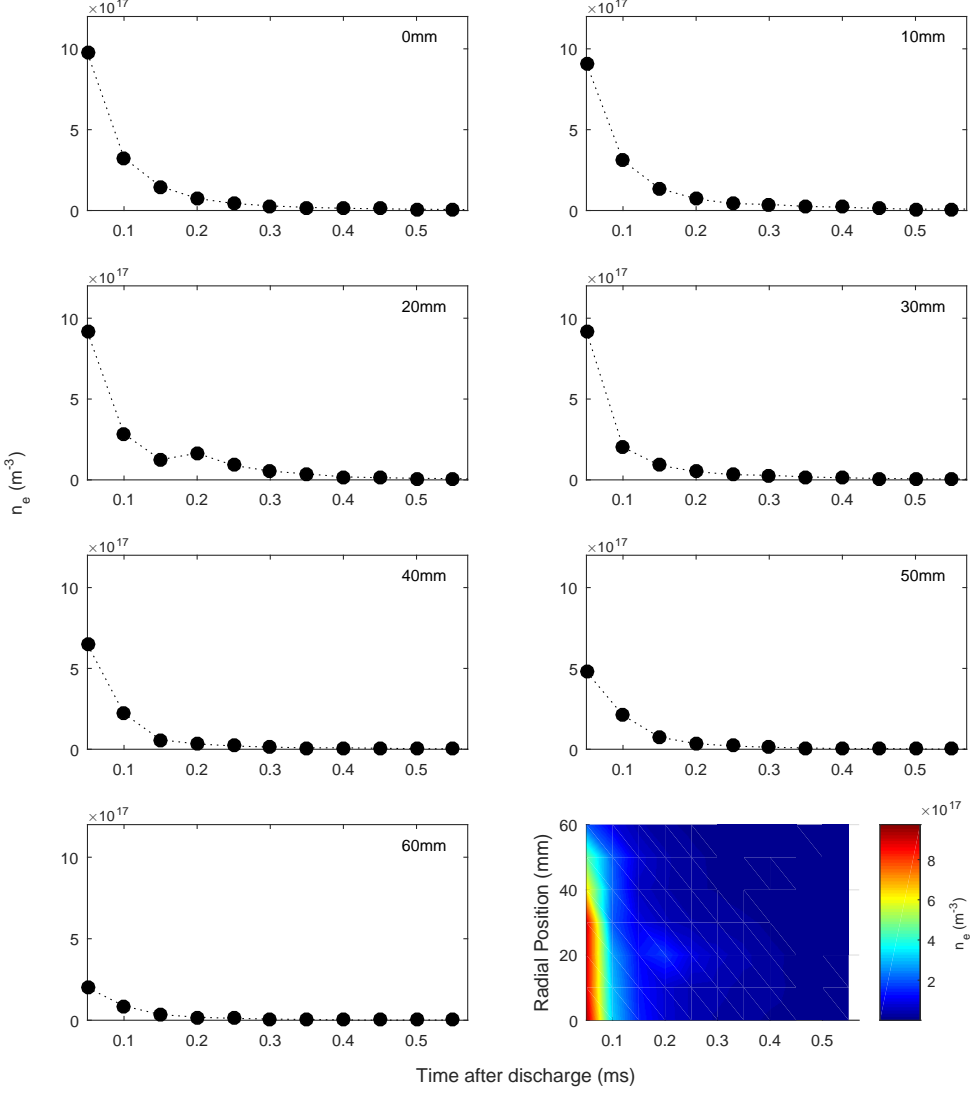


Figure 5.13: Electron density in the early afterglow of a 5ms 20kW plasma pulse with the standard operating conditions. Subplots show different radial positions, $r = 0\text{-}60\text{mm}$. A 3D plot shows the electron density as a function of time and radial position in the afterglow.

centre. At 60mm $n_e = 1 \times 10^{17} \text{ m}^{-3}$ initially, almost an order of magnitude lower than the centre. As the power is increased there is an observed greater density gradient of the plasma from the centre radially outwards consistent with previous work.[132]

The plasma density for 20kW applied RF power is shown in Figure 5.13 and shows the same behaviour observed for 5kW and 10kW, however a greater plasma density is achieved, $9 \times 10^{17} \text{ m}^{-3}$. This peak in plasma density is observed to be at the same level across the inner 30mm of the chamber. The first meaningful decrease in the initial plasma density in the radial component in the afterglow is at 40mm from the centre, which starts at $6.5 \times 10^{17} \text{ m}^{-3}$. These measurements highlight that the plasma density limit is being approached as the plasma is less confined towards the centre and the plasma density is rising further from the centre. This is creating a broader radial plasma profile, which will also contribute to further neutral depletion in the central region of the chamber.

5.2.2 Radial Atomic Hydrogen Density

The TALIF diagnostic was used to measure the radial change of the atomic hydrogen density to investigate if neutral depletion is creating a hollow profile in the density as observed by Aanesland in xenon.[121] The UV lens was translated on a linear platform to move the focus of the lens to different radial positions in the MAGPIE chamber. The detection system was also moved on a linear platform to maintain its focus on the excitation spot.

Figures 5.14-5.17 show the atomic hydrogen density evolution into the afterglow of a 5ms plasma pulse for applied RF powers of 1kW, 5kW, 10kW and 20kW respectively for four different radial positions, $r = 0, 10\text{mm}, 20\text{mm}$ and 30mm . The gas fill pressure is maintained at 10mTorr measured at the gas inlet. The magnetic fields are kept at the standard 50A:300A configuration.

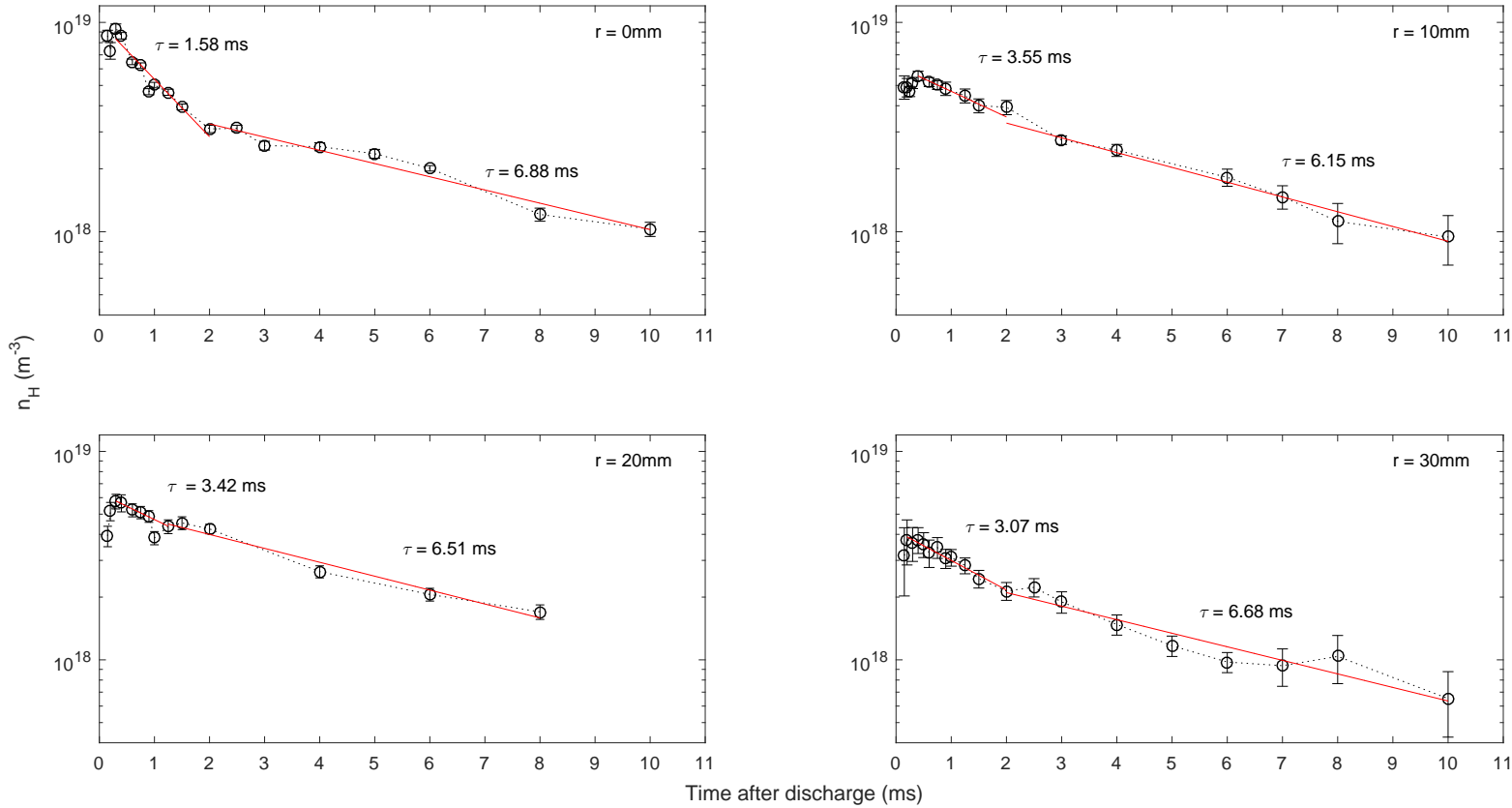


Figure 5.14: Atomic hydrogen density into the afterglow of a 1kW 5ms plasma discharge. Subfigures are at different radial positions in the target chamber $r = (0, 10, 20, 30)\text{mm}$.

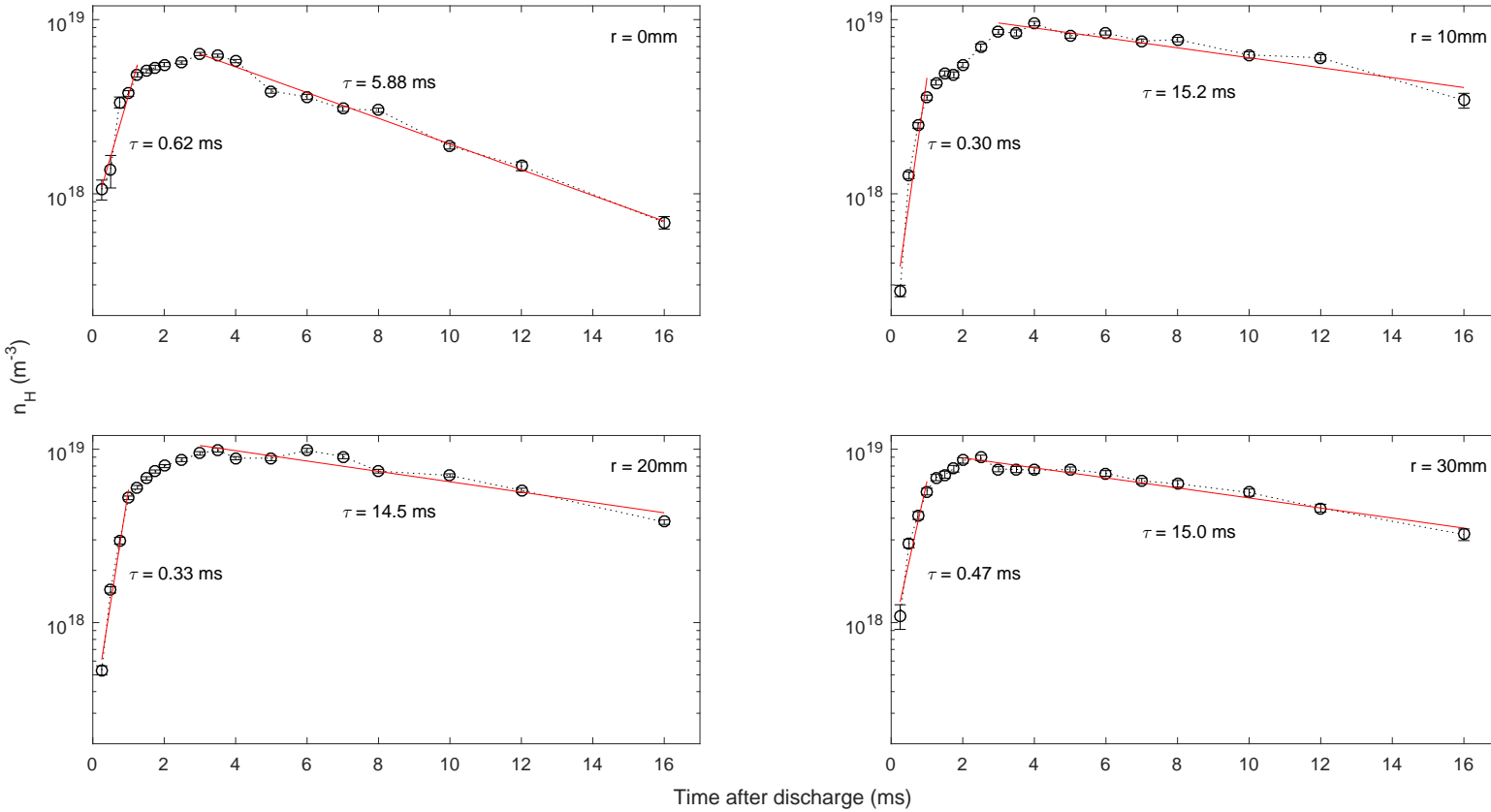


Figure 5.15: Atomic hydrogen density into the afterglow of a 5kW 5ms plasma discharge. Subfigures are at different radial positions in the target chamber $r = (0, 10, 20, 30)\text{mm}$.

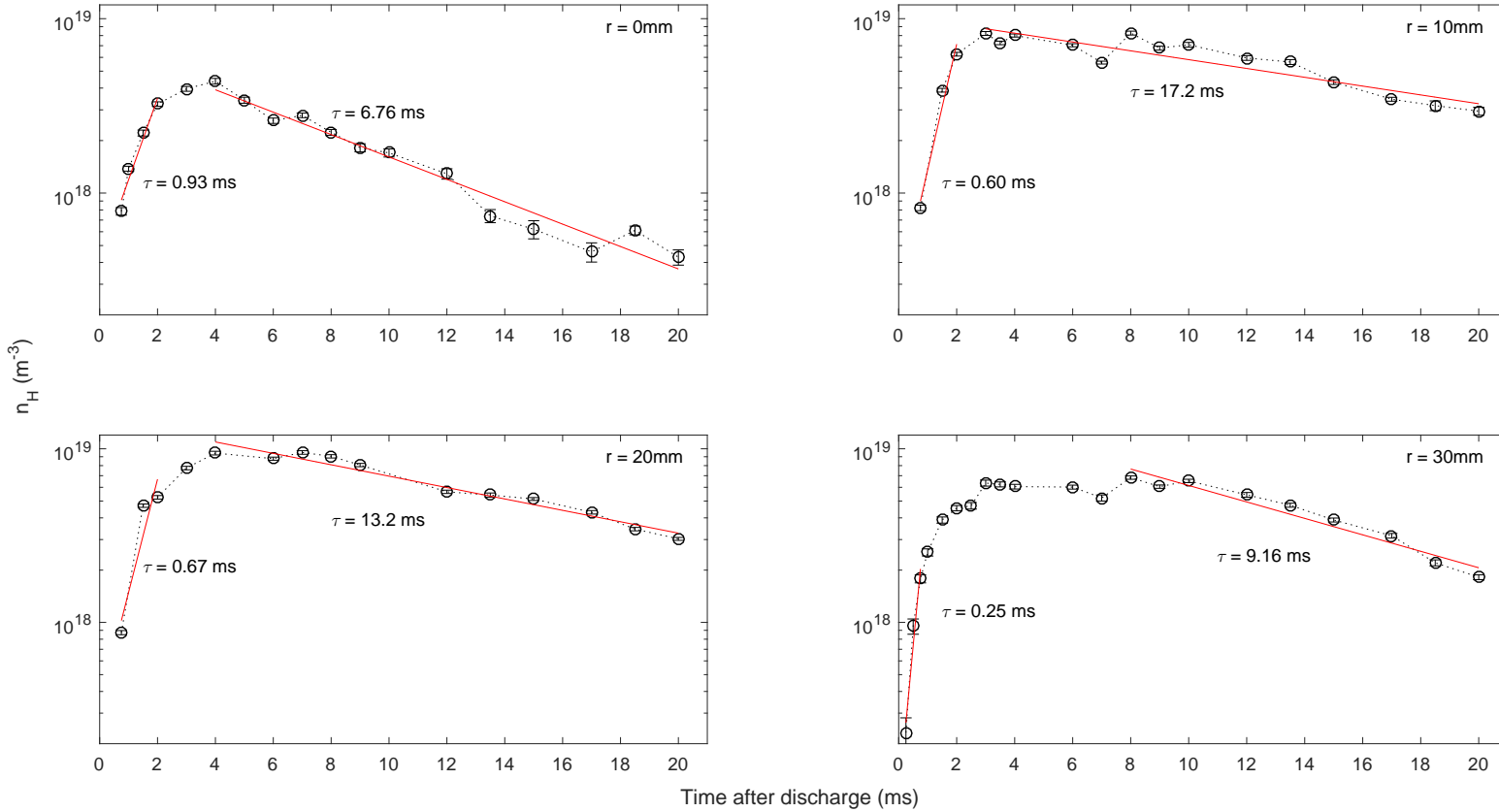


Figure 5.16: Atomic hydrogen density into the afterglow of a 10kW 5ms plasma discharge. Subfigures are at different radial positions in the target chamber $r = (0, 10, 20, 30)\text{mm}$.

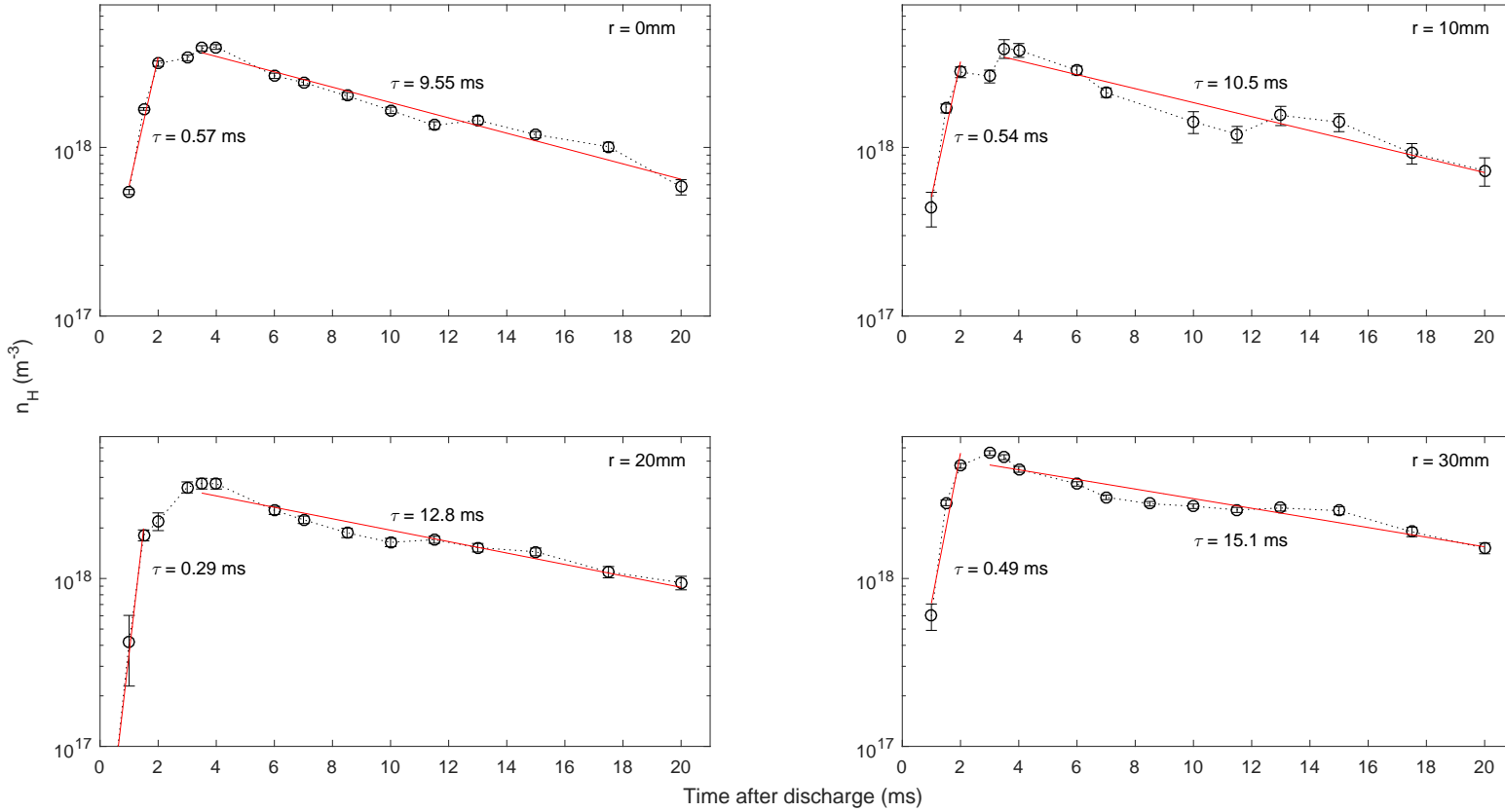


Figure 5.17: Atomic hydrogen density into the afterglow of a 20kW 5ms plasma discharge. Subfigures are at different radial positions in the target chamber $r = (0, 10, 20, 30)$ mm.

5.2. TIME RESOLVED RADIAL PROFILES

For 1kW applied RF power, it is observed that the two stage decay is consistent across all measured radial positions. The second decay rate is approximately the same for all measured radial positions $\tau_2 \approx 6\text{-}7\text{ms}$. This would suggest that it is surface losses at the walls that dictate the losses for atomic hydrogen in the later ($>2\text{ms}$) afterglow as described in the model previously. The first decay rate in the afterglow is noticeably different between the centre ($\tau_1 = 1.58\text{ms}$) and all other radial measurements ($\tau_1 \approx -3\text{ms}^{-1}$). While this may suggest that there could be a different process determining the decay rate between the centre and radially outwards, it might also be directly linked to the much higher atomic hydrogen density confined to the centre in the 1kW discharge, $1\times 10^{19}\text{m}^{-3}$ compared with $4\text{-}6\times 10^{18}\text{m}^{-3}$ maximum observed densities at further radial positions.

For the 5kW RF applied power shown in Figure 5.15, it is observed that atomic hydrogen density follows the same shape in the afterglow for all radial measurements. There is a fast increase in the H density over $\sim 1\text{ms}$, followed by a slower increase in density over the next 1-3ms. There is quite a large variation in the measured fast atomic hydrogen density increasing from 0.30ms to 0.62ms. However this fit includes only a small number of data points. This is likely creating large variation in values between the radial positions. The decay rate appears to be faster in the centre of the chamber with $\tau_1 = 5.88\text{ms}$ while the radial positions further out have a slower decay, $\tau_1 \approx 15\text{ms}$.

With 10kW applied RF power, the atomic hydrogen density is observed to initially increase at all the measured radial positions in the afterglow shown in Figure 5.16. The measured rate of increase in the early afterglow ranges from 0.93ms at the centre to 0.25ms at $r=30\text{mm}$. This fast increase is followed by a slower increase in atomic hydrogen density before decay into the afterglow. The decay rates are measured to range between 6.7ms to 17.2ms.

The same trend is observed at 20kW with a fast increase in H density initially followed by a slower increase. After the maximum density is reached at $\sim 3\text{ms}$ into the afterglow there is a consistent decrease into the remaining afterglow. The evolution of atomic hydrogen density into the afterglow at different radial positions is shown in Figure 5.17. The fast density increase is observed to have a rate varying

5.2. TIME RESOLVED RADIAL PROFILES

from 0.29ms to 0.57ms, which can also be attributed to only a small number of measurements in the early afterglow region. The decay in the later afterglow ($>3\text{ms}$) has a fairly consistent decay rate from 9 to 15ms, increasing in decay rate is observed for radial positions further from the centre. This may be due to the hydrogen leaving the centre and diffusing towards the walls, producing a slower decay further from the centre. Repeat experiments are required to determine if this increase is real or just within the error of the measurements.

As discussed in Section 5.1.4, the slower decay rate for 1kW applied RF and the single decay rate at higher powers can be attributed to atomic hydrogen diffusing to the target chamber walls where it undergoes recombination at the surface. The loss mechanism at the walls is dominant at all radial positions.

The top image in Figure 5.18 presents atomic density as both a function of time into the afterglow (along x-axis) and the radial position (along y-axis) for a 5ms plasma discharge with 1kW applied RF power. Black lines through the figure are set times in the afterglow corresponding to the densities presented in the bottom figure, which show the evolution of the density for a set of radial positions at different times into the afterglow. It is seen that very early in the afterglow ($150\mu\text{s}, 0.15\text{ms}$) there is a sharp radial profile with a higher atomic hydrogen density at the centre and decreasing radially. At $600\mu\text{s}$ (0.6ms) into the afterglow, the radial profile is becoming more uniform. The H density at the centre is still slightly higher than the next radial position at 10mm, while there is a bigger drop in density between 20mm and 30mm from the centre. Further into the afterglow, the density of hydrogen atoms becomes more radially uniform and continues to decrease with time into the afterglow, however there is still a lower density measured at $r=30\text{mm}$.

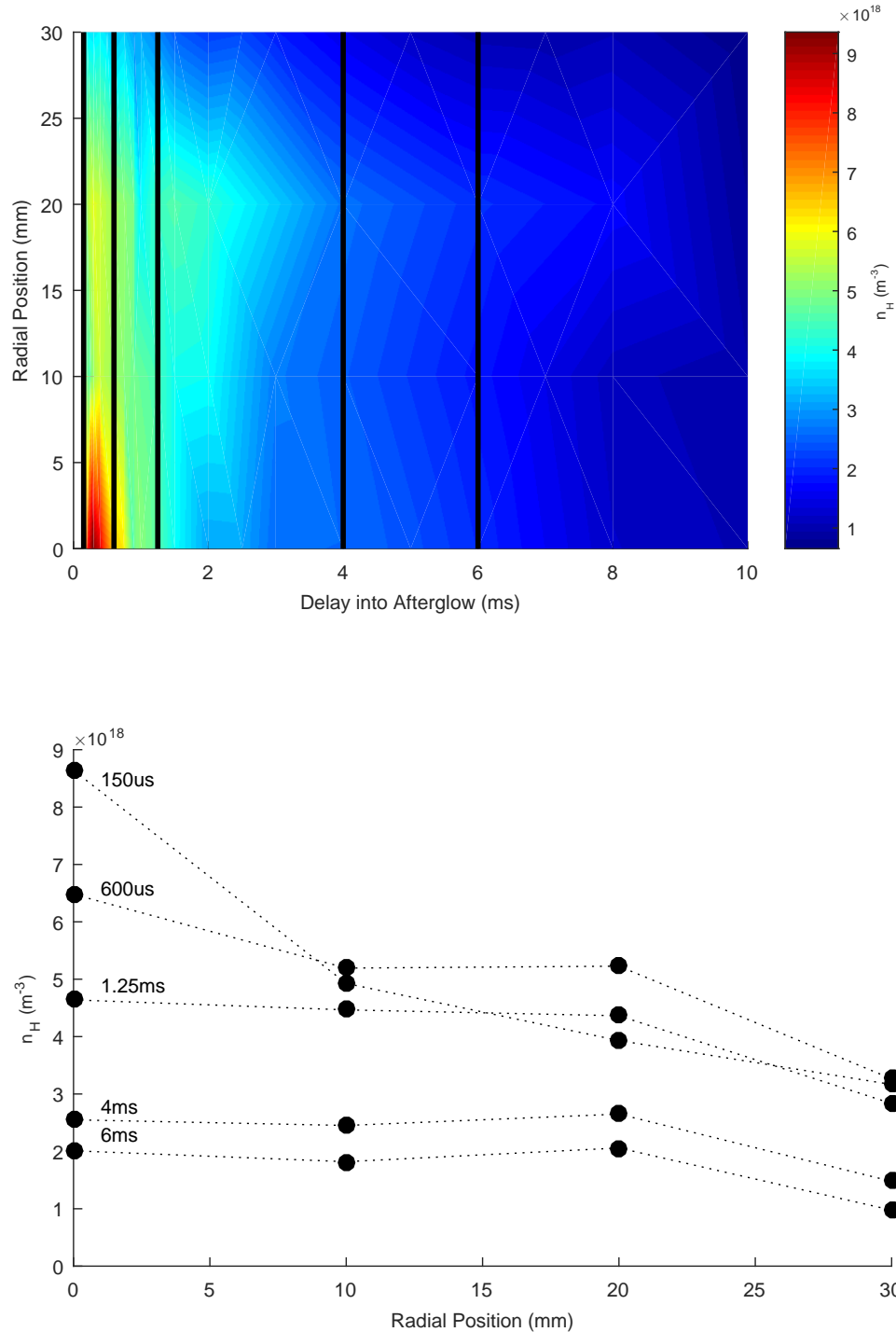


Figure 5.18: (top) Evolution of atomic hydrogen density (n_H) up to 10ms into the afterglow of the 5ms 1kW plasma pulse. (bottom) Radial atomic hydrogen densities at different times in the afterglow. Black lines on the 3D plot correspond to the shown radial data.

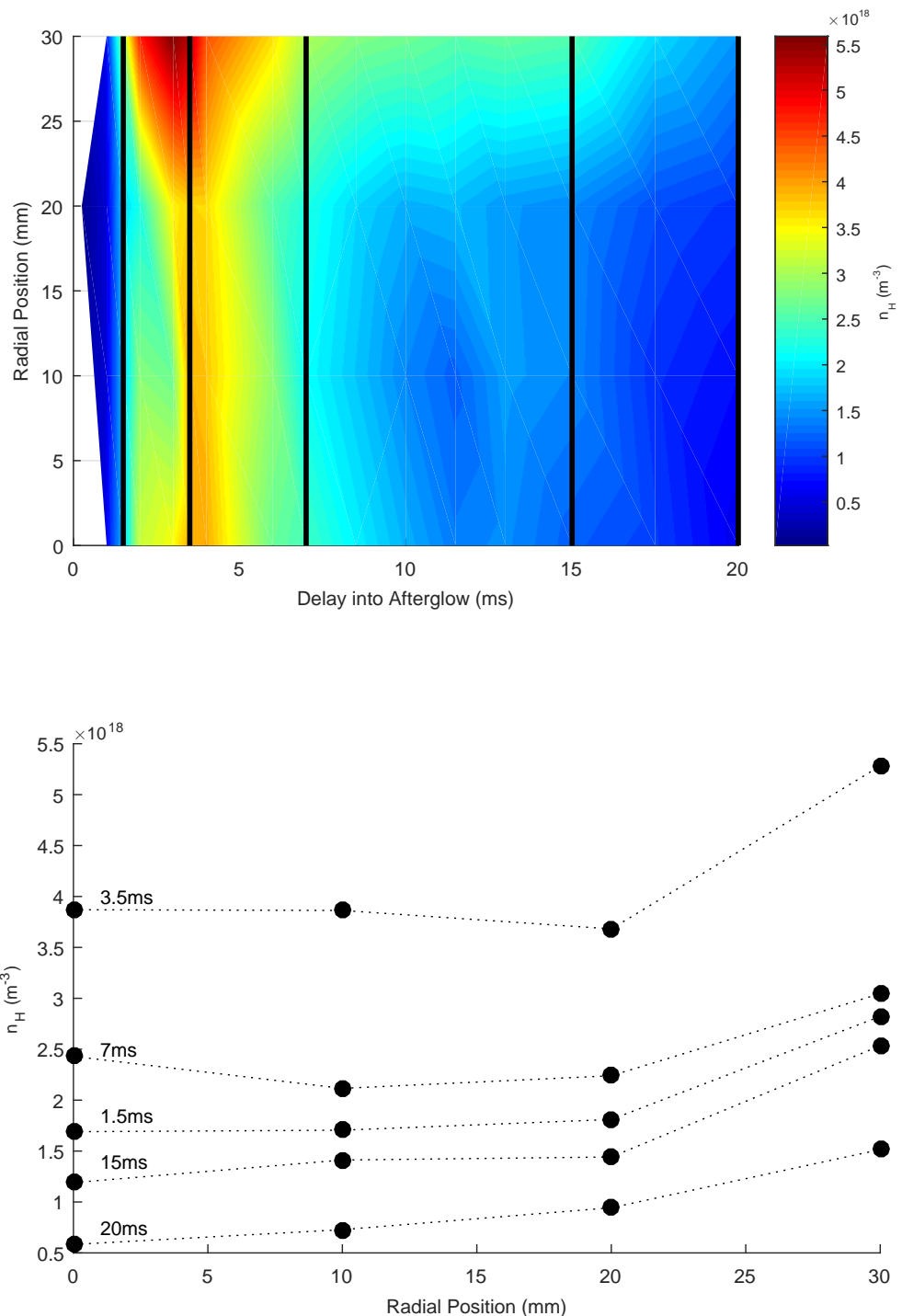


Figure 5.19: (top) Evolution of atomic hydrogen density (n_H) up to 20ms into the afterglow of the 5ms 20kW plasma pulse. (bottom) Radial atomic hydrogen densities at different times in the afterglow. Black lines on the 3D plot correspond to the shown radial data.

A similar figure is presented for the evolution of atomic hydrogen density into the afterglow for different radial positions after a 5ms 20kW plasma discharge in Figure 5.19. 3D plots for the 5kW and 10kW measurements are not presented as the same behaviour is observed in the 20kW and applies to those cases as well. The atomic hydrogen radial profiles are fairly constant across 0-20mm with an observed increase in the density at 30mm. The afterglow initially starts low in atomic hydrogen density and rapidly increases, peaking at around 3ms for all radial positions before decreasing further into the afterglow. The radial position at 30mm maintains a slightly higher density through the whole measured afterglow (<20ms).

The radial variation of atomic hydrogen density support the measurements earlier in this chapter and in Chapter 4, that neutral depletion is occurring at higher applied RF powers. The depletion of the atomic hydrogen from the core of the plasma discharge appears to be attributed to the high plasma pressure pushing the neutrals out of the core through collisions. Depletion due to gas heating could also be a large contributing factor, however the radial atomic hydrogen temperature must be considered to get an indication of the degree that gas heating has on the depletion of atomic hydrogen.

5.2.3 Radial Atomic Hydrogen Temperature Profiles

The atomic hydrogen temperature (T_H) is calculated from the Doppler broadening of the TALIF absorption as discussed in Chapter 3. The atomic hydrogen temperature (T_H) at 1ms into the afterglow of the 5ms plasma pulse for a set of input powers are shown in Figure 5.20.

It is observed that the gas temperature remains constant radially outwards from the centre to 30mm, the limit of the radial measurements with the current optical set-up. At 1kW, $T_H = 0.033\text{-}0.036\text{eV}$ for all measured radial positions. The temperature is observed to increase to between 0.041-0.048eV for 5kW, while still maintaining a fairly constant radial temperature. Further increasing the applied RF power leads to hotter atomic hydrogen. At 20kW the highest neutral temperatures are recorded at 1ms into the afterglow of up to 0.07eV.

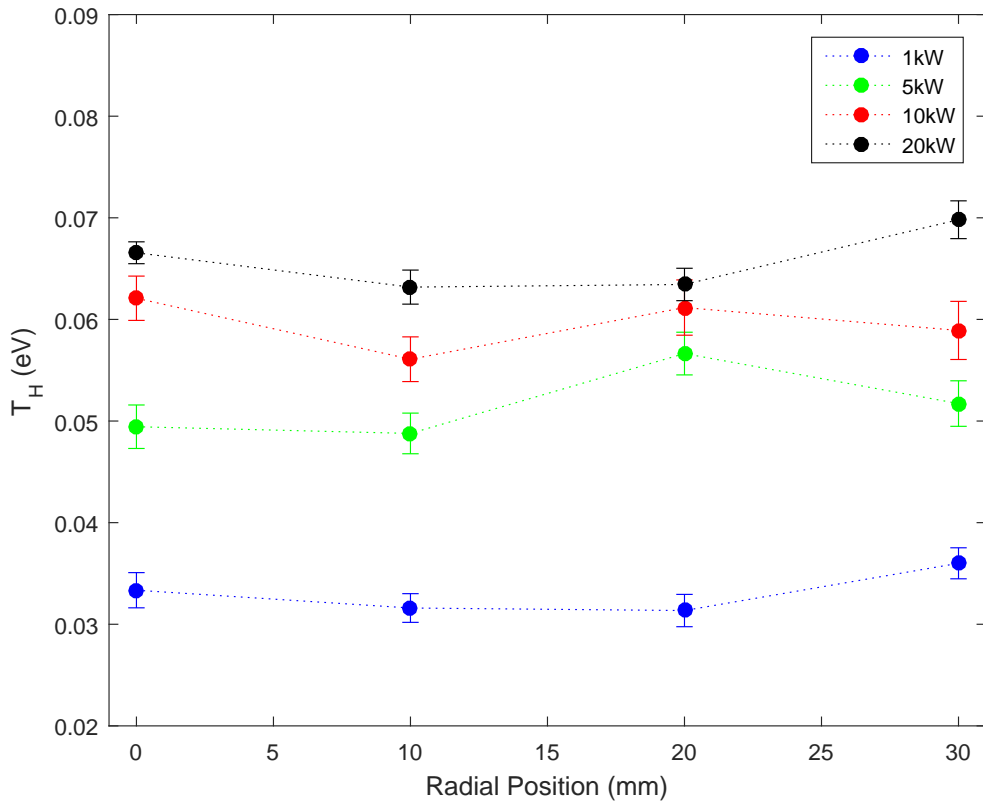


Figure 5.20: Temperature of a function of radial position for each power 1, 5, 10, 20kW. The centre of the target chamber is at $r=0$ and the chamber wall is at $r=80\text{mm}$.

This relatively flat temperature profile means that gas heating is an unlikely mechanism for explaining the observed neutral depletion, as a cooler neutral temperature is required further from the core (to set up a temperature gradient). Measurements at greater radial positions are required to fully determine that there is not a temperature gradient closer to the wall. However as the temperature profile is relatively flat, gas heating has negligible effect across the inner 30mm of the plasma.

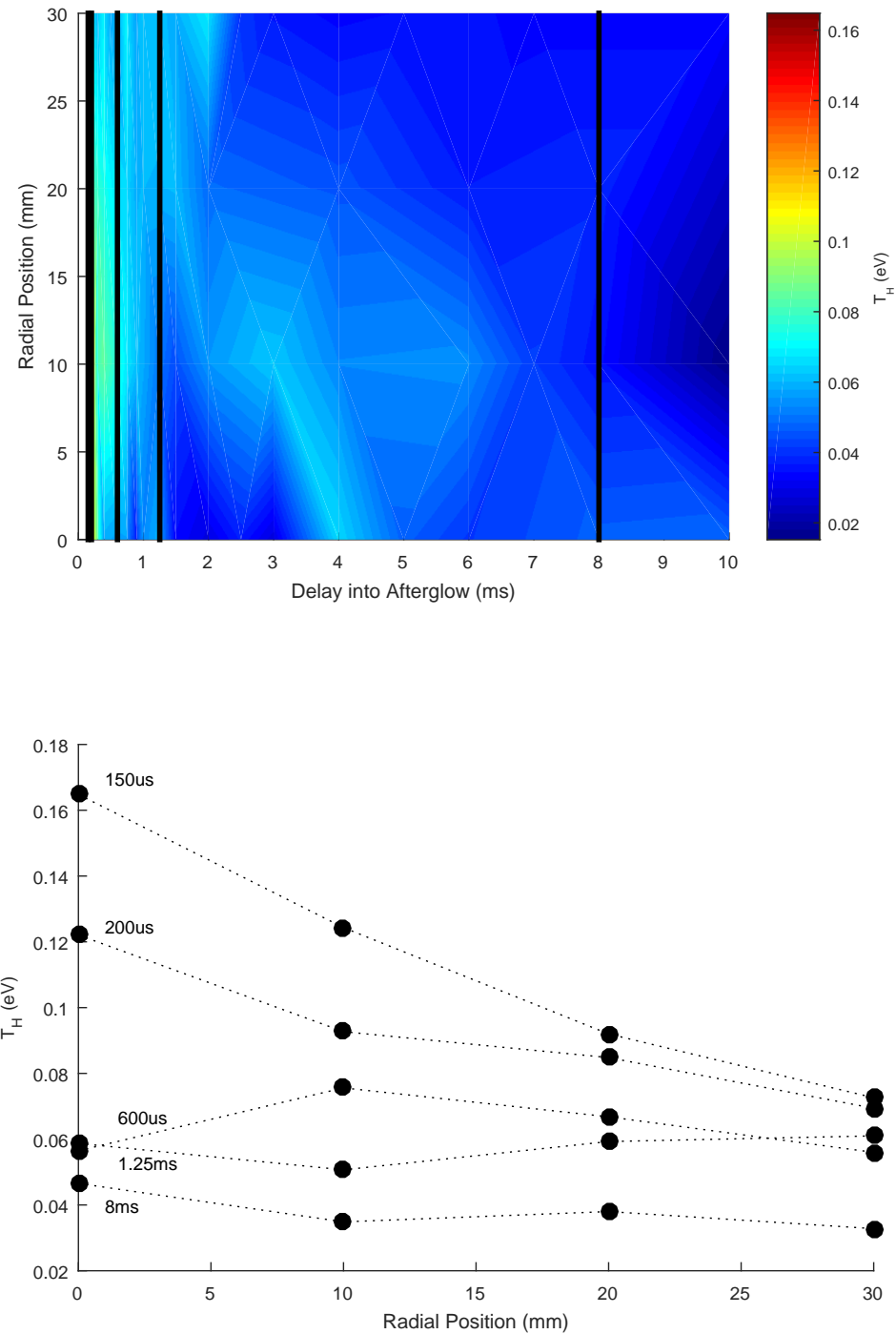


Figure 5.21: (top) Evolution of atomic hydrogen temperature (T_H) up to 10ms into the afterglow of the 5ms 1kW plasma pulse. (bottom) Radial atomic hydrogen temperatures at different times in the afterglow. Black lines on the 3D plot correspond to the shown radial data.

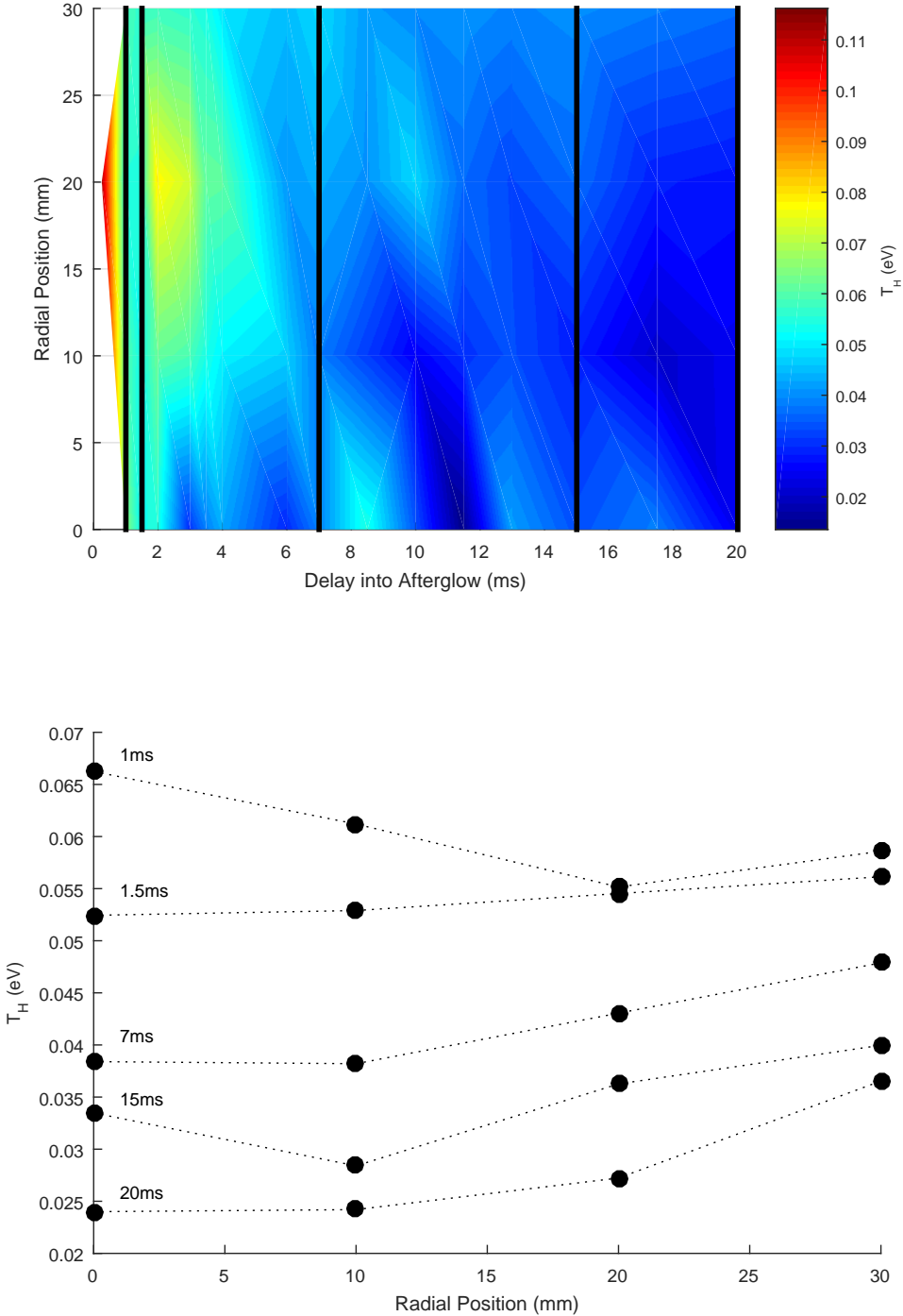


Figure 5.22: (top) Evolution of atomic hydrogen temperature (T_H) up to 20ms into the afterglow of the 5ms 20kW plasma pulse. (bottom) Radial atomic hydrogen temperatures at different times in the afterglow. Black lines on the 3D plot correspond to the shown radial data.

A plot of atomic hydrogen temperature into the afterglow of the 5ms pulse with 1kW applied RF power for radial positions 0-30mm is shown in Figure 5.21. It is observed that for 1kW applied RF power the hottest hydrogen atoms are found in the earlier afterglow and in the centre of the plasma discharge. This is comparable, if slightly warmer, to the atomic hydrogen temperature measurements by Samuell and Corr in the MAGPIE device using optical emission spectroscopy.[173] For the first $600\mu\text{s}$ (0.6ms) in the plasma afterglow there is a radial temperature gradient that is hottest in the centre of the chamber. After $600\mu\text{s}$ (0.6ms), the temperature is observed to become radially uniform and slowly cool further into the plasma afterglow.

The evolution of atomic hydrogen temperature in the afterglow of a 5ms pulse 20kW applied RF power for different radial positions is shown in Figure 5.22. Similarly to the 1kW measurements, atomic hydrogen temperature is hottest in the earliest afterglow, directly after the pulse and cools into the afterglow. Unlike for 1kW, which shows a temperature gradient, the neutral hydrogen atoms display a fairly constant radial temperature profile through most of the afterglow while appearing possibly cooler in the centre. Only the 20kW 3D plot is presented here as the 5kW and 10kW cases show similar behaviour to the 20kW atomic hydrogen temperatures.

5.3 Summary of Neutral Behaviour and Depletion

Spatially resolved atomic hydrogen densities and temperature profiles in the afterglow of a pulsed plasma have been measured using the newly established two-photon absorbed laser induced fluorescence diagnostic. It is observed for the first time that neutral depletion of atomic hydrogen is occurring in the core of the plasma in the MAGPIE device at powers greater than 4kW. As the power is increased above 4kW and the plasma switches into a helicon mode, the atomic hydrogen density in the centre is observed to decrease with increasing power, while at the edge it slightly

5.3. SUMMARY OF NEUTRAL BEHAVIOUR AND DEPLETION

increases. The pressure from the magnetically confined plasma push the neutrals out from the core leading to the neutral depletion of atomic hydrogen in the core. This depletion of the neutral species may be further enhanced by gas heating.

Time resolved measurements in the afterglow of lower power plasma (<4kW) show a two stage decay rate of atomic hydrogen density. A fast decay rate initially followed by a slower rate of decay. The slower decay rate can be explained by losses due to recombination of atomic hydrogen at the chamber walls.

The afterglow of higher power (>5kW) plasmas show the neutral density increasing into the early afterglow for the first few milliseconds to replenish the neutral depletion. After this peak occurs, the density is observed to decay into the remaining afterglow. This decay at the higher powers can also be explained as being due to atomic hydrogen recombination at the walls of the target chamber.

Radial measurements of atomic hydrogen density show that for the lower power measurements of 1kW, the density is highest at the radial centre of the chamber. It becomes more uniform further into the afterglow. At higher power measurements, the density of hydrogen atoms is fairly uniform across 0-20mm and higher than 30mm, suggesting that there is higher neutral hydrogen densities towards the chamber walls.

Investigation of the radial atomic temperature showed a uniform temperature gradient from the centre to 30mm. As the temperature is constant across the measured region, gas heating cannot be the sole cause of neutral depletion. This supports that the high plasma pressure is indeed playing a significant role in the depletion of neutral atomic hydrogen in the core of the plasma discharge.

Simulations of the hydrogen discharge using the 2D-axisymmetric model by Santoso[132] show a depletion of both the molecular and atomic hydrogen at $z=150\text{mm}$ in the target chamber. The model predicts that atomic hydrogen density will be higher than 10^{18}m^{-3} in the centre of the discharge at steady state conditions for 20kW applied RF power and increase towards the chamber walls. The model does not show depletion to the extent that has been measured in this work where during the plasma discharge and in the early afterglow atomic hydrogen was

5.3. SUMMARY OF NEUTRAL BEHAVIOUR AND DEPLETION

unable to be detected. While atomic hydrogen may not be completely depleted, it was undetectable or below detectable levels (10^{17}m^{-3}). It is important to note in work by Carmen [177] with mixed copper/neon plasma, he showed that the Cu had higher levels of depletion due to ionisation than the neon atoms. The difference in degrees of depletion may be due to their larger mass effecting their mean free paths of ionisation. Molecular hydrogen may display a different depletion profile to atomic hydrogen.

Chapter 6

Conclusion

This thesis presents research into the dynamics of atomic hydrogen in high power linear helicon plasma devices. This research has involved establishing a new two-photon absorbed laser-induced fluorescence (TALIF) diagnostic to investigate atomic hydrogen dynamics in the plasma. Atomic hydrogen density and temperature have been temporally and radially determined using the newly established TALIF diagnostic. A summary of these achievements is discussed below and future investigations and extensions to this study are suggested.

6.1 Two-Photon Absorbed Laser-Induced Fluorescence Diagnostic

A two-photon absorbed laser-induced fluorescence diagnostic has been established as part of this research. The diagnostic set-up was covered in detail, including discussion of the laser, the optics and detection system, and the acquisition and control system. A detailed description of the developed LabviewTM program that controlled the timing and data acquisition was included as part of the discussion.

The two-photon absorbed laser-induced fluorescence technique was discussed in detail, including the excitation schemes and the noble gas calibration method for

atomic hydrogen. The noble gas calibration was conducted using krypton, which has a ground state two-photon excitation scheme similar to the 205nm excitation used in this research for atomic hydrogen. The atomic hydrogen density can then be determined from the total fluorescence signal detected across a wavelength scan.

Particular attention was given to the broadening mechanisms associated with the technique to correctly determine the Doppler broadening of the fluorescence wavelength scan and hence accurately determine the temperature of the neutral atomic species. It was determined that the major broadening mechanisms that required consideration are Doppler broadening and laser line width. Pressure, Stark and Zeeman broadening effects were shown to be negligible under the operating conditions of the MAGPIE helicon plasma device. Broadening due to saturation with the laser was avoided by maintaining the laser pulse energy below the determined saturation levels for atomic hydrogen and krypton. The laser linewidth broadening due to the laser was determined to be 1.11pm using a mixed hydrogen:deuterium plasma. After accounting for other broadening contributions, the Doppler broadening of the absorption peak is used to determine the atomic hydrogen temperature.

6.2 Atomic Hydrogen Dynamics

Atomic hydrogen density and temperature has been investigated as a function of applied RF power. It is observed that the atomic hydrogen density in the centre of the MAGPIE chamber increases with increasing applied RF power up to 4kW. Above 4kW, atomic hydrogen density is observed to decrease with increasing power till approximately 15kW. Further increasing to power up to 20kW did not yield additional decrease in the density. At 20kW applied RF power it is observed that increasing the pulse length (plasma on) also led to a decrease in atomic hydrogen density. In contrast, the temperature of atomic hydrogen is observed to steadily increase with applied RF power. The decrease in neutral density at the centre of the chamber is consistent with neutral depletion occurring at high discharge powers ($>4\text{kW}$).

The depletion of neutral species is determined to be due mainly to the high plasma pressure in the plasma core. The high plasma pressure exerts a drag force on neutrals pushing them out of the centre towards the chamber edge leading to the depleted region in the centre. Depletion due to gas heating is shown to also have an effect on the depletion of neutral species compared to if the neutrals were at room temperature, but is unable to fully account for the depletion observed. Depletion due to ionisation is also investigated, however it is found that the mean free path of ionisation for atomic hydrogen was larger than the chamber diameter and also could not account for the large depletion observed.

Temporal measurements of atomic hydrogen density in the plasma afterglow showed that at lower powers (1kW) there is a two stage decay in the afterglow. It could be seen that there is a faster decay initially, followed by a second slower decay that can be attributed to recombination of atomic hydrogen atoms at the chamber walls. At higher discharge powers ($>5\text{kW}$), atomic hydrogen density is observed to initially increase over the first $\sim 3\text{ms}$ in the afterglow before plateauing and decreasing into the extended afterglow. The decay observed with the higher power discharges is also able to be explained due to recombination at the chamber walls.

The loss mechanism of atomic hydrogen is investigated and it was found that the second decay rate for the 1kW discharge could be described by diffusion towards and recombination at the target chamber walls. It is found that the two rate decay is unable to be explained by fast cooling of the atomic hydrogen and that there are two different mechanisms causing the decay of atomic hydrogen in the afterglow. Recombination at the walls is found to be the dominate mechanism for atomic hydrogen loss mechanism in the afterglow of the higher power (5-20kW) plasma discharges.

Radial measurements of atomic hydrogen density show that for the 1kW discharge atomic hydrogen is concentrated in the centre of the chamber and decreases towards the chamber walls. Increasing the applied RF power created a more uniform radial atomic hydrogen density, however at 20kW there is a slightly higher density at 30mm compared to 0-20mm. The two-rate decay in the afterglow is observed

at all radial positions at 1kW applied RF power. In comparison, at higher powers (5-20kW) there is an initial increase in atomic hydrogen density after the plasma is switched off for all measured radial positions 0-30mm. This is followed in all cases by a constant rate decrease in atomic hydrogen density.

Understanding of neutral depletion and the conditions that lead to its occurrence are of great importance to the design of new high density plasma devices, especially linear type devices such as with a helicon antenna. This work has shown that neutral depletion plays a role in the upper densities that can be achieved in these helicon type plasma sources. This has consequences for applications of the helicon sources, such neutral beam injection systems, negative ion production systems and wakefield accelerators. In turn this will effect the design of smaller laboratory plasma devices for studying fusion related plasma studies. For example, if the plasma density is limited then helicon sources may not easily be able to reach the ion fluxes that will be expected in ITER.

6.3 Future Work

Further work can be conducted on the foundation of this research is summarised and briefly discussed in this section.

- A recommended extension to the two-photon absorbed laser-induced fluorescence diagnostic is the addition of a method to accurately measure the laser wavelength and linewidth for each individual pulse. For the measurements in this thesis the laser wavelength is determined by the motor position of the grating in the dye laser and the average laser linewidth is determined by its broadening contribution on deuterium compared to hydrogen (as discussed in Chapter 3). A wavemeter or iodine absorption cell as used in [145] are upgrades that can measure the wavelength for each pulse. A homodyne-interferometer type set-up would be capable of determining the laser linewidth.[191, 192] These upgrades would allow the broadening of the scans to be more accurately determined and provide a better resolution for the atomic temperature.

6.3. FUTURE WORK

The velocity of the species can also be determined by measuring the shift in the wavelength.

- There is a large parameter space that can be investigated on MAGPIE to determine the effects on the atomic hydrogen dynamics and the depletion in the centre of the chamber. Axial measurements in MAGPIE would provide additional information on the dynamics of atomic hydrogen and neutral depletion, such as whether the neutrals are pushed out radially or axially in the chamber. The laser would need to be focused into the target chamber from the end of the MAGPIE device (compared to side on in this work) to make axial measurements. The detection system would require a new design to allow it to fit under the magnetic coils, which could be achieved with a mirror set-up or with optical fibres.
- An important aspect to investigate is the atomic hydrogen behaviour during the plasma discharge itself. Improvements to the detection system to detect densities below 10^{17}m^{-3} would help to determine the degree of depletion. Other methods such as tunable diode laser absorption spectroscopy (TDLAS) would allow line-averaged atomic hydrogen densities and temperatures to be determined.[193]
- The effect of the background fill pressure and the flow rates was not investigated as part of this research. Increasing the pressure will provide a higher molecular hydrogen density that can potentially reduce the depletion of the neutral species. While 10mTorr is close to the upper operating pressure limit in MAGPIE, the pumping rate can be reduced by the butterfly valve (discussed in Chapter 2), which will increase the density along the chamber.
- The magnetic field provides another parameter that can be controlled to investigate the effect on the neutral dynamics and depletion. Measurements of the pressure at the chamber wall presented in this thesis showed a decrease in pressure with increasing magnetic field strength. This should be further investigated to determine the mechanisms occurring under these conditions. A stronger mirror field in MAGPIE provides greater confinement of the plasma towards the centre of the chamber. It has been suggested that the increased

6.3. FUTURE WORK

field strength increases the pumping rate and creates lower densities at the chamber walls[124], however this requires further investigation.

- Measurements of molecular hydrogen will provide additional information of the behaviour of neutral species in the plasma, including density and temperature both during the plasma discharge and afterglow. It will allow actual dissociation fractions to be determined. An important question is whether the molecular hydrogen behaves similarly to atomic hydrogen. Molecular hydrogen may display different depletion profiles to atomic hydrogen, which will lead to spatially dependent reaction rates. Combined experimental measurements of both neutral atomic and molecular hydrogen in the plasma, along with other plasma species will provide empirical data for comparison of plasma models.
- As demonstrated in this thesis, hydrogen and deuterium are individually resolvable. As deuterium has twice the mass of the hydrogen atom it can lead to differences in the behaviour. This increase in mass may be enough that the depletion due to ionisation may become more dominate in the plasma discharge. This will be due to the decrease in the mean free path of ionisation for deuterium compared to hydrogen. The TALIF diagnostic can measure deuterium atoms in exactly the same way as hydrogen in this thesis.
- Krypton and xenon plasmas are also possible candidates for investigation using the newly established TALIF diagnostic. Krypton has a two-photon excitation with $2\times 204.13\text{nm}$ of the $4p_1^6S^0 \rightarrow 5p'[3/2]_2$ as discussed in Chapter 3, which fluoresces at 826.30nm . Therefore the neutral krypton can be measured using this TALIF system with only the optical filters and the wavelength sweep range requiring adjusting between measuring hydrogen and krypton. Similarly xenon has a two-photon excitation scheme within the spectral output of the dye laser of $2\times 209.25\text{nm}$. This excites the $5p_0^6 \rightarrow 4p^57f_2$ state and fluoresces at 656.00nm .[194] Heavier atoms are observed to display neutral depletion due to ionisation more readily due to their significantly shorter mean free paths of ionisation.[163] Due to krypton and xenon naturally occurring in the atomic state, it is simpler to determine the degree of depletion.

6.3. FUTURE WORK

- Nitrogen species in plasma is of particular interest due to the potential of using it as a neutral blanket for radiative cooling in the divertor region of tokamak fusion devices. Therefore the physics and chemistry of nitrogen species in a hydrogen plasma is going to be important to understand. Ammonia and other NH compounds can be created in the mixed H₂/N₂ plasma, ammonia being especially important as it cannot be processed by the cryo-pumps in ITER. Outside of fusion research ammonia is of great importance to agriculture, and the production of ammonia in plasma could have widespread benefits. Initial research has been undertaken as part of this Ph.D. but was not included as it was outside of the focus of this thesis, but is briefly mentioned here. Aspects of this work have been presented in [24]. Mixed hydrogen and nitrogen plasmas of varying percentages of composition were investigated using optical emission spectroscopy. Shown in Figure 6.1 is the spectra from 330-360nm of mixed H₂/N₂ plasmas. The top figure shows the emission output for varying percentage of the nitrogen in the gas. The bottom figure shows a spectra for a composition 20%H₂ and 80%N₂. The emission at 335.5nm is indicative of NH species and demonstrates that they are formed in the mixed plasma. This topic requires further work which can be supplemented through using the TALIF system as atomic nitrogen has a two-photon absorption of 2x206.7nm from the $2p^3 \ ^4S_{3/2} \rightarrow 3p4S_{3/2}$ fluoresces over 742-747nm. This can be excited using the current TALIF set-up and calibrated using krypton, as the TALIF system is able to investigate both hydrogen and nitrogen species in the mixed plasmas.
- Retention of hydrogen isotopes (especially tritium) in the plasma facing components is of concern. Firstly, trapped tritium affects the tritium breeding and secondly, from a safety viewpoint, tritium is a concern due to its radioactivity.[195] Due to its use in ITER, tungsten is a material of interest. The MAGPIE device has the ability to place materials into the target chamber. The TALIF diagnostic can be used to investigate the changes in behaviour of atomic hydrogen due the material, such as in the sheath region. If retained species are released from the material after the plasma discharge, then TALIF can be employed to measure the released species.

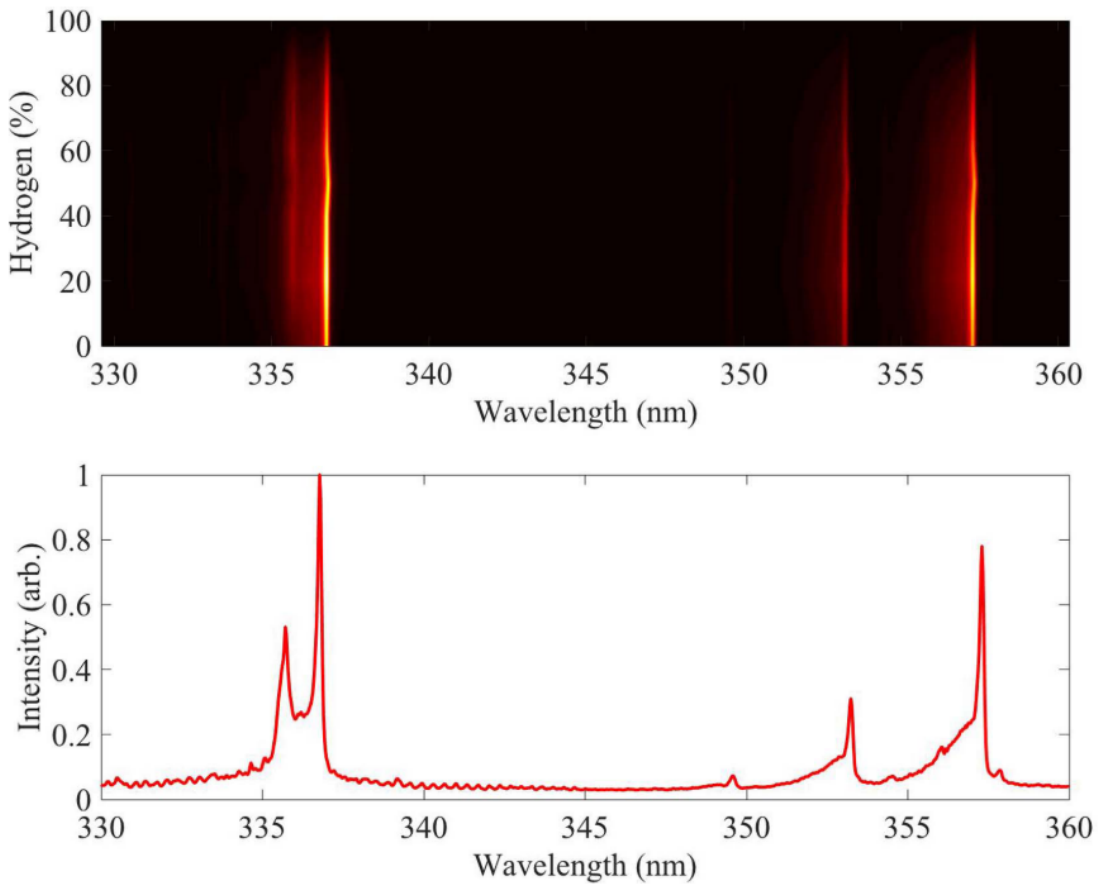


Figure 6.1: (top) Intensity plot of the optical emission spectra from 330-360nm for varying compositions of H_2/N_2 plasmas. (bottom) Individual spectra for the 20% H_2 and 80% N_2 composition.[24]

In conclusion, a newly established two-photon absorbed laser induced fluorescence diagnostic has been used to determine neutral atomic hydrogen density and temperature in the afterglow of high power (<20kW) plasma discharge in the MAGPIE device. The temporal and radial profiles have been presented. The first measurements of neutral depletion in a hydrogen have been observed and it has been concluded that depletion is due to the high plasma pressure with contributions from gas heating.

Appendix A

TALIF Dye Recipe

Reagents:

- High Purity Ethanol
- Rhodamine 610 Chloride (Rhodamine B)
- Rhodamine 640 Perchlorate (Rhodamine 101)

Dissolve 0.136g of rhodamine 610 chloride and 0.032g rhodamine 640 perchlorate in 800mL of ethanol. Mix with a magnetic stirrer until fully dissolved (~40mins). The resulting stock solution concentration is 0.17g/L RH610 and 0.04g/L RH640. Pour 600mL of stock solution into the resonator pump reservoir. Dilute the remaining 200mL stock solution with 1400mL of ethanol and pour in the amplifier pump container reservoir.

Bibliography

- [1] S. Shinohara, “Helicon high-density plasma sources: physics and applications,” *Advances in Physics: X*, vol. 3, no. 1, pp. 1–36, 2018.
- [2] D. G. Miljak and F. F. Chen, “Helicon wave excitation with rotating antenna fields,” *Plasma Sources Science Technology*, vol. 7, no. 1, pp. 61–74, 1998.
- [3] A. Fruchtman, “Neutral gas depletion in low temperature plasma,” *Journal of Physics D: Applied Physics*, vol. 50, no. 47, p. 473002, 2017.
- [4] International Energy Agency (IEA), “Internation energy agency (iea),” 2020. <https://www.iea.org/>, Last accessed on 20-02-2020.
- [5] J. Dietz and and the ITER Joint Central Team, “The ITER fusion experiment,” *Vacuum*, vol. 47, no. 6-8, pp. 911–918, 1996.
- [6] The ITER Organization, “Iter,” 2020. <https://www.iter.org/>, Last accessed on 20-02-2020.
- [7] H. Rebut, P, “Iter: the first experimental fusion reactor,” *Fusion Engineering and Design*, vol. 30, p. 85, 1995.
- [8] Our Energy, “Iter project facts,” 2015. https://www.our-energy.com/energy_facts/iter_project_facts.html, Last accessed on 20-02-2020.
- [9] A. W. Kleyn, N. J. Lopes Cardozo, and U. Samm, “Plasma-surface interaction in the context of ITER.,” *Physical Chemistry Chemical Physics*, vol. 8, no. 15, p. 1761, 2006.

- [10] T. Klinger, A. Alonso, S. Bozhenkov, R. Burhenn, A. Dinklage, G. Fuchert, J. Geiger, O. Grulke, A. Langenberg, M. Hirsch, G. Kocsis, J. Knauer, A. Kramer-Flecken, H. Laqua, S. Lazerson, M. Landreman, H. Maaßberg, S. Marsen, M. Otte, N. Pablant, E. Pasch, K. Rahbarnia, T. Stange, T. Szepesi, H. Thomsen, P. Traverso, J. L. Velasco, T. Wauters, G. Weir, and T. Windisch, “Performance and properties of the first plasmas of Wendelstein 7-X,” *Plasma Physics and Controlled Fusion*, vol. 59, no. 1, p. 014018, 2017.
- [11] J. Wesson, “Tokamaks, 4th edition,” *Contemporary Physics*, vol. 53, pp. 450–451, 09 2012.
- [12] G. Federici, C. H. Skinner, J. N. Brooks, J. P. Coad, C. Grisolia, A. A. Haasz, A. Hassanein, V. Philipps, C. S. Pitcher, J. Roth, W. R. Wampler, and D. G. Whyte, “Plasma-material interactions in current tokamaks and their implications for next step fusion reactors,” *Nuclear Fusion*, vol. 41, no. 12, p. 1967, 2001.
- [13] M. Merola, D. Loesser, A. Martin, P. Chappuis, R. Mitteau, V. Komarov, R. A. Pitts, S. Gicquel, V. Barabash, L. Giancarli, J. Palmer, M. Nakahira, A. Loarte, D. Campbell, R. Eaton, A. Kukushkin, M. Sugihara, F. Zhang, C. S. Kim, R. Raffray, L. Ferrand, D. Yao, S. Sadakov, A. Furmanek, V. Rozov, T. Hirai, F. Escourbiac, T. Jokinen, B. Calcagno, and S. Mori, “ITER plasma-facing components,” *Fusion Engineering and Design*, vol. 85, no. 10-12, p. 2312, 2010.
- [14] F. Wagner, G. Becker, K. Behringer, D. Campbell, A. Eberhagen, W. Engelhardt, G. Fussmann, J. Gernhardt, G. Gierke, G. Haas, M. Huang, F. Karger, M. Keilhacker, Q. Kluber, M. Kornherr, K. Lackner, G. Lisitano, G. G. Lister, H. M. Mayer, D. Meisel, E. R. Miiller, H. Murmann, H. Niedermeyer, W. Poschenrieder, H. Rapp, H. Bohr, F. Schneider, G. Siller, E. Speth, A. Stabler, K. H. Steuer, G. Venus, O. Vollmer, and Z. Yu, “inAdvances in Plasma Physics, edited by Regime of Imyroved Confinement and High Beta in. Neutral-Beam-Heated Divertor Discharges of the ASDEX Tokamak,” *Physics Review Letters*, vol. 49, no. 19, p. 1408, 1982.

- [15] H. J. van Eck, A. W. Kleyn, A. Lof, H. J. van der Meiden, G. J. van Rooij, J. Scholten, and P. A. Zeijlmans van Emmichoven, “Divertor conditions relevant for fusion reactors achieved with linear plasma generator,” *Applied Physics Letters*, vol. 101, no. 22, p. 224107, 2012.
- [16] A. Kreter, “Reactor-relevant plasma-material interaction studies in linear plasma devices,” *Fusion Science and Technology*, vol. 59, pp. 51–56, 01 2011.
- [17] D. Naujoks, *Plasma-Material Interaction in Controlled Fusion*, vol. 39. 2006.
- [18] W. Dekeyser, D. Reiter, and M. Baelmans, “Divertor target shape optimization in realistic edge plasma geometry,” *Nuclear Fusion*, vol. 54, no. 7, p. 073022, 2014.
- [19] P. Monier-Garbet, C. DeMichelis, P. Ghendrih, C. Grisolla, A. Grosman, R. Guirlet, J. Gunn, T. Loarer, C. E. Bush, C. Clement, Y. Corre, L. Costanzo, B. Schunke, and J. C. Vallet, “High radiation from intrinsic and injected impurities in Tore Supra ergodic divertor plasmas,” *Journal of Nuclear Materials*, vol. 290-293, pp. 925–929, 2001.
- [20] A. Kallenbach, M. Bernert, R. Dux, L. Casali, T. Eich, L. Giannone, A. Herrmann, R. McDermott, A. Mlynek, H. W. Müller, F. Reimold, J. Schweinzer, M. Sertoli, G. Tardini, W. Treutterer, E. Viezzer, R. Wenninger, and M. Wischmeier, “Impurity seeding for tokamak power exhaust: From present devices via ITER to DEMO,” *Plasma Physics and Controlled Fusion*, vol. 55, no. 12, p. 124041, 2013.
- [21] M. R. Wade, J. T. Hogan, S. L. Allen, N. H. Brooks, D. N. Hill, R. Maingi, M. J. Schaffer, J. G. Watkins, D. G. Whyte, R. D. Wood, and W. P. West, “Impurity enrichment studies with induced scrape-off layer flow on DIII-D,” *Nuclear Fusion*, vol. 38, no. 12, pp. 1839–1859, 1998.
- [22] Y. Nakamura, N. Tamura, M. Kobayashi, S. Yoshimura, C. Suzuki, M. Yoshinuma, M. Goto, G. Motojima, K. Nagaoka, K. Tanaka, R. Sakamoto, B. J. Peterson, K. Ida, M. Osakabe, and T. Morisaki, “A comprehensive study on impurity behavior in LHD long pulse discharges,” *Nuclear Materials and Energy*, vol. 12, pp. 124–132, 2017.

BIBLIOGRAPHY

- [23] N. Asakura, T. Nakano, O. Naito, and N. Oyama, “Characteristics of radiation distribution and divertor detachment in impurity seeding on JT-60U,” *Journal of Nuclear Materials*, vol. 415, no. 1, pp. S318–S321, 2011.
- [24] T. Body, S. Cousens, J. Kirby, and C. Corr, “A volume-averaged model of nitrogen-hydrogen plasma chemistry to investigate ammonia production in a plasma-surface-interaction device,” *Plasma Physics and Controlled Fusion*, vol. 60, p. 075011, 2018.
- [25] H. J. Van Eck, *The linear plasma generator Magnum-PSI*. PhD thesis, Eindhoven University of Technology, 2013.
- [26] Y. Hirooka, R. W. Conn, T. Sketchley, W. K. Leung, G. Chevalier, R. Doerner, J. Elverum, D. M. Goebel, G. Gunner, M. Khandagle, B. Labombard, R. Lehmer, P. Luong, Y. Ra, L. Schmitz, and G. Tynan, “A new plasma-surface interactions research facility: PISCES-B and first materials erosion experiments on bulk-boronized graphite,” *Journal of Vacuum Science & Technology A: Vacuum, Surfaces, and Films*, vol. 8, no. 3, pp. 1790–1797, 1990.
- [27] B. D. Blackwell, J. F. Caneses, C. M. Samuell, J. Wach, J. Howard, and C. Corr, “Design and characterization of the Magnetized Plasma Interaction Experiment (MAGPIE): a new source for plasma–material interaction studies,” *Plasma Sources Science Technology*, vol. 21, p. 055033, oct 2012.
- [28] R. S. Hemsworth, D. Boilson, P. Blatchford, M. D. Palma, G. Chitarin, H. P. De Esch, F. Geli, M. Dremel, J. Graceffa, D. Marcuzzi, G. Serianni, D. Shah, M. Singh, M. Urbani, and P. Zaccaria, “Overview of the design of the ITER heating neutral beam injectors,” *New Journal of Physics*, vol. 19, no. 2, p. 025005, 2017.
- [29] R. S. Hemsworth and T. Inoue, “Magnetic Fusion,” *Atomic Energy*, vol. 33, no. 6, pp. 1799–1813, 2005.
- [30] E. Speth, H. D. Falter, P. Franzen, U. Fantz, M. Bandyopadhyay, S. Christ, A. Encheva, M. Fröschle, D. Holtum, B. Heinemann, W. Kraus, A. Lorenz,

- C. Martens, P. McNeely, S. Obermayer, R. Riedl, R. Süß, A. Tanga, R. Wilhelm, and D. Wunderlich, “Overview of the RF source development programme at IPP Garching,” *Nuclear Fusion*, vol. 46, no. 6, p. S220, 2006.
- [31] A. Staebler, U. Fantz, P. Franzen, M. Berger, S. Christ-Koch, H. D. Falter, M. Froeschle, R. Gutser, B. Heinemann, D. Holtum, W. Kraus, C. Martens, P. McNeely, R. Nocentini, S. Obermayer, R. Riedl, E. Speth, and D. Wunderlich, “Development of a RF-driven ion source for the ITER NBI system,” *Fusion Engineering and Design*, vol. 84, no. 2-6, pp. 265–268, 2009.
- [32] B. Heinemann, H. D. Falter, U. Fantz, P. Franzen, M. Froeschle, W. Kraus, C. Martens, R. Nocentini, R. Riedl, E. Speth, and A. Staebler, “The negative ion source test facility ELISE,” *Fusion Engineering and Design*, vol. 86, no. 6-8, pp. 768–771, 2011.
- [33] U. Fantz, B. Heinemann, D. Wunderlich, R. Riedl, W. Kraus, R. Nocentini, and F. Bonomo, “Towards 20 A negative hydrogen ion beams for up to 1 h: Achievements of the ELISE test facility (invited),” *Review of Scientific Instruments*, vol. 87, no. 2, p. 02B307, 2016.
- [34] M. Bacal and M. Wada, “Negative hydrogen ion production mechanisms,” *Applied Physics Reviews*, vol. 2, no. 2, p. 021305, 2015.
- [35] J. Santoso, H. V. Willett, and C. S. Corr, “High density negative hydrogen ion production in a high power pulsed helicon discharge,” *Plasma Sources Science Technology*, vol. 27, no. 10, p. 10LT03, 2018.
- [36] S. Briefi and U. Fantz, “Investigation of helicon discharges as rf coupling concept of negative hydrogen ion sources,” *AIP Conference Proceedings*, vol. 1515, no. 1, pp. 278–283, 2013.
- [37] K. Takahashi, S. Takayama, A. Komuro, and A. Ando, “Standing Helicon Wave Induced by a Rapidly Bent Magnetic Field in Plasmas,” *Physical Review Letters*, vol. 116, no. 13, pp. 1–5, 2016.
- [38] F. F. Chen, “Helicon discharges and sources: a review,” *Plasma Sources Science Technology*, vol. 24, no. 1, p. 014001, 2015.

- [39] A. Simonin, R. Agnello, S. Bechu, J. M. Bernard, C. Blondel, J. P. Boeuf, D. Bresteau, G. Cartry, W. Chaibi, C. Drag, B. P. Duval, H. P. De Esch, G. Fubiani, I. Furno, C. Grand, P. Guittienne, A. Howling, R. Jacquier, C. Marini, and I. Morgal, “Negative ion source development for a photoneutralization based neutral beam system for future fusion reactors,” *New Journal of Physics*, vol. 18, no. 12, p. 125005, 2016.
- [40] P. Sonato, P. Agostinetti, U. Fantz, T. Franke, I. Furno, A. Simonin, and M. Q. Tran, “Conceptual design of the beam source for the DEMO Neutral Beam Injectors,” *New Journal of Physics*, vol. 18, no. 12, p. 056026, 2016.
- [41] C. Marini, R. Agnello, B. P. Duval, I. Furno, A. A. Howling, R. Jacquier, A. N. Karpushov, G. Plyushchev, K. Verhaegh, P. Guittienne, U. Fantz, D. Wünderlich, S. Béchu, and A. Simonin, “Spectroscopic characterization of H 2 and D 2 helicon plasmas generated by a resonant antenna for neutral beam applications in fusion,” *Nuclear Fusion*, vol. 57, no. 3, p. 036024, 2017.
- [42] N. Sharma, M. Chakraborty, N. K. Neog, and M. Bandyopadhyay, “Design of a helicon plasma source for ion–ion plasma production,” *Fusion Engineering and Design*, vol. 117, pp. 30–38, 2017.
- [43] G. Aad, T. Abajyan, B. Abbott, and E. Al., “Observation of a new particle in the search for the Standard Model Higgs boson with the ATLAS detector at the LHC,” *Physics Letters, Section B: Nuclear, Elementary Particle and High-Energy Physics*, vol. 716, no. 1, pp. 1–29, 2012.
- [44] S. Chatrchyan, V. Khachatryan, A. M. Sirunyan, and E. Al., “Observation of a new boson at a mass of 125 GeV with the CMS experiment at the LHC,” *Physics Letters, Section B: Nuclear, Elementary Particle and High-Energy Physics*, vol. 716, no. 1, pp. 30–61, 2012.
- [45] R. Assmann, R. Bingham, T. Bohl, E. Al., H. Vincke, M. Wing, and G. Xia, “Proton-driven plasma wakefield acceleration: A path to the future of high-energy particle physics,” *Plasma Physics and Controlled Fusion*, vol. 56, no. 8, p. 084013, 2014.

- [46] M. Koratzinos, A. P. Blondel, R. Aleksan, O. Brunner, A. Butterworth, P. Janot, E. Jensen, J. Osborne, F. Zimmermann, J. R. Ellis, and M. Zanetti, “TLEP: A high-performance circular e+e- collider to study the higgs boson,” *IPAC 2013: Proceedings of the 4th International Particle Accelerator Conference*, pp. 1658–1660, 2013.
- [47] J. M. Dawson and T. Tajima, “Laser Electron Accelerator,” *Physical Review Letters*, vol. 43, no. 4, pp. 267–270, 1979.
- [48] A. Caldwell, E. Gschwendtner, K. Lotov, P. Muggli, and M. Wing, “AWAKE Design Report A Proton-Driven Plasma Wakefield Acceleration Experiment at CERN,” tech. rep., 2013.
- [49] E. Gschwendtner, E. Adli, L. Amorim, R. Apsimon, R. Assmann, A. M. Bachmann, F. Batsch, J. Bauche, V. K. Berglyd Olsen, M. Bernardini, R. Birmingham, B. Biskup, T. Bohl, C. Bracco, P. N. Burrows, G. Burt, B. Buttenschön, A. Butterworth, A. Caldwell, M. Cascella, E. Chevallay, S. Cipiccia, H. Damerau, L. Deacon, P. Dirksen, S. Doeberl, U. Dorda, J. Farmer, V. Fedosseev, E. Feldbaumer, R. Fiorito, R. Fonseca, F. Friebel, A. A. Gorn, O. Grulke, J. Hansen, C. Hessler, W. Hofle, J. Holloway, M. Hüther, D. Jaroszynski, L. Jensen, S. Jolly, A. Joulaei, M. Kasim, F. Keeble, Y. Li, S. Liu, N. Lopes, K. V. Lotov, S. Mandry, R. Martorelli, M. Martyanov, S. Mazzoni, O. Mete, V. A. Minakov, J. Mitchell, J. Moody, P. Muggli, Z. Najmudin, P. Norreys, E. Öz, A. Pardons, K. Pepitone, A. Petrenko, G. Plyushchev, A. Pukhov, K. Rieger, H. Ruhl, F. Salveter, N. Savard, J. Schmidt, A. Seryi, E. Shaposhnikova, Z. M. Sheng, P. Sherwood, L. Silva, L. Soby, A. P. Sosedkin, R. I. Spitsyn, R. Trines, P. V. Tuev, M. Turner, V. Verzilov, J. Vieira, H. Vincke, Y. Wei, C. P. Welsch, M. Wing, G. Xia, and H. Zhang, “AWAKE, The Advanced Proton Driven Plasma Wakefield Acceleration Experiment at CERN,” *Nuclear Instruments and Methods in Physics Research, Section A: Accelerators, Spectrometers, Detectors and Associated Equipment*, vol. 829, pp. 76–82, 2016.
- [50] B. Buttenschön, N. Fahrenkamp, and O. Grulke, “A high power , high density helicon discharge for the plasma wake fi eld accelerator experiment AWAKE,”

- Plasma Physics and Controlled Fusion*, vol. 60, pp. 1 –7, 2018.
- [51] C. Linsmeier, B. Unterberg, J. W. Coenen, R. P. Doerner, H. Greuner, A. Kreter, J. Linke, and H. Maier, “Material testing facilities and programs for plasma-facing component testing,” *Nuclear Fusion*, vol. 57, no. 9, p. 092012, 2017.
- [52] X. Bonnin, R. A. Pitts, V. Komarov, F. Escourbiac, M. Merola, L. Bo, L. Wei, L. Pan, and A. S. Kukushkin, “ITER divertor plasma response to time-dependent impurity injection,” *Nuclear Materials and Energy*, vol. 12, pp. 1100–1105, 2017.
- [53] R. A. Pitts, X. Bonnin, F. Escourbiac, H. Frerichs, J. P. Gunn, T. Hirai, A. S. Kukushkin, P. C. Stangeby, G. D. Temmerman, I. Veselova, and S. Wiesen, “Physics basis for the first ITER tungsten divertor,” *Nuclear Materials and Energy*, vol. 20, no. June, p. 100696, 2019.
- [54] N. Ohno, “Plasma detachment in linear devices,” *Plasma Physics and Controlled Fusion*, vol. 59, p. 034007, feb 2017.
- [55] J. Rapp, W. R. Koppers, H. J. Van Eck, G. J. Van Rooij, W. J. Goedheer, B. De Groot, R. Al, M. F. Graswinckel, M. A. Van Den Berg, O. Kruyt, P. Smeets, H. J. Van Der Meiden, W. Vijvers, J. Scholten, M. Van De Pol, S. Brons, W. Melissen, T. Van Der Grift, R. Koch, B. Schweer, U. Samm, V. Philipps, R. A. Engeln, D. C. Schram, N. J. Lopes Cardozo, and A. W. Kleyn, “Construction of the plasma-wall experiment Magnum-PSI,” *Fusion Engineering and Design*, vol. 85, no. 7-9, pp. 1455–1459, 2010.
- [56] B. De Groot, G. J. Van Rooij, V. Veremiyenko, M. G. Von Hellermann, H. J. Van Eck, C. J. Barth, G. L. Kruijzer, J. C. Wolff, W. J. Goedheer, N. J. Lopes Cardozo, A. W. Kleyn, P. H. Smeets, S. Brezinsek, A. Pospieszczyk, R. A. Engeln, and R. P. Dahiya, “Magnum-psi, a plasma generator for plasma-surface interaction research in ITER-like conditions,” *Fusion Engineering and Design*, vol. 74, no. 1-4, pp. 155–159, 2005.
- [57] N. Ohno, D. Nishijima, S. Takamura, Y. Uesugi, M. Motoyama, N. Hattori, H. Arakawa, N. Ezumi, S. Krasheninnikov, A. Pigarov, and U. Wenzel, “Static

- and dynamic behaviour of plasma detachment in the divertor simulator experiment NAGDIS-II,” *Nuclear Fusion*, vol. 41, no. 8, pp. 1055–1065, 2001.
- [58] L. Schmitz, B. Merriman, L. Blush, R. Lehmer, R. W. Conn, R. Doerner, A. Grossman, and F. Najmabadi, “Plasma and neutral dynamics in a simulated tokamak gas target divertor,” *Physics of Plasmas*, vol. 2, no. 8, pp. 3081 – 3094, 1998.
- [59] E. M. Hollmann, A. Y. Pigarov, R. Seraydarian, D. G. Whyte, and S. I. Krasheninnikov, “Particle balance measurements during detachment in a gas-target divertor simulator,” *Physics of Plasmas*, vol. 9, no. 4, pp. 1226 – 1232, 2002.
- [60] R. P. Doerner, M. J. Baldwin, and K. Schmid, “The influence of a beryllium containing plasma on the evolution of a mixed-material surface,” *Physica Scripta*, vol. T111, pp. 75–79, 2004.
- [61] A. Pospieszczyk, M. Reinhart, B. Unterberg, S. Brezinsek, A. Kreter, U. Samm, G. Sergienko, B. Schweer, C. Salmagne, D. Reiter, M. Baelmans, D. Wunderlich, and U. Fantz, “Spectroscopic characterisation of the PSI-2 plasma in the ionising and recombining state,” *Journal of Nuclear Materials*, vol. 438, pp. S1249–S1252, 2013.
- [62] A. Kreter, C. Brandt, A. Huber, S. Kraus, S. Möller, M. Reinhart, B. Schweer, and B. Unterberg, “Linear Plasma Device PSI-2 for Plasma-Material Interaction Studies,” *Fusion Science and Technology*, vol. 68, no. 1, pp. 8–14, 2017.
- [63] H. J. N. van Eck, T. Abrams, M. A. van den Berg, S. Brons, G. G. van Eden, M. A. Jaworski, R. Kaita, H. J. van der Meiden, T. W. Morgan, M. J. van de Pol, J. Scholten, P. H. M. Smeets, G. de Temmerman, P. C. de Vries, and P. A. Zeijlmans van Emmichoven, “Operational characteristics of the high flux plasma generator Magnum-PSI,” *Fusion Engineering and Design*, vol. 89, no. 9-10, pp. 2150–2154, 2014.
- [64] J. Scholten, P. A. Zeijlmans van Emmichoven, H. J. N. van Eck, P. H. M. Smeets, G. C. de Temmerman, S. Brons, M. A. van den Berg, H. J. van der

- Meiden, M. J. van de Pol, M. F. Graswinckel, P. W. C. Groen, A. J. Poelman, and J. W. Gennuit, “Operational status of the Magnum-PSI linear plasma device,” *Fusion Engineering and Design*, vol. 88, no. 9-10, pp. 1785–1788, 2013.
- [65] J. B. O. Caughman, R. H. Goulding, T. M. Biewer, T. S. Bigelow, I. H. Campbell, J. Caneses, S. J. Diem, A. Fadnek, D. T. Fehling, R. C. Isler, E. H. Martin, C. M. Parish, J. Rapp, K. Wang, C. J. Beers, D. Donovan, N. Kafle, H. B. Ray, G. C. Shaw, and M. A. Showers, “Plasma source development for fusion-relevant material testing,” *Journal of Vacuum Science and Technology A*, vol. 35, no. 3, p. 03E114, 2017.
- [66] S. C. Thakur, C. Brandt, L. Cui, J. J. Gosselin, A. D. Light, and G. R. Tynan, “Multi-instability plasma dynamics during the route to fully developed turbulence in a helicon plasma,” *Plasma Sources Science and Technology*, vol. 23, no. 4, p. 044006, 2014.
- [67] R. A. Pitts, S. Carpentier, F. Escourbiac, T. Hirai, V. Komarov, A. S. Kukushkin, S. Lisgo, A. Loarte, M. Merola, R. Mitteau, A. R. Raffray, M. Shimada, and P. C. Stangeby, “Physics basis and design of the ITER plasma-facing components,” *Journal of Nuclear Materials*, vol. 415, no. 1, pp. S957–S964, 2011.
- [68] E. M. Hollmann, D. G. Whyte, D. Nishijima, N. Ohno, Y. Uesugi, and N. Ezumi, “Evidence for the importance of radial transport in plasma detachment in the Nagoya University Divertor Simulator (NAGDIS-II),” *Physics of Plasmas*, vol. 8, no. 7, p. 3314, 2001.
- [69] D. M. Goebel, G. Campbell, and R. W. Conn, “Plasma surface interaction experimental facility (PISCES) for materials and edge physics studies,” *Journal of Nuclear Materials*, vol. 121, no. C, pp. 277–282, 1984.
- [70] E. Kessels, “The expanding thermal plasma (etp) technique,” 2001. <http://www.vacuumcursus.nl/casussen/ExpandTermalPlasma.htm>, Last accessed on 20-02-2020.

BIBLIOGRAPHY

- [71] M. A. Lieberman and A. J. Lichtenberg, *Principles of Plasma Discharges and Materials Processing: Second Edition*. New Jersey: John Wiley and Sons, 2005.
- [72] P. Chabert and N. Braithwaite, *Physics of Radio-Frequency Plasmas*. Cambridge: Cambridge University Press, 2011.
- [73] J. Hopwood, “Review of inductively coupled plasmas for plasma processing,” *Plasma Sources Science Technology*, vol. 1, no. 2, p. 109, 1992.
- [74] F. Chen and D. Blackwell, “Upper limit to landau damping in helicon discharges,” *Physical Review Letters*, vol. 82, p. 2677, 03 1999.
- [75] J. Caneses and B. Blackwell, “Collisional damping of helicon waves in a high density hydrogen linear plasma device,” *Plasma Sources Science and Technology*, vol. 25, 09 2016.
- [76] R. W. Boswell, “Very efficient plasma generation,” *Plasma Physics and Controlled Fusion*, vol. 26, p. 1147, 1984.
- [77] F. F. Chen, “Plasma ionization by helicon waves,” *Plasma Physics and Controlled Fusion*, vol. 33, no. 4, pp. 339–364, 1991.
- [78] R. W. Boswell, “Plasma production using a standing helicon wave,” *Physics Letters A*, vol. 33, no. 7, pp. 457–458, 1970.
- [79] A. Bondi, “Van der waals volumes and radii,” *Journal of Physical Chemistry*, vol. 68, p. 441, 1964.
- [80] S. Batsanov, “Van der waals radii of elements,” *Inorganic Materials*, vol. 37, p. 871, 2001.
- [81] C. M. Samuell, *Hydrogen Plasmas and Their Interaction with Fusion-Relevant Materials*. PhD thesis, The Australian National University, 2014.
- [82] A. Hjartarson, E. Thorsteinsson, and J. Gudmundsson, “Low pressure hydrogen discharges diluted with argon explored using a global model,” *Plasma Sources Science and Technology*, vol. 19, p. 065008, 2010.

BIBLIOGRAPHY

- [83] J.-S. Yoon, M.-Y. Song, J.-M. Han, S. H. Hwang, W.-S. Chang, B. Lee, and Y. Itikawa, “Cross sections for electron collisions with hydrogen molecules,” *Journal of Physical and Chemical Reference Data*, vol. 37, no. 2, p. 913, 2008.
- [84] M. B. Shah, D. S. Elliott, and H. B. Gilbody, “Pulsed crossed-beam study of the ionisation of atomic hydrogen by electron impact,” *Journal of Physics B: Atomic, Molecular and Optical Physics*, vol. 20, pp. 3501 – 3514, 1987.
- [85] H. Tawara, Y. Itikawa, H. Nishimura, and M. Yoshino, “Cross sections and related data for electron collisions with hydrogen molecules and molecular ions,” *Journal of Physical and Chemical Reference Data*, vol. 19, no. 3, p. 617, 1990.
- [86] R. K. Janev, D. Reiter, and U. Samm, “Collision Processes in Low-Temperature Hydrogen Plasmas,” *Sciences-New York*, p. 190, 2003.
- [87] D. Gerlich and S. Horning, “Experimental investigations of radiative association processes as related to interseller chemistry,” *Chemical Reviews*, vol. 92, no. 7, p. 1509, 1992.
- [88] C. L. Liu, J. G. Wang, and R. K. Janev, “Mutual neutralization in slow $h^{+} + h^{-}$ collisions,” *Journal of Physics. B, Atomic, Molecular and Optical Physics*, vol. 39, p. 1223, 2006.
- [89] M. Tendler and D. Heifetz, “Neutral particle kinetics in fusion devices,” *Fusion Technology*, vol. 11, no. 2, pp. 289–310, 1987.
- [90] J. P. J. Dubois, K. Achkasov, D. Kogut, A. Ahmad, J. M. Layet, A. Simonin, and G. Cartry, “Negative-ion surface production in hydrogen plasmas : Determination of the negative-ion energy and angle distribution function using mass spectrometry,” *Journal of Applied Physics*, vol. 119, p. 193301, 2016.
- [91] R. M. Magee, M. E. Galante, J. Carr, G. Lusk, D. W. McCarren, and E. E. Scime, “Neutral depletion and the helicon density limit,” *Physics of Plasmas*, vol. 20, no. 12, pp. 1–6, 2013.

BIBLIOGRAPHY

- [92] C. M. Samuell and C. S. Corr, “Low-pressure hydrogen plasmas explored using a global model,” *Plasma Sources Science Technology*, vol. 25, no. 1, p. 15014, 2015.
- [93] R. P. H. Chang, “Hydrogen plasma etching of semiconductors and their oxides,” *Journal of Vacuum Science Technology*, vol. 20, no. 1, p. 45, 1982.
- [94] C. P. Tsai and D. L. McFadden, “Gas-phase atom-radical kinetics of atomic hydrogen, nitrogen, and oxygen reactions with CHF radicals,” *Journal of Physical Chemistry*, vol. 94, no. 8, pp. 3298–3300, 1990.
- [95] J. S. Yoon, Y. W. Kim, D. C. Kwon, M. Y. Song, W. S. Chang, C. G. Kim, V. Kumar, and B. J. Lee, “Electron-impact cross sections for deuterated hydrogen and deuterium molecules,” *Reports on Progress in Physics*, vol. 73, no. 11, p. 116401, 2010.
- [96] C. C. Klepper, T. E. Evans, G. Haas, G. L. Jackson, and R. Maingi, “Neutral pressure studies with a fast ionization gauge in the divertor region of the dIII-D tokamak,” *Journal of Vacuum Science & Technology A*, vol. 11, no. 2, pp. 446–450, 1993.
- [97] G. Haas and H.-s. Bosch, “In vessel pressure measurement in nuclear fusion experiments with ASDEX gauges,” *Vacuum*, vol. 51, no. 1, pp. 39–46, 1998.
- [98] J. Benedikt, D. Ellerweg, and A. von Keudell, “Diagnostics of low and atmospheric pressure plasmas by means of mass spectrometry,” *arXiv*, vol. 1, 2011.
- [99] N. Harris, *Modern Vacuum Practice*. New York: MacGraw-Hill, 1989.
- [100] L. C. Johnson and E. Hinnov, “Ionization, recombination, and population of excited levels in hydrogen plasmas,” *Journal of Quantitative Spectroscopy and Radiative Transfer*, vol. 13, no. 4, pp. 333–358, 1973.
- [101] D. Wunderlich, M. Giacomin, R. Ritz, and U. Fantz, “Yacora on the Web: Online collisional radiative models for plasmas containing H, H₂ or He,” *Journal of Quantitative Spectroscopy and Radiative Transfer*, vol. 240, p. 106695, 2020.

BIBLIOGRAPHY

- [102] S. Ma, J. Howard, B. D. Blackwell, and N. Thapar, “Measurements of electron density and temperature in the H-1 heliac plasma by helium line intensity ratios.,” *The Review of Scientific Instruments*, vol. 83, no. 3, p. 033102, 2012.
- [103] R. E. Bell, “An inversion technique to obtain full poloidal velocity profiles in a tokamak plasma a,” *Review of Scientific Instruments*, vol. 68, no. 2, pp. 1273–1280, 1997.
- [104] A. Rousseau, E. Teboul, and N. Sadeghi, “Time-resolved gas temperature measurements by laser absorption in a pulsed microwave hydrogen discharge,” *Plasma Sources Science Technology*, vol. 13, no. 1, pp. 166–176, 2004.
- [105] R. Asakawa, M. Goto, N. Sadeghi, and K. Sasaki, “Characteristics of saturation spectroscopy at the Balmer- α line of atomic hydrogen in a linear magnetized plasma source,” *Journal of Instrumentation*, vol. 7, no. 1, p. C01018, 2012.
- [106] K. Muraoka and M. Maeda, “Application of laser-induced fluorescence to high-temperature plasmas,” *Plasma Physics and Controlled Fusion*, vol. 35, no. 6, p. 633, 1993.
- [107] H. F. Döbele, T. Mosbach, K. Niemi, and V. S.-v. D. Gathen, “Laser-induced fluorescence measurements of absolute atomic densities: concepts and limitations,” *Plasma Sources Science Technology*, vol. 14, pp. S31–S41, may 2005.
- [108] R. Boswell, R. Porteous, A. Prytz, A. Bouchoule, and P. Ranson, “Some features of RF excited fully ionized low pressure argon plasma,” *Physics Letters A*, vol. 91, no. 4, p. 163, 1982.
- [109] D. A. Shapiro and H.-B. Valentini, “Hydrodynamic theory of low-pressure multi-component discharges with neutral gas depletion,” *Contributions to Plasma Physics*, vol. 31, no. 4, pp. 391–409, 1991.
- [110] S. M. Rossnagel, S. J. Whitehair, C. R. Guarnieri, and J. J. Cuomo, “Plasma induced gas heating in electron cyclotron resonance sources,” *Journal of Vacuum Science & Technology A*, vol. 8, no. 4, pp. 3113–3117, 1990.

BIBLIOGRAPHY

- [111] T. Nakano, N. Sadeghi, and R. A. Gottscho, “Ion and neutral temperatures in electron cyclotron resonance plasma reactors,” *Applied Physics Letters*, vol. 58, no. 5, pp. 458–460, 1991.
- [112] G. A. Hebner, “Spatially resolved , excited state densities and neutral and ion temperatures in inductively coupled argon plasmas,” *Journal of Applied Physics*, vol. 80, no. 5, pp. 2624 – 2636, 1996.
- [113] T. Hori, M. D. Bowden, K. Uchino, K. Muraoka, and M. Maeda, “Measurements of electron temperature, electron density, and neutral density in a radio-frequency inductively coupled plasma,” *Journal of Vacuum Science & Technology A*, vol. 14, no. 1, pp. 144–151, 1996.
- [114] A. Fruchtman, “Neutral depletion in a collisionless plasma,” *33rd EPS Conference on Plasma Physics 2006, EPS 2006*, vol. 3, no. 2, pp. 403 – 413, 2006.
- [115] J. Gilland, R. Breun, and N. Hershkowitz, “Neutral pumping in a helicon discharge,” *Plasma Sources Science Technology*, vol. 7, no. 3, pp. 416–422, 1998.
- [116] A. Fruchtman, “Energizing and depletion of neutrals by a collisional plasma,” *Plasma Sources Science Technology*, vol. 17, pp. 1 – 10, 2008.
- [117] G. R. Tynan, “Neutral depletion and transport mechanisms in large-area high density plasma sources,” *IEEE International Conference on Plasma Science*, vol. 5356, no. November 1999, p. 85, 1999.
- [118] S. Yun, K. Taylor, and G. R. Tynan, “Measurement of radial neutral pressure and plasma density profiles in various plasma conditions in large-area high-density plasma sources in various plasma conditions in large-area high-density plasma sources,” *Physics of Plasmas*, vol. 7, no. 8, pp. 3448 – 3456, 2000.
- [119] A. Fruchtman, G. Makrinich, P. Chabert, and J. M. Rax, “Enhanced plasma transport due to neutral depletion,” *Physical Review Letters*, vol. 95, no. 11, pp. 1–4, 2005.

BIBLIOGRAPHY

- [120] J. L. Rimbault, L. Liard, J. M. Rax, P. Chabert, A. Fruchtman, and G. Makrinich, “Steady-state isothermal bounded plasma with neutral dynamics,” *Physics of Plasmas*, vol. 14, no. 1, p. 013503, 2007.
- [121] A. Aanesland, L. Liard, G. Leray, J. Jolly, and P. Chabert, “Direct measurements of neutral density depletion by two-photon absorption laser-induced fluorescence spectroscopy,” *Applied Physics Letters*, vol. 91, no. 12, p. 121502, 2007.
- [122] L. Liard, J. L. Rimbault, J. M. Rax, and P. Chabert, “Plasma transport under neutral gas depletion conditions,” *Journal of Physics D: Applied Physics*, vol. 40, no. 17, pp. 5192–5195, 2007.
- [123] L. Liard, J. L. Rimbault, and P. Chabert, “Competitive effects of an axial magnetic field and of neutral gas depletion in a positive column,” *Physics of Plasmas*, vol. 16, no. 5, p. 053507, 2009.
- [124] L. Liard, A. Aanesland, and P. Chabert, “Dynamics of neutral gas depletion investigated by time- and space-resolved measurements of xenon atom ground state density,” *Journal of Physics D: Applied Physics*, vol. 45, no. 23, p. 235201, 2012.
- [125] S. Cho, “A self-consistent global model of neutral gas depletion in pulsed helicon plasmas,” *Physics of Plasmas*, vol. 6, no. 1, pp. 359 – 364, 1999.
- [126] P. McNeely and D. Wunderlich, “Neutral depletion in an H- source operated at high RF power and low input gas flow,” *Plasma Sources Science Technology*, vol. 20, no. 4, p. 045005, 2011.
- [127] D. O’Connell, T. Gans, D. L. Crinlea, U. Czarnetzki, and N. Sadeghi, “Neutral gas depletion mechanisms in dense low-temperature argon plasmas,” *Journal of Physics D: Applied Physics*, vol. 41, no. 3, p. 035208, 2008.
- [128] D. L. Crinlea, U. Czarnetzki, S. Iordanova, I. Koleva, and D. Luggenholscher, “Plasma diagnostics by optical emission spectroscopy on argon and comparison with Thomson scattering,” *Journal of Physics D: Applied Physics*, vol. 42, pp. 1 – 11, 2009.

BIBLIOGRAPHY

- [129] M. E. Galante, R. M. Magee, and E. E. Scime, *Two-Photon Absorption Laser Induced Fluorescence Measurements of Neutral Density in Helicon Plasma*. PhD thesis, University of West Virginia, 2013.
- [130] A. Fruchtman, G. Makrinich, J. L. Raimbault, L. Liard, J. M. Rax, and P. Chabert, “Neutral depletion versus repletion due to ionization,” *Physics of Plasmas*, vol. 15, no. 5, p. 057102, 2008.
- [131] A. Fruchtman, “Ambipolar and nonambipolar cross-field diffusions,” *Plasma Sources Science Technology*, vol. 18, pp. 1 –16, 2009.
- [132] J. S. Santoso, *Production of Negative Hydrogen Ions in a High-Powered Helicon Plasma Source*. PhD thesis, The Australian National University, 2018.
- [133] T. Hirai, F. Escourbiac, S. Carpentier-Chouchana, A. Fedosov, L. Ferrand, T. Jokinen, V. Komarov, A. Kukushkin, M. Merola, R. Mitteau, R. Pitts, W. Shu, M. Sugihara, B. Riccardi, S. Suzuki, and R. Villari, “Iter tungsten divertor design development and qualification program,” *Fusion Engineering and Design*, vol. 88, no. 9, pp. 1798 – 1801, 2013. Proceedings of the 27th Symposium On Fusion Technology (SOFT-27); Liège, Belgium, September 24-28, 2012.
- [134] M. A. T. Thompson, *Measuring helium nano-bubble formation in tungsten with grazing-incidence small angle X-ray scattering*. PhD thesis, The Australian National University, 2017.
- [135] J. Howard, “Coherence imaging spectro-polarimetry for magnetic fusion diagnostics,” *Journal of Physics B: Atomic, Molecular and Optical Physics*, vol. 43, no. 14, p. 144010, 2010.
- [136] R. Lester, Y. Zhai, C. Corr, and J. Howard, “Coherence imaging for ion temperature and flow measurements in a low-temperature helicon plasma source,” *Plasma Sources Science Technology*, vol. 25, no. 1, p. 015025, 2016.
- [137] J. Howard, M. Kocan, S. Lisgo, and R. Reichle, “Stokes-Doppler coherence imaging for ITER boundary tomography,” *Review of Scientific Instruments*, vol. 87, no. 11, p. 11E561, 2016.

BIBLIOGRAPHY

- [138] B. W. Longmier, E. A. Bering, M. D. Carter, L. D. Cassady, W. J. Chancery, F. R. Díaz, T. W. Glover, N. Hershkowitz, A. V. Ilin, G. E. McCaskill, C. S. Olsen, and J. P. Squire, “Ambipolar ion acceleration in an expanding magnetic nozzle,” *Plasma Sources Science Technology*, vol. 20, no. 1, p. 015007, 2011.
- [139] E. Kolemen, S. L. Allen, B. D. Bray, M. E. Fenstermacher, D. A. Humphreys, A. W. Hyatt, C. J. Lasnier, A. W. Leonard, M. A. Makowski, A. G. McLean, R. Maingi, R. Nazikian, T. W. Petrie, V. A. Soukhanovskii, and E. A. Unterberg, “Heat flux management via advanced magnetic divertor configurations and divertor detachment,” *Journal of Nuclear Materials*, vol. 463, pp. 1186–1190, 2015.
- [140] I. Langmuir and K. Blodgett, “Currents limited by space charge between concentric spheres,” *Physical Review*, vol. 23, pp. 49 – 59, 1924.
- [141] D. Ruzic, *Electric probes for low temperature plasmas*. New York City: American Vacuum Society, 1994.
- [142] I. H. Hutchinson, *Principles of Plasma Diagnostics*. Cambridge University Press, 2 ed., 2002.
- [143] Impedans Plasma Measurement, “Impedans langmuir probe,” 2020. <https://impedans.com/langmuir-probe>.
- [144] Princeton Instruments, “Isoplane sct 320 manual,” 2013. https://nstx.pppl.gov/nstxhome/DragNDrop/Operations/Diagnostics_&_Support_Sys/DIBS/IsoPlane_SCT_320_Manual.pdf, Last accessed on 7-03-2020.
- [145] M. G. H. Boogaarts, S. Mazouffre, G. J. Brinkman, H. W. P. Van Der Heijden, P. Vankan, J. A. M. Van Der Mullen, D. C. Schram, and H. F. Döbele, “Quantitative two-photon laser-induced fluorescence measurements of atomic hydrogen densities, temperatures, and velocities in an expanding thermal plasma,” *Review of Scientific Instruments*, vol. 73, no. 1, p. 73, 2002.
- [146] K. Niemi, V. Schulz-von Der Gathen, and H. F. Döbele, “Absolute calibration of atomic density measurements by laser-induced fluorescence spectroscopy

BIBLIOGRAPHY

- with two-photon excitation,” *Journal of Physics D: Applied Physics*, vol. 34, no. 15, pp. 2330–2335, 2001.
- [147] J. H. Tung, A. Z. Tang, G. J. Salamo, and F. T. Chan, “Two-photon absorption of atomic hydrogen from two light beams,” *Journal of the Optical Society of America B*, vol. 3, no. 6, pp. 837–848, 1986.
- [148] R. S. F. Chang, H. Horiguchi, and D. W. Setser, “Radiative lifetimes and two-body collisional deactivation rate constants in argon for Kr(4p 5 5p) and Kr(4p 5 5p') states,” *Journal of Chemical Physics*, vol. 73, pp. 778–790, July 1980.
- [149] V. Kaufman, “Wavelengths and Energy Levels of Neutral Kr₈₄ and Level Shifts in All Kr Even Isotopes,” *Journal of Research of the National Institute of Standards and Technology*, vol. 98, no. 6, pp. 717 – 724, 1993.
- [150] F. Brandi, W. Hogervorst, and W. Ubachs, “High-resolution vacuum-ultraviolet and ultraviolet photoionization spectroscopy of krypton,” *Journal of Physics B: Atomic, Molecular and Optical Physics*, vol. 35, no. 4, pp. 1071–1084, 2002.
- [151] D. S. Hughes and C. Eckart, “The effect of the motion of the nucleus on the spectra of Li I and Li II,” *Physical Review*, vol. 36, pp. 694 – 698, 1930.
- [152] T. Lamara, R. Hugon, and J. Bougdira, “Influence of gas temperature on the loss mechanisms of H-atoms in a pulsed microwave discharge identified by time-resolved LIF measurements,” *Plasma Sources Science Technology*, vol. 15, no. 3, pp. 526–532, 2006.
- [153] J. Bokor, R. R. Freeman, J. C. White, and R. H. Storz, “Two-Photon Excitation of the n=3 Level in H and D Atoms,” *Physical Review A*, vol. 24, no. 612, p. 223, 1981.
- [154] X. R. Duan and H. Lange, “Effect of laser property fluctuations over multi-pulses on H atom measurement by two-photon absorption laser-induced fluorescence,” *Journal of Physics B: Atomic, Molecular and Optical Physics*, vol. 37, no. 2, pp. 427–434, 2004.

BIBLIOGRAPHY

- [155] R. R. Eisberg, R., *Quantum Physics of Atoms, Molecules, Solids, Nuclei, and Particles*. John Wiley and Sons, 1985.
- [156] D. H. Oza, R. L. Greene, and D. E. Kelleher, “Collisional broadening of the Balmer-a transition of H and He+ in plasmas,” *Physical Review A*, vol. 37, no. 2, pp. 531–536, 1988.
- [157] M. A. Gigosos and V. Cardeñoso, “Journal of Physics B : Atomic , Molecular and Optical Physics Related content New plasma diagnosis tables of hydrogen Stark broadening including ion dynamics New plasma diagnosis tables of hydrogen Stark broadening including ion dynamics,” *Journal of Physics B: Atomic, Molecular and Optical Physics*, vol. 29, pp. 4795–4838, 1996.
- [158] A. Thorne, *Spectrophysics*. London: Chapman and Hall, 1985.
- [159] P. S. Moussounda and P. Ranson, “Pressure broadening of argon lines emitted by a high-pressure microwave discharge (surfatron),” *Journal of Physics B: Atomic, Molecular and Optical Physics*, vol. 20, p. 949, mar 1987.
- [160] S. Shinohara, H. Nishida, T. Tanikawa, T. Hada, I. Funaki, and K. P. Shamrai, “Development of electrodeless plasma thrusters with high-density helicon plasma sources,” *IEEE Transactions on Plasma Science*, vol. 42, no. 5, pp. 1245–1254, 2014.
- [161] A. Fruchtman and S. Shinohara, “Diamagnetism and neutrals depletion in a plasma,” *Physics of Plasmas*, vol. 24, no. 10, p. 103523, 2017.
- [162] J. F. Caneses. PhD thesis, The Australian National University, 2015.
- [163] R. M. Magee, M. E. Galante, N. Gulbrandsen, D. W. McCarren, and E. E. Scime, “Direct measurements of the ionization profile in krypton helicon plasmas,” *Physics of Plasmas*, vol. 19, no. 12, 2012.
- [164] K. Wiesemann, “A short introduction to plasma physics,” *CAS-CERN Accelerator School: Ion Sources - Proceedings*, 04 2014.
- [165] E.-K. Park, H.-J. Woo, K.-S. Chung, H. Tanaka, S. Kajita, and N. Ohno, “Effect of neutral pressure on the he plasma flow measurement in a linear device,” *Current Applied Physics*, vol. 12, no. 6, pp. 1497 – 1502, 2012.

BIBLIOGRAPHY

- [166] M. Bacal, A. M. Bruneteau, W. G. Graham, G. W. Hamilton, and M. Nachman, “Pressure and electron temperature dependence of h- density in a hydrogen plasma,” *Journal of Applied Physics*, vol. 52, no. 3, pp. 1247–1254, 1981.
- [167] R. L. Mills and K. Akhtar, “Fast H in hydrogen mixed gas microwave plasmas when an atomic hydrogen supporting surface was present,” *International Journal of Hydrogen Energy*, vol. 35, no. 6, pp. 2546–2555, 2010.
- [168] R. Mills, P. Ray, and B. Dhandapani, “Evidence of an energy transfer reaction between atomic hydrogen and argon II or helium II as the source of excessively hot H atoms in radio-frequency plasmas,” *Journal of Plasma Physics*, vol. 72, no. 4, pp. 469–484, 2006.
- [169] J. Phillips, C.-K. Chen, and R. Mills, “Evidence of the production of hot hydrogen atoms in rf plasmas by catalytic reactions between hydrogen and oxygen species,” 03 2004.
- [170] E. Tatarova, E. Felizardo, F. M. Dias, M. Lino Da Silva, C. M. Ferreira, and B. Gordiets, “Hot and super-hot hydrogen atoms in microwave plasma,” *Applied Physics Letters*, vol. 95, no. 18, pp. 5–8, 2009.
- [171] E. Felizardo, E. Tatarova, J. Henriques, F. M. Dias, C. M. Ferreira, and B. Gordiets, “Energetic hydrogen atoms in wave driven discharges,” *Applied Physics Letters*, vol. 99, no. 4, pp. 2011–2014, 2011.
- [172] M. E. Galante, R. M. Magee, and E. E. Scime, “Two photon absorption laser induced fluorescence measurements of neutral density in a helicon plasma,” *Physics of Plasmas*, vol. 21, no. 5, p. 055704, 2014.
- [173] C. M. Samuell and C. S. Corr, “Atomic and molecular hydrogen gas temperatures in a low-pressure helicon plasma,” *Plasma Sources Science Technology*, vol. 24, p. 045003, 2015.
- [174] E. Surrey and B. Crowley, “Spectroscopic measurement of gas temperature in the neutralizer of the JET neutral beam injection system,” *Plasma Physics and Controlled Fusion*, vol. 45, no. 7, pp. 1209–1226, 2003.

BIBLIOGRAPHY

- [175] M. Shimada, G. R. Tynan, and R. Cattolica, “Neutral gas density depletion due to neutral gas heating and pressure balance in an inductively coupled plasma,” *Plasma Sources Science Technology*, vol. 16, no. 1, pp. 193–199, 2007.
- [176] M. Shimada, G. R. Tynan, and R. Cattolica, “Neutral depletion in inductively coupled plasmas using hybrid-type direct simulation Monte Carlo,” *Journal of Applied Physics*, vol. 103, no. 3, p. 033304, 2008.
- [177] R. J. Carman, “Modelling of the kinetics and parametric behaviour of a copper vapour laser: Output power limitation issues,” *Journal of Applied Physics*, vol. 82, no. 1, p. 71, 1997.
- [178] M. D. Kilgore, H. M. Wu, and D. B. Graves, “Neutral transport in high plasma-density reactors,” *Journal of Vacuum Science & Technology B: Microelectronics and Nanometer Structures Processing, Measurement, and Phenomena*, vol. 12, no. 1, pp. 494–506, 1994.
- [179] X. Yan, Y. Lin, R. Huang, W. Hang, and W. W. Harrison, “A spectroscopic investigation of the afterglow and recombination process in a microsecond pulsed glow discharge,” *Journal of Analytical Atomic Spectrometry*, vol. 25, pp. 534–543, 2010.
- [180] A. Rousseau, G. Cartry, and X. Dutet, “Surface recombination of hydrogen atoms studied by a pulsed plasma excitation technique,” *Journal of Applied Physics*, vol. 89, no. 4, pp. 2074–2078, 2001.
- [181] A. Bouchoule and P. Ranson, “Study of volume and surface processes in low pressure radio frequency plasma reactors by pulsed excitation methods. i. hydrogen–argon plasma,” *Journal of Vacuum Science & Technology A*, vol. 9, no. 2, pp. 317–326, 1991.
- [182] A. D. Tserepi and T. A. Miller, “Two-photon absorption laser-induced fluorescence of H atoms: A probe for heterogeneous processes in hydrogen plasmas,” *Journal of Applied Physics*, vol. 75, no. 11, pp. 7231–7236, 1994.

BIBLIOGRAPHY

- [183] C. M. Samuell and C. S. Corr, “Ion flux dependence of atomic hydrogen loss probabilities on tungsten and carbon surfaces,” *Journal of Nuclear Materials*, vol. 451, pp. 211–215, 2014.
- [184] F. Gaboriau and J. P. Boeuf, “Chemical kinetics of low pressure high density hydrogen plasmas: Application to negative ion sources for ITER,” *Plasma Sources Science Technology*, vol. 23, no. 6, p. 065032, 2014.
- [185] D. L. Baulch, C. J. Cobos, R. A. Cox, C. Esser, P. Frank, T. Just, J. A. Kerr, M. J. Pilling, J. Troe, R. W. Walker, and J. Warnatz, “Evaluated kinetic data for combustion modelling,” *Journal of Physical and Chemical Reference Data*, vol. 21, no. 3, pp. 411–734, 1992.
- [186] S. Jacq, C. Cardinaud, L. Le Brizoual, and A. Granier, “H atom surface loss kinetics in pulsed inductively coupled plasmas,” *Plasma Science and Technology*, vol. 22, no. 5, p. 055004, 2013.
- [187] J. Lede and J. Villermaux, “Diffusion et recombinaison hétérogène simultanées des atomes d’hydrogène dans un réacteur en écoulement entre 50 et 760 torr,” *Journal de Chimie Physique*, vol. 71, pp. 85–92, 1974.
- [188] P. J. Chantry, “A simple formula for diffusion calculations involving wall reflection and low density,” *Journal of Applied Physics*, vol. 62, no. 4, pp. 1141–1148, 1987.
- [189] O. V. Ogorodnikova, “Comparison of hydrogen gas-, atom- and ion-metal interactions,” *Journal of Nuclear Materials*, vol. 277, no. 2-3, pp. 130–142, 2000.
- [190] S. Takashima, M. Hori, T. Goto, A. Kono, and K. Yoneda, “Absolute concentration and loss kinetics of hydrogen atom in methane and hydrogen plasmas,” *Journal of Applied Physics*, vol. 90, no. 11, pp. 5497–5503, 2001.
- [191] H. Ludvigsen, M. Tossavainen, and M. Kaivola, “Laser linewidth measurements using self-homodyne detection with short delay,” *Optics Communications*, vol. 155, pp. 180–186, 1998.

BIBLIOGRAPHY

- [192] S. Huang, T. Zhu, M. Liu, and W. Huang, “Precise measurement of ultra-narrow laser linewidths using the strong coherent envelope,” *Scientific Reports*, pp. 1–7, 2017.
- [193] M. Aramaki, Y. Okumura, M. Goto, S. Muto, S. Morita, and K. Sasaki, “Measurements of gas temperature in high-density helicon-wave h₂ plasmas by diode laser absorption spectroscopy,” *Japanese Journal of Applied Physics*, vol. 44, p. 6759, 09 2005.
- [194] D. Elliott, E. Scime, and Z. Short, “Novel xenon calibration scheme for two-photon absorption laser induced fluorescence of hydrogen,” *Review of Scientific Instruments*, vol. 87, no. 11, pp. 2014–2017, 2016.
- [195] R. P. Doerner, M. J. Baldwin, T. C. Lynch, and J. H. Yu, “Retention in tungsten resulting from extremely high fluence plasma exposure,” *Nuclear Materials and Energy*, vol. 9, pp. 89–92, 2016.